Density Functional Theory and Descriptor-Based Strategies for Tailoring the Properties of Nanomaterials

A Thesis

Submitted For the Degree of

DOCTOR OF PHILOSOPHY

in the Faculty of Science

by

Sukanya Ghosh

THEORETICAL SCIENCES UNIT
JAWAHARLAL NEHRU CENTRE FOR ADVANCED SCIENTIFIC RESEARCH
Bangalore – 560 064, India

JUNE 2018

To My Parents

DECLARATION

I hereby declare that the matter embodied in the thesis entitled "**Density Functional Theory and Descriptor-Based Strategies for Tailoring the Properties of Nanomaterials** " is the result of investigations carried out by me at the Theoretical Sciences Unit, Jawaharlal Nehru Centre for Advanced Scientific Research, Bangalore, India under the supervision of Prof. Shobhana Narasimhan and that it has not been submitted elsewhere for the award of any degree or diploma.

In keeping with the general practice in reporting scientific observations, due acknowledgement has been made whenever the work described is based on the findings of other investigators. Any omission that might have occurred by oversight or error of judgement is regretted.

Sukanya Ghosh

CERTIFICATE

I hereby certify that the matter embodied in this thesis entitled "**Density Functional Theory and Descriptor-Based Strategies for Tailoring the Properties of Nanomaterials** " has been carried out by Ms. Sukanya Ghosh at the Theoretical Sciences Unit, Jawaharlal Nehru Centre for Advanced Scientific Research, Bangalore, India under my supervision and that it has not been submitted elsewhere for the award of any degree or diploma.

Prof. Shobhana Narasimhan
(Research Supervisor)

Acknowledgements

The person whom I would like to thank first and the most is my Ph.D. advisor Prof. Shobhana Narasimhan. She provided me with all the possible opportunities to explore exciting and interesting area of research. She always encouraged me to think rationally in order to understand a project and analyze the results obtained. Her suggestions helped me not only to solve a problem, but also to improve the quality of the research. It would have been impossible for me to complete my projects and thesis without her constant guidance and support. She gave me chances to travel to other countries for scientific purposes and to visit renowned institutions. She not only guided me academically but also gave me valuable pieces of advice regarding the life. She helped me to overcome stress and tension in academic as well as in personal life. I have learnt a lot from her during my Ph.D. life. I am really grateful to her because without her constant support and guidance it would have been difficult for me to finish my research work.

Next, I would like to thank my collaborators: K. George Thomas, Pratap Zalake, Jerome Lagoute, Vincent Repain, Sylvie Rousset, Yannick J. Dappe, V. D. Pham, Arindam Ghosh, Nisha Mammen, Rajdeep Banerjee, Debdipto Acharya, Sourav Mondal, Devina Sharma, Aruna Nair, Rishav Harsh.

I thank my course instructors Prof. U. V. Waghmare, Prof. Subir K. Das, Prof. N. S. Vidhyadhiraja, Prof. Kavita Jain, Prof. Rajesh Ganapathy and Prof. Balasubramanian. I want to thank all the faculty from TSU. I want to acknowledge

the present and past chair persons of TSU. I am thankful to Prof. Sridhar Rajaram, Prof. M. Weinert, Prof. Hannu Häkkinen, Prof. R. Gebauer and Prof. S. Scandolo for the useful scientific discussions I had with them.

I acknowledge the financial help from the TUE-CMS, Indo-French CEFIPRA grant and JNCASR for supporting my research.

I thank everyone in the Academic Section, especially Dr. Princy and Sukanya Maam. I would like to thank Mr. Jayachandra, Ms. Jayamangala, Mr. Joydeep Deb, and all others in the Administrative Section for their help with all the administrative procedures. I thank Dr. Archana and all Dhanvantri staff. I am thankful to the CCMS staff Vijay, Anand, Anoop, Suresh for their help and support with computing facilities. I want to thank all the library staff and the hostel staff.

I thank all my past and present labmates: Mighfar, Madhura, Nisha, Kanchan, Sananda, Vasudevan, Bulumoni, Debarati, Debdipto, Rajdeep, Rajiv, Devina, Somesh, Saikat, Sourav, Nandana, and Abhishek for providing a lively and pleasant environment in the lab. We have had interactive group discussions and fun activities. My present labmates Devina, Rajdeep, Debdipto, Nandana and Abhishek helped me during my Ph.D. thesis completion.

I thank all my Ph.D. batchmates for spending many joyful moments with me. I acknowledge Prof. Pati's and Prof. Waghmare's group for their help. My respectful gratitude to Prof. C. N. R. Rao for providing excellent research facilities and scientific environment in the institute.

Finally, I thank my parents for being a source of constant support and strength for years. This thesis is dedicated to them.

Preface

In this thesis we have designed materials using density functional theory (DFT) calculations. I have also formulated descriptors that can successfully predict different target properties for the various systems studied in this thesis. Using these descriptors can considerably speed up the process of materials design.

In **Chapter 1**, we give a brief introduction to the problems studied in the thesis. The research work described in this thesis is primarily focused on two areas: molecular self-assembly and nanocatalysis.

In the first part of this thesis the organic molecules we have studied are phenyleneethynylenes and tetracyanoquinodimethane (TCNQ). We have investigated the structural and electronic properties of these organic molecules both in the gas phase and when self-assembled on graphene. Such systems are of interest for applications in molecular electronics. We have explored how the properties of such systems can be tuned by varying the chemical moieties in the molecules as well as their attachment sites. We have also studied how to tune the charge distribution within a TCNQ-graphene system by the application of an external electric field.

In the second part of my thesis We are interested in tuning the charge state of Au nanoclusters by support doping. The charge state plays an important role in determining the reactivity of these clusters. We are aided in this goal by developing a descriptor that can predict the efficacy of aliovalent doping in oxides such as MgO.

In **Chapter 2**, We discuss the main computational techniques and theoretical

formalism used in this thesis: density functional theory (DFT), the DFT-D2 technique to include dispersion interactions, time dependent density functional theory (TDDFT) to calculate excited state phenomena, the Tersoff-Hamann approach for simulation of scanning tunneling microscopy (STM) images, and the polarizable continuum model (PCM) to include solvent effects in DFT.

In **Chapter 3**, We have formulated simple descriptors to predict the structures of host and host-guest assemblies formed when phenyleneethynylene (PE) molecules comprised of different chemical motifs and various guests molecules of different sizes are deposited on graphene. As a first step, three host molecules and five guest molecules are used to construct a DFT database. The DFT results, for the preferred structure of the assemblies and the corresponding STM images, agree well with the experimental results for each host molecule, as well as each host-guest pair. To formulate a descriptor which can predict the resulting pattern, the target property is chosen to be the difference in free energy between the different self-assembled patterns possible. For the first time, simple descriptors have been identified which can successfully predict the architecture of the resulting host and host-guest assemblies. These descriptors can be computed at essentially zero computational cost, since they depend only on the structure of, and the chemical motifs present in, the isolated host and guest molecules in the gas phase. Finally, several test molecules are used to verify the predictive power of the host descriptor.

In **Chapter 4**, We have studied the electronic properties of phenyleneethynylene (PE) molecules in the gas phase and when self-assembled on graphene. The property of primary interest is their HOMO-LUMO gap, since this is responsible for their optoelectronic properties. The various PE molecules considered differ from one other in the conjugatio length, and the number and attachment sites of the alkoxy chains present in the molecule. It is found that DFT calculations can successfully explain the UV/VIS absorption spectra obtained from experiments, and a good match is also obtained between simulated and experimental STM images. Finally, descriptors are

identified and they can be correlated with the target property, viz., the HOMO-LUMO gap of the PE molecules. The HOMO-LUMO gaps depend on the conjugation length when the number and attachemnt sites of the alkoxy chains remain constant. In the case of the PE molecules with same conjugation length, this descriptor is found to be the shortest distance between two oxygen atoms present in the alkoxy chains in the PE molecules. The validity of this descriptor is verified by considering a large number of test cases. It is found that the HOMO-LUMO gap of PE molecules depends not only on the shortest oxygen-oxygen distance, but also on the electron conjugation present. The presence of conjugation lowers the HOMO-LUMO gap, as does deposition on graphene.

In **Chapter 5**, We investigate the possibility of using an external electric field to tune the charge transfer between graphene and an adsorbed monolayer of TCNQ, and hence the charge density in graphene. A monolayer of TCNQ is deposited on two kinds of substrates: either pristine or nitrogen-doped graphene. DFT calculations are first performed to investigate the electric field dependence on the charge transfer and the electric dipole in the combined TCNQ monolayer on pristine graphene system; these results are interpreted in combination with STM experiments performed by our collaborators. The effect of nitrogen-doping in graphene on the movement of energy levels, and the change in the charge state of an adsorbed TCNQ monolayer on it, are also studied. In both calculations and experiments, the movement of molecular levels due to the electric field is observed. The electric field causes opposite shifts in the molecular states and the Dirac point of graphene. The shifts in these energy levels depend on the magnitude and polarity of the electric field. Electron transfer between TCNQ and graphene, and thus the charge density in graphene, is tuned by the electric field. Combining this effect with nitrogen-doping of graphene permits one to perform selective reduction of a single TCNQ in monolayer. These results suggest a novel way of tuning the charge density in graphene for device applications.

In **Chapter 6**, a method is proposed to measure the ionicity of bonds in binary

compounds from first-principles calculations. I use the ratio of the "Bader charge" ($\mathcal{Q}_T$) to the nominal oxidation state (OS) as a measure of ionicity in binary compounds. Several different cations and anions are chosen, with different electronegativities and covalent radii. It is found that the ratio of the difference in electronegativities, $\Delta\chi$, and the difference in atomic radii, ΔR, can be used as a descriptor to predict our target property $\mathcal{Q}_T/OS$. It is found that when $\Delta\chi/\Delta R > 4$, the compound is purely ionic. It is notable that we find that both $\Delta\chi$ and ΔR are important in determining the ionicity of bonds.

In **Chapter 7**, it is proposed and demonstrated that substrate doping can be used as a technique to tune the charge state of supported Au nanoclusters. Considering the model systems of monomers and dimers of Au on doped MgO supports, it is found that the charge state of Au nanocatalysts can be tuned by depositing them on various doped MgO substrates. As a first step, MgO is doped with different acceptor and donor type impurities which can be either cationic or anionic. It is found that the difference in electronegativity ($\Delta\chi$), and the difference in atomic radii (ΔR) between the cation and the anion can be used to predict the efficacy of a dopant. Finally $\Delta\chi/\Delta R$ is used as a descriptor to find efficient dopants for MgO, for which the ratio of Bader charge ($\mathcal{Q}_T$) to the nominal oxidation (OS) state approaches 1. Using this descriptor it is found that Li is the best acceptor dopant for MgO, while both the donor dopants Al and F perform equally well. This finding is then used to tune the charge state of Au nanoclusters supported on doped MgO substrates. We have successfully made Au monomer positively charged on Li-doped and Na-doped MgO. Therefore, using a simple descriptor we are able to successfully predict the efficacy of a dopant and can apply it to tune the charge state of deposited Au nanocatalysts.

In **Chapter 8**, the main conclusions in each chapter are summarized and possible directions for future work are discussed.

List of Publications

1. "Descriptor-Based Rational Design of Two-Dimensional Self-Assembled Nanoarchitectures Stabilized by Hydrogen Bonds", P. Zalake, S. Ghosh, S. Narasimhan and K. George Thomas, *Chem. Mater.* **29** (17), 7170 (2017).

2. "Descriptors for the Reactivity of Au Nanocatalysts: Evaluating the Performance of the *d*-band center, the Effective Coordination Number and the Dual-Center Descriptor", Nisha Mammen, Sukanya Ghosh, Rajdeep Banerjee, Debdipto Acharya, Sourav Mondal, Devina Sharma and Aruna Nair and Shobhana Narasimhan (submitted).

3. "Tuning Interfacial Charge Transfer Between Organic Molecules and Graphene by Tip-induced electric Field and Nitrogen Doping", V.D. Pham, S. Ghosh, F. Joucken, M. Pelaez-Fernandez, V. Repain, C. Chacon, A. Bellec, Y. Girard, S. Rousset, Y. J. Dappe, S. Narasimhan, J. Lagoute (under revision).

4. "Descriptor for the Efficacy of Aliovalent Doping and its Applications for Charging Supported Au Clusters", S. Ghosh, N. Mammen and S. Narasimhan (preprint available).

5. "Verifying Oxide Doping as a Route to Charging Supported Au Nanoparticles: ab initio DFT Calculations", S. Ghosh, N. Mammen and S. Narasimhan (in preparation).

6. “Simple Descriptor to Determine HOMO-LUMO gap of Organic Molecules”, S. Ghosh, P. Zalake, S. Narasimhan and K. George Thomas (in preparation).

List of Abbreviations

$\mathcal{E}$	Electric field
$\mathcal{Q}_{\mathrm{T}}$	Topological charge
ρ	Charge density
$d_{\mathrm{O-O}}$	Distance between oxygen atoms
E_{D}	Energy of Dirac point
E_{F}	Fermi energy
E_{HOMO}	Energy of HOMO
E_{LUMO}	Energy of LUMO
OS	Oxidation state
1D	One-dimensional
2D	Two-dimensional
BSSE	Basis Set Superposition Error
BZ	Brillouin Zone
DFT	Density Functional Theory

DZP Double Zeta Polarized

GGA Generalized Gradient Approximation

HEX Hexagonal

HOMO Highest Occupied Molecular Orbital

KS Kohn Sham

LIN Linear

LUMO Lowest Unoccupied Molecular Orbital

meV mili electron-volts

ML Monolayer

PBE Perdew, Burke and Ernzerhof

PDOS Projected Density of States

PE Phenyleneethynylene

QE Quantum ESPRESSO

SAM Self-Assembled Monolayer

SIESTA Spanish Initiative for Electronic Simulations with Thousands of Atoms

STM Scanning Tunneling Microscopy

STS Scanning Tunneling Spectroscopy

TCNQ Tetracyanoquinodimethane

TDDFT Time-dependent density functional theory

Contents

List of Figures

List of Tables

Chapter 1

Intro

1.1 Rational Design of Materials

In materials science, there is a constant quest to discover new materials. The discovery of novel advanced materials feeds technological innovation. For example, one might hope to find a new material that is harder than diamond, or which shows more electroconductivity than copper or silver. Until now, to develop or identify a material with desired properties, this has occurred either by accidental discoveries or by a process of trial and error. Both these methods are not efficient or scientifically satisfactory. Therefore it is desirable to replace this by a program of rational materials design.

Experiments play an important role in designing new materials. However, experiments are often time-consuming, expensive, and require a significant amount of manpower. These factors involve a lot of uncertainty and limitations in the discovery of materials.

Computer simulations are another way to design materials. Since the experimental techniques have some incompleteness or limitations, in order to understand the properties of the materials more fundamentally or in a detailed manner, modern materials research often requires close integration between computation and experiments.

There are a large number of computational techniques which are used as tools

to develop new materials. The most useful and popular computational methods are: electronic structure calculations based on density functional theory,[1, 2] Monte Carlo simulations,[3, 4] molecular dynamics techniques,[5] and phase-field methods.[6] Usually, computation is quicker and less expensive than experiments. So computer simulation often offers a better route for the rational design of materials, since it may avoid the troublesome trial-error cycle and one can also lessen the need for strenuous experiments.

However, there are some shortcomings in relying heavily on calculations for rational materials design. Most of the time, supercomputing facilities are required to apply all these techniques to investigate material properties. The computational cost depends on the size and/or number of the systems one has to study and also on the requirement of the accuracy of results. Moreover, despite considerable advances in theoretical techniques, there remain classes of systems and properties where the accuracy of the results obtained in computational calculations remains questionable.

So to design materials rationally one needs to find alternative routes, instead of getting mired down by experimental hazards and computational difficulties. It has come to be realized that the rational design of materials can be considerably aided by identifying simple parameter(s), called descriptors.

1.1.1 Descriptors

Descriptors are combinations of physically meaningful parameters of a system which correlate well with the property of interest. Descriptors provide a cheaper and quicker alternative for predicting the property of interest. The idea of formulating descriptors has already been used in the literature to predict different properties of materials, e.g., the catalytic activity of transition metal elements, or the crystal structure of three-dimensional octet compounds, etc.[7–9]

To carry out the rational design of materials using descriptors, one needs to follow a few steps. The first step is to decide the target property for which the descriptor has to be identified. Then density functional theory calculations are performed to

create a database called the training set. Once the calculations are done, these results have to be analyzed. After analyzing the results obtained from the calculations, a descriptor would be formulated either by using physical/chemical intuition and/or regression analysis or with the help of machine learning algorithms. In the next step, the descriptor would be verified for the test or validation set. Once the descriptor is identified successfully, it can be applied to design new improved materials with the desired property or properties.

For a descriptor to be successful, the time taken to evaluate it should be much less than that required to perform a complete first-principles calculation or program of experiments, yet the descriptor should correlate well with the property of interest. The main advantage of the descriptor is that it saves considerable time, yet enables one to rapidly shortlist a group of candidate systems that can be explored further using more detailed and accurate methods.

Target Properties Studied Using Descriptors

In this thesis, we have studied materials using density functional theory (DFT) calculations and have formulated descriptors that can successfully predict different target properties for the various systems studied here. The use of these descriptors can considerably speed up the process of materials design.

In chapter 3, we have used descriptors to study the structures of self-assembled monolayers of phenyleneethynylene (PE) molecules. The difference in free energy between various possible self-assembled patterns is chosen as the target property to formulate a descriptor which can predict the resulting pattern. Apart from performing calculations on the systems constituting a DFT database, additional test molecules are chosen to validate the descriptor. Finally, it is found that the descriptor can successfully predict the resulting self-assembled patterns formed not only for the systems constituting the DFT database (training set), also for the test cases (validation set). Thus, for the first time, simple descriptors have been identified which can successfully predict molecular architectures. Importantly, these descriptors can

be computed at essentially zero computational cost, since they depend only on the structure of, and number of chemical motifs present in the isolated molecules in the gas phase.

In chapter 4, the HOMO-LUMO gaps of different PE molecules are considered as the target property. The HOMO-LUMO gap of the molecules in the training set is obtained from DFT calculations. We have identified a descriptor that can be correlated well with the target property. This descriptor is found to be the shortest distance between two oxygen atoms present in the alkoxy chains in the PE molecules. We have verified the validity of this descriptor by considering a large number of test cases.

We have studied the self-assembly and electronic structure of the acceptor-type molecule tetracyanoquinodimethane (TCNQ) on graphene in Chapter 5, under the application of an external electric field. From the combined DFT and experimental results, we find that both the molecular states and the graphene Dirac point shift simultaneously (in energy) in opposite directions, and that the TCNQ/graphene system acts like an induced dipole. The charge transfer between TCNQ and graphene can be tuned by the external electric field. Further, our results show that doping of graphene with a nitrogen atom causes selective reduction of a single TCNQ molecule in the monolayer. In the future, this work can could be extended for other molecule/substrate combinations, e.g., for any donor type molecule on boron-doped graphene, or depositing a combination of acceptor and donor type molecules on graphene or other substrates under an electric field. Before formulating descriptors that can predict how a certain property (or properties) of different molecule/substrate combinations can be influenced by the electric field, we need to study some more adsorbate-substrate combinations to create the database, this is the future direction of the work reported in Chapter 5.

A simple method is proposed to measure the ionicity of bonds in binary compounds from first- principles calculations and using a descriptor, in Chapter 6. Several cations

and anions are chosen, with different electronegativities and covalent radii. We use different binary compounds which are composed of the cations and anions of those elements. The ratio of the "Bader charge" ($\mathcal{Q}_T$) to the nominal oxidation state (OS) is considered to be the measure of the ionicity in these binary compounds. Therefore $\mathcal{Q}_T/OS$ is the target property in this case. For a perfect ionic compound, $\mathcal{Q}_T/OS$ should approach 1. We find that the ratio of the difference in electronegativities ($\Delta\chi$) to the difference in atomic radii between the cations and anions (ΔR) forming the compound can be used as a descriptor to predict the target property $\mathcal{Q}_T/OS$, and hence the ionicity, in binary compounds. We find that the ionicity increases with $\Delta\chi/\Delta R$, and gets saturated at 1 when $\Delta\chi/\Delta R > 4$.

In chapter 7, we use support doping to tune the charge state of deposited nanoclusters. As model systems, We use monomers and dimers of Au deposited on a doped MgO support. First, MgO is doped with different acceptor and donor type impurities which can be either cationic or anionic. For this purpose, my primary aim is to find the best acceptor and donor type dopants for MgO. As in Chapter 6, the ratio of the topological charge ($\mathcal{Q}_T$) to the nominal oxidation state (OS) of the dopants is used as the target property, to determine the efficacy of the dopant. It is found that the difference in electronegativity ($\Delta\chi$), and the difference in atomic radii (ΔR) between the cation and the anion can be used as a descriptor to predict the efficacy of a dopant. For the best dopant, the value of $\mathcal{Q}_T/OS$ should approach 1. Using $\Delta\chi/\Delta R$ as the descriptor, it is found that Li performs as the best acceptor type dopant, while both Al and F perform equally well as donor type dopants. Next, these findings are then used to tune the charge state of Au nanoclusters supported on doped MgO substrates. It is found that the charge state of the supported Au nanoclusters can be explained by using this simple descriptor. This implies that, without performing DFT calculations, but by just knowing the dopant and calculating $\Delta\chi/\Delta R$, one can predict the performance of a dopant in tuning the charge state of the supported Au nanoclusters deposited on a support doped with that impurity.

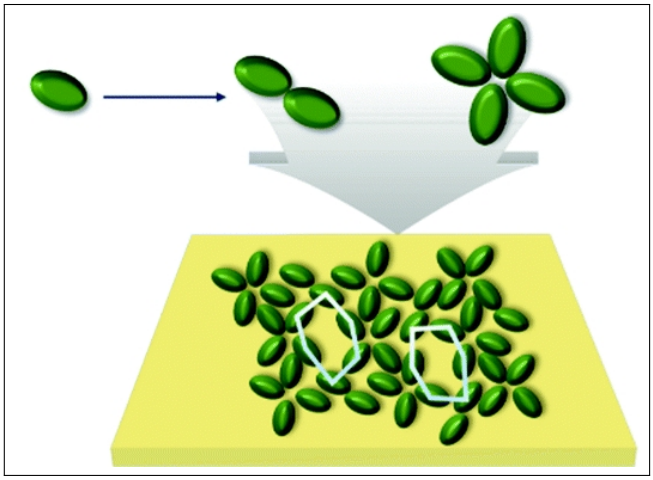

Figure 1.1: Schematic model of two-dimensional molecular self-assembly on surfaces. The self-assembled pattern is formed by the organization of the building blocks.[10] This figure is taken with permission from Ref. 10 ©(2016) Royal Society of Chemistry.

The main advantage of this descriptor is: $\Delta\chi$ is an already known quantity and ΔR can be evaluated at very low computational cost. Therefore, formulating a simple descriptor, one can successfully predict the efficacy of a dopant, and then apply this knowledge to tune the charge state of deposited Au nanocatalysts.

1.2 Molecular Self-Assembly

The first part of my thesis is focused on self-assembly of organic molecules. Self-assembly can occur everywhere, from the atomic to planetary scale, with the aid of different kinds of interactions provided the appropriate conditions are satisfied. Systems built through molecular self-assembly lie at the interface between materials science, chemistry, molecular biology, polymer science, and engineering.[11–15]

Molecular self-assembly is the spontaneous and reversible organization of the building blocks into ordered structures stabilized by various noncovalent interactions. These interactions include those responsible for weak chemical bonds, such as hydrogen bonding, $\pi - \pi$ stacking, electrostatic, van der Waals, steric and dipole-dipole interactions.[16, 17] Though these interactions are not strong, the collective effect of these interactions results in stable patterns. The molecular self-assembly is a process based on multiple weak intermolecular forces which can cause the creation of

different macroscopic patterns from relatively simple building blocks. Self-assembly is a bottom-up process which involves pre-existing components, which are distinct parts of a disordered structure; this process is reversible, and can be controlled by proper design of the components. The key engineering principle when building molecular self-assembled architectures is to design the molecular building blocks in a programmed manner.[18] The main principles responsible for the formation of molecular self-assembly are chemical complementarity and structural compatibility. This is similar to a lock and key mechanism, where size, shape, and orientation are important in order to have a complementary and compatible fitting.

We have studied self-assembly of different types of phenyleneethynylene (PE) molecules in Chapter 3 and Chapter 4. Chapter 3 is focused on the structural and geometrical properties of the PE molecules, while electronic properties of the PE molecules are investigated in Chapter 4. The PE molecules studied in this thesis differ from each other with respect to the number of chemical motifs present. In Chapter 5, the interaction between a self-assembled monolayer of the acceptor type molecule tetracyanoquinodimethane (TCNQ) and pristine or nitrogen-doped graphene is studied.

1.2.1 Types of Self-Assembly

Self-assembly arises due to spontaneous organization of individual units into an ordered pattern. Different kinds of self-assembly exist in nature. The self-assembled patterns can differ based on the types of building blocks involved, the physical properties of the assemblies, e.g., their dimensions, mechanisms, etc., which are responsible for forming the assembly.

Self-assembly exists everywhere in nature at both miscroscopic and macroscopic scales, e.g., from the assembly of stars and planets in the galaxy, flocks of birds in the sky, to the schools of fish in the ocean. In the world of materials also self-assembly can be achieved in different kinds of systems, e.g., organic molecules,[19–21] inorganic compounds,[22–24], metal-organic complexes,[25–27] and biomaterials.[28–30] Some

examples of the organic molecules which can form self-assembled architectures are: oligo-phenyleneethynylene (OPE),[31–33] poly-phenyleneethynylene,[34, 35] oligothiophene (OT),[36, 37] tetracynoquinodimethane (TCNQ),[38, 39] tetrathiafulvalene (TTF),[40] etc., and also the assembly of different acids, e.g., phosphonic acids,[41] amino acids,[42, 43] terephthalic acid etc.[44, 45] Common examples of the self-assembly built by inorganic compounds are: assemblies of gold nano particles,[46, 47] architecturse formed by different metal ions, e.g., Cu ions etc.[48] Self-assembly can occur in biomaterials also, and the most well-known examples are the self-assembly of DNA and RNA.[49–52]

Self-assembled patterns exist in different dimensions. Previous authors have studied self-assembled patterns in zero-dimensional non-centrosymmetric nanostructures, one-dimensional nanoscale objects, two-dimensional monolayers and three-dimensional structures. Zero-dimensional self-assembly is observed in quantum dots,[53, 54] while one-dimensional self-assembled structures are found in nanorods, nanoribbons, etc.[55, 56] The most common examples of two-dimensional self-assembled patterns are monolayers of organic molecules.[57–60] Three-dimensional self-assembled patterns are observed in colloids,[61] silica fibers,[62] three-dimensional crystals designed from DNA, etc.[63–65]

There are mainly two types of self-assembled patterns, based on the mechanisms responsible for the resulting pattern: static and dynamic.[66, 67] In static self-assembly, the ordered structures are formed when a system reaches an energy minimum, and they do not dissipate energy. The most common examples of static self-assembly are supramolecular systems, nanoparticles, nanorods, and liquid crystals. In dynamic self-assembly, the interactions responsible for the formation of self-assembled patterns between components only occur if the system dissipates energy.[68] Examples of dynamic self-assembly are the solar system, galaxies, oscillating and reaction-diffusion reactions, weather patterns, etc. In dynamic self-assembly, the components interact with each other in a complex manner. The study of dynamic self-assembly is in its

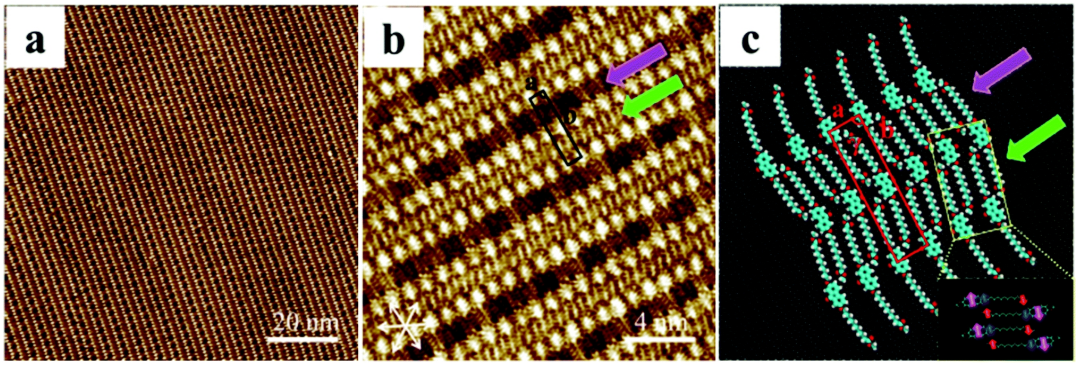

Figure 1.2: (a) Large-scale and (b) high-resolution STM images of 7-bis(10-n-alkoxycarbonyl-decyloxy)-9-fluorenone derivatives showing the linear pattern at the 1-phenylotane/graphite interface. The molecular rows with different stretching directions are denoted by purple (dark stripe) and green (bright stripe) arrows, respectively. (c) The proposed packing model for the linear structure. The dipole alignments of fluorenone cores, ether group and ester group are reflected in the enlarged section.[69] This figure is taken with permission from Ref. 69 ©(2017) Royal Society of Chemistry.

starting stage at the present moment.[66]

1.2.2 Noncovalent Interactions in Molecular Self-Assembly

Molecular self-assembly occurs due to the spontaneous organization of molecular building blocks. The physical properties of the building blocks, such as size, shape, charge state, surface area, polarizability, dipole moment, mass, etc., determine the interactions among them, and hence play an important role in stabilizing the resulting pattern. The choice and design of the individual components that organize themselves into desired patterns are the main ingredients in determining the self-assembled patterns.

The self-assembled patterns involve various non-covalent interactions, e.g., hydrogen bonds, van der Waals interactions, $\pi - \pi$ interactions, metallo-ligand interactions, etc. The non-covalent interactions are generally weak, with energies ranging from 5 kJ mol^{-1} to 250 kJ mol^{-1}.[70]

van der Waals Interactions

The van der Waals interaction is the weakest non-covalent interaction.[69, 71–73] It is also known as the dispersion interaction, whose strength reduces with increase in

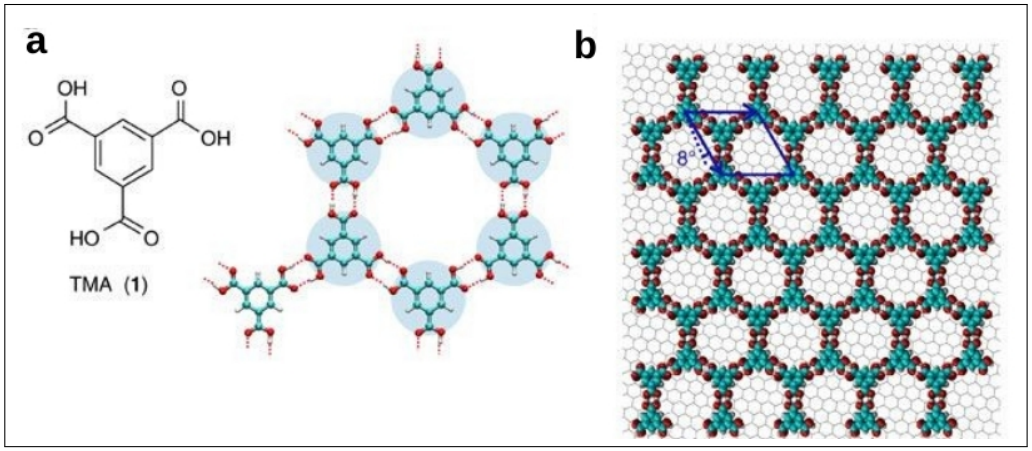

Figure 1.3: (a) Formation of hydrogen bonds between neighboring trimeric acid (TMA) molecules. (b) Honey-comb network of TMA molecules is stabilized by the formation of hydrogen bonds between the COOH groups of the neighboring TMA molecules.[74] This figure is taken with permission from Ref. 74 ©(2018) Macmillan Publishers Limited, part of Springer Nature.

distance between adjacent atoms or molecules taking part in this interaction. Weak van der Waals interactions play a dominant role in the stabilization and formation of highly ordered two-dimensional assemblies on surfaces. However, they do not provide directionality during the formation of self-assembled patterns on the surfaces. van der Waals interactions exist, for example, in the self-assembled patterns shown in Fig. 1.2.

Hydrogen Bonding

Hydrogen bonding is the most important interaction for stabilizing the supramolecular architectures.[75–79] Hydrogen bonding can be denoted as X-H—A, this denotes the formation of a hydrogen bond between a hydrogen atom (H) and an electronegative atom (A). The strength of the interaction and hence the lengths of the hydrogen bond, are dictated by the difference in electronegativity between H and A. The energy of hydrogen bonds varies in a wide range.[80]

The energy of moderate hydrogen bonding falls in the range of 4 – 15 kcal mol^{-1}. The hydrogen bonds which fall above and below this range are classified as strong and weak hydrogen bonds respectively. The energy of weak hydrogen bonds is less than 4 kcal mol^{-1} and they provide weak directionality. The most common examples

of weak hydrogen bonds are X-H—O and X-H—π, where X = C, N, etc. These weak hydrogen bonds play an important role in the fields of structural chemistry and biology. The strength of the moderate hydrogen bonds varies in the range of 4 – 15 kcal mol^{-1} and, provide directionality. Such bonds are found in carboxylic acids, alcohols, and biomolecules. Strong hydrogen bonds are quasi-covalent in nature. The strength of strong hydrogen bonds varies in the range of 15 — 40 kcal mol^{-1} and they provide high directionality. Such hydrogen bonds are commonly observed in hydrated protons, HF complexes, and acid dimers. Fig. 1.3 shows self-assembled patterns stabilized by the formation of hydrogen bonds.

1.2.3 Advantages and Applications of Molecular Self-Assembly

Advantages

Molecular self-assembly is one of the most promising fields of research in chemistry, materials science, molecular biology, polymer science, and engineering. Self-assembled structures are important from the fundamental as well as technological aspects. The properties of self-assembly are sensitive to the arrangement and electronic characteristics of the building blocks. Self-assembled architectures contain information regarding the physical and chemical characteristics of the individual components, e.g., size, shape, surface properties, charge, polarizability, magnetic dipole, mass, etc.. These properties are responsible for determining the interactions among the units of the self-assembled patterns. The choice and design of components that organize themselves into desired patterns and functions, is the key feature in determining their applications.[42, 81–83]

There are two main approaches in designing materials and constructing devices: top-down and bottom-up approach. Top-down methods to design materials are capital oriented, and limited in their ability to provide raw materials in large quantities. It is also difficult to achieve fine features at nanometer scale or less. Self-assembly is a bottom-up approach, since it occurs by the 'automatic' arrangement of the

building blocks in some ordered manner. There are major advantages of the bottom-up techniques, hence self-assembly, which is able to handle components in large quantities, can be used to construct devices at the molecular scale. Nanostructures can be built from self-assembly at lower cost than the devices constructed from the top-down approach.

Bottom-up methods can provide nanostructures in large quantities. Self-assembly is a process which can successfully consider a large number of components together which are involved in pattern formation, e.g., crystallization can involve $\sim 10^{27}$ molecules,[84, 85] while self-assembly of proteins typically involves thousands of molecules.[86, 87]

Though top-down methods are versatile, they can not provide features at the atomic or molecular scale. Bottom-up approaches are useful to construct materials at the molecular scale. Constructing nanostructures using biological components is a technologically important area, e.g., fabrication of DNA and protein arrays,[28, 29, 86, 87] manipulating or examining the biological cells with nanometer scale probes, etc., are examples of the phenomena which require the combination of numerous components of small size.

Self-assembly is a parallel process since it can involve a large number of components at a time and does not involve any expensive technique to construct the nanostructures. Therefore, self-assembly always has an advantage in cost over other methods of fabrication.

Applications

Molecular self-assembly is used in optical, electronic, thermal, mechanical, and biological applications,[11–13] as liquid crystals,[84, 85] gels,[88, 89] also as the materials for molecular-scale electronics, photovoltaic cells,[90], solar cells,[91–93] elctronic devices,[94, 95] and drug delivery devices.[96, 97] Self-assembly is an approach which can lead human civilization towards a world of molecular-based devices and technology for all our useful purposes, e.g., Fig. 1.4 shows a molecule-based FET.

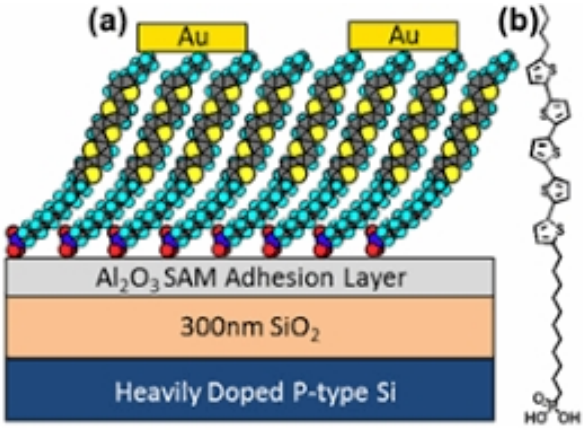

Figure 1.4: (a) Self-assembled monolayer of BQT-PA on nanolayers of aluminum oxide, are shown to enable low-voltage organic field-effect transistors (OFETs) through dielectric and interface engineering on rigid and plastic substrates.(b) Chemical structure of a single BQT-PA molecule.[98] This figure is taken with permission from Ref. 98 ©(2011) Elsevier.

During the last few decades, there is an increasing demand for shrinking the technology and devices down in size. For example, within only fifty years we have gone from the very first computer (ENIAC) weighing 27 tonnes, to the MacBook, which has a weight of a little over a kilogram. We can see the result of this progress towards the reduction in size for almost all kinds of devices around us, e.g., from our phones to tiny transport drones. Recently, human civilization has reached the stage where one can engineer machines which are so tiny so that they can enter the human body to deliver drugs or can even perform minute operations. Machines of this size cannot be built by simply reducing the size of their components. This implies we must build them using bottom-up approach, i.e., by using atoms or molecules as the building blocks. Materials made out of molecular self-assembly guide us towards the direction to construct devices at the molecular scale.

Molecules that contain π-conjugated units, e.g., oligo-phenyleneethynylenes (OPE), oligothiophenes (OT), oligophenylenevinylenes (OPV), and oligophenylenes (OP) are an important class of building blocks, since their self-assemblies are important not only from the fundamental aspect, but also to fabricate systems for organic electronic and photovoltaic applications, due to their highly conducting nature.[99, 100] Both

their length and the chemical motifs, like the alkyl chains and the functional groups attached to these kinds of molecules, control the optoelectronic properties of the building blocks,[101] and hence of the resulting supramolecular patterns. These kinds of molecules are used as rectifiers for heterometallic molecular junctions,[102] molecular wires, [99, 100, 103] etc. Molecular self-assembly formed by the 'perfect' combination of molecules having donor or acceptor type behavior can drive the formation of organic light-emitting diodes, [104–107] organic field-effect transistors,[36, 37, 108, 109] etc., with promising electronic and/or optical properties. Molecular self-assembly is also used in the fields of catalysis[110–112] and biomedical applications.[113, 114].

Often it is important to deposit these assemblies on surfaces, in order to use them in various possible applications. The interactions between molecular self-assemblies and surfaces are often useful for fundamental interest as well as technological applications. For example, the self-assembly of molecules on graphene has potential applications in graphene-based field-effect devices.[115, 116]

Such systems are important because of their huge relevance for applications in organic electronics, which is a rapidly growing field in modern technology. This field is important not just from the point of fundamental science, but also because it is recognized as one of the most promising and competitive areas for future industrial applications. In spite of low carrier mobility, low electronic and optical stability the organic materials have some advantages which make them important for technological applications. These materials are compatible with large area processes, they require low-temperature processing which requires a low cost. These molecules and polymers are compatible with inorganic semiconductors and can be tailored easily for specific electronic or optical properties. In particular, the expansion of this field is supported by the development of active components which can be easily processable, are energy friendly, flexible, and cheap.

Scientists have already proposed molecular machines built out of molecular self-assembly, such as a molecular car, a molecular elevator, etc. These ideas of making

molecular machines are now at a very early stage,[117–119] we hope they could be successfully developed in the near future.

1.3 Nanocatalysis

The second part of my thesis is focused on nanocatalysis. The charge state of supported nanocatalysts is investigated using density functional theory calculations and descriptors.

Catalysts are materials that open favorable pathways for chemical reactions. The presence of catalysts is necessary to improve the reaction rate. Catalysts play an important role in our lives. More than 90% of industrial processes are dependent on catalysts. Catalytic processes are involved in the production of polymers, plastics, fabrics, synthetic rubbers, cosmetics, etc. Important applications of nanocatalysts are in water purification,[120, 121] fuel cells,[122, 123] biodiesel production,[124, 125] dyes etc.[126, 127] The catalyst dependent production of clean energy from the renewable energy sources, such as the generation of hydrogen from non-edible biomass, is important for fuel cells and transportation fuels. To save the environment from harmful gases, catalysts are used to reduce emissions of toxic or otherwise undesirable gases like CO, NO and hydrocarbons from mobile vehicles. The pharmaceutical industry uses catalysts for the production of medicines and drugs which are used to save lives and cure diseases. Fig. 1.5(a) shows bimetallic Pt-Au nanocatalysts supported on In_2O_3, which have applications in the detection of acetone, which is useful to diagnose diabetes.[128]

In this era of nanotechnology, all the devices and technologies are proceeding towards smaller sizes, along with improved properties. Reduction in dimensionality usually leads to an improvement in catalytic properties. The main idea for understanding the concept of nanocatalysis involves the ratio of surface area to volume, since, when an object becomes larger, its surface area increases to a lesser extent compared to its volume. Therefore, objects with smaller sizes have more surface

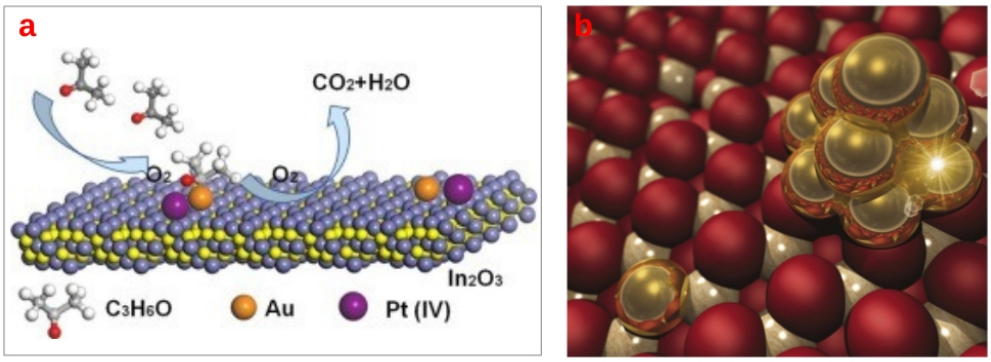

Figure 1.5: (a) Bi-metallic Pt-Au nanocatalysts supported on In_2O_3 are useful for the detection of acetone, which can be utilized to diagnose diabetes.[128] This figure is taken with permission from Ref. 128 ©(2018) Elsevier. (b) Au nanoparticles deposited on a CeO_2 support show good catalytic activity for the water gas shift reaction.[129] This figure is taken with permission from Ref. 129 ©(2010) Royal Society of Chemistry.

area with respect to their volume. For chemical reactions, this feature has important implications. High surface-area-to-volume ratios of nanocatalysts improve the rate of chemical reactions. Also, importantly, at the nanoscale, materials achieve many additional or enhanced properties which their macroscopic counterparts do not possess.

Since many years, several elements and materials such as iron, aluminum, titanium dioxide, silica, and clay have been used as catalysts in the form of ultrafine particles. The reason for the significant increase in reactivity when the catalyst size was reduced, was not fully understood in the beginning. It was initially considered that the increase in reactivity arises only due to the increase in the proportion of the surface elements which are catalytically active, i.e., the increase in the surface to volume ratio. Later, with the development of nanoscience, and the better understanding of phenomena at the nanoscale, it has been proved that in addition to the increase in surface area and heterogeneity of atomic structure, nanoparticles also exhibit quantum size effects in their electronic structure. When the dimensionality reduces from the extended bulk systems to the two-dimensional layers, to one-dimensional wires and to zero-dimensional clusters, there is a decrease in the coordination number of the atoms

in the system. This is another important reason for the tremendous increase in the reactivity of materials upon the reduction in size. Moreover, reduction in the size of the nanoparticles used as catalysts allows us to use less quantity of the catalyst material, and considering the fact that many important catalysts used today are precious metals, this is a great advantage in using nanoparticles as catalysts.

1.3.1 Catalytic Reactions

A catalytic reaction is a thermodynamically feasible chemical reaction, where the addition of a particular chemical substance increases the rate of the reaction, but the substance itself does not undergo any chemical change. The chemical species which enhances the reaction rate is called a catalyst. A catalyst can increase the speed of a reaction in one of the three ways: it can decrease the activation energy for the reaction, it can act as a promoter and bring the reactive species together more efficiently, or it can create a higher rate of production of one species when many other products could be formed. Nanocatalysts can be used in all these ways mentioned, depending on their requirement. Thus, catalysts work by providing an alternative mechanism for a chemical reaction, by involving a different transition state leading to a lower energy barrier; this is shown schematically in Fig. 1.6.

A catalyst can accelerate the rates of both the forward and reverse reactions. Another important property of a catalyst is its effect on selectivity. The presence of different catalysts can result in different product distribution from the same starting material. For example, decomposition of ethanol in the presence of boron phosphate gives ethylene and diethyl ether as the products,[131] while when Mo_2C/carbon is used as the catalysts for the same reaction, hydrogen and acetaldehyde are produced.[132]

Types of Catalytic Reactions

There are two main types of catalytic reactions: heterogeneous and homogeneous.

Heterogeneous Catalysis

In heterogeneous catalysis, the catalyst(s) and the reactants exist in different

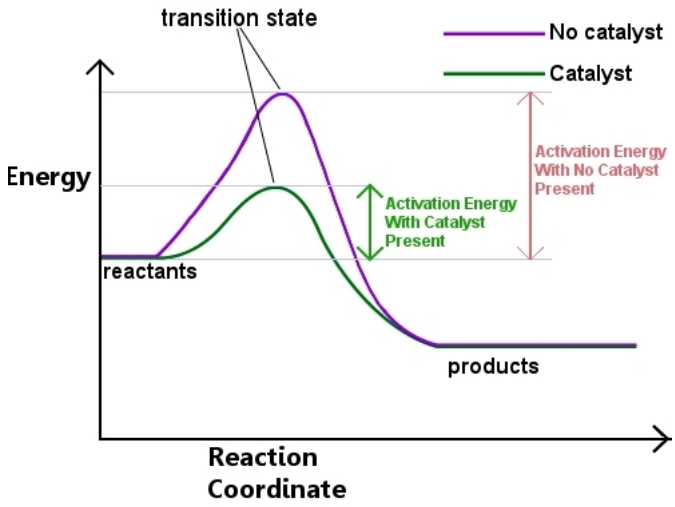

Figure 1.6: Schematic diagram showing the activation energy barrier for a given reaction in the presence and absence of a catalyst. The purple path is when the chemical reaction takes place without any catalyst, while the green path shows the reaction mechanism in the presence of the catalyst. The activation energy barrier reduces when the catalyst is present.[130] This figure is taken with permission from Ref. 130 ©(2017) chemicool.com.

phases. The most common examples of heterogeneous catalysis are the reactions of liquids or gases in the presence of solid catalysts.[133, 134]

The entire surface of a solid catalyst does not show catalytic activity to enhance the rate of a reaction. There are only certain sites on the catalyst surface which actually participate in the chemical reaction and these sites are known as the active sites on the catalysts. The chemical activity of a catalyst is directly proportional to the number of these active sites available on the surface.

Heterogeneous catalysis takes place through a few steps. If the reactant exists in the fluid phase then at the first step, transportation of the reactant occurs towards the external surface of the catalysts from the bulk fluid. Next, diffusion of the reactants takes place from the external area to the internal catalytic surface followed by the adsorption of the reactants onto the active sites of the catalyst. Reaction on the catalyst surface produces the product. Desorption of the product occurs from the active sites of the catalyst. The product diffuses from the interior part of the catalyst to the external surface. Finally, transfer of the product takes place from the external

surface of the catalyst to the bulk fluid. [135]

Homogeneous Catalysis

In the case of homogeneous catalysis, the catalyst exists in the same phase as the reactants, i.e., all the reactants and catalysts are either in one single liquid or gaseous phase. Most of the industrial homogeneous catalytic processes are carried out in the liquid phase. The production of polyethylene in the presence of organometallic catalysts, ester hydrolysis involving general acid-base catalysts, and enzyme catalyzed processes are some of the important examples of industrial homogeneous catalytic processes.[136, 137]

1.3.2 Rational Design of Nanocatalysts

It is a desirable goal to produce new or improved catalysts which represent significant progress, both economically and intellectually. Better catalysts could have a longer lifetime, could be cheaper, and/or could be more effective in lowering the activation barriers than existing catalysts. One should also consider environmental demands while making any improvement in these catalysts, and for this purpose, any polluting chemical reaction should ideally be replaced with an environmentally friendly alternative.

Computational studies also play an important role in the rational design of better catalysts. The field of computational catalysis started in the 1990s,[138] mainly due to the development of more powerful computers, which could be used to carry out numerous calculations based on sophisticated computational methods like density functional theory[1] and quantum mechanics/molecular mechanics. [139] In the present scenario it is possible to investigate catalytic reactions at surfaces in great detail, and with enough accuracy using computational studies as well as experiments. Sometimes computational approaches become easier and more accurate than experiments, since experiments based on catalysis can be very complex, time-consuming and expensive. Using computation, one can investigate the effect of several individual parameters which are responsible for the reactivity and the performance of

a catalyst. Computational studies focus on the understanding of the mechanisms of catalytic processes and can provide fruitful suggestions regarding which parameter(s) can be tuned, and how, for enhancing the desired property of the catalyst.

Using a large amount of data from computational calculations, one can also develop models that can explain trends in the reactivity of several catalysts; one popular example of such a model is the *d*-band model suggested by Hammer and Nørskov.[140, 141] This model suggests that the reactivity of a transition metal element can be predicted just by looking at its *d*-band density of states. A single parameter can be extracted from the density of states of the *d*-band, which is called the *d*-band center, this is actually the weighted average of the *d*-band density of states. This parameter is useful to predict the reactivity of different catalysts and it helps one to select appropriate catalysts for particular reactions.[142]

1.3.3 Methods to Control Catalytic Activity of Nanoparticles

Nanoclusters are very often placed on an oxide support when they are used in applications. These supports play a crucial role in improving properties like the reactivity and stability of the nanoclusters. The support can improve the reactivity of the deposited clusters in three ways: (1) by tuning the charge state of the cluster,[143–147] (2) by modifying the morphology of the cluster,[146, 147] and also (3) by the presence of new catalytically active sites at the cluster-support interface.[143, 144] The most common examples of nanocatalysts widely used for scientific and industrial purposes are Au, Pt, Pd, Ni, Cu, Fe and Rh.[46, 47, 148–152] Fig. 1.5 shows an example of gold catalysis, where Au nanoparticles deposited on CeO_2, show catalytic activity for the water gas shift reaction.

The charge state and morphology of the supported nanocatalysts depend on the nature of the support.[153] One way is through charge transfer from an appropriately chosen (pristine) support. [129, 154–164] Depending on the difference in work function

between the nanoclusters and the support, electron transfer can take place from the support to the deposited nanocatalysts or vice-versa. Oxides like MgO, CaO, TiO_2, Al_2O_3 and CeO_2 are the most commonly used supports for nanocatalysts. The electronic properties of the oxide supports can be modified by doping with impurity atoms,[165–170] introducing oxygen vacancies,[154, 171–175] and placing the oxide on a metal slab.[154, 155, 176–180] Other ways of tuning the charge state of the nanoparticles are by alloying,[173, 181–184] or applying an external electric field.[185] Substrate doping is a very easy and efficient technique to tune the properties of supported nanocatalysts. Doping a support with a specific impurity can significantly modify its electronic properties, which can be used to tune the charge states of deposited nanoparticles.

Monomers and dimers of Au are chosen as the nanocatalysts in Chapter 7. Bulk Au is inert but it shows surprisingly good catalytic activity in nano dimensions.[186] The catalytic activity of Au nanoparticles depends on their charge state. CO, C_2H_4 and H_2 bind more strongly on positively charged Au clusters, [157, 187–192] which are also better catalysts for several reactions such as the dissociation of water.[165] However, negatively charged clusters are better catalysts for O_2 dissociation, [193–195] the conversion of CO to CO_2,[196–198] NO to NO_2,[199, 200] as well as the oxidation of methanol[201] and the oxidation of propylene.[202, 203]

The change in the morphology and change in the charge state are intimately connected. Importantly, the change in morphology of supported Au nanoparticles induced by aliovalent doping of the oxide support has been not only predicted theoretically,[167] but also confirmed experimentally.[204] Doping the support with an electron donor makes the adsorbed Au nanoclusters negatively charged, while doping with an acceptor is expected to create electron deficiency in the support, which should increase the tendency of the support to withdraw electrons from the Au cluster, thus making it positively charged. However, due to the high electronegativity of Au, making the Au clusters positively charged can be a challenging task, and is of

great interest.

MgO is considered as the oxide support and in my calculations, we have doped MgO substitutionally with aliovalent dopants. We have chosen different acceptor and donor type impurities to dope MgO. MgO is doped with both cationic and anionic dopants. The doping of different oxide supports with donor-type impurities, and their role in tuning the charge state of deposited nanoclusters have already been studied by previous authors. In my study, we dope MgO support with donor as well as acceptor-type impurities. Au nanoclusters are then deposited on the doped MgO supports. It is found that the charge state of the nanoclusters can be tuned by depositing them on the doped supports. The charge on the supported Au nanoclusters can be further modified by placing the doped MgO support on a metal slab, which is Mo for our case. Finally, a simple descriptor is formulated which can predict the performance of the dopant and also its application in tuning the charge state of the Au nanoclusters deposited on the doped support. When the metal support is used, we find that the charge state and morphology of the deposited nanoparticles can be predicted by making use of the work function of the support as a descriptor.

In all the investigations described in this thesis, the main computational method we have used is density functional theory (DFT).[1, 2]

The main conclusions from each chapter, and a brief outlook for future prospects, are summarized in Chapter 8 of this thesis.

Bibliography

[1] P. Hohenberg and W. Kohn *Phys. Rev.*, vol. 136, p. B864, 1964.

[2] W. Kohn and L. J. Sham *Phys. Rev.*, vol. 140, p. A1133, 1965.

[3] J. M. Hammersley and D. C. Handscomb. Dordrecht: Springer Netherlands, 1964.

[4] C. Jacoboni and L. Reggiani *Rev. Mod. Phys.*, vol. 55, pp. 645–705, 1983.

[5] S. Nosé *Molecular Physics*, vol. 52, pp. 255 – 268, 1984.

[6] R. Folch, J. Casademunt, A. Hernández-Machado, and L. Ram´irez-Piscina *Phys. Rev. E*, vol. 60, pp. 1734–1740, 1999.

[7] L. M. Ghiringhelli, J. Vybiral, S. V. Levchenko, C. Draxl, and M. Scheffler *Phys. Rev. Lett.*, vol. 114, no. 15, p. 105503, 2015.

[8] F. Gältl, P. Müller, P. Uchupalanun, P. Sautet, and I. Hermans *Chem. Mater.*, vol. 29, no. 15, pp. 6434–6444, 2017.

[9] Y. Zheng, K. Song, J. Jung, C. Li, Y.-U. Heo, M.-S. Park, M. Cho, Y.-M. Kang, and K. Cho *Chem. Mater.*, vol. 27, no. 9, pp. 3243–3249, 2015.

[10] S. Yang, A. Jeon, R. W. Driver, Y. Kim, E. H. Jeon, S. Kim, H.-S. Lee, and H. Lee *Phys. Chem. Chem. Phys.*, vol. 18, pp. 14172 – 14176, 2016.

[11] J. M. Lehn *Chemica Scripta.*, vol. 28, p. 237, 1988.

[12] J. M. Lehn *Science*, vol. 295, pp. 2400 – 2403, 2002.

[13] D. S. Lawrence, T. Jiang, and M. Levett *Chemical Reviews*, vol. 95, pp. 2229 – 2260, 1995.

[14] J. M. Lehn *Angew. Chem., Int. Ed.*, vol. 29, pp. 1304 – 1319, 1990.

[15] D. J. Prockop and A. Fertala *J. Struct. Biol.*, vol. 122, pp. 111 – 118, 1998.

[16] G. Desiraju *Acc. Chem. Res.*, vol. 35, pp. 565 – 573, 2002.

[17] J. A. A. W. Elemans, A. E. Rowan, and R. J. M. Nolte *J. Mater. Chem.*, vol. 13, pp. 2661 – 2670, 2003.

[18] P. J. Stang and B. Olenyuk *Acc. Chem. Res.*, vol. 30, pp. 502 – 518, 1997.

[19] P. S. W. Rachel K Smith, Penelope A Lewis *Prog. surf. sci.*, vol. 75, pp. 1 – 68, 2004.

[20] J. van der Lit, J. L. Marsman, R. S. Koster, P. H. Jacobse, S. A. den Hartog, D. Vanmaekelbergh, R. J. M. Klein Gebbink, L. Filion, and I. Swart *J. Phys. Chem. C*, vol. 120, pp. 318 – 323, 2016.

[21] M. A. Belen, C. Diego, P. Inigo, V. Giovanni, B. Alessandro, P. Jan, S. Karol, D. F. Steven, P. Francesco, M. Mario, N. K. Andrei, M. Manuel, and M. Aurelio *Angew. Chem. Int. Ed.*, vol. 56, pp. 6946 – 6951, 2017.

[22] M.-P. Pileni *Angew. Chem. Int. Ed.*, vol. 40, pp. 685 – 693, 2007.

[23] Y. Zheng, Y. Huang, Z. M. Abbas, and B. C. Benicewicz *Polym. Chem.*, vol. 8, pp. 370 – 374, 2017.

[24] X. G. Qiao, O. Lambert, J.-C. Taveau, P.-Y. Dugas, B. Charleux, M. Lansalot, and E. Bourgeat-Lami *Macromolecules*, vol. 50, pp. 3796 – 3806, 2017.

[25] S. M. Oburn, D. C. Swenson, S. V. S. Mariappan, and L. R. MacGillivray *J. Am. Chem. Soc.*, vol. 139, pp. 8452 – 8454, 2017.

[26] M. Fujita *Chem. Soc. Rev.*, vol. 27, pp. 417 – 425, 1998.

[27] G. Lal, S. J. Lee, D. M. Spasyuk, and G. K. H. Shimizu *Chem. Commun.*, vol. 54, pp. 1722 – 1725, 2018.

[28] C. G. Evans and E. Winfree *Chem. Soc. Rev.*, vol. 46, pp. 3808 – 3829, 2017.

[29] H. He, K. Rahimi, M. Zhong, A. Mourran, D. R. Luebke, H. B. Nulwala, M. Möller, and K. Matyjaszewski *Nat. Commun.*, vol. 46, pp. 3808 – 3829, 2017.

[30] S. Zhang *Nat. Biotech.*, vol. 21, pp. 1171 – 1178, 2003.

[31] S. Zhang, Y. Geng, Y. Fan, W. Duan, K. Deng, D. Zhao, and Q. Zeng *Phys. Chem. Chem. Phys.*, vol. 19, pp. 31284 – 31289, 2017.

[32] S. Werner, J. Ebenhan, M. Poppe, S. Poppe, H. Ebert, C. Tschierske, and K. Bacia *Polymers*, vol. 9, p. 476, 2017.

[33] L. Cheng, J. Yang, Y. Yao, D. W. Price, S. M. Dirk, and J. M. Tour *Langmuir*, vol. 20, pp. 1335 – 1341, 2004.

[34] M. R. Pinto, B. M. Kristal, and K. S. Schanze *Langmuir*, vol. 19, pp. 6523 – 6533, 2003.

[35] C. Y.-S. Chung and V. W.-W. Yam *J. Am. Chem. Soc.*, vol. 133, pp. 18775 – 18784, 2011.

[36] E. Schillinger, E. MenaOsteritz, J. Hentschel, H. G. Börner, and P. Bäuerle *Adv. Mater.*, vol. 21, pp. 1562 – 1567, 2009.

[37] P. Leclére, M. Surin, P. Viville, R. Lazzaroni, A. F. M. Kilbinger, O. Henze, W. J. Feast, M. Cavallini, F. Biscarini, A. P. H. J. Schenning, and E. W. Meijer *Chem. Mater.*, vol. 16, pp. 4452 – 4466, 2004.

[38] P. J. Blowey, L. A. Rochford, D. A. Duncan, D. A. Warr, T.-L. Lee, D. P. Woodruff, and G. Costantini *Faraday Discuss.*, vol. 204, pp. 97 – 110, 2017.

[39] C. Wackerlin, C. Iacovita, D. Chylarecka, P. Fesser, T. A. Jung, and N. Ballav *Chem. Commun.*, vol. 47, pp. 9146 – 9148, 2011.

[40] M. Souto, C. Rovira, I. Ratera, and J. Veciana *Cryst. Eng. Comm.*, vol. 19, pp. 197 – 206, 2017.

[41] E. S. Gawalt, M. J. Avaltroni, N. Koch, and J. Schwartz *Langmuir*, vol. 17, pp. 5736 – 5738, 2001.

[42] G. Whitesides, J. Mathias, and C. Seto *Science*, vol. 254, pp. 1312–1319, 1991.

[43] H. Lu, J. Wang, Z. Song, L. Yin, Y. Zhang, H. Tang, C. Tu, Y. Lin, and J. Cheng *Chem. Commun.*, vol. 50, pp. 139 – 155, 2014.

[44] B. Quiroga Arganaraz, L. J. Cristina, L. M. Rodriguez, A. Cossaro, A. Verdini, L. Floreano, J. D. Fuhr, J. E. Gayone, and H. Ascolani *Phys. Chem. Chem. Phys.*, vol. 20, pp. 4329 – 4339, 2017.

[45] A. Della Pia, D. Luo, R. Blackwell, G. Costantini, and N. Martsinovich *Faraday Discuss.*, vol. 204, pp. 191 – 213, 2018.

[46] Y. Ofir, B. Samanta, and V. M. Rotello *Chem. Soc. Rev.*, vol. 37, pp. 1814 – 1825, 2008.

[47] S. Lin, M. Li, E. Dujardin, C. Girard, and S. Mann *Adv. Mater.*, vol. 17, pp. 2553 – 2559, 2005.

[48] B. Paul, L. JeanMarie, A. DeCian, and J. Fischer *Angew. Chem. Int. Ed.*, vol. 32, pp. 69 – 72, 1993.

[49] J. Sharma, R. Chhabra, A. Cheng, J. Brownell, Y. Liu, and H. Yan *Science*, vol. 323, pp. 112–116, 2009.

[50] S. M. Douglas, H. Dietz, T. Liedl, B. Högberg, F. Graf, and W. M. Shih *Nat. Commun.*, vol. 459, pp. 414 – 418, 2009.

[51] T. H. LaBean, J. H. Reif, and N. C. Seeman *Nat. Commun.*, vol. 407, pp. 493 – 496, 2000.

[52] S. H. Ko, M. Su, C. Zhang, A. E. Ribbe, W. Jiang, and C. Mao *Nat. Chem.*, vol. 2, pp. 1050 – 1055, 2010.

[53] H. Mattoussi, J. M. Mauro, E. R. Goldman, G. P. Anderson, V. C. Sundar, F. V. Mikulec, and M. G. Bawendi *J. Am. Chem. Soc.*, vol. 122, pp. 12142 – 12150, 2000.

[54] D. Cui, B. Pan, H. Zhang, F. Gao, R. Wu, J. Wang, R. He, and T. Asahi *Anal. Chem.*, vol. 80, pp. 7996 – 8001, 2008.

[55] L. C. Palmer and S. I. Stupp *Accounts of Chemical Research*, vol. 41, pp. 1674 –1684, 2008.

[56] L. Zang, Y. Che, and J. S. Moore *Acc. Chem. Res.*, vol. 41, pp. 1596 – 1608, 2008.

[57] W. Liu, X. Luo, Y. Bao, Y. P. Liu, G.-H. Ning, I. Abdelwahab, L. Li, C. T. Nai, Z. G. Hu, D. Zhao, B. Liu, S. Y. Quek, and K. P. Loh *Nat. Chem.*, vol. 9, pp. 563 – 570, 2017.

[58] S. De Feyter and F. C. De Schryver *Chem. Soc. Rev.*, vol. 32, pp. 139 – 150, 2003.

[59] M. Pfeffermann, R. Dong, R. Graf, W. Zajaczkowski, T. Gorelik, W. Pisula, A. Narita, K. Mllen, and X. Feng *J. Am. Chem. Soc.*, vol. 137, pp. 14525 – 14532, 2015.

[60] F. Silly *J. Phys. Chem. C*, vol. 121, pp. 10413 – 10418, 2017.

[61] M. Y. Ben Zion, X. He, C. C. Maass, R. Sha, N. C. Seeman, and P. M. Chaikin *Science*, vol. 358, pp. 633–636, 2017.

[62] H.-Y. Mi, X. Jing, H.-X. Huang, and L.-S. Turng *Materials Letters*, vol. 204, pp. 45 – 48, 2017.

[63] J. Zheng, J. J. Birktoft, Y. Chen, T. Wang, R. Sha, P. E. Constantinou, S. L. Ginell, C. Mao, and N. C. Seeman *Nature*, vol. 461, pp. 74 – 77, 2009.

[64] L. L. Ong, N. Hanikel, O. K. Yaghi, C. Grun, M. T. Strauss, P. Bron, J. Lai-Kee-Him, F. Schueder, B. Wang, P. Wang, J. Y. Kishi, C. Myhrvold, A. Zhu, R. Jungmann, G. Bellot, Y. Ke, and P. Yin *Nat. Commun.*, vol. 552, pp. 72 – 77, 2017.

[65] F. Xu, D. Wu, Y. Huang, H. Wei, Y. Gao, X. Feng, D. Yan, and Y. Mai *ACS Macro Lett.*, vol. 6, pp. 426 – 430, 2017.

[66] G. M. Whitesides and B. Grzybowski *Science*, vol. 295, pp. 2418 – 2421, 2002.

[67] J. V. I. Timonen, M. Latikka, L. Leibler, R. H. A. Ras, and O. Ikkala *Science*, vol. 341, pp. 253–257, 2013.

[68] G. Kokot, G. V. Kolmakov, I. S. Aranson, and A. Snezhko *Sci. Rep.*, vol. 7, p. 14726, 2017.

[69] M. Dong, K. Miao, Y. Hu, J. Wu, J. Li, P. Pang, X. Miao, and W. Deng *Phys. Chem. Chem. Phys.*, vol. 19, pp. 31113–31120, 2017.

[70] G. R. Desiraju *Nature*, vol. 8, pp. 397 – 400, 2001.

[71] K. Tahara, S. Lei, J. Adisoejoso, S. De Feyter, and Y. Tobe *Chem. Commun.*, vol. 46, pp. 8507 – 8525, 2010.

[72] H.-Y. Gao, H. Wagner, P. A. Held, S. Du, H.-J. Gao, A. Studer, and H. Fuchs *Appl. Phys. Lett.*, vol. 106, p. 081606, 2015.

[73] H. Ascolani, M. W. van der Meijden, L. J. Cristina, J. E. Gayone, R. M. Kellogg, J. D. Fuhr, and M. Lingenfelder *Chem. Commun.*, vol. 50, pp. 13907 – 13909, 2014.

[74] J. D. Cojal Gonzlez, M. Iyoda, and J. P. Rabe *Nat. Commun.*, vol. 8, p. 14717, 2017.

[75] N. A. Wasio, R. C. Quardokus, R. P. Forrest, C. S. Lent, S. A. Corcelli, J. A. Christie, K. W. Henderson, and S. A. Kandel *Nature*, vol. 507, pp. 86 – 89, 2014.

[76] T. Kato, H. Kihara, U. Kumar, T. Uryu, and J. M. J. Fréchet *Angew. Chem. Int. Ed.*, vol. 33, pp. 1644 – 1645, 1994.

[77] D. C. Sherrington and K. A. Taskinen *Chem. Soc. Rev.*, vol. 30, pp. 83 – 93, 2001.

[78] X. Zhu, R. Zou, P. Sun, Q. Wang, and J. Wu *Polym. Chem.*, vol. 9, pp. 69 – 76, 2018.

[79] S. Griessl, M. Lackinger, M. Edelwirth, M. Hietschold, and W. M. Heckl *Sing. Mol.*, vol. 3, pp. 25 – 31, 2002.

[80] T. Steiner and G. R. Desiraju *Chem. Commun.*, pp. 891 – 892, 1998.

[81] V. Balzani, A. Credi, and M. Venturi *Chem. Euro. J.*, vol. 3, pp. 25 – 31, 2002.

[82] S. Srinivasan, V. K. Praveen, R. Philip, and A. Ajayaghosh *Angew. Chem.*, vol. 120, pp. 5834 – 5838, 2008.

[83] L. Zhi and K. Mullen *J. Mater. Chem.*, vol. 18, pp. 1472 – 1484, 2008.

[84] T. Kato *Science*, vol. 295, pp. 2414 – 2418, 2002.

[85] J. P. F. Lagerwall, C. Schütz, M. Salajkova, J. Noh, J. Hyun Park, G. Scalia, and L. Bergström *Npg Asia Mater.*, vol. 6, pp. 2414 – 2418, 2014.

[86] H. Yan, S. H. Park, G. Finkelstein, J. H. Reif, and T. H. LaBean *Science*, vol. 301, pp. 1882–1884, 2003.

[87] L. Yan, L. Chenxiang, L. Hanying, and Y. Hao *Angew. Chem.*, vol. 117, pp. 4407 – 4412, 2005.

[88] Y. Habibi, L. A. Lucia, and O. J. Rojas *Chem. Rev.*, vol. 110, pp. 3479 – 3500, 2010.

[89] H. A. R., E. Beatriu, M. JuanF., and S. DavidK. *Angew. Chem. Int. Ed.*, vol. 47, pp. 8002 – 8018, 2008.

[90] K. M. Coakley, Y. Liu, M. D. McGehee, K. L. Frindell, and G. D. Stucky *Adv. Funct. Mater.*, vol. 13, pp. 301 – 306, 2003.

[91] C. Cabanetos, A. El Labban, J. A. Bartelt, J. D. Douglas, W. R. Mateker, J. M. J. Fréchet, M. D. McGehee, and P. M. Beaujuge *J. Am. Chem. Soc.*, vol. 135, pp. 4656 – 4659, 2013.

[92] J. Nelson *Science*, vol. 293, pp. 1059 – 1060, 2001.

[93] J. Peet, A. J. Heeger, and G. C. Bazan *Acc. Chem. Res.*, vol. 42, pp. 1700 – 1708, 2009.

[94] D.-L. Long, E. Burkholder, and L. Cronin *Chem. Soc. Rev.*, vol. 36, pp. 105 – 121, 2007.

[95] B. A. Parviz, D. Ryan, and G. M. Whitesides *IEEE Trans, Adv, Pack.*, vol. 26, pp. 233 – 241, 2003.

[96] A. Rösler, G. W. Vandermeulen, and H.-A. Klok *Adv. Drug Del. Rev.*, vol. 53, pp. 95 – 108, 2001.

[97] R. A. Hirst, B. Escuder, F. J. Miravet, and K. D. Smith *Angew. Chem. Int. Ed.*, vol. 47, pp. 8002 – 8018, 2008.

[98] D. O. Hutchins, O. Acton, T. Weidner, N. Cernetic, J. E. Baio, G. Ting, D. G. Castner, H. Ma, and A. K.-Y. Jen *Org. Elec.*, vol. 13, pp. 464 – 468, 2012.

[99] L. A. Bumm, J. J. Arnold, M. T. Cygan, T. D. Dunbar, T. P. Burgin, L. Jones, D. L. Allara, J. M. Tour, and P. S. Weiss *Science*, vol. 271, pp. 1705–1707, 1996.

[100] W. B. Davis, W. A. Svec, M. A. Ratner, and M. R. Wasielewski *Nature*, vol. 396, pp. 60–63, 1998.

[101] H. Valkenier, C. M. Guedon, T. Markussen, K. S. Thygesen, S. J. van der Molen, and J. C. Hummelen *Phys. Chem. Chem. Phys.*, vol. 16, pp. 653 – 662, 2014.

[102] J. G. Kushmerick, J. Lazorcik, C. H. Patterson, R. Shashidhar, D. S. Seferos, and G. C. Bazan *Nano Lett.*, vol. 4, pp. 639 – 642, 2004.

[103] T. Shimidzu, H. Segawa, F. Wu, and N. Nakayama *J. Photochem. and Photobio. A: Chem.*, vol. 92, pp. 121 – 127, 1995.

[104] V. Bliznyuk, B. Ruhstaller, J. P. Brock, U. Scherf, and S. A. Carter *Adv. Mater.*, vol. 11, pp. 1257 – 1261, 1999.

[105] D. A. Pardo, G. E. Jabbour, and N. Peyghambarian *Adv. Mater.*, vol. 12, pp. 1249 – 1252, 2000.

[106] J. E. Malinsky, G. E. Jabbour, S. E. Shaheen, J. D. Anderson, A. G. Richter, T. J. Marks, N. R. Armstrong, B. Kippelen, P. Dutta, and N. Peyghambarian *Adv. Mater.*, vol. 11, pp. 227 – 231, 1999.

[107] C. ShunChi, L. Jie, B. Jayesh, Y. Yang, O. Jun, and K. Junji *Adv. Mater.*, vol. 11, pp. 734 – 737, 1999.

[108] P. T. Herwig and K. Müllen *Adv. Mater.*, vol. 11, pp. 480 – 483, 1999.

[109] B. S. Santhosh, P. Seelam, and A. Ayyappanpillai *Angew. Chem. Int. Ed.*, vol. 51, pp. 1766 – 1776, 2012.

[110] W. Shanshan, L. Yongguang, X. Siying, M. Cong, L. Joonwon, Z. Jiong, K. D. Seok, Y. Minyong, Y. D. Ki, L. Myongsoo, K. S. Ouk, and H. Zhegang *Angew. Chem.*, vol. 129, pp. 11669 – 11672, 2017.

[111] Y. Zhou and H. C. Zeng *Chem. Mater.*, vol. 29, pp. 6076 – 6086, 2017.

[112] H. Zhang, L.-Y. Guo, J. Jiao, X. Xin, D. Sun, and S. Yuan *ACS Sustain. Chem. & Eng.*, vol. 5, pp. 1358 – 1367, 2017.

[113] S. Czarnecki and A. Bertin *Chem. Euro. J.*, vol. 24, 2018.

[114] Z. Yongfeng, H. Wei, L. Jinyao, Z. Xinyuan, and Y. Deyue *Adv. Mater.*, vol. 22, pp. 4567 – 4590, 2010.

[115] P. Sol´is-Fernández, S. Okada, T. Sato, M. Tsuji, and H. Ago *ACS Nano*, vol. 10, pp. 2930 – 2939, 2016.

[116] B. C. Worley, R. T. Haws, P. J. Rossky, and A. Dodabalapur *J. Phys. Chem. C*, vol. 120, pp. 12909 – 12916, 2016.

[117] B. L. Feringa *Angew. Chem. Int. Ed.*, vol. 56, pp. 11060 – 11078, 2017.

[118] S. Kassem, T. van Leeuwen, A. S. Lubbe, M. R. Wilson, B. L. Feringa, and D. A. Leigh *Chem. Soc. Rev.*, vol. 46, pp. 2592 – 2621, 2017.

[119] W. R. Browne and B. L. Feringa *Nat. Nanotech.*, vol. 1, pp. 25 – 35, 2006.

[120] Y. Liu, J. Li, X. Qiu, and C. Burda *Water Prac. and Tech.*, vol. 1, p. 73, 2006.

[121] V. Likodimos, C. Han, M. Pelaez, A. G. Kontos, G. Liu, D. Zhu, S. Liao, A. A. de la Cruz, K. OShea, P. S. M. Dunlop, J. A. Byrne, D. D. Dionysiou, and P. Falaras *Indus. & Eng. Chem. Res.*, vol. 52, pp. 13957 – 13964, 2013.

[122] J. Prabhuram, X. Wang, C. L. Hui, and I.-M. Hsing *J. Phys. Chem. B*, vol. 107, pp. 11057 – 11064, 2003.

[123] M. Simes, S. Baranton, and C. Coutanceau *Appl. Catal. B: Environ.*, vol. 93, pp. 354 – 362, 2010.

[124] F. Qiu, Y. Li, D. Yang, X. Li, and P. Sun *Bio. Tech.*, vol. 102, pp. 4150 – 4156, 2011.

[125] M. Mirzajanzadeh, M. Tabatabaei, M. Ardjmand, A. Rashidi, B. Ghobadian, M. Barkhi, and M. Pazouki *Fuel*, vol. 139, pp. 374 – 382, 2015.

[126] A. Safavi and S. Momeni *J. Haza. Mater.*, vol. 201, pp. 125 – 131, 2012.

[127] Y. Liu, X. Chen, J. Li, and C. Burda *Chemosphere*, vol. 61, pp. 11 – 18, 2005.

[128] R.-J. Ma, G.-D. Li, X. Zou, R. Gao, H. Chen, and X. Zhao *Sens. and Act. B: Chem.*, vol. 270, pp. 247 – 255, 2018.

[129] C. Zhang, A. Michaelides, and S. Jenkins *Phys. Chem. Chem. Phys.*, vol. 13, pp. 22 – 33, 2010.

[130] "Definition of a catalyst." http://www.chemicool.com/definition/catalyst.html". [Online; accessed February-2018].

[131] J. Moffat and A. Riggs *J. Catal.*, vol. 28, pp. 157 – 160, 1973.

[132] R. Barthos, A. Széchenyi, Á. Koós, and F. Solymosi *Appl. Catal. A: Gen.*, vol. 327, pp. 95 – 105, 2007.

[133] N. Mizuno and M. Misono *Chem. Rev.*, vol. 98, pp. 199 – 218, 1998.

[134] A. T. Bell *Science*, vol. 299, pp. 1688–1691, 2003.

[135] Q. Zhang, W. Zhou, W. Qian, R. Xiang, J. Huang, D. Wang, and F. Wei *J. Phys. Chem. C*, vol. 111, pp. 14638–14643, 2007.

[136] D. J. Cole-Hamilton *Science*, vol. 299, pp. 1702–1706, 2003.

[137] C. L. Hill and C. M. Prosser-McCartha *Coord. Chem. Rev.*, vol. 143, pp. 407 – 455, 1995.

[138] W. Thiel *Angew. Chem. Int. Ed.*, vol. 53, pp. 8605–8613, 2014.

[139] A. Warshel and M. Levitt *J. Mol. Bio.*, vol. 103, pp. 227–249, 1976.

[140] B. Hammer and J. Nørskov in *Impact of Surface Science on Catalysis* (B. C. Gates and H. Knozinger, eds.), vol. 45 of *Advances in Catalysis*, pp. 71 – 129, Academic Press, 2000.

[141] B. Hammer and J. Nørskov *Surf. Sci.*, vol. 343, no. 3, pp. 211 – 220, 1995.

[142] J. K. Nørskov, T. Bligaard, J. Rossmeisl, and C. H. Christensen *Nature Chem.*, vol. 1, pp. 37–46, 2009.

[143] M. S. Chen and D. W. Goodman *Catal. Today*, vol. 111, pp. 22 – 33, 2006.

[144] L. M. Molina and B. Hammer *Phys. Rev. Lett.*, vol. 90, p. 206102, 2003.

[145] Z. Yan, S. Chinta, A. A. Mohamed, J. P. Fackler, and D. W. Goodman *J. Am. Chem. Soc.*, vol. 127, pp. 1604 – 1605, 2005.

[146] C. Harding, V. Habibpour, S. Kunz, A. N.-S. Farnbacher, U. Heiz, B. Yoon, and U. Landman *J. Am. Chem. Soc.*, vol. 131, pp. 538 – 548, 2009.

[147] D. Ricci, A. Bongiorno, G. Pacchioni, and U. Landman *Phys. Rev. Lett.*, vol. 97, p. 036106, 2006.

[148] H. Koga, T. Kitaoka, and H. Wariishi *J. Mater. Chem.*, vol. 19, pp. 5244 – 5249, 2009.

[149] S. J. Yoo, T.-Y. Jeon, K.-S. Lee, K.-W. Park, and Y.-E. Sung *Chem. Commun.*, vol. 46, pp. 794 – 796, 2010.

[150] Y. Shao, S. Zhang, C. Wang, Z. Nie, J. Liu, Y. Wang, and Y. Lin *J. Power Sources*, vol. 195, pp. 4600 – 4605, 2010.

[151] A. Bakr Ahmed Amine Nassr, A. Quetschke, E. Koslowski, and M. Bron *Electroch. Acta*, vol. 102, pp. 202 – 211, 2013.

[152] M. Simes, S. Baranton, and C. Coutanceau *Appl. Catal. B: Environ.*, vol. 93, pp. 354 – 362, 2010.

[153] M. Haruta *Catal. Today*, vol. 36, p. 153, 1997.

[154] P. Frondelius, H. Häkkinen, and K. Honkala *New J. Phys.*, vol. 9, p. 339, 2007.

[155] L. Giordano, M. Baistrocchi, and G. Pacchioni *Phys. Rev. B*, vol. 72, p. 115403, 2005.

[156] S. Dong, Y. Zhang, X. Zhang, J. Mao, and Z. Yang *App. Surf. Science*, vol. 426, pp. 554–561, 2017.

[157] N. Lopez and J. K. Nørskov *J. Am. Chem. Soc.*, vol. 124, pp. 11262–11263, 2002.

[158] X. Lin, B. Yang, H.-M. Benia, P. Myrach, M. Yulikov, A. Aumer, M. A. Brown, M. Sterrer, O. Bondarchuk, E. Kieseritzky, J. Rocker, T. Risse, H.-J. Gao, N. Nilius, and H.-J. Freund *J. Am. Chem. Soc.*, vol. 132, pp. 7745–7749, 2010.

[159] Y. G. Wang, D. Mei, V. A. Glezakou, J. Li, and R. Rousseau *Nat. Commun.*, vol. 6, 2015.

[160] J.-C. Liu, Y.-G. Wang, and J. Li *J. Am. Chem. Soc.*, vol. 139, pp. 6190–6199, 2017.

[161] M. M. Schubert, S. Hackenberg, A. C. van Veen, M. Muhier, V. Pizak, and R. J. Behm *J. Catal.*, vol. 197, pp. 113–122, 2001.

[162] A. R. Puigdollers, P. Schlexer, and G. Pacchioni *J. Phys. Chem. C*, vol. 119, pp. 15381–15389, 2015.

[163] M. Gao, A. Lyalin, and T. Taketsugu *Catalysts*, vol. 1, pp. 18–39, 2011.

[164] A. R. Puigdollers, P. Schlexer, and G. Pacchioni *J. Phys. Chem. C*, vol. 119, pp. 15381–15389, 2015.

[165] J. Graciani, A. Nambu, J. Evans, J. A. Rodriguez, and J. F. Sanz *J. Am. Chem. Soc.*, vol. 130, pp. 12056–12063, 2008.

[166] S. Prada, L. Giordano, and G. Pacchioni *J. Phys. Chem. C*, vol. 116, pp. 5781–5786, 2012.

[167] N. Mammen, S. Narasimhan, and S. de Gironcoli *J. Am. Chem. Soc.*, vol. 133, no. 9, pp. 2801–2803, 2011.

[168] N. Mammen, S. de Gironcoli, and S. Narasimhan *J. Chem. Phys.*, vol. 143, no. 14, p. 144307, 2015.

[169] F. Stavale, X. Shao, N. Nilius, H.-J. Freund, S. Prada, L. Giordano, and G. Pacchioni *J. Am. Chem. Soc.*, vol. 134, pp. 11380–11383, 2012.

[170] S. Prada, L. Giordano, and G. Pacchioni *J. Am. Chem. Soc.*, vol. 117, no. 19, pp. 9943–9951, 2013.

[171] L. A. Kappers, R. L. Kroes, and E. B. Hensley *Phys. Rev. B*, vol. 1, pp. 4151–4157, 1970.

[172] B. Yoon, H. Häkkinen, U. Landman, A. S. Wörz, J.-M. Antonietti, S. Abbet, K. Judai, and U. Heiz *Science*, vol. 307, pp. 403–407, 2005.

[173] L. Ma, K. Laasonen, and J. Akola *J. Phys. Chem. C.*, vol. 121, pp. 10876–10886, 2008.

[174] A. Del Vitto, G. Pacchioni, F. Delbecq, and P. Sautet *J. Phys. Chem. B*, vol. 109, pp. 8040–8048, 2005.

[175] Z. Yang, R. Wu, Q. Zhang, and D. W. Goodman *Phys. Rev. B*, vol. 65, p. 155407, 2002.

[176] P. Frondelius, H. Häkkinen, and K. Honkala *Phys. Rev. B*, vol. 76, p. 073406, 2007.

[177] K. Honkala and H. Häkkinen *J. Phys. Chem. C*, vol. 96, pp. 1200–1204, 1992.

[178] V. Simic-Milosevic, M. Heyde, N. Nilius, T. Knig, H.-P. Rust, M. Sterrer, T. Risse, H.-J. Freund, L. Giordano, and G. Pacchioni *J. Am. Chem. Soc.*, vol. 130, pp. 7814–7815, 2008.

[179] J. Nevalaita, H. Häkkinen, and K. Honkala *J. Phys. Chem. C.*, vol. 121, pp. 10824–10831, 2017.

[180] T. Risse, S. Shaikhutdinov, N. Nilius, M. Sterrer, and H. J. Freund *Acc. Chem. Res.*, vol. 41, pp. 949–956, 2008.

[181] L. Rout, A. Kumar, R. S. Dhaka, G. N. Reddy, S. Giri, and P. Dash *App. Catal. A: General*, vol. 538, pp. 107–122, 2017.

[182] C. Gao, Y. Hu, M. Wang, M. Chi, and Y. Yin *J. Am. Chem. Soc.*, vol. 136, pp. 7474–7479, 2014.

[183] L. Zhang, A. Wang, J. T. Miller, X. Liu, X. Yang, W. Wang, L. Li, Y. Huang, C.-Y. Mou, and T. Zhang *ACS Catal.*, vol. 4, pp. 1546–1553, 2014.

[184] T. Joseph, K. V. Kumar, A. Ramaswamy, and S. Halligudi *Catal. Commun.*, vol. 8, pp. 629–634, 2007.

[185] B. Yoon and U. Landman *Phys. Rev. Lett.*, vol. 100, p. 056102, 2008.

[186] M. Haruta and M. Daté *Applied Catalysis A: General*, vol. 222, pp. 427–437, 2001.

[187] A. Prestianni and A. Martorana *J. Phys.Chem. B*, vol. 110, pp. 12240–12248, 2006.

[188] A. Corma and H. Garcia *Chem. Soc. Rev.*, vol. 37, pp. 2096–2126, 2008.

[189] X. Wu, L. Senapati, and S. K. Nayak *J. Chem. Phys.*, vol. 117, pp. 4010–4015, 2002.

[190] Z. P. Liu and P. Hu *J. Am. Chem. Soc.*, vol. 124, pp. 14770–14779, 2002.

[191] A. Lyalin and T. Taketsugu *J. Phys. Chem. C*, vol. 114, pp. 2484–2493, 2010.

[192] G.-J. Kang, Z. X. Chen, and X. He *J. Chem. Phys.*, vol. 130, p. 034701, 2009.

[193] B. Yoon, H. Häkkinen, and U. Landmann *J. Phys. Chem. A*, vol. 107, pp. 4066–4071, 2003.

[194] A. Lyalin, K. Uosaki, and T. Taketsugu *Electrocatalysis*, vol. 9, pp. 182–188, 2017.

[195] Z. P. Liu and P. Hu *J. Am. Chem. Soc.*, vol. 124, pp. 14770–14779, 2002.

[196] J. Good, P. N. Duchesne, P. Zhang, W. Koshut, and M. Zhou *Catalysis Today*, vol. 280, pp. 239–245, 2017.

[197] W. Y. Hernández, F. Alic, S. Navarro-Jaen, M. A. Ceneteno, P. Vermier, P. V. D. Voot, and A. Verberckmoes *J. Mater. Sci.*, vol. 52, pp. 4727–4741, 2017.

[198] C. Zhang, B. Yoon, and U. Landman *J. Am. Chem. Soc.*, vol. 129, pp. 2228–2229, 2007.

[199] J. Elliott, J. Duay, O. Simoska, J. B. Shear, and K. A. Stevenson *Am. J. Analyt. Chem.*, vol. 89, pp. 1267–1274, 2017.

[200] E. V. Milsom, J. Novak, M. Oyama, and F. Marken *Electrochem. Commun.*, vol. 9, pp. 436–442, 2007.

[201] L. A. Calzada, S. E. Collins, C. W. Han, V. Ortalan, and R. Zanella *Appl. Catal. B: Environ.*, vol. 207, pp. 79–92, 2017.

[202] E. E. Stangland, K. B. Stavens, R. P. Andres, and W. Delgass *J. Catal.*, vol. 191, pp. 332–347, 2000.

[203] U. B. S., T. Susumu, H. Toshio, and H. Masatake *Chem. Lett.*, vol. 27, pp. 1277–1278, 1998.

[204] F. Stavale, X. Shao, N. Nilius, H.-J. Freund, S. Prada, L. Giordano, and G. Pacchioni *J. Am. Chem. Soc.*, vol. 134, no. 28, pp. 11380–11383, 2012.

Chapter 2

Methods

2.1 Introduction

Atoms are the building blocks of materials, and the atoms contain nuclei and electrons. Similar to the world of living things, interactions take place in the world of materials also when these building blocks approach each other. The structural and electronic properties of materials are the results of the interactions between the atoms, or more precisely between the nuclei and electrons. Therefore one has to deal with many interacting particles to investigate the properties of any material. However, it is very difficult to study a system of many interacting particles using a general quantum mechanical treatment.

Density Functional Theory (DFT) is one of the most successful and popular quantum mechanical methods to calculate the electronic properties of matter. It is a successful theoretical formalism to solve the quantum many-body problem. It can be applied very accurately for a wide range of materials, from atoms, molecules and nano-structured systems to crystalline solids and surfaces. DFT is a clever way to map the quantum many-body system onto a system of non-interacting fermions in an effective field. Perhaps the most important feature regarding DFT is that it is completely *ab initio*, i.e., it takes only the atomic numbers and the atomic masses of the atoms in the material as inputs for the computation, and uses no empirical data

from experiments. In its original formulation, this theory computes the ground state properties of interacting many-electron systems. The ground state properties can be determined by using functionals which are functions of another function: in Density Functional Theory the energy of the system can be expressed as a functional of the spatially-dependent electron density. We will briefly discuss regarding some of the relevant formalisms of density functional theory in this chapter.

2.2 The Quantum Many-Body Problem

The Hamiltonian of a many-body interacting system consisting of nuclei and electrons is given by:[1]

$$\hat{H} = -\sum_{I} \frac{\hbar^2}{2M_I}\nabla_I^2 - \frac{\hbar^2}{2m_e}\sum_{i}\nabla_i^2 + \frac{1}{2}\sum_{I\neq J}\frac{Z_I Z_J e^2}{|\mathbf{R}_I - \mathbf{R}_J|} - \sum_{i,I}\frac{Z_I e^2}{|\mathbf{r}_i - \mathbf{R}_I|} + \frac{1}{2}\sum_{i\neq j}\frac{e^2}{|\mathbf{r}_i - \mathbf{r}_j|}, \tag{2.1}$$

where the nuclear masses, nuclear positions and the atomic numbers of the atoms in the system are given by M_I, $\mathbf{R}_I$ and Z_I respectively. The indices I and J run over all the nuclei in the system; $\mathbf{r}_i$, m_e and e are the electronic positions, mass and charge respectively, with indices i, j that run over all the electrons in the system, and $\hbar$ is Planck's constant divided by 2π. The first two terms on the right-hand-side (RHS) of the equation are the nuclear and electronic kinetic energy contributions to the Hamiltonian, respectively. The remaining terms represent the Coulombic interactions between pairs of nuclei, between pairs consisting of a nucleus and an electron, and between pairs of electrons, respectively.

It is a difficult task to solve the many-body Schrödinger equation. Certain approximations are used to make this problem feasible; these are: the Born-Oppenheimer or adiabatic approximation, Density Functional Theory (which is exact in principle, but approximate in practice), and the pseudopotential approximation (within DFT). These approximations are described in the next few sections.

2.2.1 Born-Oppenheimer or Adiabatic Approximation

The Born-Oppenheimer approximation, named after Max Born and J. Robert Oppenheimer, is based on the assumption that the nuclear and electronic degrees of freedom in atoms, molecules or crystals can be separated from each other. The masses of the nuclei are much greater than that of the electrons ($M_I >> m_e$) and they tend to move much slower than the electrons. The electrons can respond almost instantaneously to any change in the nuclear positions. Thus the nuclei can be considered as effectively stationary on the electronic time-scales. Therefore, the nuclei can be considered to be frozen in a single arrangement, and when the nuclei move they only see a smeared out potential from the speedy electrons. When solving the time-independent Schrödinger equation, it can be assumed that the nuclei are stationary, and one can solve the equation for the electronic ground-state first, and then calculate the energy of the system in that configuration and solve for the nuclear motion. In the Born-Oppenheimer approximation the nuclear motion is separated from the electronic motion.[2].

In Eq. (2.1), $\hat{H}$ cannot be separated into nuclear and electronic parts due to the term representing the interaction between nuclei and electrons. On applying the Born-Oppenheimer approximation to Eq. (2.1), the first term on the RHS, i.e., the kinetic energy of the nucleus, becomes very small, and can be treated as a perturbation. The wavefunctions and energies of the electrons have only a parametric dependence on the nuclear positions $\mathbf{R}$. The wavefunction of the total system, $\Psi(\mathbf{R}, \mathbf{r})$ can be written as:

$$\Psi(\mathbf{R}, \mathbf{r}) = \sum_s \phi(\mathbf{R})\psi(\mathbf{R}, \mathbf{r}) \tag{2.2}$$

where $\{\psi(\mathbf{R}, \mathbf{r})\}$ is a complete set of electronic eigenstates for each $\mathbf{R}$, and $\phi(\mathbf{R})$ is the nuclear wavefunction. $\mathbf{r}$ and $\mathbf{R}$ are the position vectors which denote the set of all position vectors $\{\mathbf{r}_i\}$ and $\{\mathbf{R}_I\}$ for the electrons and the nuclei respectively.

Now, the electronic part of the many-body equation in Eq. (2.1) which describes

a system of interacting electrons for a fixed nuclear configuration, can be re-written as:

$$\left[-\frac{\hbar^2}{2m_e}\sum_i \nabla_i^2 + \frac{1}{2}\sum_{I\neq J}\frac{Z_I Z_J e^2}{|\mathbf{R}_I - \mathbf{R}_J|} - \sum_{i,I}\frac{Z_I e^2}{|\mathbf{r}_i - \mathbf{R}_I|} + \frac{1}{2}\sum_{i\neq j}\frac{e^2}{|\mathbf{r}_i - \mathbf{r}_j|}\right]\psi(\mathbf{R},\mathbf{r}) = E_e(\mathbf{R})\psi(\mathbf{R},\mathbf{r}). \tag{2.3}$$

In the above equation, the term involving interactions between pairs of nuclei is quite frequently neglected [second term on the left-hand-side (LHS)], since in this case $\mathbf{R}$ is just a parameter. Therefore this term is just a constant and shifts the eigenvalues only by some constant.

The equation for the nuclear part can be written as:

$$\left[-\sum_I \frac{\hbar^2}{2M_I}\nabla_I^2 + E_e(\mathbf{R})\right]\phi(\mathbf{R}) = \varepsilon\phi(\mathbf{R}). \tag{2.4}$$

$E_e(\mathbf{R})$ is the solution of Eq. (2.3). $E_e(\mathbf{R})$ is called the Born-Oppenheimer potential energy surface, and when this term is known, Eq. (2.4) can be solved easily. However, the solution to Eq. (2.3), is not very simple or straightforward within the quantum mechanical approach. Therefore, to solve the system of interacting electrons for fixed nuclear positions, one requires further approximations to deal with the Coulomb two-body terms and the exchange and correlation interactions between the electrons.

2.3 Density Functional Theory

Density functional theory treats the electron density as the basic variable, rather than the many-body wavefunction. This conceptual difference makes the calculations much simpler since the density is a function of three spatial variables, i.e., the three Cartesian coordinates, and yet can give us all the information contained in the many-body wavefunction (which is a $3N$-variable quantity). Thus, it is a complete reformulation of the Schrödinger equation. So, instead of solving for the many-body wavefunction one has to solve for the total electron density. The modern formalism of Density Functional Theory was developed by P. Hohenberg and W. Kohn in 1964,

when the authors proved that the density plays a crucial role in determining the ground state properties of a quantum many-body system. [3] The formulation subsequently developed by W. Kohn and L. J. Sham in 1965 has become the fundamental procedure for electronic structure calculation.[4] Density Functional Theory was a landmark development in the field of computational science that enabled electronic structure theory to be applied to real problems, and led to the Nobel Prize in Chemistry being awarded to Walter Kohn in 1998.

The density operator $\hat{n}(\mathbf{r})$ for a system of N electrons is given by:[1]

$$\hat{n}(\mathbf{r}) = \sum_{i=1}^{N} \delta(\mathbf{r} - \mathbf{r}_i), \tag{2.5}$$

The electronic density, $n(\mathbf{r})$, is determined from the many-electron wavefunction using the electronic density operator, as given below:[1]

$$n(\mathbf{r}) = \frac{\langle \psi \, | \hat{n}(\mathbf{r}) | \, \psi \rangle}{\langle \psi | \psi \rangle} = \frac{\int d\mathbf{r}_1, d\mathbf{r}_2, ..., d\mathbf{r}_N \sum_{i=1}^{N} \delta(\mathbf{r} - \mathbf{r}_i) |\psi(\mathbf{r}_1, \mathbf{r}_2, ..., \mathbf{r}_N)|^2}{\int d\mathbf{r}_1, d\mathbf{r}_2, ..., d\mathbf{r}_N |\psi(\mathbf{r}_1, \mathbf{r}_2, ..., \mathbf{r}_N)|^2}, \tag{2.6}$$

Using the electronic density, the ground state total energy of a system can be calculated using the equation:

$$E = \langle \psi | \hat{H}_e | \psi \rangle = \langle - \sum_i \frac{\hbar^2}{2m_e} \nabla_i^2 + \frac{1}{2} \sum_{i \neq j} \frac{e^2}{|\mathbf{r}_i - \mathbf{r}_j|} \rangle + \int d\mathbf{r} V_{ext}(\mathbf{r}) n(\mathbf{r}). \tag{2.7}$$

The terms in angular brackets in Eq. (2.7) are universal for all electronic systems. Therefore, the properties of any system are determined by the last term containing V_{ext} and the electronic density $n(\mathbf{r})$. In this way, DFT further simplifies the problem by replacing the many-body interacting electron system with a single-electron non-interacting system and including a parameter that incorporates all the many-body effects in the system through a term that describes the exchange and correlation between the electrons.

2.3.1 Hohenberg-Kohn Theorems

Density Functional Theory, developed by Hohenberg and Kohn in 1964, makes two remarkable statements which are known as the Hohenberg-Kohn theorems.[3]

Theorem I: For any system of interacting particles in an external potential $V_{ext}(\mathbf{r})$, the potential is determined uniquely, up to an additive constant, by the ground state particle density $n_0(\mathbf{r})$. [1]

This theorem implies that the ground-state electron density (within an additive constant) determines the external potential of the Schrödinger equation. Using the external potential $V_{ext}(\mathbf{r})$, the Schrödinger equation can be solved to determine the many-body wavefunction and from the wavefunction the electronic density (which is an observable) can be determined. This allows a self-consistent procedure to be utilized to determine the true ground state density and the true ground state wavefunction of the system.

Theorem II: A universal functional for the energy $E[n]$ in terms of $n(\mathbf{r})$ can be defined, valid for any external potential $V_{ext}(\mathbf{r})$. For any particular $V_{ext}(\mathbf{r})$, the global minimum value of this functional gives the exact ground state energy of the system. The density $n(\mathbf{r})$ that minimizes the functional is the exact ground state density $n_0(\mathbf{r})$.[1]

The ground state total energy of a system can be written as functional of the density $n(\mathbf{r})$,

$$E[n] = F[n] + \int d\mathbf{r} V_{ext}(\mathbf{r}) n(\mathbf{r}). \tag{2.8}$$

The term $F[n]$ is a universal functional of the density and is the same for all electronic systems. $F[n]$ does not depend on the external potential V_{ext}. Instead of dealing with $3N$ variables (like the many-electron wavefunction) it depends on a function of three variables (i.e., the electron density n). The second term on the RHS in Eq. (2.8) contains the information regarding the electron-nuclear interactions. If

the functional form of $F[n]$ were known, then the electron density could be varied until the energy obtained from the functional is minimized. This provides the prescription for finding the ground-state electron density and total energy of the system.

The story is not complete here however, since the exact form of the universal functional $F[n]$ is not known. A major contribution to this functional is the kinetic energy term, which involves a gradient over each electronic coordinate and it is not possible to write an exact analytical form of the kinetic energy as a functional of the total density. The electron-electron Coulombic repulsion is a two-particle term.

In principle DFT is exact, but one needs to make approximations due to our lack of knowledge about the exact functional form. The next most important step is to construct an approximate form for $F[n]$. The exchange and correlation energies play a significant role for a system of many interacting particles. To describe the behavior of such a system, the exchange and correlation energies need to be defined accurately. In the case of a non-interacting system, the antisymmetry of the wave-function requires the particles to have the same spin and they occupy distinct orthogonal orbitals, and thus the particles become spatially separated. For a system of interacting electrons, all the particles repel each other, and exchange leads to a lowering of the energy. The interactions between the electrons make the motion of the particles to be correlated which can further reduce the energy of the mutual interaction. A very useful and effective approximation for the universal energy functional $F[n]$ was proposed by Kohn and Sham in 1965.[4] This formulation of the Kohn-Sham equations is the main reason for the success of Density Functional Theory.

2.3.2 Kohn-Sham Representation

The Hohenberg-Kohn theorem is not complete since it cannot provide information about the exact form of the functional $F[n]$. After the Hohenberg-Kohn theorems were published, Kohn and Sham developed another approach which makes DFT feasible. The aim of the Kohn-Sham approach was to replace the interacting many-body system with a simpler auxiliary system.

The Kohn-Sham formulation takes advantage of the power of DFT without sacrificing its accuracy (i.e., including exchange and correlation effects). The Kohn-Sham (K-S) formulation [4] maps a N-electron interacting many-body problem onto an effective non-interacting problem comprised of N single-electrons with the same electronic density. The orbitals occupied by these N electrons are called the Kohn-Sham states. According to Pauli's exclusion principle, each state can contain two electrons. $\psi_s(\mathbf{r})$ are the fictitious states, which are related to the true ground state electronic density by:

$$n_0(\mathbf{r}) = 2\sum_{s=1}^{N/2} |\psi_s(\mathbf{r})|^2, \tag{2.9}$$

where s is an index that runs over all the occupied Kohn-Sham states,[1] and the factor of 2 arises from spins. The summation goes over all the individual electron wavefunctions that are occupied by electrons. Therefore the term inside the summation is the probability that an electron in an individual orbital $\psi_s(\mathbf{r})$ is located at position $\mathbf{r}$. The factor of 2 appears because electrons have spin and the Pauli exclusion principle states that each individual electron orbital can be occupied by two separate electrons of different spins. Thus, $n(\mathbf{r})$ contains a great amount of information which is actually physically observable from the full wavefunction solution to the Schrödinger equation, which is a function of $3N$ coordinates.[4]

The Kohn-Sham equations provide a route to find the ground-state electron density. Kohn and Sham chose to write the total energy functional as:

$$E[n] = T_0[n] + E_H[n] + \int V_{ext}(\mathbf{r})n(\mathbf{r})d\mathbf{r} + E_{xc}[n] = F[n] + \int V_{ext}(\mathbf{r})n(\mathbf{r})d\mathbf{r}. \tag{2.10}$$

Each term in the above equation is described below:

- Here, $T_0[n]$ is the kinetic energy of the non-interacting fictitious electrons. [1]

$$T_0[n] = -2\frac{\hbar^2}{2m_e}\sum_{s=1}^{N/2}\langle\psi_s|\nabla^2|\psi_s\rangle, \tag{2.11}$$

- $E_H[n]$ is the Hartree energy, defined as the Coulomb interaction between the electrons, neglecting the exchange and correlation effects. The expression for the Hartree energy, E_H, is given by,[4]

$$E_H[n] = \frac{e^2}{2}\int\frac{n(\mathbf{r})n(\mathbf{r}')}{|\mathbf{r}-\mathbf{r}'|}d\mathbf{r}d\mathbf{r}', \tag{2.12}$$

- V_{ext} is the external potential arising from the nuclei and any other external fields.

- The residual energy contribution due to the exchange and correlation effects can be combined together into the exchange and correlation energy E_{xc} which is given by the equation:

$$E_{xc}[n] = F[n] - (T_0[n] + E_H[n])\,. \tag{2.13}$$

  The Eq. (2.13) explicitly shows that the exchange-correlation energy is just the difference between the kinetic and internal interaction energies of the true interacting many-body system.

The functional forms of $T_0[n]$ and $E_H[n]$ are known and can be easily calculated. The functional forms for the rest of the energy contributions, however, are not known and are dumped into the third term, $E_{xc}[n]$. Different approximations have been made for this exchange-correlation term with varying levels of both the accuracy and computational costs: some of these approximations are described in the next section.

Applying the Kohn-Sham representation of the universal function $F[n]$, Eq. (2.10)

can be written as:

$$E_0[n_0] = T_0[n] + E_H[n] + E_{xc}[n] + \int V_{ext}(\mathbf{r})n(\mathbf{r})d\mathbf{r}, \tag{2.14}$$

$$= T_0[n] + \int V_{KS}(\mathbf{r})n(\mathbf{r})d\mathbf{r}, \tag{2.15}$$

where V_{KS} is assumed to be the effective potential or Kohn-Sham (K-S) potential experienced by the fictitious non-interacting electrons and can be written as:

$$V_{\mathrm{KS}}[n(\mathbf{r})] = V_H[n(\mathbf{r})] + V_{xc}[n(\mathbf{r})] + V_{ext}[n(\mathbf{r})]. \tag{2.16}$$

where $V_H[n(\mathbf{r})] = \frac{\delta E_H}{\delta n(\mathbf{r})}$ is the Hartree potential and $V_{xc}[n(\mathbf{r})] = \frac{\delta E_{xc}}{\delta n(\mathbf{r})}$ is the exchange-correlation potential which is the functional derivative of exchange-correlation energy. [4]

The Kohn-Sham Hamiltonian can be written as:[5]

$$\left\{ -\frac{\hbar^2}{2m_e}\nabla^2 + V_{\mathrm{KS}}[n(\mathbf{r})] \right\}\psi_\alpha(\mathbf{r}) = E_\alpha\psi_\alpha(\mathbf{r}). \tag{2.17}$$

To find the true ground-state electron density and total energy one can use Eqs. (2.9), (2.16) and (2.17) self-consistently. The basic procedure of the self-consistent loop is mentioned in a flowchart, see Fig. 2.1.

A self-consistent iterative procedure is performed starting from a trial input density n^{inp}. At the first step, a trial (input) density n^{inp} has to be decided or guessed (usually from a combination of atomic wavefunctions and plane waves). This input density is used to calculate the Kohn-Sham potential. The Kohn-Sham equations are solved to get the Kohn-Sham wavefunctions. The new density (output) n^{out} is obtained from these Kohn-Sham (K-S) wavefunctions. Self-consistency is achieved if the initial and new densities are identical or lower than a pre-defined tolerance, then the ground state density has been found. Otherwise one must select a new trial density after some mixing (defined in the function f) with the input density to make

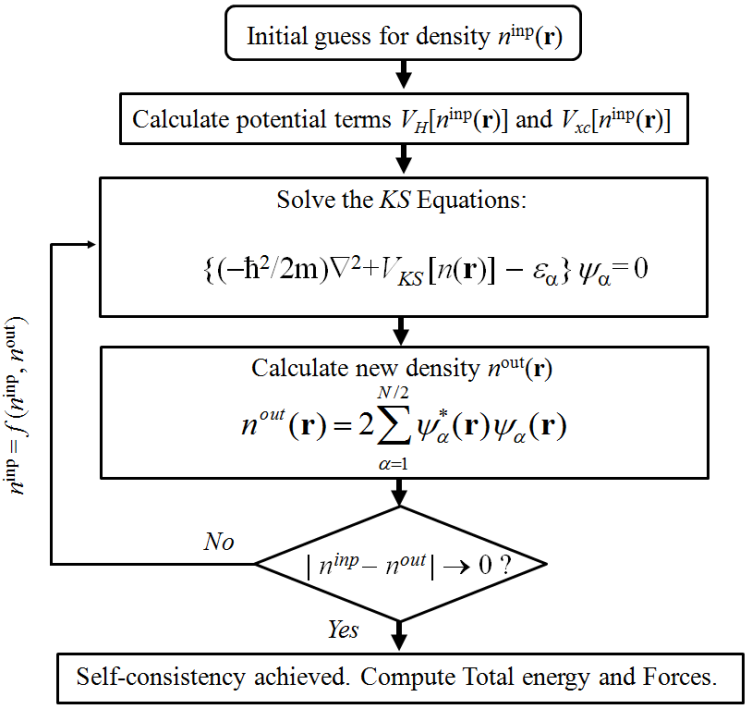

Figure 2.1: Flow chart demonstrating the self-consistency loop used to iteratively solve the Kohn-Sham equations

the convergence faster. The iterative procedure is continued until convergence is achieved.

If one could start with a good guess for the electronic density, n^{inp}, the K-S potential could be calculated from Eq. (2.16); using the K-S potential, Eq. (2.17) could be solved to determine the K-S states, $\psi_s(\mathbf{r})$; and to complete the loop, the electronic density, n^{out} can be extracted as an observable of the K-S states. The output density obtained by solving the K-S equation, can be combined with the input density using a mixing scheme. This mixing between the output and input densities gives a new input density which can be fed to the self-consistent loop for the next iteration. This procedure is continued until the difference between the input and output densities becomes lower than a pre-defined tolerance value. Various mixing schemes exist that help speed up convergence, the most common one being the modified Broyden's mixing method.[6, 7]

Upon achieving convergence in the self-consistent loop, the electronic ground state energy can be calculated. To obtain the total ground state energy of the system, the

Coulomb interaction energy between the nuclei is added to the electronic energy.[1]

2.3.3 Exchange-Correlation Functionals

According to the Kohn-Sham formalism, the ground state properties of any system can be determined by minimizing the energy functional, and this can be achieved by finding a self-consistent solution to a set of single-particle equations. There is one major issue with the K-S formulation, i.e., to solve the Kohn-Sham equations one has to specify the exchange-correlation functional $E_{xc}[n]$.

The exchange energy arises because electrons obey Pauli's exclusion principle, i.e., electrons of same the spin avoid each other. The exchange component describes the energy lowering due to anti-symmetrization. The correlation energy is defined as the energy lowering since the negatively charged electrons tend to avoid each other in a real system. The correlation energy results from complicated many-body interactions between the electrons. To reduce the Coulombic repulsion between each other, the electrons screen themselves. The exact functional forms of the exchange and correlation energies are not known. Therefore, the functional forms of the exchange and correlation energies are approximated to calculate various properties of the system.[8]

Local Density Approximation

The Local Density Approximation (LDA) deals with only the local density at each space point. In this simplest approximation, the effect of the exchange and correlation is assumed to be local in nature.[9–11] The exchange-correlation energy density is assumed to be the same as that in a homogeneous electron gas of that local density. The LDA helps us to completely define the Kohn-Sham equations. According to this approximation, the exchange-correlation energy for a density $n(\mathbf{r})$ is given by:

$$E_{xc}^{LDA} = \int n(\mathbf{r})\epsilon_{xc}(n)d\mathbf{r}, \tag{2.18}$$

where $\epsilon_{xc}(n)$ is the exchange-correlation energy per particle of a uniform electron

gas of density n. The exchange-correlation potential is then given by: [12]

$$v_{xc}^{LDA}[n(\mathbf{r})] = \frac{\delta E_{xc}^{LDA}}{\delta n(\mathbf{r})} = \epsilon_{xc}(n) + n(\mathbf{r})\frac{\partial \epsilon_{xc}}{\partial n}, \tag{2.19}$$

The exchange energy density for the homogeneous electron gas can be approximated analytically or computed using Quantum Monte Carlo.[13]

One needs to determine the exchange-correlation energy for a uniform electron gas of a given density to deal with practical purposes or realistic systems. The exchange-correlation energy is split into exchange and correlation potentials $\epsilon_{xc}(n) = \epsilon_x(n) + \epsilon_c(n)$. The form of exchange potential can be derived from the Dirac functional. [14]

$$\epsilon_x[n(\mathbf{r})] = -\frac{3}{4}(\frac{3}{\pi})^{\frac{1}{3}} n(\mathbf{r}), \tag{2.20}$$

The accurate values for $\epsilon_c(n)$ can be determined from Quantum Monte Carlo (QMC) calculations. [10] They are then interpolated to provide an analytic form for $\epsilon_c(n)$. [11]

Though the LDA seems to be a very drastic approximation, it works remarkably well for most solid systems. There are some limitations of the LDA. It overestimates the exchange but underestimates the correlations. The LDA follows certain sum rules for the exchange-correlation hole. However, the sum rules for the exchange hole and the correlation hole separately are not satisfied. The LDA almost always underestimates the lattice parameter for a given element compared to the experimental value. The energy differences calculated using LDA are often significantly larger than the experimental values. Also, the difference between the highest occupied and lowest unoccupied molecular orbitals (HOMO-LUMO gap) is often very much underestimated in the LDA. Therefore, one needs to consider some other functional to obtain a better or more accurate value of HOMO-LUMO gap.

Generalized Gradient Approximations

The LDA does not take into account the variation of the electron density from one place to another. In a real system the electron density is usually not homogeneous. To take the inhomogeneity of the electron density into account, one has to consider not just the electron density but also the gradient of the electronic density. Different ways have been proposed to do this[15–17] and these are collectively known as the Generalized Gradient Approximations (GGA). The exchange correlation function can then be written as:

$$E_{xc}^{\mathrm{GGA}} = \int d\mathbf{r}\ n(\mathbf{r})\epsilon_{xc}(n, |\nabla n(\mathbf{r})|), \tag{2.21}$$

where $\epsilon_{xc}(n, |\nabla n(\mathbf{r})|)$ is the exchange-correlation energy per electron, that depends on the local density $n(\mathbf{r})$ as well as the gradient of the density $|\nabla n(\mathbf{r})|$.

There are a large number of distinct GGA functionals that are used in the literature. Two of the most widely used functionals in calculations involving solids are the Perdew-Burke-Ernzerhof functional (PBE) [15, 16] and the Perdew-Wang functional (PW91)[17]. The GGA is often known to underbind, which results in computed lattice constants being larger than the experimental values.

2.3.4 Hybrid functionals

Density functional theory is an efficient method to compute the energetics for a wide variety of materials in their ground state. The energy eigenvalues obtained by solving the Kohn-Sham equations in standard DFT calculations do not include the excitation energies. Therefore, the band gap of any material calculated using standard DFT technique is always underestimated compared to its experimental value. The poor estimation of the band gap in DFT leads to some unfortunate consequences and wrong interpretations regarding the properties of the materials. In the case of some systems this underestimation even wrongly makes the band gap to be zero, which gives a qualitatively incorrect description of the ground state, i.e., the material is

found to be a metal rather than a semiconductor or an insulator. The efficiency and accuracy in standard DFT calculations are limited especially when we need to study properties which depend explicitly on excited state energies.

To improve the computed values of band gaps, hybrid functionals have been developed, which are considered to be more reliable than the GGA and/or LDA functionals to calculate band gaps in solids or HOMO-LUMO gaps in molecules, atomic enthalpies, transition or excited state geometries and vibrational frequencies. The hybrid functionals are formulated by a linear combination of the Hartree-Fock exchange functional and any number of other exchange and correlation functionals, like GGA and/or LDA. The weight of each individual functional is evaluated by fitting the predictions made by the corresponding functional to the experimental or calculated data. However, the weights can be set *a priori* in the case of the adiabatic connection functionals.[18] Some examples of popular hybrid functionals are: B3LYP,[19, 20] PBE0,[21] HSE,[22] and Meta hybrid GGA.[23]

The hybrid exchange functional used in this thesis is the B3LYP (Becke, three-parameter, Lee-Yang-Parr). The B3LYP exchange-correlation functional has the following form:

$$E_X = E_X^{LDA} + a_0(E_X^{HF} - E_X^{LDA}) + a_X(E_X^{GGA} - E_X^{LDA}) + E_c^{LDA} + a_c(E_X^{GGA} - E_X^{LDA}) \tag{2.22}$$

where the value of the coefficients are: $a_0 = 0.20$, $a_X = 0.72$ and $a_c = 0.81$. E_X^{GGA} is the Becke 88 exchange functional,[24] and E_C^{GGA} is the correlation functional of Lee, Yang and Parr in the generalized gradient approximations.[25] E_X^{HF} is the non-local Hartree-Fock exchange energy and E_c^{LDA} is the local density approximation to the correlation functional.

B3LYP is a very popular hybrid functional. This functional is not conveniently employed in the plane wave basis sets yet, but B3LYP is efficiently employed for the localized basis sets, e.g., Gaussian basis sets.

2.3.5 Basis Sets

The Density Functional Theory method aims to compute properties of interest without recourse to experimental data. To do this one needs to find the Kohn-Sham wavefunctions. Since these are generally unknown, it is usual to expand them in terms of a set of known functions. The K-S states are usually expanded in terms of a basis set, therefore their information is stored as a number of coefficients in the computer. An appropriate basis set needs to be chosen for a density functional theory calculation. There are different kinds of basis sets like plane waves,[26, 27] Gaussian functions, localized atomic orbitals[28] and Muffin Tin Orbitals.[29] In this thesis, we have used plane wave and localized atomic orbital basis sets, as implemented in the Quantum ESPRESSO[26] and SIESTA [28] packages, respectively.

The larger the number of basis functions contained in the basis set, the better will be the computational accuracy, but the slower will be the calculation speed. The time needed to solve the Kohn-Sham equations in a computational calculation is (for exact matrix diagonalization) roughly proportional to the cube of the number of basis functions considered, various techniques can be used to reduce the computational cost.

Plane Wave Basis Set

In the case of periodic systems the potential has the following property:

$$V(\mathbf{r} + z\mathbf{a}) = V(\mathbf{r}) \tag{2.23}$$

where $\mathbf{a}$ is lattice vector and z is an integer. Using Bloch's theorem [30] the wavefunction can be written as a product of a cell periodic part and a wavelike part

$$\psi_i(\mathbf{r}) = e^{i\mathbf{kr}} f_i(\mathbf{r}) \tag{2.24}$$

Due to its periodicity $f(\mathbf{r})$ can be expanded in terms of a set of plane waves

$$f_i(\mathbf{r}) = \sum_G c_{i,\mathbf{G}} e^{i\mathbf{G}.\mathbf{r}} \tag{2.25}$$

where $\mathbf{G}$ are reciprocal lattice vectors.

According to Bloch's theorem, the wavefunction of an electron placed in a periodic potential can be written in terms of the plane wave and a periodic function.[30] This suggests that, when working with extended periodic systems, one can use a set of mutually orthonormal plane waves to expand the wavefunction. The K-S states can be expanded in terms of plane waves:[5]

$$\psi_{s,\mathbf{k}}(\mathbf{r}) = \sum_{\mathbf{G}} c_{s,\mathbf{k}+\mathbf{G}} e^{i(\mathbf{k}+\mathbf{G})\cdot\mathbf{r}} \tag{2.26}$$

where $\mathbf{G}$ is a reciprocal lattice vector, and $\mathbf{k}$ is a wavevector in the first Brillouin zone. Any observable of the wavefunction can be calculated by summing over the occupied Bloch states at a given $\mathbf{k}$ point and then integrating over all $\mathbf{k}$-points within the Brillouin zone.

The number of plane waves used can be easily increased until the energy converges; however, this will increase the matrix size and thus the computational time. To compromise between computational accuracy and computational cost, one truncates this expansion with a kinetic energy cutoff: keeping all plane waves $e^{i(\mathbf{k}+\mathbf{G})\cdot r}$, such that $(\hbar^2/2m_e)|\mathbf{k}+\mathbf{G}|^2 \leq E_{cut}$.[1, 31] A plane wave basis set is used,e.g., in the Quantum ESPRESSO and VASP packages.[26, 32]

Plane wave basis sets can also be used to perform calculations on non-periodic systems such as isolated molecules. To accomplish this, the molecule is placed at the center of a periodic supercell. If the supercell is large enough, the interactions between the molecules in neighboring cells becomes negligible.

If the described wavefunction of the electron oscillates very rapidly or is very highly peaked in a region of space, a large number of plane waves will be required to

accurately represent it. The high computational expense due to this can be reduced by using pseudopotentials, which are described in Section 1.6 further below.

Localized Basis Set

The wavefunction for isolated atoms and molecules exponentially decays to zero at large distances. This suggests that one might want to use basis functions for these calculations that do likewise. Atomic orbitals are one kind of atom-centered basis functions that decay exponentially.[33] Other localized basis sets are Slater-type orbitals (STO) [34] and Gaussian-type orbitals (GTO).[35]

STOs can be represented as: [34]

$$\phi_{STO}^{nlm\zeta}(r,\theta,\phi) = \alpha Y_{lm}(\theta,\phi) r^{n-1} e^{-\zeta r},$$

where α is a normalization constant and $Y_{lm}(\theta,\phi)$ is a spherical harmonic and n, l, and m are principal, orbital angular momentum and magnetic quantum numbers, respectively. ζ determines the radius of the orbit. The exponential dependence on distance is the same as for the hydrogen atom.

GTOs (in spherical coordinates) are given by:

$$\phi_{GTO}^{nlm\zeta}(r,\theta\,\phi) = \alpha Y_{lm}(\theta,\phi) r^{(2n-2-l)} e^{-\zeta r^2}.$$

For both STOs and GTOs, the angular dependence of the wavefunction is contained in the spherical harmonics, and the values of l and m determine the type of the orbital (e.g., $l = 0$ is a s type orbital, $l = 1$ a p orbital, etc.).

The main difference between STOs and GTOs is the power of r in the exponent. The r dependence in the exponent in the STOs is a better representation than that of GTOs. GTOs have a zero slope at the nucleus ($r = 0$) and fall off rapidly with distance, whereas STOs have a cusp and decay slower than GTOs. These factors suggest that a larger number of GTOs are needed to form a suitable basis set than STOs.[34] GTOs are more commonly used in calculations due to their better efficiency

than STOs.[36]

The accuracy of a calculation depends on the size of the basis set. Increasing the number of basis functions improves the quality of the calculation, e.g., in SIESTA one talks of a minimal basis set: one basis function per atomic orbital, double zeta: two basis functions per atomic orbital and triple zeta: three basis functions per atomic orbital. Additional higher angular momentum (d, f orbitals) basis functions may also be added to attempt to account for polarization effects, e.g., double zeta polarized (DZP) basis set. [37]

2.3.6 Pseudopotential Approximation

The wavefunctions of a given atom are the eigenstates of the atomic Hamiltonian. The electronic states of an atom fall into three main categories. (i) Core states: which are highly localized and do not take part in chemical bonding, (ii) valence states: which are located far from the nucleus, hence extended and responsible for chemical bonding, and (iii) semi-core states: these states are in between the core and valence states. They are localized and polarisable, but usually do not contribute directly to chemical bonding. [38]

The core states are localized in the vicinity of the nucleus. In an atom, the core electrons are tightly bound to the nucleus, and their wavefunctions are highly peaked in the region close to the nucleus. Therefore, a large number of plane-wave components are required for the plane-wave expansion of the wavefunctions to represent such steep wavefunctions. The valence states are oscillating in nature near the core region to maintain orthogonality with the core electrons. This rapid oscillation of the valence electrons causes large kinetic energy in the core region, which roughly cancels the large potential energy due to the strong Coulomb potential.[39] The valence electrons are much more weakly bound to the nucleus than the core electrons.

Therefore, it is convenient to replace the strong Coulomb potential and the core electrons by an effective pseudopotential. The rapidly oscillating valence electron wave-functions in the core region can be replaced by the pseudo-wave-functions,

which shows smooth variation in the core region instead of rapid oscillation. In this context, Slater suggested a possible solution in 1937, where the plane-wave expansion was augmented with the solutions of the atomic problem in spherical regions around the atoms. In the augmented plane wave (APW) method the potential was assumed to be spherically symmetric inside the spheres, and zero outside. [40] Conyers Herring, in 1940, proposed an alternative method in order to overcome the shape approximation of the potential in the APW method. According to this approach, the valence wavefunctions are represented as a linear combination of plane waves and core wavefunctions. [41] In this way, one can go a step beyond the APW approach to eliminate the core states by replacing them with an effective potential or pseudopotential. The pseudopotential approximation has to be developed carefully in order to reproduce the properties of the true potential.

To formulate pseudopotentials one has to follow two main steps. At the first step the core electrons are removed from the calculation, and the interaction of the valence electrons with the nucleus plus the core states (including orthogonalization) is replaced by an effective, screened potential. The effective potential depends on the angular momentum of the valence electrons.

In the second step, the interaction between the core electrons and the ions, which is known as the ion-electron interaction that includes the orthogonality of the valence wavefunctions to the core states, is replaced by a softer pseudopotential. The solution of the atomic Schrödinger equation using the pseudopotential gives a pseudo-wavefunction which is different from the true wavefunction.

The pseudopotential, however, is constructed in such a way it should keep certain features the same as for the all-electron potential, e.g., the scattering properties, phase shifts, etc. The main concept behind developing a pseudopotential is that the pseudo wavefunctions should have the scattering properties identical to the valence and core electrons. The pseudopotential will be angular momentum dependent since the scattering properties depend on the angular momentum component of the valence

wavefunction. Pseudopotentials with an angular momentum dependence are called non-local pseudopotentials.

While developing a pseudowavefunction for an atom, one has to decide a core radius r_c. The pseudo wavefunction matches exactly with the true wavefunction beyond this radius. Inside this core radius, the pseudo wavefunction is designed to be nodeless and non-oscillating. The replacement of the actual atomic wavefunction with the pseudo wavefunction reduces the number of Fourier components and makes the calculation computationally cheaper.[42] The Kohn-Sham equations are then inverted to obtain the pseudopotential using the pseudo wavefunction.

A pseudopotential should follow certain properties.[42] (1) The pseudo wavefunction and its first and second derivatives should match smoothly at the core radius cutoff. (2) The pseudopotential should have the property of transferability, so that it would be able to treat different chemical environments. (3) It used to be believed that a good pseudopotential should conserve the electronic charge of an atom; such pseudopotentials are called norm-conserving pseudopotentials.[43]

Norm-conserving pseudopotentials

The most important and necessary condition to obtain the exchange-correlation energy accurately is that the real and pseudo wavefunctions should be identical outside the core region, so that both wavefunctions should give the same charge densities. The norm-conserving pseudopotentials should satisfy:

$$\int_0^{r_c} \psi^*_{AE}(\mathbf{r})\psi^*_{AE}(\mathbf{r})d\mathbf{r} = \int_0^{r_c} \psi^*_{ps}(\mathbf{r})\psi_{ps}(\mathbf{r})d\mathbf{r}, \tag{2.27}$$

where ψ_{AE} and ψ_{ps} are the all-electron and pseudo wavefunctions, respectively. The condition in Eq. (2.27) ensures that the all-electron and pseudo wavefunctions are equal outside the core region.[44] In practice, this can be achieved by using a non-local pseudopotential which uses a different potential for each angular momentum component of the pseudopotential. This kind of pseudopotential can describe the

scattering properties from the ion core very well. The non-local norm-conserving pseudopotentials can describe the scattering properties of an ion in a variety of atomic environments which makes them highly transferable.

Ultrasoft pseudopotentials

One more step forward in the field of electronic structure calculations was the introduction of ultrasoft pseudopotentials, suggested by D. Vanderbilt.[45] The development of ultrasoft pseudopotentials reduces the limitations of norm-conservation, and lowers the computational cost. That portion of the electronic charge which is not conserved in the pseudo wavefunction is included by adding an 'augmentation' charge in the core region of the pseudo wavefunction. To deal with this augmented charge, in addition to the plane wave energy cutoff, one has to introduce a larger cut off for the electronic charge density. The value of this charge density cut off should typically be 8 to 12 times the value of the energy cutoff for the plane wave basis sets.

2.3.7 k-point sampling

Physical quantities like the total energy, the density of states, etc. are obtained by integrating over all the wavevectors in the first Brillouin zone (BZ). The number of **k** points in a zone is infinite, and in principle, the electronic wavefunction needs to be calculated at each **k**-point. Hence, this would lead to an infinite computational cost. Instead of integrating over the infinite number of **k**-points in the BZ, one has to, in practice, sum over a finite number of discrete **k**-points. Monkhorst and Pack suggested a method to generate a uniform set of points according to the symmetry of the system, using the formula:[46]

$$\mathbf{k}_{n_1,n_2,n_3} = \sum_{\beta=1}^{3} \frac{2n_\beta - N_\beta - 1}{2N_\beta}\mathbf{b}_\beta \qquad (n_\beta = 1, 2, 3, ..., N_\beta), \tag{2.28}$$

where N_β is the number of divisions in reciprocal space along the βth direction (β = 1, 2, 3) and $\mathbf{b}_1, \mathbf{b}_2$ and $\mathbf{b}_3$ are the primitive reciprocal lattice vectors.

Using a similar equation Quantum ESPRESSO allows the possibility to generate a uniform grid of k-points with an offset. When there is no offset, $sk_\beta = 0$, in the case where the grid is displaced by half a grid step in the corresponding direction, the values of sk_β are 1. The formula used is:[26]

$$\mathbf{k}_{n_1,n_2,n_3} = \sum_{\beta=1}^{3} \frac{2(n_\beta - 1) + sk_\beta}{2N_\beta}\mathbf{b}_\beta \qquad (n_\beta = 1, 2, 3, ..., N_\beta), \tag{2.29}$$

As the number of k-points considered in the Brillouin zone increases, better accuracy is achieved in the calculation. However, the higher the number of k-points, the calculation would be more expensive since the computational time scales linearly with the number of k-points used in the calculations. As a first step in reducing computational cost, symmetries of the system are usually used to reduce the BZ to the irreducible BZ. In that case, one needs to consider only the k-points in the irreducible BZ for the calculation.[47]

In the case of isolated systems or very large supercells, it would be enough if the k-space is sampled only at the Brillouin zone origin $\mathbf{k} = (0, 0, 0)$, also known as the Γ point. For artificially periodic supercells, one can choose only one division along the aperiodic (artificially periodic) directions.[47]

2.3.8 Smearing

We have already mentioned that any observable of the wavefunction is obtained by carrying out a summation over all the occupied states at a given **k**-point, and then integrating over all the **k**-points in the first Brillouin zone (BZ). In the case of metals the Brillouin zone can be divided into regions occupied and unoccupied by electrons. The surface in **k** space that separates the occupied region from the unoccupied region is called the *Fermi surface*. For metals at temperature T=0, the occupancy falls like a step function at the Fermi energy. Then, to accurately evaluate integrals in **k** space, one has to use a very large number of **k**-points to reproduce the Fermi surface accurately, because the functions that are integrated change discontinuously from

non-zero values to zero in reciprocal space. [48] Using a large number of **k**-points is not an efficient way to evaluate such integrals, since it increases the computational time hugely. Moreover, another problem is that band crossings above and below the Fermi level may lead to convergence issues while calculating the total energy using the self-consistent field loop.[47]

One way to get rid of this problem is by replacing the sharp, discontinuous step function (at temperature $T = 0$) at the Fermi energy (E_F), with a smoother function. This smoothening of the discontinuous step function allows partial occupancies at E_F. Therefore, the discontinuity in the occupancies near the Fermi energy is smeared out due to this smoother function. This smoothening of electron occupancies ensures faster convergence with respect to the number of **k**-points but does not necessarily give the right answer. The higher is the smearing, the faster would be the convergence with respect to k-points, but, typically, the lower is the accuracy.[47]

For this purpose, several successful techniques have been employed to smear out the sharp Fermi function. A popular smearing method was developed by Methfessel and Paxton, where the step function is expanded in terms of Hermite functions, which are the products of Hermite polynomials and Gaussian functions.[49] This technique suffers from the problem of negative occupancies which can cause problems in visualizing densities of states. Gaussian smearing[50] is another popular smearing technique, where the energy levels are broadened by Gaussian functions but the errors introduced in this method can be large. A new smearing technique was introduced by Marzari and Vanderbilt which is found to be more accurate than the Methfessel and Paxton and Gaussian techniques, without having the problem of negative occupancies.[51] In this scheme, the Dirac delta function is approximated using a Gaussian function multiplied by a first order polynomial.

2.3.9 Force Calculations: Hellmann-Feynman theorem and Structural Optimization

The aim of geometry optimization of any system is to the generate its optimal (lowest energy) structure from an arbitrary initial state. To determine the optimized geometry of a system one has to compute the forces on the atoms in a system efficiently and accurately. The forces acting on the atoms in a system can be calculated by obtaining the first derivative of the total energy with respect to the atomic positions. This procedure could, in principle, be carried out by performing a large number of self-consistent calculations that need to be carried out for a number of different atomic configurations. Hellmann and Feynman proved the existence of a simpler method to compute the forces in a system: according to their theorem, the derivative of the total energy is equal to the expectation value of the derivative of the Hamiltonian:[52]

$$F_I = -\frac{\partial \langle E(\mathbf{R}_I) \rangle}{\partial \mathbf{R}_I} = -\left\langle \frac{\partial H}{\partial \mathbf{R}_I} \right\rangle, \tag{2.30}$$

here $E(\mathbf{R_I})$ is the total energy for a given set of nuclear co-ordinates $\{\mathbf{R}_I\}$. This force can then be used to find the ground state coordinates of the atoms in a system, by moving the atoms (using some minimization scheme) until the forces on all the atoms are zero.

Geometries of the systems studied in this thesis are optimized using Broyden-Fletcher-Goldfarb-Shanno (BFGS) and conjugate-gradient (CG) algorithms. BFGS is the most popular quasi-Newton approach used to solve the unconstrained nonlinear optimization problems.[53–56] Quasi-Newton methods require only the gradient of the function to be computed at each iteration. BFGS is much faster than the steepest descent methods. Instead of solving the Hessian matrix exactly BFGS algorithm evaluates it approximately. This approach makes the calculation more efficient and less expensive. Conjugated-gradient (CG) algorithm is the most popular iterative

technique to solve a system of linear equations.[57] This method is often implemented as an iterative algorithm. The systems which are too large to be handeled by any direct method CG technique wis applicable to those sparse systems.

2.3.10 Spin-Polarized Density Functional Theory

The spin of electrons is important to study the magnetic and spintronic properties of the systems. In the formulation of spin-polarized DFT, the total electron density is split into the spin up and spin down electronic densities. The coupled Kohn-Sham equations are solved to find the solution for each spin. The spin-polarized electronic densities are given by:

$$n^{\sigma}(\mathbf{r}) = 2\sum_{s=1}^{N^{\sigma}} \psi_s^{\sigma *}(\mathbf{r})\psi_s^{\sigma}(\mathbf{r}), \tag{2.31}$$

where $\sigma = \{\uparrow, \downarrow\}$, represents the spin of the electron, and N^{σ} is the number of orbitals of spin σ. The total electronic density of the spin-polatized system is the sum of the spin up and spin down electronic densities: $n(\mathbf{r}) = n^{\uparrow}(\mathbf{r}) + n^{\downarrow}(\mathbf{r})$. The magnetic moment of the spin polarized system is given by: $m(\mathbf{r}) = n^{\uparrow}(\mathbf{r}) - n^{\downarrow}(\mathbf{r})$.

Only collinear magnetism is studied, without any spin-orbit interaction, in the simplest version of the spin-polarized DFT.

The Kohn-Sham equations for each spin are given by:

$$\left\{ -\frac{\hbar^2}{2m_e}\nabla^2 + V_{\mathrm{KS}}^{\sigma}(\mathbf{r}) \right\} \psi_s^{\sigma}(\mathbf{r}) = \epsilon_s^{\sigma}\psi_s^{\sigma}(\mathbf{r}). \tag{2.32}$$

V_{KS}^{σ} is the Kohn-Sham potential, which is given by:

$$V_{\mathrm{KS}}^{\sigma}(\mathbf{r}) = V_{ext}(\mathbf{r}) + V_H(\mathbf{r}) + V_{xc}^{\sigma}(\mathbf{r}), \tag{2.33}$$

The exchange-correlation potential now includes a spin-dependent part. The spin dependency in the system arises only from the exchange-correlation potential. In the

case of a spin-polarized system the exchange-correlation potential is defined as:

$$V_{xc}^{\sigma}(\mathbf{r}) = \frac{\delta E_{xc}[n(\mathbf{r}), m(\mathbf{r})]}{\delta n^{\sigma}(\mathbf{r})}, \tag{2.34}$$

To deal with spin-polarized systems all the equations mentioned above are solved in a similar manner to the non-spin-polarized Kohn-Sham equations.

2.3.11 Dispersion Interactions and the DFT-D2 Method

The dispersion interactions (which are also known as van der Waals interactions or London interactions) between atoms and molecules play an important role in many chemical systems. For example,the structures of DNA, proteins, and host-guest systems, as well as the adsorption geometries of many molecules on surfaces are controlled by dispersion interactions.

The relationship between electron-electron correlations and long-range interactions was initially examined by London in 1930.[58] London found that though the time-averaged electron density around an atom or molecule has zero dipole moment, oscillations of electrons cause deformations of the electron density, which result in a transient dipole moment. This instantaneous dipole moment can induce a temporary dipole moment on other atoms or molecules by distorting their electron density. These dipoles have a net interaction with each other. London showed that the general form of the interaction between two spherically symmetric atoms at large distance is:

$$V_{disp} = \frac{C}{r^6}, \tag{2.35}$$

where r is the distance between the atoms and C is a combination of physical constants which include some of the same information that is incorporated in the dispersion of the refractive index of a material with respect to the wavelength of light. Therefore these interactions are termed as dispersion interactions.[48] A very common example of systems dominated by dispersion interactions are the dimers of the rare-gas atoms,

e.g., He, Ne and Ar. These atoms are known to be less chemically reactive, but these gases can be liquefied at sufficiently low temperatures, which implies that attractive interactions exist between rare gas atoms.[59]

Standard DFT calculations do not incorporate dispersion interactions. One solution to overcome the drawbacks of DFT regarding dispersion forces is to simply add, by hand, a dispersion-like contribution to the total energy between each pair of atoms in a material. The DFT-D2 functional by Grimme adds an additional term to the DFT total energy in order to include the contribution of dispersion forces, or van der Waals interactions:[60]

$$E_{DFT-D2} = E_{KS-DFT} + E_{disp}, \tag{2.36}$$

where E_{KS-DFT} is the usual self-consistent Kohn-Sham DFT energy and E_{disp} is the dispersion correction, given by:

$$E_{disp} = -s_6 \sum_{i=1}^{N_{at}-1} \sum_{j=i+1}^{N_{at}} \frac{C_6^{ij}}{R_6^{ij}} f_{dmp}(R_{ij}), \tag{2.37}$$

where N_{at} is the number of atoms in the system, C_6^{ij} is the dispersion coefficient for atom pair ij:

$$C_6^{ij} = \sqrt{C_6^i C_6^j}, \tag{2.38}$$

and s_6 is a global scaling factor that depends on the exchange correlation functional.[61] For example, the valuesof s_6 have been determined for several different DFT functionals: PBE ($s_6 = 0.75$), BLYP ($s_6 = 1.2$), and B3LYP ($s_6 = 1.05$).[60] R_{ij} is the interatomic distance. To get rid of near singularities for small R, a damping function f_{dmp} must be used, which is given by:

$$f_{dmp}(R_{ij}) = \frac{1}{1 + e^{-d(R_{ij}/R_r - 1)}}, \tag{2.39}$$

where R_r is the sum of atomic van der Waals radii.[62] d is a damping parameter, typically the value of d is set to be 20.[60]

2.3.12 Time Dependent Density Functional Theory

Standard DFT formulated by P. Hohenberg and W. Kohn is useful to study the ground state properties of a quantum many-body system.[4] This technique does not deal with excited state phenomena. Time-dependent density functional theory (TDDFT) is an extension of standard DFT. TDDFT is a quantum many-body formalism which deals with dynamical systems, i.e., those which are not in a stationary state. TDDFT is a popular and efficient theory used in physics and chemistry to study the excited state properties of many-body systems in the presence of time-dependent potentials. The effect of time-dependent electric or magnetic field on molecules and solids can be investigated with the help of TDDFT to extract features like accurate values of band gaps, absorption spectra, frequency-dependent electronic response properties, optical properties and various excited state phenomena.

TDDFT is based on the time-dependent extension of the Hohenberg-Kohn (HK) theorem, derived by Runge and Gross in 1984.[63] TDDFT is also in principle exact, like standard DFT, and there exists a one-to-one mapping between the time-dependent effective potential and the time-dependent electronic density. Similar to standard DFT, in the case of TDDFT also the time-dependent electron density can be evaluated from the time-dependent electronic wavefunction. Another task in this context is to derive the effective potential of a fictitious non-interacting system which gives back the electronic density, which is similar to the density of any interacting system. It is a complicated task to construct such a system for TDDFT, since the time-dependent effective potential at any given instant depends on the density at all previous times.

The time-dependent Kohn-Sham Hamiltonian, acting on the time-dependent

wavefunction, is:

$$\left\{ -\frac{\hbar^2}{2m_e}\nabla^2 + V_{\mathrm{KS}}[n(\mathbf{r},t)] \right\}\psi_\alpha(\mathbf{r},t) = i\frac{\delta}{\delta t}\psi_\alpha(\mathbf{r},t), \tag{2.40}$$

where $\psi_\alpha(\mathbf{r},t)$ is the time-dependent wavefunction and $V_{\mathrm{KS}}[n(\mathbf{r},t)]$ is the time-dependent Kohn-Sham potential.

The time-dependent electronic density $n(\mathbf{r},t)$ is given by:

$$n(\mathbf{r},t) = \sum_{\alpha=1}^{N} |\psi_\alpha(\mathbf{r},t)|^2. \tag{2.41}$$

The time-dependent potential $V_{\mathrm{KS}}[n(\mathbf{r},t)]$ can be written as:

$$V_{\mathrm{KS}}[n(\mathbf{r},t)] = V_{ext}[n(\mathbf{r},t)] + V_H[n(\mathbf{r},t)] + V_{xc}[n(\mathbf{r},t)], \tag{2.42}$$

where $V_{ext}[n(\mathbf{r},t)]$, $V_H[n(\mathbf{r},t)]$ and $V_{xc}[n(\mathbf{r},t)]$ are the time-dependent external potential, the Hartree energy and the exchange-correlation potential, respectively. In the limit of slowly varying $V_{ext}[n(\mathbf{r},t)]$, the time-dependent exchange correlation potential $V_{xc}[n(\mathbf{r},t)]$ is calculated by using the adiabatic local density approximation (ALDA). $V_{xc}[n(\mathbf{r},t)]$ is the functional derivative of E_{xc} with respect to the time dependent electron density,

$$V_{xc}(\mathbf{r},t) = \frac{\delta E_{xc}[n]}{\delta n_t(\mathbf{r})}. \tag{2.43}$$

Under the application of a time-varying or frequency-dependent perturbation, the linear response of a molecule or solid can be expressed through a frequency-dependent dynamic polarizability, $\alpha(\omega)$.

$$\alpha(\omega) = \frac{2}{3}\sum_i \frac{\omega_{\lambda i}|\mu_{\lambda i}|^2}{\omega_{\lambda i} - \omega^2} = \frac{f_{\lambda i}}{\omega_{\lambda i} - \omega^2}, \tag{2.44}$$

where $\omega_{\lambda i}$ is the energy difference between the initial state i and the excited state λ, and $\mu_{\lambda i}$ is the dipole moment arising due to the electronic transition between the

state i to the state λ. $\mu_{\lambda i}$ is known as transition dipole moment,[64] it determines the strength of interaction between a charge distribution and an electric field that causes a transition between two states. When a system is perturbed by an external electric field that results in a transition from ψ_i to ψ_λ, the dipole moment integral corresponding to this transition is given by:

$$\langle \mu \rangle_T = \int \psi_\lambda^* \hat{\mu} \psi_i d\tau \tag{2.45}$$

The transition probability is proportional to $\mu_T^* \mu_T$, i.e., the square of the transition dipole moment.

In Eq. (2.44) the term $f_{\lambda i}$ is the oscillator strength, which is a dimensionless quantity that gives the probability of absorption or emission of electromagnetic radiation in transition between energy levels of an atom or molecule.[65]

2.4 Simulation of STM Image: Tersoff-Hamann Approach

In surface science, one of the most fundamental problems is to determine the surface structure. The invention of the scanning tunneling microscope (STM) in 1983 by Binnig and Rohrer provided a promising tool to investigate the properties of surface structure in real space, including non-periodic structures.[66–68] In the STM, a small metal (e.g., Au) tip is brought close enough to the surface so that quantum mechanical tunneling can occur between the sample and the tip through the vacuum, this tunneling should be finite and measurable. The STM tip scans the surface in two dimensions, while the height of the tip is adjusted to make the tunneling current constant. The STM can operate either in constant height or in constant current mode, depending on the nature of the surface and requirement. Since the tip can also be used to attach, detach and move atoms, STM is also widely used to fabricate structures on surfaces in a range starting from 100 nm down to the

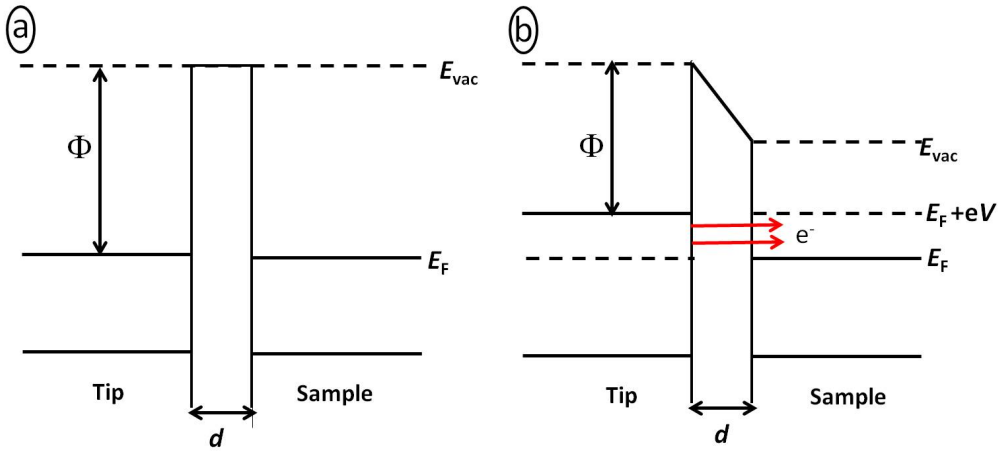

Figure 2.2: Schematic diagram showing the energy level alignment between the tip and the sample (a) in absence of any bias volatge and (b) when the bias voltage V is applied. E_{F} and E_{vac} are the Fermi energy and vacuum energy, respectively. Φ is the work function and d is the tip-sample distance. This figure is adapted from Ref. 69 with permission.

atomic dimensions.

In the STM technique, when the distance d between the metal tip and the conducting surface becomes sufficiently small (< 10 Å), then electrons can tunnel through the vacuum barrier. When a bias voltage V is applied between the tip and the sample, then theelectron tunneling effect results in a net flow of electric current across the gap; the direction of the tunneling current depends on the polarity of the bias voltage applied.

Fig. 2.2 shows a schematic depiction of energy level alignments between the tip and the sample before and after the bias voltage is applied between them. When the tip is brought close to the sample, the Fermi levels of the sample and the tip get aligned up to the same height with respect to the vacuum, in the absence of any bias voltage, see Fig. 2.2(a). In this figure, Φ is the work function of the STM tip, which is metallic in nature. For simplicity, we consider that the value of the work function is the same for both the STM tip and the sample. E_{F} and E_{vac} are the common Fermi level and vacuum energy, respectively, for the combined tip-sample system. Now, when a bias voltage is applied, then the Fermi levels of the tip and the

sample become shifted with respect to each other, depending on the polarity of the voltage eV applied. In the schematic diagram shown in Fig. 2.2(b), the bias voltage is applied from tip to sample, which shifts E_{F} of the tip above E_{F} of the sample. Therefore, the tip becomes more occupied than the sample and thus electrons can flow from the tip to the sample, causing a net tunneling current. This current has an exponential dependence on the tip-sample separation d, and the magnitude of the tunneling current could be in a range from 10 pA to 10 nA.

According to Fermi's golden rule, the transition probability from the initial state i to the final state f is given by:

$$R_{i\to f} = \frac{2\pi}{\hbar}|M_{fi}|^2\delta(E_i - E_f), \tag{2.46}$$

where M_{fi} is the matrix element of the perturbation potential which causes a transition between the initial state i and the final state f. Energy conservation is ensured by the δ-function.

Using Eq. (2.46), the current flowing from the tip to the sample, $I_{t\to s}$ under an applied bias V can be written as:

$$I_{t\to s} = \frac{2\pi e}{\hbar}\int |M_{ts}|^2 N_t(E - eV)N_s(E)f_t(E - eV)[1 - f_s(E)]dE. \tag{2.47}$$

In the same way, the current flowing from the sample to the tip can be written as:

$$I_{s\to t} = \frac{2\pi e}{\hbar}\int |M_{ts}|^2 N_t(E - eV)N_s(E)f_s(E - eV)[1 - f_t(E)]dE, \tag{2.48}$$

where $I_{x\to y}$ is the current flowing from x to y. $N(E)$ is the total density of states. $f(E) = [exp(E - E_F)/k_BT + 1]^{-1}$ is the Fermi-Dirac (F-D) distribution function. In the situation discussed above, electrons from the occupied states of the tip (N_t, f_t)

can tunnel to the unoccupied states (N_s, $[1-f_s]$) of the sample, when a bias voltage V is applied. Thus due to the applied voltage the Fermi level of the tip gets shifted by an energy eV with respect to the sample Fermi level.

The F-D distribution becomes a step function at $T = 0$ and the net tunneling current from the tip to the sample can be written as:

$$I(T=0) = \int_{E_F}^{E_F+eV} |M_{ts}|^2 N_t(E-eV) N_s(E) dE, \tag{2.49}$$

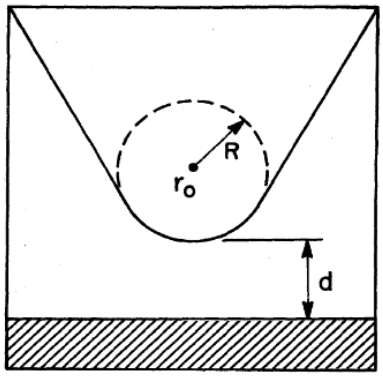

Figure 2.3: Schematic diagram showing the geometry of the STM tip. The tip is assumed to be spherical in shape. R is the radius of curvature, d is the nearest tip-sample distance and r_0 is the center of curvature of the tip. The shaded region shows the surface of the sample.[70]. This figure is taken with permission from Ref. 70 ©American Physical Society.

Now, to calculate the tunneling current, the first and most important step is to evaluate the matrix element M_{ts}. The matrix element is related to the overlap between the tip and the sample wavefunctions. Therefore, to determine M_{ts}, the tip and sample wavefunctions are required. The wavefunction of the sample is very straightforward and easy to determine. But in the case of the STM tip, its exact atomic structure and chemical nature are not known.

Tersoff and Hamann in 1983 suggested a method to interpret STM images, this method is still very popular and useful to the STM community.[70] According to the Tersoff-Hamann method the unknown structure of the tip is replaced by a simple

model. The wavefunction of the outermost tip atom is assumed to be an atomic s-wavefunction, which is spherical in shape. Since the wavefunction decays exponentially into the vacuum, only those orbitals which are localized at the outermost tip atom will play an important role for the tunneling process.

The choice of the wavefunction of the STM tip is responsible for the main success of the Tersoff and Hamann theory. Since the exact structure of the tip is unknown it can be modeled as a locally spherical potential (Fig. 2.3), with curvature R about the center r_0. The functional form of the tip wavefunction is given by:

$$\Psi_t(r) = \kappa R e^{\kappa R} \frac{e^{-\kappa|r-r_0|}}{\kappa|r-r_0|}, \tag{2.50}$$

where $\kappa = \sqrt{\frac{2m\phi}{\hbar}}$, Φ is the work function, which represents the barrier height for electron tunneling from tip to sample or vice versa.

Writing the tip wavefunction as a two-dimensional Fourier sum and assuming the surface of the sample S to be a parallel plane, one finds that the matrix element M_{ts} is proportional to the sample wavefunction Ψ_s evaluated at the tip's center of curvature:

$$M_{ts} \propto \Psi_s(r_0), \tag{2.51}$$

Therefore, the net tunneling current flowing from the tip to the sample can be written as:

$$I = I_t - I_s \propto V N_t(E_F) \sum_s |\Psi_s(r_0)|^2 \delta(E_s - E_F), \tag{2.52}$$

In Eq. (2.52) the sum is the local density of states (LDOS) of the sample at the Fermi level evaluated at the tip center. The tunneling current I in the final and simplified form can be written as:

$$I \propto V N_t \text{ LDOS}(r_0, E_F) \tag{2.53}$$

The Tersoff-Hamann approach is a novel technique for the simulation of the STM images. STM images help us to investigate the geometric and electronic properties of the surface. The main quantity which is imaged in the STM is the local density of states of the sample. The Tersoff-Hamann model is successful in most of the cases, but it fails for the cases where the surface corrugation is significant. The corrugation amplitudes of the sample surfaces predicted by this model are too small, compared to the actual situation. This discrepancy arises partially due to the strict assumption of a *s*-like wavefunction of the STM tip, as pointed out by Chen *et al.*[71]

In this thesis, using the Tersoff-Hammann approach, the STM images are simulated in the constant height mode.

2.5 Codes Used

Density Functional Theory as implemented in the Quantum ESPRESSO[26] and SIESTA [28] packages, is used in this thesis for obtaining various properties of materials, such as optimized structure, adsorption energies, charge states, densities of states etc., as described in the later chapters in this thesis.

The atomistic structures of the systems, charge redistribution plots, molecular orbital plots, simulated STM images reported in this thesis, were obtained using the software packages XCrySDen[72] and VESTA.[73] All two-dimensional graphs in the thesis were plotted using the Xmgrace software, and three-dimensional plots were obtained using gnuplot.

Bibliography

[1] R. M. Martin, *Electronic Structure Basic Theory and Practical Methods*. Cambridge University Press, 2004.

[2] M. Born and J. R. Oppenheimer *Ann. Physik*, vol. 84, pp. 457 – 484, 1927.

[3] P. Hohenberg and W. Kohn *Phys. Rev.*, vol. 136, pp. B864–B871, 1964.

[4] W. Kohn and L. J. Sham *Phys. Rev.*, vol. 140, pp. A1133–A1138, 1965.

[5] K. Ulman, *First Principles Investigations of Nanomaterials for Electronic, Spintronic and Gas Storage Applications*. PhD thesis, Jawaharlal Nehru Centre for Advanced Scientific Research, Bangalore, India, 2015.

[6] D. D. Johnson *Phys. Rev. B*, vol. 38, pp. 12807–12813, 1988.

[7] D. Vanderbilt and S. G. Louie *Phys. Rev. B*, vol. 30, pp. 6118–6130, 1984.

[8] O.V.Gritesnko, P. Schipper, and E. J. Baerends *J. Chem. Phys.*, vol. 107, p. 5007, 1997.

[9] R. O. Jones and O. Gunnarsson *Rev. Mod. Phys.*, vol. 61, pp. 689–746, 1989.

[10] D. M. Ceperley and B. J. Alder *Phys. Rev. Lett.*, vol. 45, pp. 566–569, 1980.

[11] S. J. Vosko, L. Wilk, and M. Nusair *Can. J. Phys.*, vol. 58, pp. 1200–1211, 1980.

[12] R. G. Parr and W. Yang, *Density Functional Theory of Atoms and Molecules*. Oxford University Press, 1989.

[13] M. Caffarel and P. Claverie *J. Chem. Phys.*, vol. 88, pp. 1088–1099, 1988.

[14] P. A. M. Dirac *Cambridge Phil. Soc.*, vol. 26, pp. 376–385, 1930.

[15] J. P. Perdew, K. Burke, and M. Ernzerhof *Phys. Rev. Lett.*, vol. 77, pp. 3865–3868, 1996.

[16] J. P. Perdew, K. Burke, and M. Ernzerhof *Phys. Rev. Lett. (E)*, vol. 78, pp. 1396–1396, 1997.

[17] J. P. Perdew and Y. Wang *Phys. Rev. B*, vol. 46, pp. 12947–12954, 1992.

[18] J. P. Perdew, M. Ernzerhof, and K. Burke *J. Chem. Phys.*, vol. 105, no. 22, pp. 9982–9985, 1996.

[19] K. Kim and K. D. Jordan *J. Phys. Chem.*, vol. 98, pp. 10089–10094, 1994.

[20] P. J. Stephens, F. J. Devlin, C. F. Chabalowski, and M. J. Frisch *J. Phys. Chem.*, vol. 98, pp. 11623–11627, 1994.

[21] J. P. Perdew, M. Ernzerhof, and K. Burke *J. Chem. Phys.*, vol. 105, no. 22, pp. 9982–9985, 1996.

[22] J. Heyd, G. E. Scuseria, and M. Ernzerhof *J. Chem. Phys.*, vol. 118, no. 18, pp. 8207–8215, 2003.

[23] Y. Zhao and D. G. Truhlar *Theor. Chem. Acc.*, vol. 120, pp. 215–241, 2008.

[24] A. D. Becke *Phys. Rev. A*, vol. 38, pp. 3098–3100, 1988.

[25] C. Lee, W. Yang, and R. G. Parr *Phys. Rev. B*, vol. 37, pp. 785–789, 1988.

[26] P. Giannozzi, S. Baroni, N. Bonini, M. Calandra, R. Car, C. Cavazzoni, D. Ceresoli, G. Chiarotti, M. Cococcioni, I.Dabo, A. D. Corso, S. de Gironcoli, S. Fabris, G. Fratesi, R. Gebauer, U. Gerstmann, C. Gougoussis, A. Kokalj, M. Lazzeri, L. Martin-Samos, N. Marzari, F. Mauri, R. Mazzarello, S. Paolini, A. Pasquarello, L. Paulatto, C. Sbraccia, S. Scandolo, G. Sclauzero, A. P. Seitsonen, A. Smogunov, P. Umari, and R. M. Wentzcovitch *J. Phys. Condens. Matter*, vol. 21, p. 395502, 2009.

[27] X. Gonze, J.-M. Beuken, R. Caracas, F. Detraux, M. Fuchs, G.-M. Rignanese, L. Sindic, M. Verstraete, G. Zerah, F. Jollet, M. Torrent, A. Roy, M. Mikami, P. Ghosez, J.-Y. Raty, and D. C. Allan *Comput. Mater. Sci.*, vol. 25, pp. 478–492, 2002.

[28] J. M. Soler, E. Artacho, J. D. Gale, A. García, P. O. J. Junquera, and D. Sánchez-Portal *J. Phys.: Condens. Matter*, vol. 14, pp. 2745–2779, 2002.

[29] O. K. Andersen, *Electronic Structure and Physical Properties of Solids. The Uses of the LMTO Method*. Springer, 2000.

[30] C. Kittel, *Introduction to Solid State Physics*. Wiley - India, 2007.

[31] G. P. Francis and M. C. Payne *J. Phys. Condens. Matter*, vol. 2, pp. 4395–4404, 1990.

[32] G. Kresse and J. Hafner *Phys. Rev. B*, vol. 47, pp. 558–561, 1993.

[33] E. R. Davidson and D. Feller *Chemical Reviews*, vol. 86, pp. 681–696, 1986.

[34] F. J. Jensen, *Introduction to Computational Chemistry*. Wiley, Chichester, 1999.

[35] P. Manninen and J. Vaara *J. Comput. Chem.*, vol. 27, pp. 434–445, 2006.

[36] A. L. Magalhães *J. Chem. Educ.*, vol. 91, pp. 2124–2127, 2014.

[37] E. Anglada, J. M. Soler, J. Junquera, and E. Artacho *Phys. Rev. B*, vol. 66, pp. 205101–205104, 2002.

[38] G. Lever, *Large Scale Quantum Mechanical Enzymology*. PhD thesis, Magdalene College University of Cambridge, 2014.

[39] W. H. E. Schwarz, E. M. van Wezenbeck, E. J. Baerends, and J. G. Snijders *J. Phys. B*, vol. 22, pp. 1762–1774, 1989.

[40] J. C. Slater. *Phys. Rev.*, vol. 51, pp. 846–851, 1937.

[41] C. Herring. *Phys. Rev.*, vol. 57, pp. 1169–1177, 1940.

[42] S. Narasimhan, "Atoms and pseudopotentials." http://www.iiserpune.ac.in/~smr2626/hands_on/week1/july1/pseudopotentials.pdf, 2014. [Online; accessed February-2018].

[43] D. R. Hamann, M. Schlüter, and C. Chiang *Phys. Rev. Lett.*, vol. 43, pp. 1494–1497, 1979.

[44] M. C. Payne, M. P. Teter, D. C. Allan, T. A. Arias, and J. D. Joannopoulos *Rev. Mod. Phys.*, vol. 64, pp. 1045–1097, 1992.

[45] D. Vanderbilt *Phys. Rev. B*, vol. 41, pp. 7892–7895, 1990.

[46] H. J. Monkhorst and J. D. Pack *Phys. Rev. B*, vol. 13, pp. 5188–5192, 1976.

[47] S. Narasimhan, ""k-points" or brillouin zone sums in electronic structure calculations." http://www.iiserpune.ac.in/~smr2626/hands_on/week1/july1/bzsums_mastani.pdf, 2014. [Online; accessed February-2018].

[48] D. S. Sholl and J. A. Steckel, *Density Functional Theory A Practical Introduction*. Wiley, 2009.

[49] M. Methfessel and A. T. Paxton *Phys. Rev. B*, vol. 40, pp. 3616–3621, 1989.

[50] C. L. Fu and K. M. Ho *Phys. Rev. B*, vol. 28, pp. 5480–5486, 1983.

[51] N. Marzari, D. Vanderbilt, A. D. Vita, and M. Payne *Phys. Rev. Lett.*, vol. 82, pp. 3296–3299, 1999.

[52] R. P. Feynman *Phys. Rev.*, vol. 56, pp. 340–343, 1939.

[53] C. G. Broyden *IMA J. Appl. Math.*, vol. 6, pp. 76–90, 1970.

[54] R. Fletcher *Comput. J.*, vol. 13, pp. 317–322, 1970.

[55] D. Goldfarb *Math. Comp.*, vol. 24, pp. 23–26, 1970.

[56] D. F. Shanno *Math. Comp.*, vol. 24, pp. 647–656, 1970.

[57] O. Axelsson and V. Barker, *Finite Element Solution of Boundary Value Problems: Theory and Computation*. Classics in Applied Mathematics, Society for Industrial and Applied Mathematics (SIAM, 3600 Market Street, Floor 6, Philadelphia, PA 19104), 1984.

[58] F. London, *On the Theory And System of Molecular Forces, Quantum Chemistry*. World Scientific, 2012.

[59] Y. Zhao and D. G. Truhlar *J. Phys. Chem. A*, vol. 108, pp. 6908–6918, 2004.

[60] S. Grimme *J. Comput. Chem.*, vol. 27, pp. 1787–1799, 2006.

[61] R. Peverati and K. K. Baldridge *J. Chem. Theory Comput.*, vol. 4, pp. 2030–2048, 2008.

[62] S. Grimme *J. Comput. Chem.*, vol. 25, pp. 1463–1473, 2004.

[63] E. Runge and E. K. U. Gross *Phys. Rev. Lett.*, vol. 52, pp. 997–1000, 1984.

[64] C. Yamada and E. Hirota *J. Chem. Phys.*, vol. 78, pp. 669–671, 1983.

[65] A. F. Starace *Phys. Rev. A*, vol. 3, pp. 1242–1245, 1971.

[66] G. Binnig, H. Rohrer, C. Gerber, and E. Weibel *Phys. Rev. Lett.*, vol. 49, pp. 57–61, 1982.

[67] G. Binnig and H. Rohrer *Surf. Sci.*, vol. 126, no. 1, pp. 236 – 244, 1983.

[68] G. Binnig, H. Rohrer, C. Gerber, and E. Weibel *Phys. Rev. Lett.*, vol. 50, pp. 120–123, 1983.

[69] "Scanning tunneling microscopy." http://hoffman.physics.harvard.edu/research/STMintro.php, 2010. [Online; accessed February-2018].

[70] J. Tersoff and D. R. Hamann *Phys. Rev. Lett.*, vol. 50, pp. 1998–2001, 1983.

[71] A. Selloni, P. Carnevali, E. Tosatti, and C. D. Chen, *Scanning Tunneling Microscopy*, pp. 168–171. Dordrecht: Springer Netherlands, 1993.

[72] A. Kokalj *Comp. Mater. Sci.*, vol. 28, pp. 155–168, 2003.

[73] K. Momma and F. Izumi *J. Appl. Crystallogr.*, vol. 44, pp. 1272–1276, 2011.

Chapter 3

Descriptors for the Self-Assembly of Organic Molecules in Two-Dimensions

In this chapter, our aim is to study self-assembled architectures built from molecular building blocks placed on a substrate, and to formulate suitable descriptors which can successfully predict the resulting self-assembled patterns. This work has been done in collaboration with the experimental group of Prof. K. George Thomas and his student Pratap Zalake (IISER Thiruvananthapuram, India). Most of the results presented in this chapter have been published by us in Chem. Mater., 2017, 29(17), 7170-7182 (Ref. 43). The experimental results discussed in this chapter have already been mentioned in the PhD thesis of Dr. Pratap Zalake.[1]

3.1 Introduction

3.1.1 Self-assembly and its applications

Self-assembly can be found everywhere in nature, e.g., from the molecular self-assembly in DNA or RNA to the co-assembly of stars and planets in the universe. It is defined as the association of numerous individual entities without any external

stimuli. The formation of a self-assembled pattern is a reversible process in which pre-existing parts or components of a system form the structures of a pattern. Molecular self-assembly is the spontaneous organization of molecular building blocks arranged together by various non-covalent interactions. This has now emerged as a new powerful approach in the field of chemical synthesis, polymer science, materials science, and engineering.

The self-assembly of organic molecules offers great promise for constructing devices at the nanoscale.[2, 3] There is now a growing awareness that if one wants to construct machines at the molecular level, one must build them from the bottom-up, i.e., using atoms or molecules as the building blocks, using self-assembly. Molecular self-assembly provides a route for designing and constructing systems with atomic precision. In this era, we are almost at a stage where we could engineer machines that can enter the human body and deliver drugs, or can even perform minute operations. Using supramolecular self-assembly it is possible to construct devices such as supramolecular switches, molecular elevators, molecular cars [see Fig. 3.1(a)] and other molecular machines. Supramolecular switches have attracted considerable interest during the last decade due to their unique properties and prominent role in the fields of organic chemistry and materials science [see Fig. 3.1(b)].[4] Molecular machines convert chemical, electrical, optical, and heat energy into kinetic energy. Molecular self-assembly can also be used to build components in molecular electronic circuits,[5, 6] solar cells,[7] coatings,[8] and nanomachines.[9, 10]

Molecular self-assembly can be influenced by either substrate-molecule or molecule-molecule interactions, or by both.[12–14] Various kinds of intermolecular interactions are responsible for the two-dimensional (2D) self-assembly of molecules on surfaces. These interactions include hydrogen bonding, van der Waals interactions, and metallo-ligand interactions (co-ordination interactions). [15] Among these interactions, hydrogen bonding (XH—A) is the one that is most widely used to stabilize 2D supramolecular assemblies. This is an attractive interaction between a hydrogen

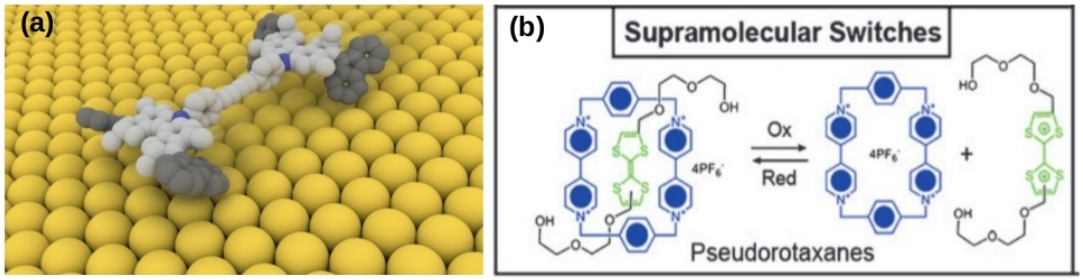

Figure 3.1: (a) A molecular 'nanocar' travels across a metal surface, propelled by bonding changes. A single molecule containing two identical paddle units connected by a carbon-carbon double bond.[11] This figure is taken with permission from Ref. 11 ©(2011) American Chemical Society. (b) Supramolecular switches comprise two components interacting with one another through non-covalent bonding interactions. An external stimulus can be used to disturb these interactions, so that the two components dissociate from one another. Pseudorotaxanes are one of the most versatile of such supramolecular switches and can be dissociated and re-assembled using a variety of stimuli such as light.[4] This figure is taken with permission from Ref. 4 ©(2010) Royal Society of Chemistry.

atom of a molecule and an electronegative atom A of another molecule. The electronegativity difference between H and A determines the strength of the hydrogen bond. The interaction strength of hydrogen bonding spans over a wide range, within the limit from van der Waals bonds to covalent bonds.[16] Hydrogen bonds can be classified into different categories, such as (i) very weak, (ii) weak, (iii) strong, or (iv) very strong. Among these, the first two types fall within the domain of van der Waals interactions and they do not provide directionality in 2D networks. The energy associated with strong and very strong hydrogen bonds is comparable to that of electrostatic and covalent interactions; these bonds provide directionality to the molecular architectures in 2D assemblies.[17] Therefore, strong hydrogen bonding (e.g., between acid dimers or amide dimers) plays a key role in stabilizing supramolecular patterns on surfaces.[15, 18–20]

Host-guest chemistry is one of the most important fields in supramolecular chemistry. A molecule (host) can bind another molecule (guest) to develop a host-guest complex. Host-guest chemistry deals with complexes which are composed of molecules or ions that are held together by various non-covalent bonds. In host-guest systems,

a molecular assembly formed by host molecules can accommodate guest molecules depending on their size, shape and recognition sites. Host-guest chemistry is characterized by molecular recognition and interactions through non-covalent interactions. When building host-guest systems, the primary aim is to design such assemblies which can serve as hosts for specific guest molecules. The hosts can be engineered so that they possess cavities that can accommodate the guest molecules. The host-guest complexes formed in 2D can be used for a range of applications,[21] for example, donor-acceptor pairs having charge transfer properties and photoresponsive or electroresponsive molecular switches.[2, 22–25] The size and shape of the cavities formed in the host assembly which serve as the 'home' for the guest molecules, are determined by a delicate balance between various non-covalent interactions.[21, 26–34] In some cases, the interactions between host and guest molecules can trigger structural transformation of the host assemblies.[35–39]

3.1.2 Descriptors

Descriptors are a combination of physically meaningful parameters of a system that correlate well with the property of interest. Descriptors are useful for the rational design of materials. The importance of descriptors has long been recognized, e.g., in the prediction of the crystal structure of octet compounds,[40] the catalytic activity of nanoparticles,[41] and the adsorption strength of transition metals in zeolites.[42] To be effective, descriptors should be quicker to use than performing experiments or first-principle calculations, yet be accurate.

Ideally, one wish to have the ability to design made-to-measure nanostructures. For this, one needs to know, *a priori*, which molecular building blocks to choose in order to obtain a desired architecture. This aim could be achieved if one could identify suitable descriptors that correlate molecular properties with the resulting supramolecular self-assembled nanostructure. In this chapter, we extend such an approach by using a set of organic molecules that consist of specific combinations of chemical motifs. We use these chemical motifs as the molecular 'lego' to formulate

descriptors to predict the pattern of the resulting self-assembly.[43] The 2D nature of these networks helps us to formulate low-dimensional structural descriptors; it also makes these systems easier to study experimentally, as one can use scanning tunneling microscopy (STM) to obtain precise structural information in 2D with atomic resolution.[44–46] STM is a suitable method for studying self-assembly on surfaces, since, unlike in electron microscopy, one can image molecular organization on surfaces at the air-solid or liquid-solid interface,[47, 48] by varying the temperature, and under a variety of conditions ranging from ambient to high vacuum conditions.[49] STM can also provide information about the electronic properties of the molecules on surfaces.[50, 51] Density functional theory (DFT) calculations can play a crucial role in helping us progress toward a descriptor-based design strategy. The geometry and configuration of the self-assembled architectures observed in the STM experiments are considered as the starting guess for the DFT calculations, followed by performing the geometry optimization and energetics study of the self-assembled structures. So, experiments help us to select the desired geometry of the molecular assemblies to proceed for the DFT calculations. In the 'Results' section below we have presented the experimental STM images, together with the atomistic structures (obtained from DFT), and the consequent simulated STM images, to make a comparison between theory and experiment. Finally, we find that the DFT results not only confirm the experimental results in all cases, they also help to determine the driving forces responsible for the self-assembly and provide precise quantitative values for the strengths of the corresponding interactions. Further, free energies computed using DFT serve as target values when formulating appropriate descriptors.

3.2 Systems

We consider three host molecules and five guest molecules as possible building blocks of the host and host-guest systems assembled on graphene. The three host molecules are labeled as PE4A, PE4B, and PE3A (see Fig. 3.2), they are all different

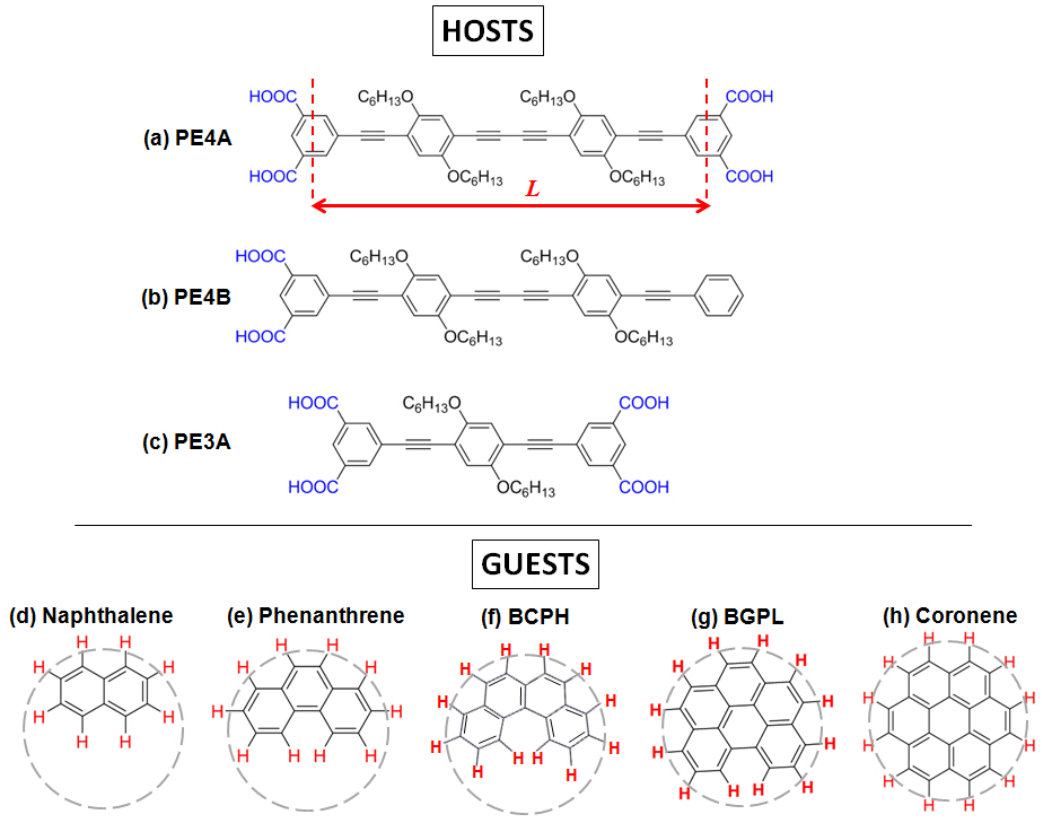

Figure 3.2: Host and guest molecules used in this study. The hosts are labeled as: (a) PE4A, (b) PE4B, and (c) PE3A. See text for a description of the convention used when labeling the hosts. The red arrow indicates how the length L of the host molecules is defined. The guests are (d) naphthalene, (e) phenanthrene, (f) benzo-c-phenanthrene (BCPH), (g) benzo-ghi-perylene (BGPL), and (h) coronene. The dashed gray circles are drawn so as to pass through the maximum number of peripheral H atoms in the guest molecules (see text for description). Reprinted with permission from Ref. 43 ©(2017) American Chemical Society.

carboxylic acid derivatives of phenyleneethynylene. The host molecules differ in the length of their central backbone and/or the number of carboxyl groups attached at the meta positions of the terminal phenyl rings. The length of the host molecule, L, is defined as the distance between the centers of the phenyl rings at the two ends of the central backbone (see the red arrow in Fig. 3.2). The value of L is larger (2.35 nm) for PE4A and PE4B than for PE3A (1.39 nm); also PE4A and PE4B have a greater number of alkoxy side chains than PE3A (four vs. two). We use the labeling convention for host molecules (as well as test case molecules considered further below) as PEnX, where n is the number of phenyl groups in the central backbone and X

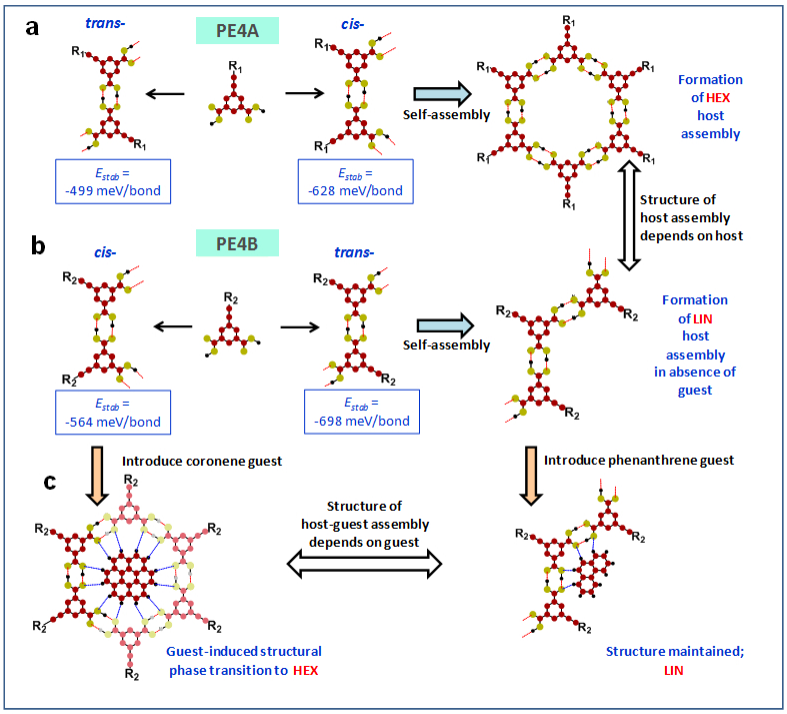

Figure 3.3: Schematic representation showing the formation of HEX and LIN patterns of PE4A and PE4B. (a) Host-host hydrogen bonds between two molecules of PE4A can take either *cis-* or *trans-* arrangements. DFT calculations on two PE4A molecules bonded in the two orientations show that the *cis-* is energetically favored, resulting in the formation of a HEX host assembly in the absence of guest. (b) In contrast, for PE4B, the *trans-* orientation is favored over the *cis-*; therefore, the host assembly forms in the LIN pattern. (c) Since coronene cannot fit in the LIN cavity, there is a guest-induced structural transition to the HEX, and 12 host-guest hydrogen bonds (indicated by blue lines) are formed per guest molecule; however, when phenanthrene is the guest, the LIN pattern is maintained. Reprinted with permission from Ref. 43 ©(2017) American Chemical Society.

provides further structural information; X = A (B) indicates that two COOH groups are present at both ends (only one end) of the backbone. For both X = A and X = B, the number of alkoxy side chains attached to the central backbone = $2(n-2)$.

The terminal carboxyl groups are important because the host molecules can self-assemble by forming dimeric hydrogen bonds between the COOH groups of neighboring molecules; these dimers will constitute a part (in LIN) or the whole (in HEX) of the rims of cavities in which the guest molecules can be accommodated. We note that in all three hosts considered by us, the carboxyl groups are attached symmetrically, in pairs, at meta positions of the terminal phenyl ring(s) of the central

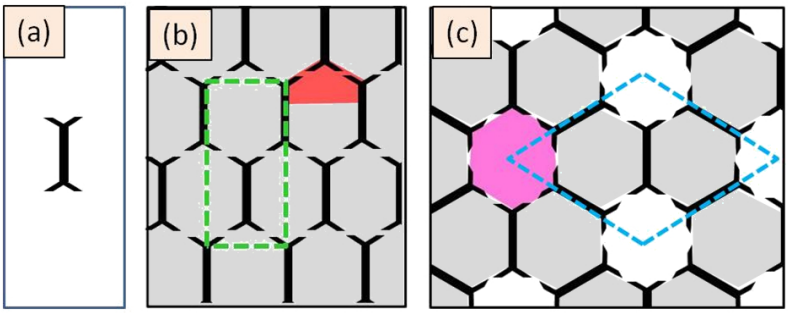

Figure 3.4: Schematic representation showing the formation of periodic HEX and LIN patterns of the host molecules. The red and magenta regions show the pentagonal and hexagonal cavities, respectively. The green and blue lines indicate the unit cell boundaries. The gray regions show the area occupied by the alkoxy chains. Reprinted with permission from Ref. 43 ©(2017) American Chemical Society.

backbone. This makes it possible to have two competing arrangements, LIN and HEX, while in other situations (e.g., when there is a single carboxyl group attached at either a para or a meta position) the formation of the HEX structure is not possible.[52, 53]

The aromatic core of the PE molecules can have either a *cis*- or a *trans*- orientation. The aromatic rings in *cis* orientation with the COOH groups attached to their meta positions lead to the formation of the HEX pattern, see Fig. 3.3(a). The LIN pattern is formed when the aromatic rings are in the *trans*- orientation [Fig. 3.3(b)]. In the case of PE4A the *cis*- orientation of the COOH groups is responsible for the resulting HEX pattern. The LIN pattern of PE4B is formed when the COOH groups are in the *trans*- orientation.

In the LIN patterns, dimeric hydrogen bonds are formed between the COOH groups of the neighboring molecules. The molecular building blocks are assembled in a zigzag fashion to form this pattern. The LIN pattern is less porus and more closely packed than the HEX. It contains pentagonal cavities, these are shown by the red area in Fig. 3.4(b). The terminal COOH groups form two sides of the small pentagonal cavities, two more sides are formed by the backbones of two neighboring host molecules, and the fifth side is formed by an alkoxy side chain. This small pentagonal cavity can in principle accommodate those guest molecules which can fit within the cavity. This cavity becomes slightly enlarged due to bending of the alkoxy

side chains when a guest is placed inside the cavity.

In the HEX pattern of PE4A, the building blocks are arranged in such a fashion that they form cyclic hexagonal networks. These networks are composed of 12 hydrogen bonds arising from interactions between 12 carboxylic acid groups of neighboring PE molecules. These COOH groups form the perimeter of an empty hexagonal cavity (shown by a green arrow in Fig. 3.5). Every hexagonal cavity is surrounded by six triangular cavities, each of which contains six and three alkoxy side chains for PE4A and PE3A, respectively, from three different molecules present per unit cell (see Figs. 3.5 (a) and (c). The HEX pattern is more porous than the LIN pattern. The gray regions in Fig. 3.4 show the area covered by the alkoxy side chains.

We consider five guest molecules: naphthalene, phenanthrene, benzo-c-phenanthrene (BCPH), benzo-ghi-perylene (BGPL), and coronene (see Fig. 3.2). The guest molecules have been chosen primarily so that they can be complementary to the host molecules, in terms of size, shape, and interactions, which makes it possible to form host-guest assemblies from all 15 host-guest pairs.

3.3 Computational Methods

Density functional theory (DFT) calculations were performed using the SIESTA package.[54, 55] We used a double-ζ polarized basis set with a confinement energy of 0.01 Ry. The mesh cutoff size of the real-space grid was taken to be 250 Ry. Troullier-Martins norm-conserving pseudopotentials were used.[56] Exchange-correlation interactions were treated within the PBE form of the generalized gradient approximation (GGA).[57] To study the dispersion interactions the DFT-D2 treatment was applied.[58] A vacuum region with dimension > 16 Å was introduced along non-repeating directions. For the large unit cells used in this study, the Brillouin zone was sampled at the zone center Γ only. Geometry optimization was performed using the conjugate gradient (CG) algorithm. All atomic coordinates were relaxed until the forces on all atoms were smaller than 0.03 eV/Å. Basis set superposition

errors were eliminated by applying the counterpoise correction procedure.[59, 60] The simulated STM images were obtained using the Tersoff-Hamann approach.[61]

As already mentioned, the host molecules can arrange themselves into two kinds of stable patterns, either hexagonal (HEX) or linear (LIN), see Fig. 3.4. Since the experimental STM images show that the host building blocks can form either HEX or LIN pattern depending on their chemical motifs, to determine the lowest energy configuration we compare the energetics between HEX and LIN patterns formed by each host molecule (this is discussed in detail in later sections). In all cases, the unit cells used correspond to the primitive unit cell of the corresponding HEX or LIN pattern of the molecular assembly. In HEX patterns the primitive unit cells contain three host molecules for PE4A and PE3A, and six host molecules for PE4B. In the LIN patterns, there are two host molecules present per unit cell for all three host molecules. In all cases, the unit cell contains only one guest molecule (when present). The initial coordinates of the molecules in the gas phase are obtained using the Gaussview software package. The unit cell parameters are varied stepwise, with the constraint that they should be commensurate with the underlying lattice constant of graphene. The geometry optimization of the molecules is done following a three-step procedure: (i) the coordinates of the isolated molecules are relaxed using DFT. Next, for each set of cell parameters: (ii) a monolayer of molecules is assembled in either the HEX or LIN pattern in the gas phase (i.e., no graphene substrate) and the coordinates are further relaxed, with the constraint that they remain in the xy plane, (iii) this monolayer is then placed on graphene and the coordinates are further relaxed, with no geometric constraints. The unit cell parameters are varied to obtain the lowest energy configuration. The experimental details can be found in the main manuscript and Supporting Information of Ref. 43.

We note that further below, in the section discussing the energetics of the molecular self-assemblies using DFT, the sign convention is such that a negative sign represents an attractive interaction.

Table 3.1: Results from DFT for geometries and energetics of the HEX and LIN arrangements of the host molecules when adsorbed on graphene. In addition to results for the three host molecules (training set) PE4A, PE4B and PE3A, results are also given for three other host molecules that constitute test cases (validation set) PE3C, PE2C and PE3B, which are discussed later in this chapter. N_{host} is the number of host molecules contained in the 2D primitive unit cell, whose optimal size is given by the cell parameter(s) a (in HEX) or a,b (in LIN). We see that the optimal lattice parameters as obtained from DFT are very close to those determined from the STM experiments. The corresponding geometries are also given in Fig. 3.5 and Fig. 3.21 below. $E_{\text{ads}}^{\text{host}}$ is the adsorption energy, $E_{\text{stab}}^{\text{gas}}$ and $E_{\text{stab}}^{\text{G}}$ are the stabilization energies of host assemblies in the gas phase and on graphene, respectively.

Host molecule →		PE4A	PE4B	PE3A	PE3C	PE2C	PE3B
HEX	N_{host} (molecules/cell)	3	6	3	3	3	6
	a [DFT](nm)	4.23	5.23	3.24	3.24	2.49	4.23
	a [expt](nm)	4.2 ± 0.1	5.2 ± 0.1	3.2 ± 0.1	NA	NA	NA
	$E_{\text{ads}}^{\text{host}}$ (meV/Å^2)	−13.1	−14.2	−16.8	−14.2	−15.5	−17.51
	$E_{\text{stab}}^{\text{gas}}$ (meV/Å^2)	−4.78	−4.10	−7.28	−7.04	−8.71	−4.8
	$E_{\text{stab}}^{\text{G}}$ (meV/Å^2)	−4.69	−3.91	−7.14	−6.88	−8.55	−4.62
LIN	N_{host} (molecules/cell)	2	2	2	2	2	2
	a [DFT](nm)	1.49	1.49	1.49	1.49	1.49	1.49
	a [expt](nm)	NA	1.5 ± 0.1	1.5 ± 0.1	NA	NA	NA
	b [DFT] (nm)	6.38	5.17	3.88	3.88	2.59	3.42
	b [expt](nm)	NA	5.2 ± 0.1	3.9 ± 0.1	NA	NA	NA
	$E_{\text{ads}}^{\text{host}}$ (meV/Å^2)	−12.0	−15.2	−17.1	−11.9	−15.7	−18.96
	$E_{\text{stab}}^{\text{gas}}$ (meV/Å^2)	−4.03	−4.64	−7.38	−6.10	−8.77	−5.57
	$E_{\text{stab}}^{\text{G}}$ (meV/Å^2)	−3.93	−4.55	−7.25	−6.01	−8.62	−5.35

3.4 Results

3.4.1 Host assemblies

We first consider the arrangements formed by each of the host molecules alone, in the absence of guests. Each host can form two types of stable periodic arrangements, the HEX and the LIN, as already mentioned. As already mentioned in Section 3, the unit cell parameters of the assemblies are varied to get the lowest energy configuration. The optimized unit cell parameters of the host assemblies are reported in Table 3.1.

In order to demonstrate the utility of descriptors, we have chosen a set of host molecules that exhibits a rich diversity in the lowest-energy arrangements of its

constituents. From experiments, it is found that when deposited on graphene, PE4A assembles in the HEX pattern, PE4B in the LIN pattern, and PE3A in a random glass-like pattern. To understand why PE4A, PE4B, and PE3A assemble differently, we perform DFT calculations, both in the gas phase and on graphene, and then compare the DFT results with STM experiments.

Host assemblies in the gas phase

First, we compute and compare the stabilization energies of the host assemblies in the HEX and LIN patterns in the gas phase. The stabilization energy of the host assembly in the gas phase ($E^{\text{gas}}_{\text{stab}}$) is defined as:

$$E^{\text{gas}}_{\text{stab}} = E^{\text{ml}}_{\text{host}} - N_{\text{host}} E^{\text{iso}}_{\text{host}}, \tag{3.1}$$

where $E^{\text{ml}}_{\text{host}}$ and $E^{\text{iso}}_{\text{host}}$ are the total energies of the host monolayer and the isolated host molecule, respectively. N_{host} is the number of host molecules present per unit cell. The stabilization energy ($E^{\text{gas}}_{\text{stab}}$) is a measure of the intermolecular interactions.

The HEX pattern of PE4A is found to be energetically more stable than the corresponding LIN pattern. The stabilization energies of the HEX and LIN patterns in the gas phase are -4.78 meV/Å^2 and -4.03 meV/Å^2, respectively. The HEX pattern of PE4A consists of repeating "rotelli" units, i.e., like a wagon wheel with six spokes and a cavity in the middle.[52] The optimum length of the hexagonal cavity is found to be 1.32 nm which is in fairly good agreement with the experimental value of 1.1 nm. The LIN pattern of PE4B is found to be more stable than the flower-like HEX pattern with stabilization energies of -4.10 meV/Å^2 and -4.64 meV/Å^2 in the HEX and LIN patterns respectively. The HEX and LIN patterns of PE3A are found to be almost energetically degenerate with stabilization energies of -7.28 meV/Å^2 and -7.38 meV/Å^2, respectively. This is similar to what was found by previous authors for a structurally similar molecule, which we label as PE2C (see Fig. 3.20),[19] and will also be discussed further below. Atomistic structures of the host assemblies in

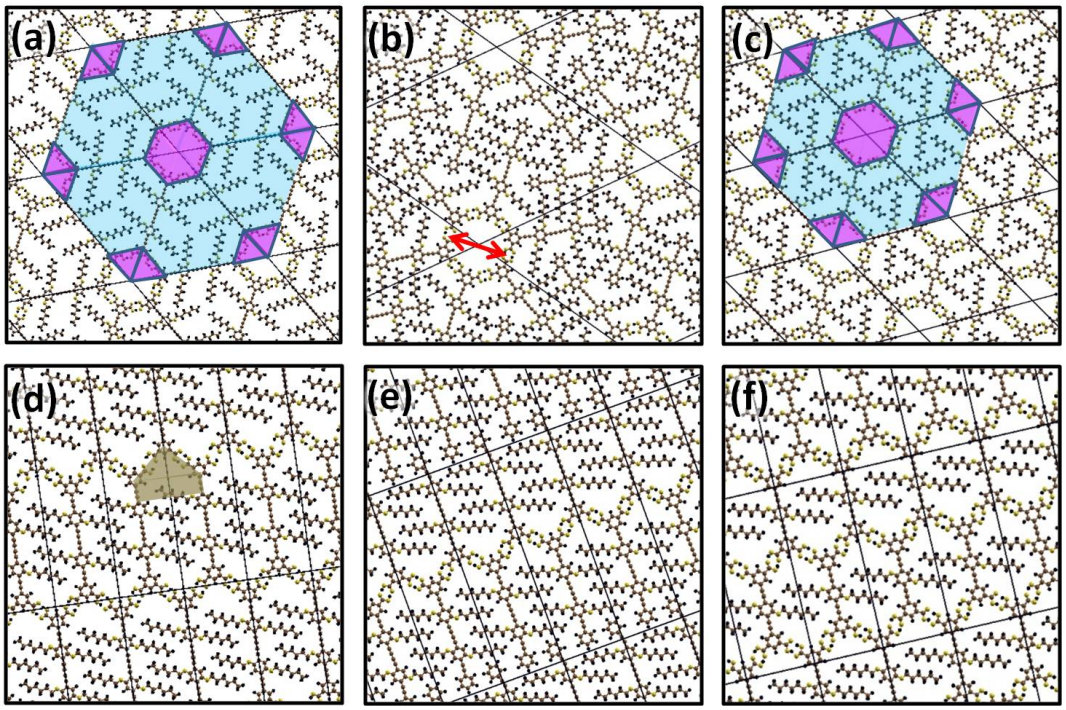

Figure 3.5: Atomistic structures of the lowest energy patterns of the host assemblies in HEX and LIN patterns in the gas phase, obtained from DFT. (a) PE4A, (b) PE4B and (c) PE3A in HEX pattern. LIN pattern of (d) PE4A, (e) PE4B and (f) PE3A. The regions colored in magenta and gray indicate the hexagonal and pentagonal cavities, respectively. In the HEX patterns of PE4A and PE3A, the hexagonal cavities are surrounded by six triangular cavities, shown by the cyan regions. Color scheme for atomic spheres: C, brown; H, black and O, yellow. The red arrow in (b) shows the length of HEX cavity. The black lines are boundaries of primitive unit cells.

both HEX and LIN patterns in the gas phase are shown in Fig. 3.5. The values of $E_{\rm stab}^{\rm gas}$ for the lowest energy configuration in both the HEX and LIN patterns of each host molecule are reported in Table 3.1.

We have calculated the strength of various interactions arising in the host assemblies and find that there is a large range of interaction strengths. To extract the strength of various interactions we consider two host molecules, which form an isolated dimer either via forming hydrogen bonding between COOH groups, or aromatic CH—π interaction between the aromatic head groups or alkyl CH—acetylene π interaction along the length of the molecular backbone. The distance between the two molecules in the dimer is kept the same as obtained after geometry optimization of the

host-assembly so as to evaluate the strength of the relevant interaction. This enables us to extract the contribution of a particular interaction to the net stabilization energy of the assembly.

To calculate the strength of hydrogen bonds formed between the neighboring COOH groups we consider two host molecules which are bonded in either *trans*- or *cis*- orientations (see Fig. 3.3) in the gas phase by keeping the bond distance the same as obtained after the geometry optimization of the host assembly. The hydrogen bond strength between COOH groups for the isolated dimer is given by:

$$E_{\mathrm{BE}}^{\mathrm{COOH}} = \frac{E_{\mathrm{dimer}}^{\mathrm{COOH}} - 2E_{\mathrm{host}}^{\mathrm{iso}}}{n_{\mathrm{COOH}}}, \tag{3.2}$$

where $E_{\mathrm{dimer}}^{\mathrm{COOH}}$ is the total energy of the carboxylic acid (COOH) dimer. n_{COOH} is the number of hydrogen bonds formed between the COOH groups of the isolated dimer, and this number is equal to two. The strength of the hydrogen bond between the COOH groups is found to be: PE4A (HEX): -0.628 meV/bond, PE4A (LIN): -499 meV/bond, PE4B (HEX): -564 meV/bond, PE4B (LIN): -698 meV/bond, PE3A (HEX): -624 meV/bond, PE3A (LIN): -578 meV/bond. These magnitudes of H bond-strengths between COOH groups are at the upper limit of the range of values found by previous authors for the same type of bond in various compounds.[34, 62] For example, the interaction between COOH groups in the HEX and LIN patterns of PE4A and PE4B molecules, are shown in Figs. 3.6 and 3.7, respectively by the red circles.

Apart from the strong hydrogen bonding between COOH groups, there are other non-covalent interactions, e.g., aromatic CH—π and alkyl CH—acetylene π interactions between the neighboring host molecules. We calculate the strength of these interactions using:

$$E_{\mathrm{BE}}^{\mathrm{CH}-\pi} = \frac{E_{\mathrm{dimer}}^{\mathrm{CH}-\pi} - 2E_{\mathrm{host}}^{\mathrm{iso}}}{n_{\mathrm{CH}-\pi}}, \tag{3.3}$$

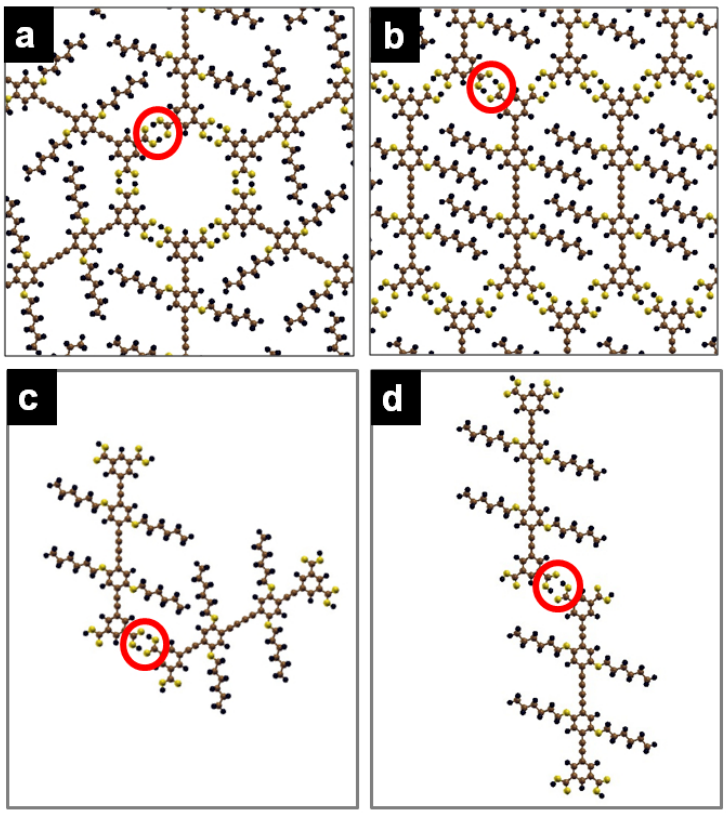

Figure 3.6: Atomistic structures of the (a) HEX and (b) LIN patterns of PE4A in the gas phase. The interaction between COOH groups via hydrogen bond formation is shown by red circles. Dimers of PE4A in the (c) HEX and (d) LIN patterns, corresponding to the *cis*- and *trans*- orientations respectively, of the aromatic core. These dimers are used to evaluate the strength of the corresponding interactions. Color scheme for atomic spheres: C, brown; H, black and O, yellow.

where $E_{\text{dimer}}^{\text{CH}-\pi}$ is the total energy of the host dimer taking part in CH-π (aromatic CH—π or alkyl CH—acetylene π) interactions. $n_{\text{CH}-\pi}$ is the number of CH—π interactions between two host molecules in the isolated dimer, $n_{\text{CH}-\pi} = 4$ for both aromatic CH—π and alkyl CH—acetylene π interactions between the isolated dimers.

Aromatic CH—π interactions are present in the LIN pattern of PE4B between the phenyl head groups of neighbouring molecules [see the blue ellipse in Fig. 3.7(b)]. The alkyl CH—acetylene π interactions occur in the HEX pattern of PE4B along the length of the molecular backbone [see the green ellipse in Fig. 3.7(a)]. The strength of aromatic CH—π and alkyl CH—acetylene π interactions is found to be -98 meV and -173 meV, respectively.

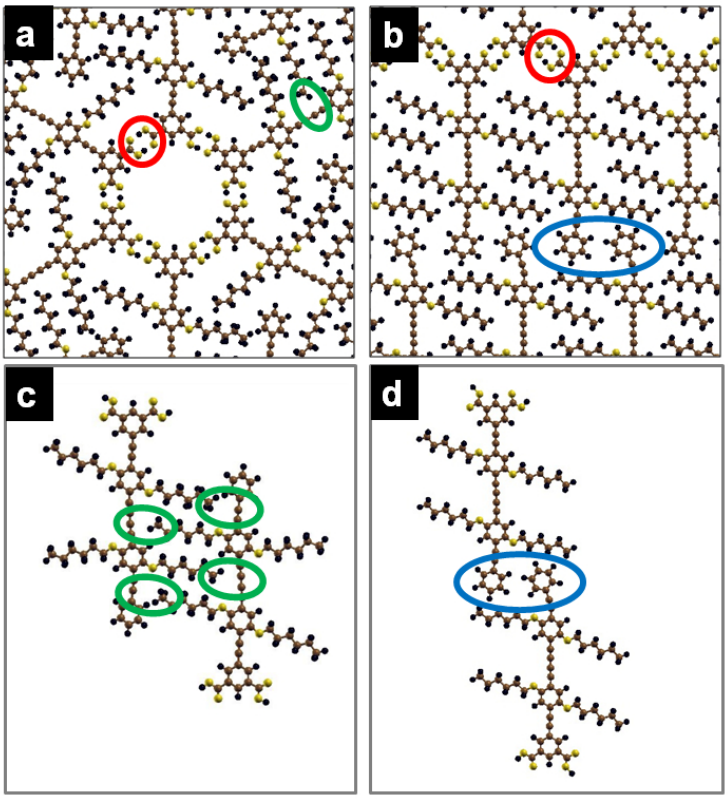

Figure 3.7: (a) HEX and (b) LIN patterns of PE4B in the gas phase. (c) Aromatic CH—π and (d) alkyl CH—acetylene π interactions between the dimers of PE4B. These isolated dimers are considered to extract the strength of the corresponding interactions. Red circles show interaction between COOH groups. The green ellipse in HEX and blue ellipse in LIN show alkyl CH—acetylene π and aromatic CH—π interactions, respectively. Color scheme for atomic spheres: C, brown; H, black and O, yellow.

Finally, the interactions between alkoxy side chains of neighboring host molecules depend on their orientation, relative separation, and alignment.[63] We extract this interaction strength E_{s} using:

$$\frac{E_{\mathrm{stab}}^{\mathrm{gas}}}{A} = \frac{n_{\mathrm{COOH}}E_{\mathrm{COOH}} + n_{\mathrm{others}}E_{\mathrm{others}} + n_{\mathrm{s}}E_{\mathrm{s}}}{A}, \tag{3.4}$$

where $\frac{E_{\mathrm{stab}}^{\mathrm{gas}}}{A}$ is the stabilization energy of the host assembly per unit cell area in the gas phase. n_{COOH}, n_{others} and n_{s} are the number of hydrogen bonds between COOH groups, other interactions (e.g., aromatic CH—π or alkyl CH—acetylene π), and steric interactions, respectively present per unit cell of the assembly. The first two

terms in the right-hand side of Eq. (3.4) are already determined from Eqs. (3.2) and (3.3). After solving Eq. (3.4) for each host assembly, we find that the strength of this steric interaction varies in a range from −18 to +63 meV depending on the relative alignment of the alkoxy chains in the unit cell of the host assemblies. Though these interactions are comparatively weak, these steric interactions between alkoxy side chains are important because they determine the lengths of hydrogen bonds between COOH head groups, which in turn determine the main energetic contributions to the stabilization of the assembly.

To summarize, we find that hydrogen bonds between the COOH groups at the termini of the central backbones are the strongest among all the interactions, and are primarily responsible for stabilizing the host assemblies.

Host assemblies on graphene

After studying the host assemblies in the gas phase, we want to see the effect of the graphene substrate on the molecular architectures of different host molecules. First, we study the energetics of the assemblies formed by different host molecules, and then compare the DFT results with experimental STM observations. We have simulated STM images of the lowest energy configuration of the assemblies formed by the host molecules. The rigid, planar, and highly conducting nature of the phenyleneethynelene molecules makes them ideal for experimental STM studies.[47, 64–67]

The adsorption energy of each host assembly on graphene, per unit cell, is given by:

$$E_{\text{ads}}^{\text{host}} = E_{\text{host/G}} - N_{\text{host}} E_{\text{host}}^{\text{iso}} - E_{\text{G}}, \tag{3.5}$$

where $E_{\text{host/G}}$, $E_{\text{host}}^{\text{iso}}$ and E_{G} are the total energies of the host assembly adsorbed on graphene, the isolated host molecule in the gas phase, and the monolayer of graphene, respectively. N_{host} is the number of host molecules present per unit cell. For PE4A and PE4B, our theoretical results indicate a clear preference for one of

the two patterns considered. For the optimized unit cell parameters (see Table 3.1) in the case of PE4A, $E_{\text{ads}}^{\text{host}}$ is -13.1 meV/Å^2 and -12.0 meV/Å^2 in the HEX and LIN patterns, respectively, indicating that the former is favored. In contrast, for PE4B, $E_{\text{ads}}^{\text{host}}$: -14.2 meV/Å^2 and -15.2 meV/Å^2 for HEX and LIN, respectively, and therefore the latter is favored. Both of these energetic preferences are in agreement with the structure observed in STM experiments, shown in Fig. 3.8 (a) and (d). However, for PE3A, we find our calculations yield almost degenerate values for $E_{\text{ads}}^{\text{host}}$ for HEX and LIN: -16.8 meV/Å^2 and -17.1 meV/Å^2, respectively. Previous authors have pointed out that, given the feasibility of moving smoothly from the HEX to the LIN without introducing defects, for molecules where the HEX and LIN become almost equal in energy, the system can become arrested in a glass-like structure. As a result, one observes a seemingly random arrangement of molecules on the substrate.[19, 38] This is indeed what we observe in the STM images for PE3A, see Fig. 3.8(g), though the LIN is found locally in some regions, shown by dashed turquoise lines in Fig. 3.8(g). Such glassy phases are long-lived metastable states; it should be possible to observe their transition to the crystalline ground state by annealing the system, either experimentally or in simulations.[32, 38, 68]

$E_{\text{ads}}^{\text{host}}$ serves as a combined measure of both the interactions between the host molecules and the interactions between the host and graphene substrate. In contrast, we can (as for the gas phase) define a stabilization energy E_{stab} that serves as a measure of only intermolecular interactions. The stabilization energy of a host assembly on graphene is given by:

$$E_{\text{stab}}^{\text{G}} = E_{\text{host/G}} - N_{\text{host}} E_{\text{host/G}}^{\text{single}} + (N_{\text{host}} - 1) E_{\text{G}}, \tag{3.6}$$

where $E_{\text{host/G}}^{\text{single}}$ is the total energy of a single host molecule on graphene.

We obtain values of $E_{\text{stab}}^{\text{G}}$ for PE4A in the HEX and LIN patterns on graphene that are -4.69 meV/Å^2 and -3.93 meV/Å^2, respectively. The HEX and LIN patterns of PE4B have $E_{\text{stab}}^{\text{G}}$ values of -3.91 meV/Å^2 and -4.55 meV/Å^2, respectively. The

values of $E^{\mathrm{G}}_{\mathrm{stab}}$ for the HEX and LIN patterns of PE3A are -7.10 meV/Å^2 and -7.25 meV/Å^2, respectively. Therefore, from the values of $E^{\mathrm{G}}_{\mathrm{stab}}$ for the host assemblies we find that the HEX pattern of PE4A is more stable than its LIN pattern, whereas for PE4B the lowest energy configuration is LIN, and PE3A is likely to form a random glass-like pattern, since both the HEX and LIN patterns are almost equally favorable. If we compare the values of $E^{\mathrm{gas}}_{\mathrm{stab}}$ and $E^{\mathrm{G}}_{\mathrm{stab}}$, then we see that the lowest energy pattern of the host assemblies remains the same for any host molecular building block in the absence or presence of graphene. Also, the values of E_{stab} do not change appreciably when the molecules are deposited on graphene. Hence, we can say that graphene has a negligible effect on the ground state geometries of the host molecules, as well as the energetics of self-assembly, as has been reported also by previous authors who have studied the self-assembly of similar molecules on graphene.[31–33] Comparing our DFT predictions for the favored pattern with results from the STM experiments, we find that the theoretical results are in excellent agreement with the experimental observations for all three host assemblies (see Fig. 3.8).

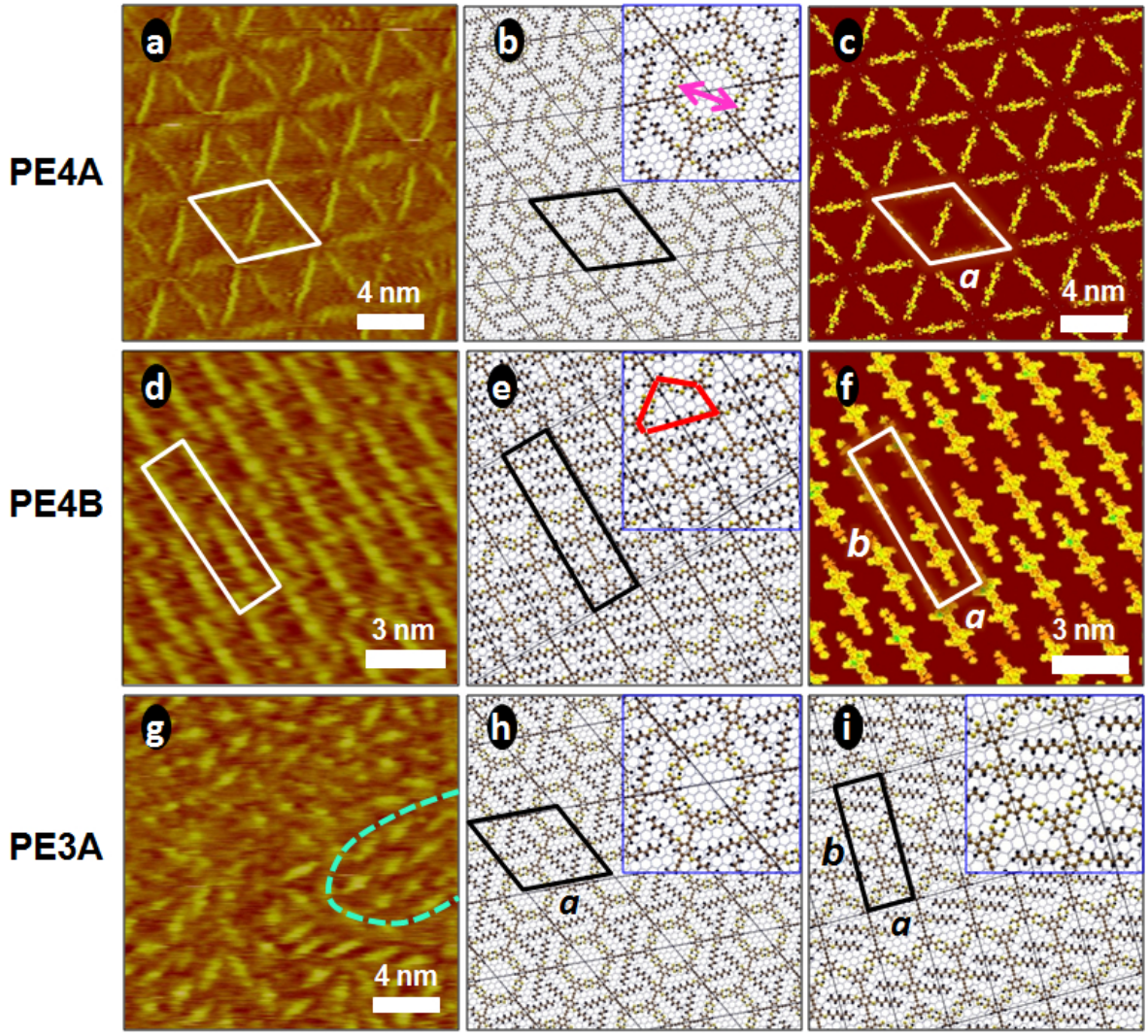

Figure 3.8: STM images and atomistic structures of host assemblies on graphene. Experimental STM images of (a) PE4A in HEX, (d) PE4B in LIN and (g) PE3A in the random arrangement. The turquoise dashed line in (g) encloses a domain where, locally, the LIN pattern is observed. Atomistic structures of (b) PE4A in HEX, (e) PE4B in LIN, (h) PE3A in HEX, and (i) PE3A in LIN. Atomic colors: C of host, brown; H, black; O, yellow; C of graphene, gray. The insets are zoomed in view of the corresponding atomistic structures. The magenta arrow in (b) indicates the size of the hexagonal cavity in HEX (1.3 nm), while the red pentagon in (e) indicates the perimeter of the pentagonal cavity in LIN. Simulated STM images of (c) PE4A in HEX (V_{bias} =−2720 mV) and (f) PE4B in LIN (V_{bias}=−1720 mV). Reprinted with permission from Ref. 43 ©(2017) American Chemical Society.

3.4.2 Guest molecules on graphene

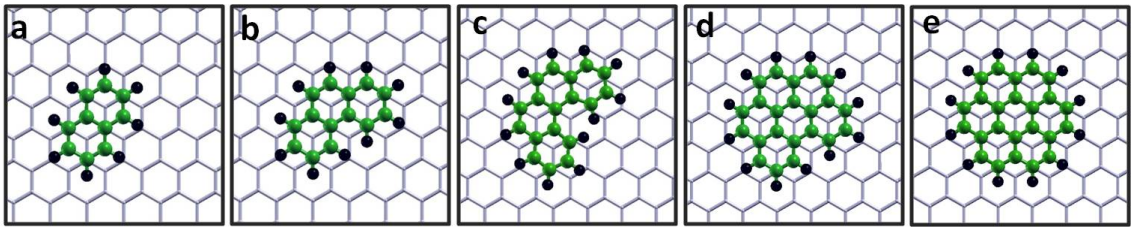

Figure 3.9: Adsorption of different guest molecules on graphene: (a) naphthalene, (b) phenanthrene, (c) benzo-c-phenanthrene (BCPH), (d) Benzo-ghi-perylene (BGPL) and (e) coronene on graphene. Color scheme for atoms: green, C of guests; black, H of guests and gray, C of graphene.

We study the adsorption of the guest molecules naphthalene, phenanthrene, benzo-c-phenanthrene (BCPH), benzo-ghi-perylene (BGPL), and coronene on graphene. The lowest energy structures of the guest molecules adsorbed on graphene are shown in Fig. 3.9.

We compute the adsorption energy ($E_{\text{ads}}^{\text{guest}}$) of the guest molecules on graphene, which is given by:

$$E_{\text{ads}}^{\text{guest}} = E_{\text{guest/G}} - E_{\text{guest}} - E_{\text{G}}, \tag{3.7}$$

where the three terms on the right-hand-side of the equation are the total energies of the guest molecule on graphene, the guest molecule in the gas phase, and the bare graphene substrate, respectively. In this way, we obtain values of $E_{\text{ads}}^{\text{guest}}$ to be -1.43 eV, -1.32 eV, -1.11 eV, -0.89 eV and -0.67 eV for coronene, BGPL, BCPH, phenanthrene and naphthalene, respectively. These results are in good agreement with previous DFT and experimental results, wherever available.[69, 70] In Fig. 3.10 we plot $E_{\text{ads}}^{\text{guest}}$ as a function of the number of carbon atoms in the molecule, and we obtain a linear relationship. This is because the interaction between graphene and these five molecules is dominated by London dispersion interactions, and the interaction between C molecules in the adsorbate and graphene is much stronger than the interaction between a C molecule in graphene and a H molecule in the adsorbate.

As an example, charge redistribution plots between coronene and graphene are

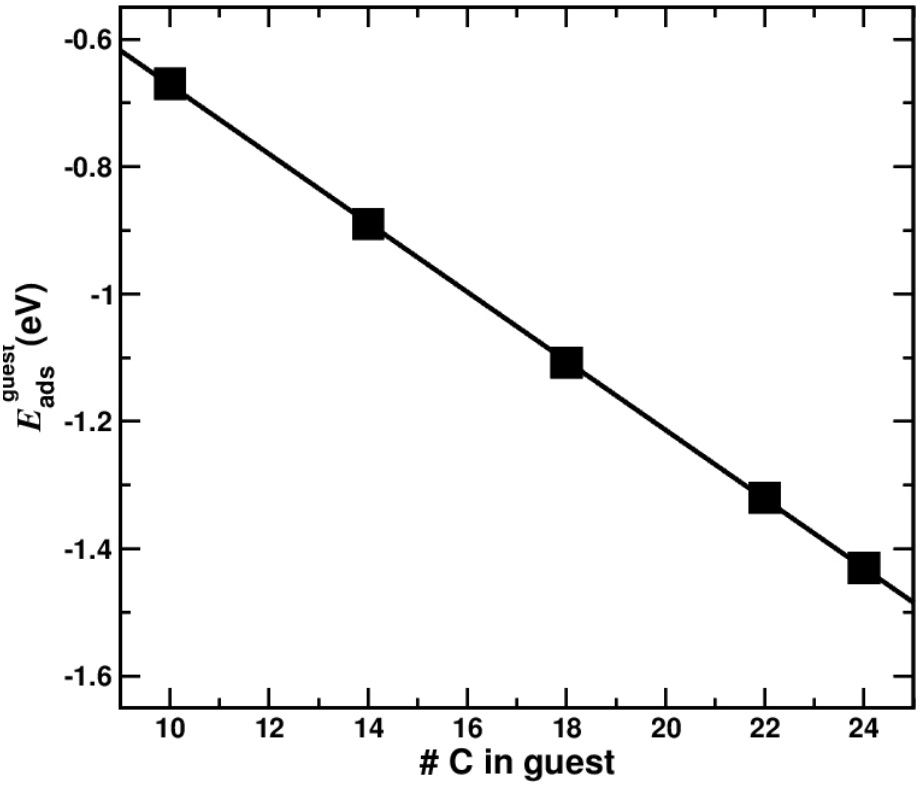

Figure 3.10: Adsorption energy of the guest molecules on graphene as a function of the number of carbon (C) atoms present in the guest molecule. This plot shows a linear relationship between $E_{\text{ads}}^{\text{guest}}$ and number of C atoms present in the guest molecules.

shown in Fig. 3.11, where the red and blue lobes indicate electron accumulation and depletion respectively. The plots show the charge density difference ($\Delta\rho$) between coronene and graphene, which is computed using:

$$\Delta\rho = \rho_{\text{coro/G}} - \rho_{\text{coro}} - \rho_{\text{G}}, \tag{3.8}$$

where $\rho_{\text{coro/G}}$, ρ_{coro} and ρ_{G} are the charge densities of coronene adsorbed on graphene, a coronene molecule in the gas phase (frozen in the adsorbed geometry) and the graphene monolayer, respectively. In the side view in Fig. 3.11(b) we see alternating layers of electron accumulation and depletion between coronene and graphene.

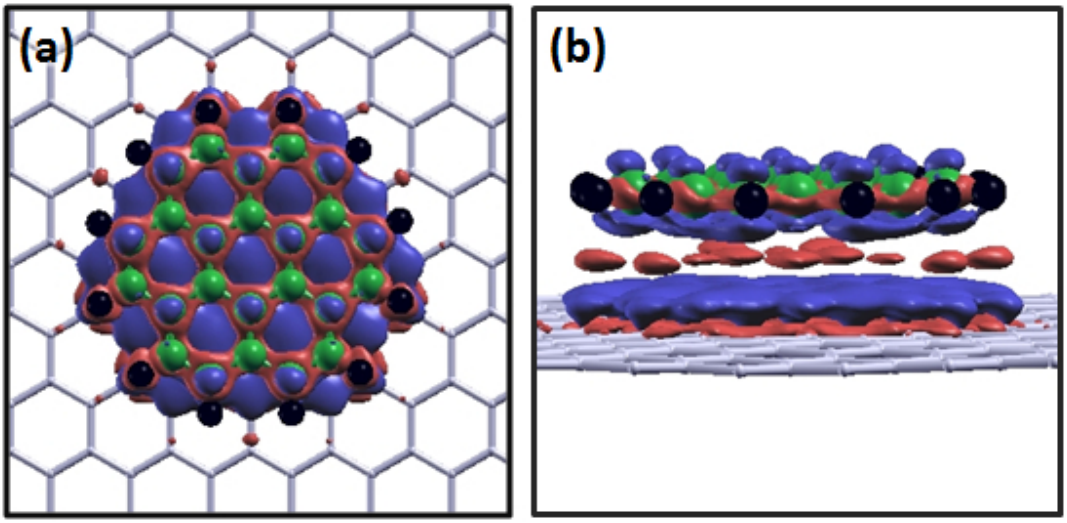

Figure 3.11: Charge redistribution plot of coronene on graphene. (a) Side view and (b) top view, drawn at iso surface value 0.0003 e/bohr^3. Red lobes: electron accumulation and blue lobes: electron depletion. Color scheme for atoms: green, C of guests; black, H of guests and gray, C of graphene.

3.4.3 Host-Guest Interactions and Structural Reorganization

We now examine if and how the host assemblies change in the presence of guest molecules. The size of the guest, the nature of the host, and the energy lowering due to host-guest interactions play a significant role in determining the features of the host-guest complex. Among the guests considered by us, naphthalene and phenanthrene can fit inside both the smaller pentagonal cavities in the LIN pattern and the larger hexagonal cavities in the HEX; however, only the latter can accommodate BCPH, BGPL, and coronene, due to their larger size. We have computed the energetics and charge transfer of the host-guest complexes in the gas phase as well as on graphene, and we find that host-guest interactions are almost identical in the two situations. Therefore, here we present the results for host-guest complexes on graphene only.

We first present results for the case where the host is PE4A. Recall that PE4A assembles in the HEX pattern in the absence of any guest. The cavities formed in the HEX pattern can accommodate all five guest molecules considered in this study. The STM images of PE4A in the absence [recall Figs. 3.8 (a)–(c)] and presence of the guest look very similar [see Fig. 3.12 (a)–(c)], except that the guest molecule

is imaged as a bright blob at the intersection of the six spokes. As an example, Figs. 3.12 (a) and (c) show experimental and simulated STM images, respectively, for PE4A + coronene; we see that they are in excellent agreement in all respects. PE4A remains in the HEX pattern in presence of all the guests considered in this study. STM images and atomistic structures of PE4A with other guests are shown Fig. 3.13. In order to investigate the host-guest interactions, we need to compute $\Delta\rho_{\rm hg}$, the charge redistribution in the presence of the guest, and $\Delta E_{\rm hg}$, the host-guest interaction energy. These are given by:

$$\Delta\rho_{\rm hg} = \rho_{\rm host-guest/G} - \rho_{\rm host/G} - \rho^{\rm iso}_{\rm guest/G} + \rho_{\rm G}, \tag{3.9}$$

$$\Delta E_{\rm hg} = E_{\rm host-guest/G} - E_{\rm host/G} - E^{\rm iso}_{\rm guest/G} + E_{\rm G}, \tag{3.10}$$

where $\rho_{\rm host-guest/G}$, $\rho_{\rm host/G}$, $\rho^{\rm iso}_{\rm guest/G}$, and $\rho_{\rm G}$ are the electronic charge densities, obtained from DFT, of the host-guest complex on graphene, the host complex on graphene, an isolated guest molecule on graphene, and a monolayer of graphene, respectively. $E_{\rm host-guest/G}$ and $E^{\rm iso}_{\rm Guest/G}$ are the total energies per unit cell of the host-guest system on graphene and an isolated guest molecule adsorbed on graphene, respectively; all other terms have been defined already. Note that $\Delta\rho_{\rm hg}$ contains information about charge redistribution as a result of host-guest interactions only, since terms resulting from host-graphene and guest-graphene interactions have been subtracted out; similarly, $\Delta E_{\rm hg}$ contains only the interaction between host and guest molecules. As examples, we show our results for $\Delta\rho_{\rm hg}$, see Fig.3.14 (a)-(f) and $\Delta E_{\rm hg}$ (see Fig. 3.15) when PE4A is in the HEX pattern and all the guest molecules are placed inside its hexagonal cavity.

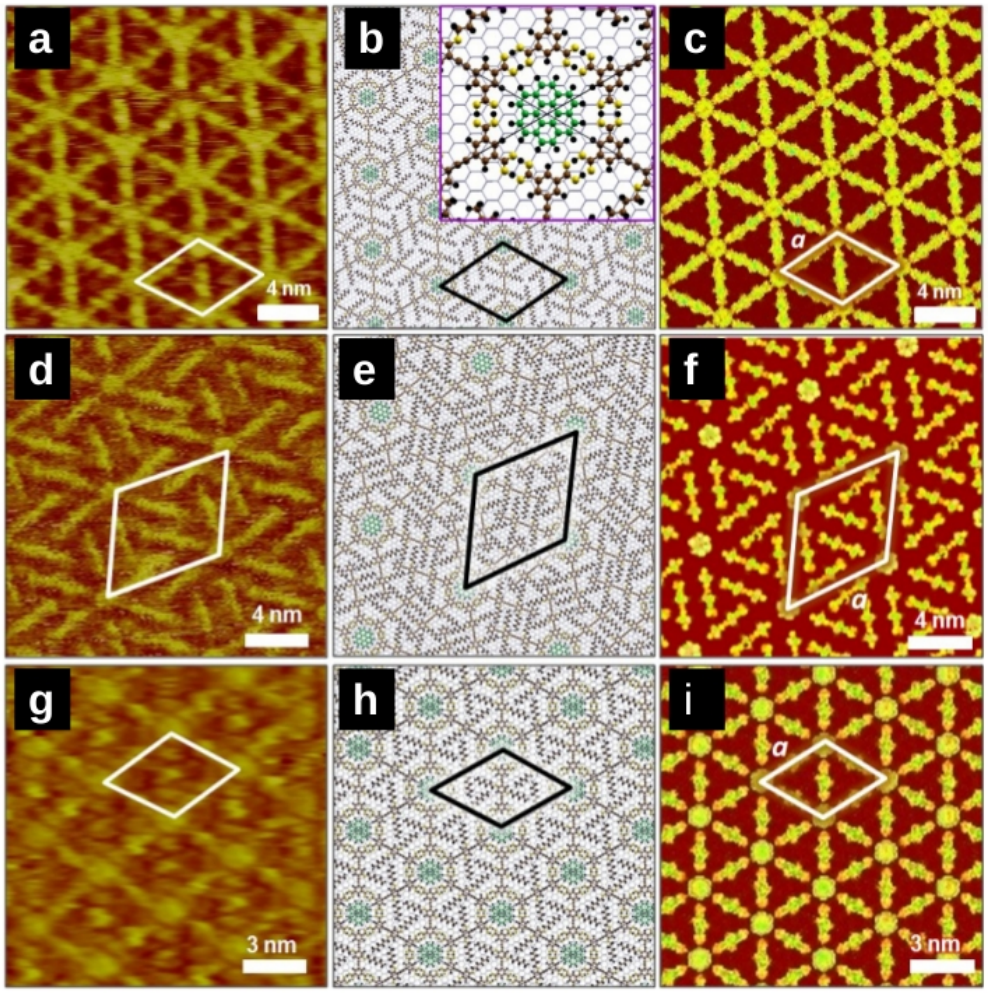

Figure 3.12: Formation of host-guest complexes on HOPG/graphene when the guest is coronene. (a) Experimental STM images of (a) PE4A + cornene (scan size: 40×40 nm^2; $V_{\text{bias}} = -600$ mV; $I_{\text{t}} = 120$ pA), (d) PE4B + coronene (scan size: 20×20 nm^2; $V_{\text{bias}} = -1500$ mV; $I_{\text{t}} = 150$ pA) and (g) PE3A + coronene (scan size: 15×15 nm^2; $V_{\text{bias}} = -257$ mV; $I_{\text{t}} = 553$ pA). Atomistic structures of HEX patterns of (b) PE4A (inset is zoomed in view), (e) PE4B and (h) PE3A respectively, all with coronene as guest. Color scheme for atoms: brown, C of PE4A; yellow, O; black, H; green, C of guest and gray, C of graphene. Simulated STM images of (c) PE4A + coroene, (f) PE4B + coronene and (i) PE3A + coronene, all at $V_{\text{bias}} = -2720$ mV. The thin black lines indicate unit cell boundaries, and the rhombi marked by thick black/white lines indicate a single unit cell; a is the lattice constant of the host-guest assembly. Reprinted with permission from Ref. 43 ©(2017) American Chemical Society.

We calculate the host-guest interaction energy, ΔE_{hg}, for each host-guest assembly. For example, in Fig. 3.15, we plot ΔE_{hg} as a function of the number of C-H—O bonds for PE4A in the HEX pattern, for different guest molecules. We see that ΔE_{hg} varies perfectly linearly with the number of host-guest hydrogen bonds. From

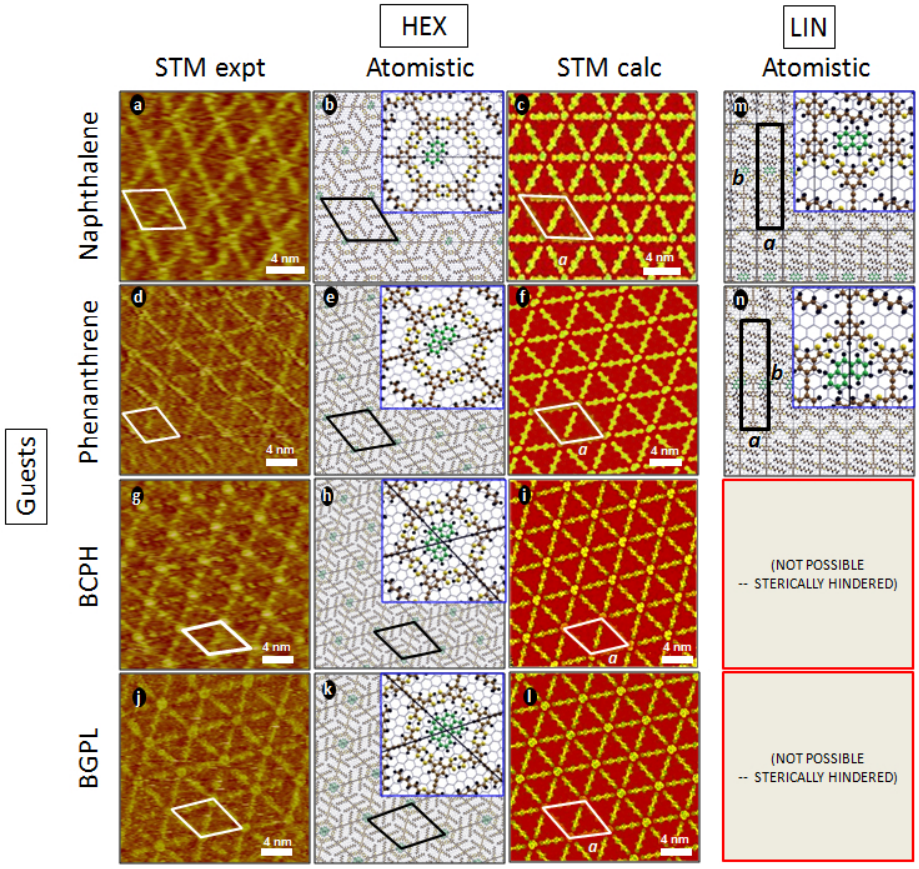

Figure 3.13: STM images and atomistic structures of PE4A with different guest molecules on graphene in HEX (a)-(l) and LIN (m)-(n) pattern. Experimental STM images of PE4A with (a) naphthalene, (d) phenanthrene, (g) BCPH, and (j) BGPL in the HEX pattern. The corresponding atomistic structures of PE4A with (b) naphthalene, (e) phenanthrene, (h) BCPH and (k) BGPL as guest in HEX pattern. Simulated STM images of PE4A with (c) naphthalene, (f) phenanthrene, (i) BCPH, and (l) BGPL. Atomistic structures of PE4A with (m) naphthalene and (n) phenanthrene in LIN pattern. Atomic colors: C of host: brown, H: black, O: yellow, C of graphene: gray, C of guest: green.

the slope of this graph, the energy per C-H—O bond is obtained to be −82 meV (−1.89 kcal/mol). The theoretically obtained H—O bond distance is found to be 2.37 Å for all the host-guest complexes in the HEX arrangements of PE4A. The values obtained by us for the bond lengths and interaction energies are in good agreement with the values for CH—O bonds reported in the literature.[71–73] Note that though the energy per C-H—O bond is low, their collective effect plays an important role in stabilizing the host-guest assemblies.

The periphery of each guest molecule considered in this study is composed of

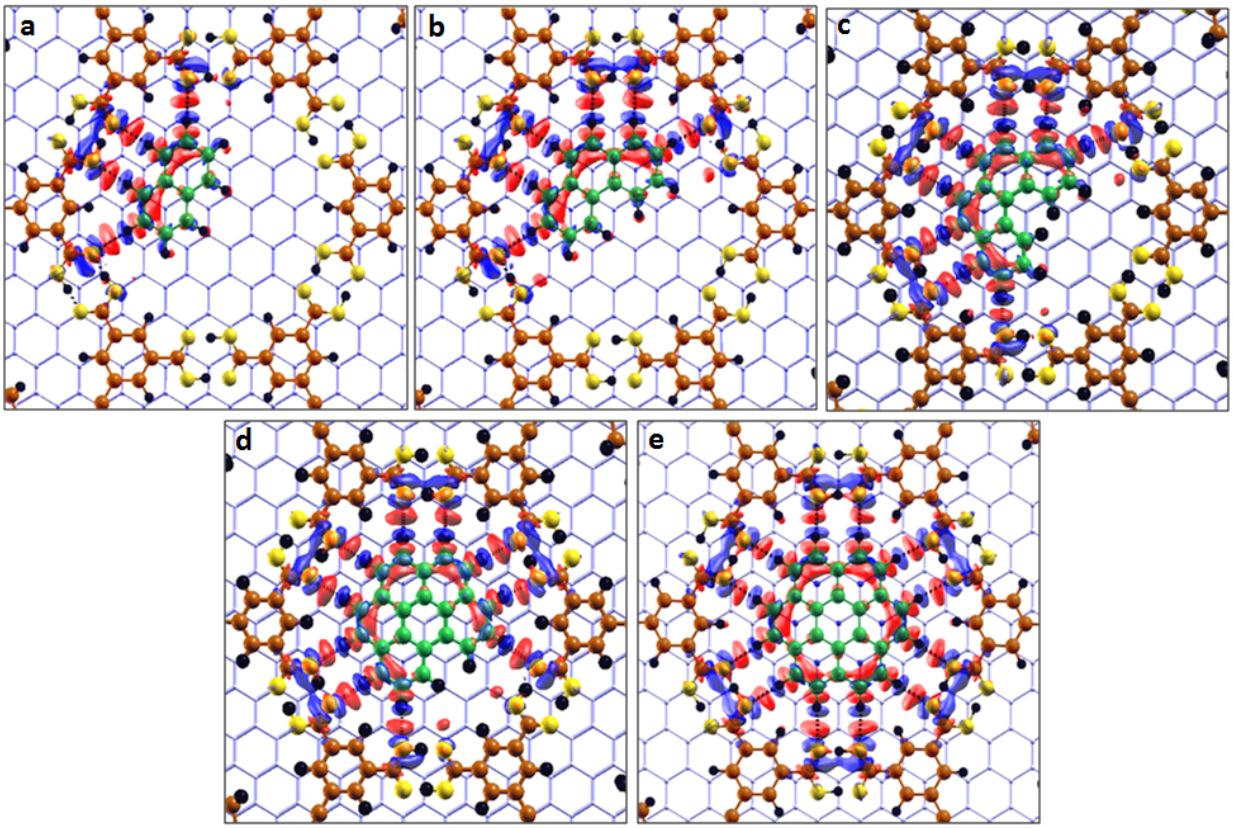

Figure 3.14: Theoretically computed charge redistribution plots between PE4A and (a) naphthalene, (b) phenanthrene, (c) benzo-c-phenanthrene (BCPH), (d) benzo-ghi-perylene (BGPL) and (e) coronene, on graphene. Red and blue lobes indicate electron accumulation and depletion, respectively, plotted at an isosurface value of 0.0002 e/bohr^3. Note the clear signatures of 4, 6, 8, 10 and 12 host-guest hydrogen bonds in (a), (b), (c), (d) and (e), respectively. Color scheme for atoms: brown, C of PE4A; yellow, O; black, H; green, C of guest and gray, C of graphene. Reprinted with permission from Ref. 43 ©(2017) American Chemical Society.

C-H groups. The number of these C-H groups situated along the periphery of the guests depends on the size of the guest molecules, e.g., the number of C-H groups varies from 4 to 12 from the smallest guest naphthalene to the largest guest coronene. When a guest molecule is placed inside the cavity formed by the host molecules, then the peripheral C-H groups are available to form hydrogen bonds with the O atoms of the terminal COOH groups of the hosts. The host-guest assemblies become stabilized by the formation of these C-H—O bonds between the host and guest molecules. For example, in the HEX assemblies of PE4A, the guest molecules are placed inside the hexagonal cavity, and their peripheral C-H groups form hydrogen bonds with the

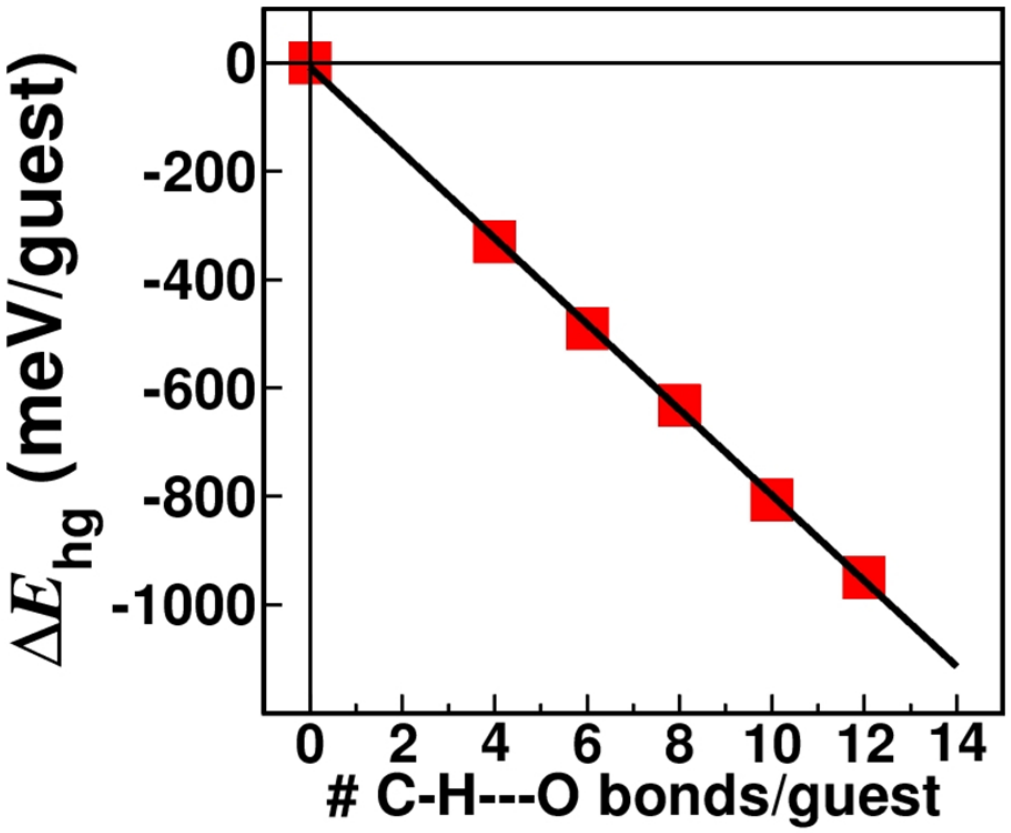

Figure 3.15: Host-guest interaction energy. Linear dependence of theoretically determined host-guest interaction energy ($\Delta E_{\rm hg}$) on the number of CH−O hydrogen bonds formed between PE4A in the HEX pattern and the guest molecules; these bonds are clearly visible in Fig. 3.14. Reprinted with permission from Ref. 43 ©(2017) American Chemical Society.

O atoms in the inner rim of the cavity. The isosurfaces of the charge redistribution $\Delta\rho_{\rm hg}$ between the host PE4A and the five guests, are shown in Figs. 3.14 (a)–(e). The red and blue lobes indicate electron accumulation and depletion, respectively. The plot of $\Delta\rho_{\rm hg}$ for each host-guest complex features lines of alternating red and blue lobes. Each line indicates the formation of a hydrogen bond between a C-H group on the periphery of the guest and an O atom on the inner rim of the HEX cavity of PE4A. In Fig. 3.14 we see very clearly that the number of host-guest hydrogen bonds is 4, 6, 8, 10 and 12 when the guest is naphthalene, phenanthrene, BCPH, BGPL, and coronene, respectively.

Next, we consider the case where the host is PE4B, whose LIN cavities are large enough to accommodate naphthalene and phenanthrene with some distortion of the

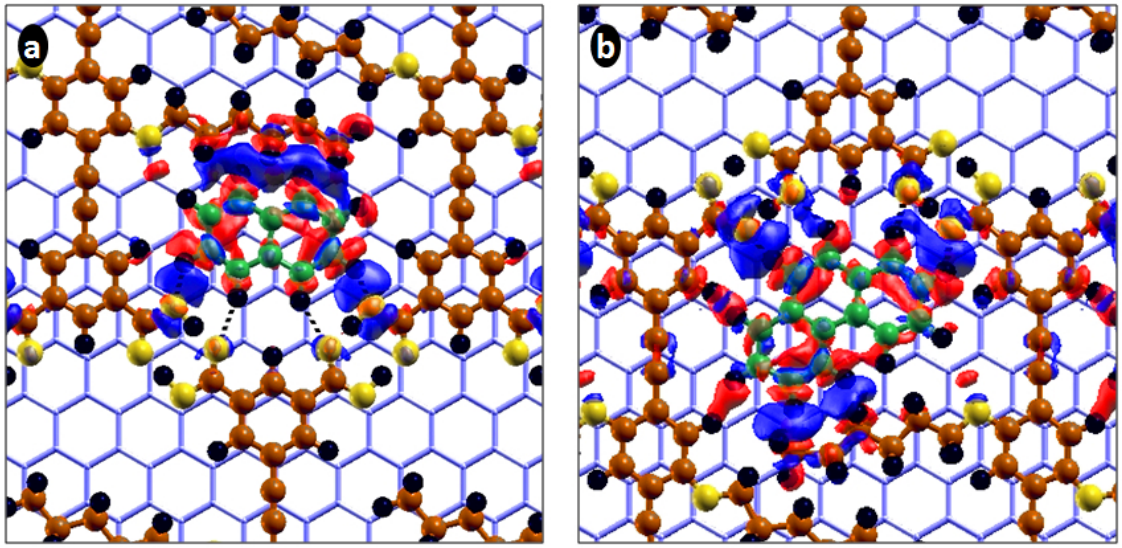

Figure 3.16: Theoretically computed charge redistribution plots between PE4B in the LIN pattern with different guest molecules. PE4B (a) naphthalene and (b) phenanthrene on graphene. Red and blue lobes indicate electron accumulation and depletion respectively, plotted at an isosurface value of 0.0002 e/bohr^3. Note the clear signatures of eight and ten host-guest hydrogen bonds in (a) and (b), respectively. Atomic colors: brown: C of PE4B; yellow: O, black: H; green: C of guest; gray: C of graphene.

alkoxy side chains [see Figs. 3.17(g) and (h)] but not the remaining guest molecules. The experimental STM images show that the LIN pattern is maintained in the presence of naphthalene and phenanthrene. Interestingly, however, we find that when the guest is BCPH, BGPL, or coronene, there is a structural transition. The arrangement of PE4B shifts from the LIN to a HEX pattern consisting of interlocked asterisks, with hexagonal cavities large enough to accommodate these guest molecules; see, e.g., Figs. 3.12(d)-(f) when the guest is coronene and Figs. 3.17(c)-(f) for BCPH and BGPL, respectively. In the STM images, each coronene molecule is imaged as a bright disk, as shown in Fig. 3.12(d)-(f). Charge redistribution plots of PE4B in the LIN pattern with naphthalene and phenanthrene as guest molecules are shown in Figs. 3.16 (a) and (b), respectively.

Finally, we consider the case where PE3A is the host. It is noteworthy that here too the introduction of certain guest molecules (in fact, all those considered here except for naphthalene) has a significant impact on the random glass-like organization

it displays in the absence of any guest, inducing a disorder-to-order transition, see Figs. 3.12(g)-(i) and Fig. 3.18 (b)-(j). The presence of phenanthrene, BCPH, BGPL or coronene as the guest causes a structural transition for the PE3A monolayer on graphene from a disordered structure to the ordered HEX pattern. Energy lowering due to the formation of 6 to 12 CH—O host-guest hydrogen bonds per guest molecule drives the reorganization.

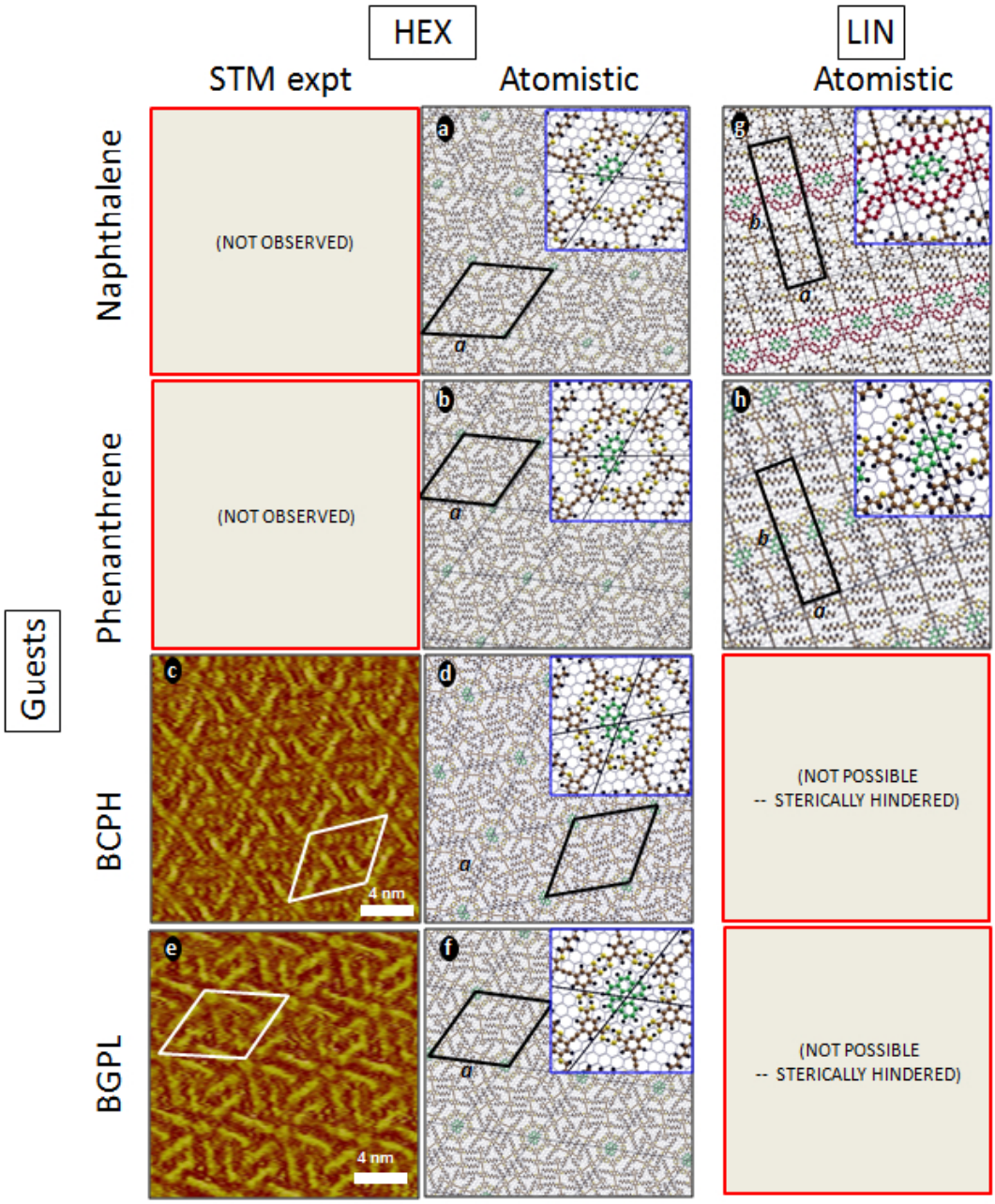

Figure 3.17: Atomistic structures from DFT and experimental STM images of PE4B with various guests in (a)–(f) HEX and (g)–(h) LIN patterns. Atomistic structures of PE4B with (a) naphthalene, (b) phenanthrene, (d) BCPH and (f) BGPL (PE4B in HEX); (g) naphthalene and (h) phenanthrene (PE4B in LIN). Experimental STM images of PE4B with (c) BCPH (scan size: 20 × 20 nm^2; V_{bias}=−1018 mV; I_{t}=120 pA) and (e) BGPL (scan size: 20 × 20 nm^2; V_{bias}=−1500 mV; =150 pA). The black/white lines indicate the unit cell; with a and b are the unit cell parameter. Atomic colors: C of host: brown, H: black, O: yellow, C of graphene: gray, C of guest: green.

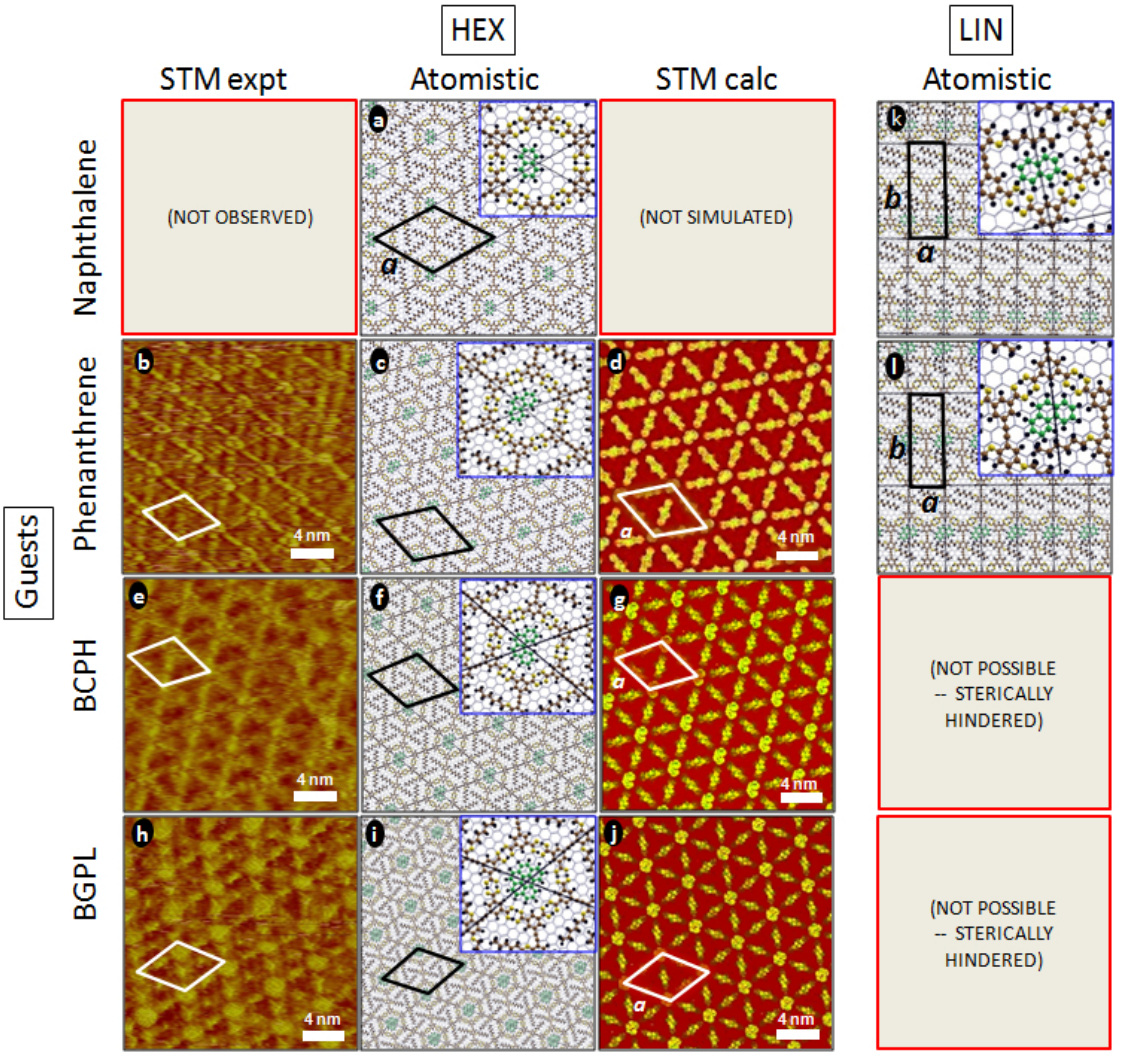

Figure 3.18: STM images and atomistic structures of PE3A with various guests in HEX (a)-(j) and LIN (k)-(l) patterns. Experimental STM images of PE3A with (b) phenanthrene (scan size: 20×20 nm^2; $V_{\text{bias}} = -553$ mV; $I_{\text{t}} = 229$ pA), (e) BCPH (scan size: 20×20 nm^2; $V_{\text{bias}} = -600$ mV; $I_{\text{t}} = 450$ pA) and (h) BGPL (scan size: 20×20 nm^2; $V_{\text{bias}} = -1214$ mV; $I_{\text{t}} = 122$ pA) as guests in HEX pattern. Atomistic structures from DFT of PE3A with (a) naphthalene, (c) phenanthrene, (f) BCPH and (i) BGPL in HEX pattern; (k) naphthalene and (l) phenanthrene in LIN pattern. Simulated STM images of PE3A with (d) phenanthrene, (g) BCPH and (j) BGPL as guests. Simulated STM images are obtained at $V_{\text{bias}} = -2720$ mV. The black/white lines indicate the unit cell; with a and b are the unit cell parameters. Atomic colors: C of host: brown, H: black, O: yellow, C of graphene: gray, C of guest: green.

3.4.4 Descriptors

We now formulate two descriptors, one for the host molecules and one for the guest molecules. Their forms have been determined primarily so as to maximize the

correlation between the two descriptors and the property we wish to predict, which in all cases is whether the HEX or LIN pattern will be energetically favored. Since the ratio of host to guest molecules is different in the unit cell of HEX and LIN patterns, in order to determine the energetically favored pattern we compare the energetics between these two patterns as obtained per unit cell.

Host descriptor

The three host molecules (PE4A, PE4B, and PE3A) studied by us form three different kinds of patterns. These host molecules differ from each other by the length of the backbone (L), the number of terminal COOH groups (N_{COOH}) and the number of side alkoxy chains (N_{alkoxy}). Therefore these three parameters, may be believed to be primarily responsible for determining the favored pattern of the host assembly.

To formulate the host descriptor we have tried several functional forms for the descriptor, which contain the three parameters N_{COOH}, N_{alkoxy} and L. The primary aim in formulating the host descriptor is that it should have a direct correlation with the difference in Gibbs free energy (ΔG) between the HEX and LIN patterns of each host molecule. For the host assemblies, the change in Gibbs free energy per unit area upon adsorption on graphene is given by:

$$\Delta G = (\frac{1}{A})(E_{\mathrm{host/G}} - N_{\mathrm{host}}\mu_{\mathrm{host}} - N_{\mathrm{G}}\mu_{\mathrm{G}}), \tag{3.11}$$

where μ_{host} and μ_{G} are the chemical potentials of the host molecules and graphene atoms, respectively, taken as the total energies of an isolated host molecule in the gas phase, and a carbon atom in a graphene monolayer, respectively. N_{host} and N_{G} are the number of host molecules and carbon atoms of graphene, respectively, present in the unit cell of area A. Note that we are assuming that entropic contributions to ΔG approximately cancel out between the HEX and the LIN patterns, and are therefore neglecting them. This also implies that, as formulated, there is no explicit temperature dependence present in Eq. 3.11. Note that all the terms in it are evaluated from DFT

calculations carried out at temperature $T = 0$ K for both the host assemblies and host-guest complexes.

The term $(\Delta G_{\mathrm{HEX}} - \Delta G_{\mathrm{LIN}})$ is chosen as our target property to determine the host descriptor, since the difference in Gibbs free energy between the HEX and the LIN patterns of a particular host molecule determines the energetically stable pattern for the corresponding host. We see that $(\Delta G_{\mathrm{HEX}} - \Delta G_{\mathrm{LIN}})$ for the host assemblies follows the trend: PE4B $<$ PE3A $<$ PE4A. Hence, if we want to obtain a direct correlation between the host descriptor (η) and $(\Delta G_{\mathrm{HEX}} - \Delta G_{\mathrm{LIN}})$ then the host descriptor should also have the same trend. While trying with several possible forms of the host descriptor using the three parameters N_{COOH}, N_{alkoxy} and L we realize, based on physical intuition, that when forming a combined descriptor, N_{COOH} and L should be placed in the numerator, and N_{alkoxy} in the denominator with some power < 1. Also, to prevent the host descriptor becoming infinite in the absence of any alkoxy chains we introduce a term of the form $1+N_{\mathrm{alkoxy}}$, instead of N_{alkoxy}, in the denominator. Therefore, we start with a trial form of the host descriptor η: $\eta = N_{\mathrm{COOH}}^{\alpha} \times (L)^{\beta} / \, [1+(N_{\mathrm{alkoxy}})^{\gamma}]$. The power α of N_{COOH} is set $= 1$ (based on our finding, from DFT calculations, that the main stabilization of the assembly comes from the formation of dimeric hydrogen bonds between COOH groups, and should be linearly proportional to the number of such bonds). The powers β and γ are required to be integers or simple fractions and are determined so as to minimize the error obtained by a linear fit. Finally, from regression analysis, we find that the mean square error for the fit gets minimized when $\beta = 1$ and $\gamma = 1/8$ when we plot $(\Delta G_{\mathrm{HEX}} - \Delta G_{\mathrm{LIN}})$ vs. η.

Thus, starting from our physical and chemical intuition and carrying out a linear regression to the DFT data, the form of the host descriptor (η) is given by:

$$\eta = \frac{(N_{\mathrm{COOH}} \times L)}{[1 + (N_{\mathrm{alkoxy}})^{1/8}]} \tag{3.12}$$

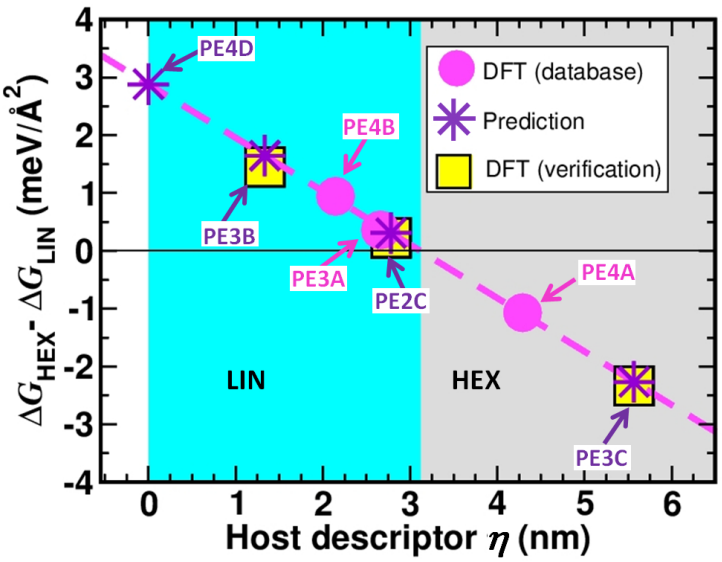

Figure 3.19: Differences in Gibbs free energy between competing structures for host assemblies correlate linearly with the host descriptor η, which can then be used as a predictor. The ordinate is the difference in the change in Gibbs free energy between the HEX and LIN phases. The pink dots show the results from DFT calculations for the three host molecules PE4A, PE4B, and PE3A. The indigo stars show the predictions from the descriptor η for the four test cases PE2C, PE3C, PE3B, and PE4D, and the yellow squares show the verification from DFT for some test cases. The cyan and gray shaded regions indicate domains where the LIN and HEX patterns, respectively, are energetically favored. Note that due to the near-degeneracy of HEX and LIN for PE3A and PE2C, experiment finds a 2D glass featuring random organization. Reprinted with permission from Ref. 43 ©(2017) American Chemical Society.

Note that this form of the descriptor does not have any direct or easy physical interpretation. This is also true for other descriptors developed by previous authors for predicting the structure of three-dimensional octet compounds.[40]

We plot $(\Delta G_{\rm HEX} - \Delta G_{\rm LIN})$ vs. η in Fig. 3.19. The pink dots in Fig. 3.19 show our results from DFT for $(\Delta G_{\rm HEX} - \Delta G_{\rm LIN})$, the difference in ΔG between the HEX and the LIN patterns, plotted as a function of η, for the three host molecules. We see that, using the form of η specified in Eq. 3.12, we obtain a linear correlation between η and $(\Delta G_{\rm HEX} - \Delta G_{\rm LIN})$. The dashed line represents a linear fit to the data represented by the dots; its equation is given by $(\Delta G_{\rm HEX} - \Delta G_{\rm LIN}) = 2.879 - 0.924\eta$. The cyan and gray shaded regions in Fig. 3.19 indicate domains where, respectively, the LIN pattern is energetically favored $(\Delta G_{\rm HEX} - \Delta G_{\rm LIN} > 0)$ and the HEX is favored

($\Delta G_{\mathrm{HEX}} - \Delta G_{\mathrm{LIN}} < 0$). The positions of the three pink dots on this graph again reflects the fact that while PE4A and PE4B have a strong preference for the HEX and LIN arrangements, respectively (lying well within the gray and cyan domains on this graph), this is not true for PE3A, since it lies close to the LIN/HEX boundary. From the graph, one can see that the transition from LIN to HEX occurs at $\eta = 3.12$ nm.

Validation of the Descriptor Now, we want to examine whether the form of the host descriptor shown in Eq. 3.12 is also valid for other host molecules, i.e., whether the descriptor can also predict the favored pattern for the assembly of other host molecules which belong to the same class as the original host molecules, but do not constitute a part of the original database that was used when determining the form of the descriptor. So, to truly gauge the efficacy of η as a descriptor, we next examine how well it performs in predicting the correct structural arrangement for the self-assembly of molecules other than the three host molecules originally considered. In order to do that we consider four additional molecules. Molecule PE2C, PE3C, PE3B, and PE4D are labeled as "test cases"; their chemical structures are depicted in Fig. 3.20. We continue with the labeling convention PEnX, where n is the number of phenyl rings present in the central backbone, here X = C [D] indicates that both ends of the central backbone of the molecule have two [zero] COOH groups attached at meta positions, and there are zero [2(n - 2)] alkoxy side chains. PE3B has COOH groups at only one end of the backbone and has two alkoxy side chains.

In order to predict the energetically favored pattern using the host descriptor η, we evaluate the corresponding values of η for all the four test molecules, as given by Eq. 3.12 and determine where these fall with respect to the boundary value of $\eta = 3.12$ nm. Accordingly (see the indigo stars in Fig. 3.19), PE3C is predicted to form HEX, PE2C to form a 2D glass-like random pattern, and PE3B and PE4D to form the LIN pattern. We find that these predictions are in agreement with experiment and theory for all three cases where data is available from the literature, i.e., for

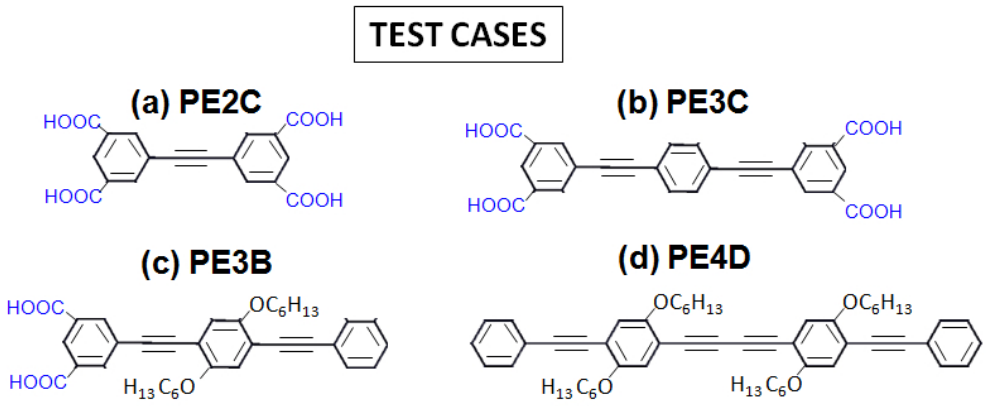

Figure 3.20: Host Molecules Used for Verification. The hosts are labeled (a) PE2C, (b) PE3C, (c) PE3B, and (d) PE4D. Reprinted with permission from Ref. 43 ©(2017) American Chemical Society.

PE4D,[52] PE3C, [19, 74] and PE2C.[19] We are not aware of any previous work on PE3B, for which our prediction of a LIN pattern awaits experimental confirmation.

We can go further: we next use the equation of the dashed line in Fig. 3.19, to obtain a quantitative prediction for the value of $(\Delta G_{\mathrm{HEX}} - \Delta G_{\mathrm{LIN}})$ for each test case; the stars in the graph have been drawn accordingly. These predictions can then be verified by performing DFT calculations on the HEX and LIN patterns on the test cases. These results are shown by the yellow squares in the graph, note that PE4D cannot form a HEX pattern because of the absence of COOH terminal groups, and can therefore only form a LIN pattern. We see that the purple stars (prediction) and yellow squares (validation) fall almost directly on top of each other. This confirms that the predictions regarding the resulting patterns of host assemblies made using the host descriptor η are extremely accurate: for PE3C, PE2C, and PE3B, we find that the error in the difference in ΔG is $<$0.09 meV/Å^2 (see Fig. 3.21 for the atomistic structures of the host assemblies for the test cases).

Guest descriptor

In the previous section, we obtained a host descriptor that could help us to predict the pattern of resulting host assemblies. But, the story is not complete with the host descriptor alone. Recall the fact that some of the host assemblies undergo a

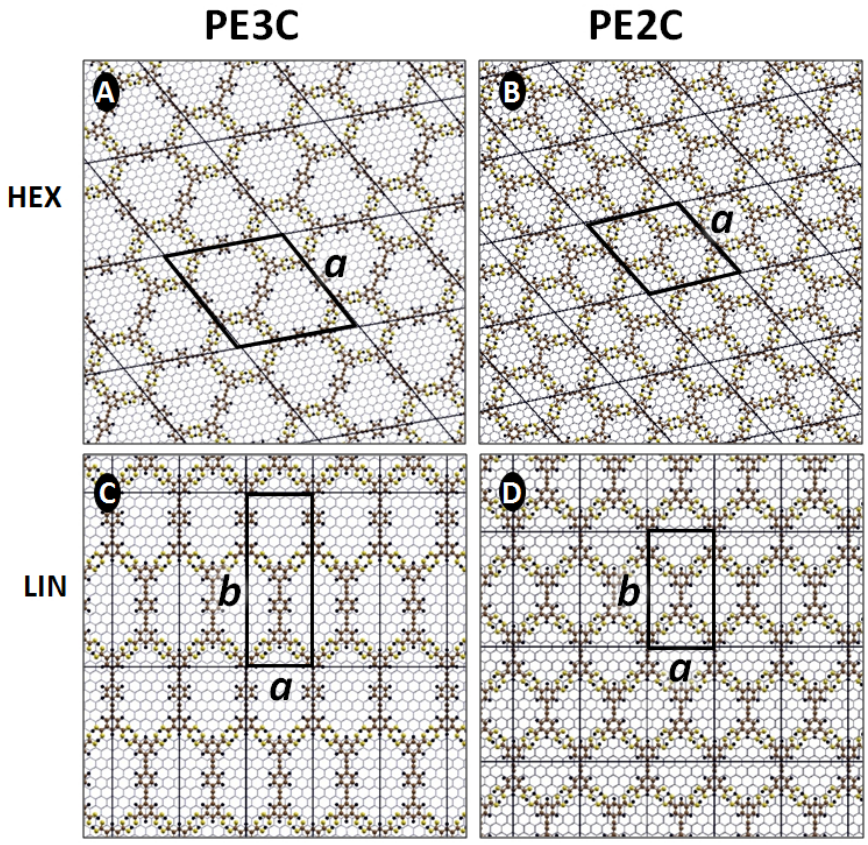

Figure 3.21: Atomistic structures of host assemblies of the test molecules on graphene. All coordinates have been relaxed using DFT calculations. Black rhombi and rectangles mark the boundaries of the unit cells for the HEX and LIN patterns, respectively. Atomic colors: C of host: brown, H: black, O: yellow, C of graphene: gray, C of guest: green.

structural transformation in the presence of specific guest molecules. To predict the guest-induced structural transformation of the host assemblies one needs to introduce a descriptor for the guest molecules as well.

To formulate the guest descriptor, we consider the polygons formed by thehydrogen atoms situated on the periphery of the guests. The guest descriptor ν, is then determined to be the maximum number of vertices of this polygon through which a single circle can be drawn. The values of ν are found to be 4, 6, 8, 10, and 12 when the guests are naphthalene, phenanthrene, BCPH, BGPL, and coronene, respectively. (See the dashed circles in Fig. 3.2; in the case of naphthalene, note that another circle with smaller radius can also be drawn, this also passes through four vertices situated along its periphery).

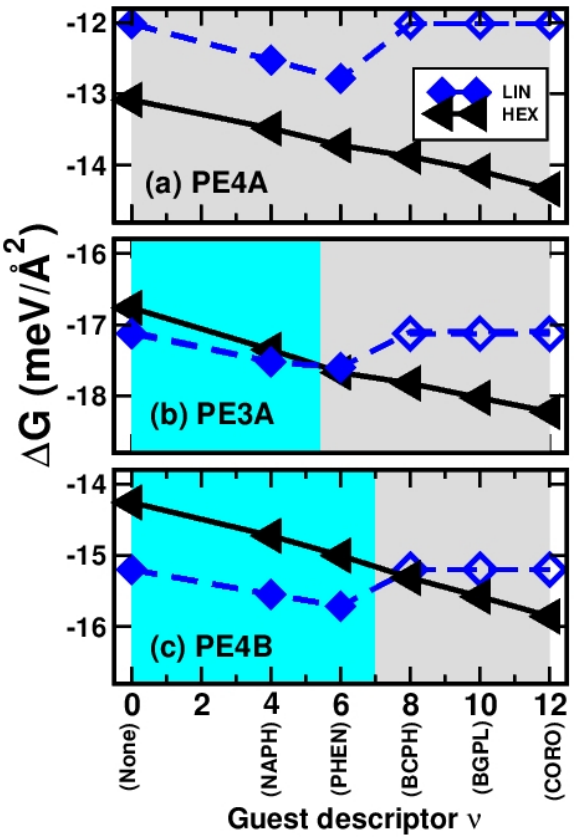

Figure 3.22: Correlation between DFT results for host-guest energetics and guest descriptor ν. Plots show the change in Gibbs free energy (ΔG) of (a) PE4A, (b) PE3A, and (c) PE4B in the presence of different guest molecules. The values of ν corresponding to the following guests are labeled: none, naphthalene, phenanthrene, benzo-c-phenanthrene, benzo-ghi-perylene, and coronene. The black triangles, solid blue diamonds, and open blue diamonds show ΔG of the HEX, LIN, and phase-segregated host and guest, respectively. Domains, where HEX and LIN are preferred, are shaded gray and cyan, respectively; the position of the phase boundary in (c) is approximate. Refer to text for details. Reprinted with permission from Ref. 43 ©(2017) American Chemical Society.

For the host-guest complexes the change in Gibbs free energy per unit area upon adsorption on graphene is given by:

$$\Delta G = (\frac{1}{A})(E_{\text{host/G}} - N_{\text{host}}\mu_{\text{host}} - N_{\text{guest}}\mu_{\text{guest}} - N_{\text{G}}\mu_{\text{G}}), \tag{3.13}$$

where μ_{guest} and N_{guest} are the chemical potential of the isolated guest and the number of guest molecules per unit cell, respectively.

In Fig. 3.22, we have plotted ΔG for each host-guest combination as a function

of guest descriptor ν, in both the HEX and the LIN patterns, when the host is (a) PE4A, (b) PE3A, and (c) PE4B. For the cases where the guest molecule cannot be accommodated in the cavities of the LIN, the values of ΔG for host+guest in the LIN have been computed under the condition where the host and the guest are phase-segregated, with the host being self-assembled in the LIN pattern on graphene and the guest molecules being in the gas phase.

From Fig. 3.22 it can be seen very clearly that all three hosts form different assemblies without any guest. Fig. 3.22 (a) shows ΔG of the HEX and the LIN patterns when the host is PE4A and the guest molecules are varied from naphthalene to coroene. $\nu = 0$ indicates the situation when no guest is present in the host assembly. The black line for the HEX pattern always lies below the blue line of the LIN. Therefore, the calculations predict that, for all the guests, PE4A remains in the HEX pattern. In the case of PE4B, in Fig. 3.22 (c), the blue line is below the black line when the guests are naphthalene and phenanthrene, i.e., PE4B remains in LIN for these two guests but undergoes a structural transition from the LIN to the HEX pattern when the guest is either BCPH, BGPL, or coronene. The black and blue lines lie closer to each other for PE3A in Fig. 3.22 (b), than for PE4A or PE4B. This happens due to the near-degeneracy between the HEX and LIN patterns, which prevents PE3A from showing any long-range order, except when the guest is BCPH, BGPL, or coronene. Again, for PE3A, the HEX pattern becomes more favorable than the LIN when the guests become larger than naphthalene, though the difference in ΔG is rather small for phenanthrene.

When we compare the results for energetics obtained from DFT with the experimental data for STM, we get excellent agreement between experiment and theory for the favored structure, for every single host-guest combination. More importantly, one also sees from Fig. 3.22 that ν works as a good descriptor to successfully determine the energetics of the host-guest assemblies, since ΔG correlates linearly with ν. For the HEX patterns, this is obvious, since ν is exactly equal to the number of (identical)

hydrogen bonds which are formed between the host and the guest molecules (recall the red and blue lobes observed in Fig. 3.14). However, it is not so clear why for the LIN patterns also we find correlation between ΔG and ν (except when the host-guest complex cannot form due to steric reasons). The number of the host-guest hydrogen bonds formed in the LIN patterns are hard to define precisely because the LIN pattern has lower symmetry than the HEX pattern, and therefore, the C-H—O bonds formed between the host and guest molecules in the LIN geometry are not all identical with respect to bond length and bond strength (see Fig. 3.16).

2D Structure Map

Finally, we will combine the host descriptor (η) and guest descriptor (ν) to plot a two-dimensional structure map in descriptor space, where the two axes are the host and guest descriptors η and ν. In Fig. 3.23, here the circle symbols are colored according to the values of $(\Delta G_{\mathrm{HEX}} - \Delta G_{\mathrm{LIN}})$, for the corresponding host-guest assembly. There is a clear trend where the value of this difference increases as a function of (η, ν) as one moves from the lower left corner of the map to the upper right. It is very evident that there is a clustering of the HEX and LIN phases in the descriptor space; such clustering further proves that we have succeeded in identifying appropriate descriptors. In the region of descriptor space shaded gray, the HEX pattern is favored (both experimentally and theoretically), whereas the region shaded with cyan, the LIN pattern is favored (again, both experimentally and theoretically). The boundary between the HEX and the LIN phases is defined by the two solid lines: the vertical line corresponds to the constraint of steric hindrance (larger guest molecules do not fit in the LIN cavities), while the slanting line defines the phase boundary where the LIN and HEX patterns become energetically degenerate. Note that for systems that lie close to the phase boundary determined by the slanting line, experiments tend to find a random organization corresponding to the 2D glass. There is an abrupt jump in the values of $(\Delta G_{\mathrm{HEX}} - \Delta G_{\mathrm{LIN}})$ at the phase boundary which is determined by the constraint of steric hindrance. This happens because the value of

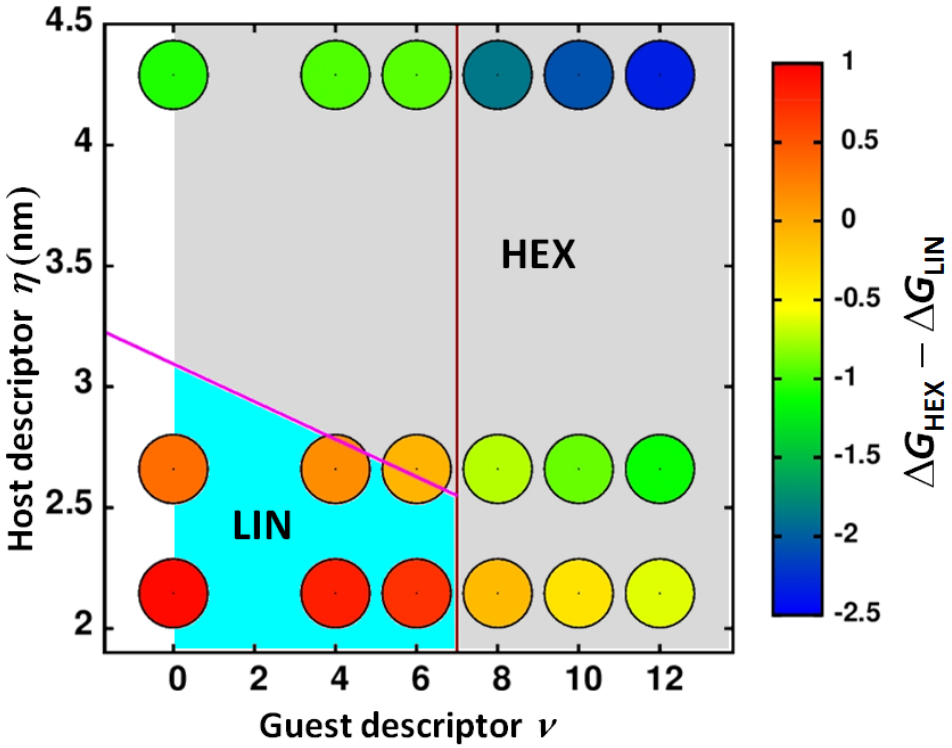

Figure 3.23: Two-dimensional structure map in the descriptor space. The cyan and gray shaded regions indicate domains where the LIN and HEX patterns are favored, respectively; note the clustering in (ν, η) space. The symbols indicate systems for which experiments and calculations are presented in this Chapter; the colors of the circles indicate the theoretically computed differences between the changes in Gibbs free energies of the HEX and LIN patterns for the host-guest system specified by (η, ν), according to the color bar on the right-hand side. Experiments show that systems that lie close to the phase boundary shown by the slanting magenta line tend to form a 2D glass exhibiting a random organization of molecules. Reprinted with permission from Ref. 43 ©(2017) American Chemical Society.

$\Delta G_{\rm LIN}$ on the right-hand side of this phase boundary is computed when the host and guest molecules are phase segregated (these jumps can be seen clearly in the blue dashed lines in the graphs of Fig. 3.22).

Now, if we want to predict the structure of any other host-guest assembly, it is a simple matter to compute the values of η and ν for this host-guest combination, see where this point lies on this 2D structure map, and accordingly one can predict (very quickly) whether the host-guest assembly will form in the HEX or LIN pattern, or get arrested into a random glass-like pattern.

3.5 Conclusions

In this chapter, we have shown the advantages and plausibility of a descriptor-based design strategy for two-dimensional supramolecular architectures. For the first time, we have succeeded in identifying descriptors for self-assembly of molecules on surfaces. These descriptors are trivial to compute since they depend only on the geometry and form of isolated host and guest molecules in the gas phase. [43]

We have studied the structures formed by the self-assembly of organic molecules on graphene. The self-assembled architectures are held together by various non-covalent interactions. We have worked with a "training set" of three hosts and five guests. Both STM experiments and DFT calculations show that the three hosts assemble in three different types of patterns (porous HEX, nonporous LIN, and random 2D glass) in the absence of any guest. Interestingly, the presence of specific guest molecules can change the structure of some of the host assemblies. Depending on the particular host-guest pair, host assemblies can undergo a structural transition from disorder-to-order or from LIN to HEX. Remarkably, experimental observations and DFT predictions for the thermodynamically favored structures of the host-guest assemblies agree for all 18 cases studied here. This confirms that theoretical study of non-covalent interactions are now advanced enough so that they can be successfully applied to investigate structural properties of supramolecular architectures not to give just correct qualitative trends but also quantitative information.

Using intuition and a regression analysis applied to a numerical database obtained from DFT calculations we have identified two simple but effective descriptors (one for the hosts and one for the guests) that correlate molecular form and formula to supramolecular architecture. These two descriptors meet all the possible and necessary requirements that a successful descriptor should have: (i) they can be obtained at zero computational cost since these descriptors are formulated based on the structure and geometry of the isolated host and guest molecules, and the corresponding chemical motifs. All these features are very trivial to determine; (ii) there is a very nice

correlation between the descriptors and the target properties, viz., the energies of the host or host-guest complexes and hence their resulting self-assemblies; and (iii) the structures of a given type perfectly cluster in the descriptor space. Once such structure map is established by combining the host and guest descriptors, it can be used to design the nanostructures of desired architectures and properties. The main advantage of such structure maps is that they could guide us in choosing proper molecules which can lead to achieve desired geometries and/or functionalities.[43] We have validated our descriptors for some "test" cases, and obtained excellent agreement with both experimental and theoretical data in the literature (where available). Also some additional DFT calculations have been performed by us to verify the accuracy of the predictions made using the descriptors for the test molecules. The descriptors formulated by us are, obviously, not universal: their form is limited to the particular types of host and guest molecules used in this study. These descriptors would have to be modified appropriately for molecules having different types of chemical motifs and structures. In this context, the possible extensions would be to consider, e.g., different lengths of the molecular backbone, making the number of alkoxy side chains odd, varying the terminal groups (some groups other than COOH) and/or their attachment sites, and also changing the chemical structure of the molecular backbone.

We believe that this study represents an interesting initial step in demonstrating how one can proceed by using the descriptor-based strategies to design self-assembled patterns on surfaces. This kind of approach could, in principle, be feasible in any supramolecular system where one wishes to construct structure maps using the constituent molecules which lead to the resulting assembly. In this chapter, we considered our target property to be the energetically favored pattern of the assembly. Descriptor-based strategies could also be used to consider other properties, e.g., optical activity, electrical conductivity, or chemical reactivity. To the best of our knowledge, this is the first time that a strategy has been developed to predict the self-assembled geometries formed by the host and the host-guest molecules on two-dimensional

surfaces using descriptors. Our descriptors are simple as well as accurate.

Bibliography

[1] Z. P. Mohan, *Supramolecular Organization of Phenyleneethynylenes on Surface: Role of Hydrogen Bonding and Host-Guest Interactions*. PhD thesis, Indian Institute of Science Education and Research Thiruvananthapuram, India, 2015.

[2] J. V. Barth *Nature*, vol. 437, pp. 671–679, 2005.

[3] J. V. Barth *Annu. Rev. Phys. Chem.*, vol. 58, pp. 375–407, 2007.

[4] R. Klajn, J. F. Stoddart, and A. B. Grzybowski *Chem.Soc.Rev.*, vol. 39, pp. 2203–2237, 2015.

[5] W. Szymaski, J. M. Beierle, H. A. V. Kistemaker, W. A. Velema, and B. L. Feringa *Chem. Rev.*, vol. 11, pp. 6114–6178, 2013.

[6] L. Zhang, X. Zhong, E. Pavlica, S. Li, A. Klekachev, G. Bratina, T. W. Ebbesen, E. Orgiu, and P. Samori *Nat. Nanotech.*, vol. 113, p. 900, 2016.

[7] H. Ouchi, X. Lin, T. Kizaki, D. D. Prabhu, F. Silly, T. Kajitani, T. Fukushima, K.-i. Nakayama, and S. Yagai *Chem. Commun.*, vol. 52, pp. 7874–7877, 2016.

[8] E. S. Cho, J. Kim, B. Tejerina, T. M. Hermans, H. Jiang, H. Nakanishi, M. Yu, A. Z. Patashinski, S. C. Glotzer, F. Stellacci, and B. A. Grzybowski *Nat. Mater.*, vol. 11, pp. 978–985, 2012.

[9] W. R. Browne and B. L. Feringa *Nat. Nanotech.*, vol. 1, pp. 25–35, 2006.

[10] A. Faulkner, T. van Leeuwen, B. L. Feringa, and S. J. Wezenberg *J. Am. Chem. Soc.*, vol. 138, pp. 13597–13603, 2016.

[11] B. L. Feringa *Angew. Chem. Int. Ed.*, vol. 56, pp. 11060–11078, 2017.

[12] Y. Yang and C. Wang *Chem. Soc. Rev.*, vol. 38, pp. 2576–2589, 2009.

[13] T. Kudernac, S. B. Lei, J. A. A. W. Elemans, and S. De Feyter *Chem. Soc. Rev.*, vol. 38, pp. 402–421, 2009.

[14] B. A. Hermann, L. J. Scherer, C. E. Housecroft, and E. C. Constable *Adv. Funct. Mater.*, vol. 16, pp. 221–235, 2009.

[15] K. Iritani, K. Tahara, S. De Feyter, and Y. Tobe *Langmuir*, vol. 33, pp. 4601–4618, 2017.

[16] G. R. Desiraju *Acc. Chem. Res.*, vol. 35, pp. 565–573, 2002.

[17] T. Steiner and G. R. Desiraju, "Distinction between the weak hydrogen bond and the van der waals interaction," *Chem. Commun.*, vol. 8, pp. 891–892, 1998.

[18] S. Clair, S. Pons, A. P. Seitsonen, H. Brune, K. Kern, and J. V. Barth *J. Phys. Chem. B*, vol. 108, pp. 14585–14590, 2004.

[19] H. Zhou, H. Dang, J. H. Yi, A. Nanci, A. Rochefort, and J. D. Wuest *J. Am. Chem. Soc.*, vol. 129, pp. 13774–13775, 2007.

[20] L. Kampschulte, T. L. Werblowsky, R. S. K. Kishore, M. Schmittel, W. M. Heckl, and M. Lackinger *J. Am. Chem. Soc.*, vol. 130, pp. 8502–8507, 2008.

[21] G. M. Credo, A. K. Boal, K. Das, T. H. Galow, V. M. Rotello, D. L. Feldheim, and C. B. Gorman *J. Am. Chem. Soc.*, vol. 124, pp. 9036–9037, 2002.

[22] J. Chen, M. A. Reed, A. M. Rawlett, and J. M. Tour *Science*, vol. 286, pp. 1550–1552, 1999.

[23] S. Wieghold, J. Li, P. Simon, M. Krause, Y. Avlasevich, C. Li, J. A. Garrido, U. Heiz, P. Samor´i, K. Müllen, F. Esch, J. V. Barth, and C.-A. Palma *Nat. Commun.*, vol. 7, p. 10700, 2016.

[24] M. Kim, J. N. Hohman, Y. Cao, K. N. Houk, H. Ma, A. K.-Y. Jen, and P. S. Weiss vol. 331, pp. 1312–1315, 2011.

[25] V. Ferri, M. Elbing, G. Pace, M. Dickey, M. Zharnikov, P. Samori, M. Mayor, and M. Rampi *Angew. Chem. Int. Ed.*, vol. 47, pp. 3407–3409, 2008.

[26] P. Wei, X. Yan, T. R. Cook, X. Ji, P. J. Stang, and F. Huang *ACS Macro Letters*, vol. 5, pp. 671–675, 2016.

[27] S. Abb, L. Harnau, R. Gutzler, S. Rauschenbach, and K. Kern *Nat. Commun.*, vol. 7, p. 10335, 2016.

[28] M.-S. Bonifazi, D. and A. Llanes-Pallas *Chem. Eur. J.*, vol. 15, pp. 7004–7025, 2009.

[29] D. Bonifazi, H. Spillmann, A. Kiebele, M. de Wild, P. Seiler, F. Cheng, H.-J. Güntherodt, T. Jung, and F. Diederich *Angew. Chem.*, vol. 116, pp. 4863–4867, 2004.

[30] T. Kaposi, S. Joshi, T. Hoh, A. Wiengarten, K. Seufert, M. Paszkiewicz, F. Klappenberger, D. Ecija, L. orevi, T. Marangoni, D. Bonifazi, J. V. Barth, and W. Auwrter *ACS Nano*, vol. 10, pp. 7665–7674, 2016.

[31] C.-A. Palma, M. Bonini, A. Llanes-Pallas, T. Breiner, M. Prato, D. Bonifazi, and P. Samori *Chem. Commun.*, pp. 5289–5291, 2008.

[32] A. Llanes-Pallas, C.-A. Palma, L. Piot, A. Belbakra, A. Listorti, M. Prato, P. Samor´i, N. Armaroli, and D. Bonifazi *J. Am. Chem. Soc.*, vol. 131, pp. 509–520, 2009.

[33] S. Furukawa, K. Tahara, F. C. De Schryver, M. Van der Auweraer, and S. Tobe, Y.and De Feyter *Angew. Chem., Int. Ed.*, vol. 46, pp. 2831–2834, 2007.

[34] C. Fu, P. J. Beldon, and D. F. Perepichka *Chem. Mater.*, vol. 29, pp. 2979–2987, 2017.

[35] J. Teyssandier, S. D. Feyter, and K. S. Mali *Chem. Commun.*, vol. 52, pp. 11465–11487, 2016.

[36] G. Velpula, T. Takeda, J. Adisoejoso, K. Inukai, K. Tahara, K. S. Mali, Y. Tobe, and S. De Feyter *Chem. Commun.*, vol. 53, pp. 1108–1111, 2017.

[37] M. Shen, Z. Luo, S. Zhang, S. Wang, L. Cao, Y. Geng, K. Deng, D. Zhao, W. Duan, and Q. Zeng *Nanoscale*, vol. 8, pp. 11962–11968, 2016.

[38] Q.-N. Zheng, L. Wang, Y.-W. Zhong, X.-H. Liu, T. Chen, H.-J. Yan, D. Wang, J.-N. Yao, and L.-J. Wan *Langmuir*, vol. 30, pp. 3034–3040, 2014.

[39] Y. Li, J. Wan, K. Deng, X. Han, S. Lei, Y. Yang, Q. Zheng, Q. Zeng, and C. Wang *J. Phys. Chem. C*, vol. 11, pp. 6540–6544, 2011.

[40] L. M. Ghiringhelli, J. Vybiral, S. V. Levchenko, C. Draxl, and M. Scheffler *Phys. Rev. Lett.*, vol. 114, pp. 105503–105508, 2015.

[41] J. K. Nørskov, F. Abild-Pedersen, F. Studt, and T. Bligaard *Proc. Natl. Acad. Sci.*, vol. 108, pp. 937–943, 2011.

[42] F. Goltl, P. Muller, P. Uchupalanun, P. Sautet, and I. Hermans *Chem. Mater.*, vol. 29, pp. 6434–6444, 2017.

[43] P. Zalake, S. Ghosh, S. Narasimhan, and K. G. Thomas *Chem. Mater.*, vol. 29, pp. 7170–7182, 2017.

[44] L. Verstraete, J. Greenwood, B. E. Hirsch, and S. De Feyter *ACS Nano*, vol. 10, pp. 10706–10715, 2016.

[45] T. W. Odom, J.-L. Huang, and C. M. Lieber *J. Phys.: Condens. Matter*, vol. 14, pp. R145–R167, 2002.

[46] A. Ciesielski, P. J. Szabelski, W. Rżysko, A. Cadeddu, T. R. Cook, P. J. Stang, and P. Samori *J. Am. Chem. Soc.*, vol. 135, pp. 6942–6950, 2013.

[47] P. Samori *J. Mater. Chem.*, vol. 14, pp. 1353–1366, 2004.

[48] H. Roder, E. Hahn, H. Brune, J. P. Bucher, and K. Kern *Nature*, vol. 366, pp. 141–143, 1993.

[49] S. Weigelt, C. Bombis, C. Busse, M. M. Knudsen, K. V. Gothelf, E. Lgsgaard, F. Besenbacher, and T. R. Linderoth *ACS Nano*, vol. 2, pp. 651–660, 2008.

[50] Z. J. Donhauser, B. A. Mantooth, K. F. Kelly, L. A. Bumm, J. D. Monnell, J. J. Stapleton, D. W. Price, A. M. Rawlett, D. L. Allara, and P. S. Tour, J. M.; Weiss *Science*, vol. 292, pp. 2303–2307, 2001.

[51] T. W. Odom, J.-L. Huang, and C. M. Kim, P.; Lieber *Nature*, vol. 391, pp. 62–64, 1998.

[52] P. Zalake and K. G. Thomas *Langmuir*, vol. 29, pp. 2242–2249, 2013.

[53] A. R. Ramesh and K. G. Thomas *Chem. Commun.*, vol. 46, pp. 3457–3459, 2010.

[54] J. M. Soler, E. Artacho, J. D. Gale, A. Garcia, J. Junquera, P. Ordejón, and D. Sánchez-Portal *J. Phys.: Condens. Matter*, vol. 14, p. 2745, 2002.

[55] D. Sànchez-Portal, P. Ordejón, E. Artacho, and J. M. Soler *Int. J. Quantum Chem.*, vol. 65, pp. 453–461, 1997.

[56] N. Troullier and J. L. Martins *Phys. Rev. B: Condens. Matter Mater. Phys.*, vol. 43, pp. 1993–2006, 1991.

[57] J. P. Perdew and M. Burke, K.; Ernzerhof *Phys. Rev. Lett.*, vol. 77, pp. 3865–3868, 1996.

[58] S. Grimme *J. Comput. Chem.*, vol. 27, pp. 1787–1799, 2006.

[59] S. F. Boys and F. Bernardi *Mol. Phys.*, vol. 19, pp. 553–566, 1970.

[60] B. Brauer, M. K. Kesharwani, and J. M. L. Martin *J. Chem. Theory Comput.*, vol. 10, pp. 3791–3799, 2014.

[61] J. Tersoff and D. R. Hamann *Phys. Rev. Lett.*, vol. 50, pp. 1998–2001, 1983.

[62] T. Beyer and S. L. Price *J. Phys. Chem. B*, vol. 104, pp. 2647–2655, 2000.

[63] K. Tahara, S. B. Lei, J. Adisoejoso, S. De Feyter, and Y. Tobe *Chem. Commun.*, vol. 46, pp. 8507–8525, 2010.

[64] K. Yoosaf, P. V. James, A. R. Ramesh, C. H. Suresh, and K. G. Thomas *J. Phys. Chem. C*, vol. 111, pp. 14933–14936, 2007.

[65] W. Hong, H. Li, S.-X. Liu, Y. Fu, J. Li, V. Kaliginedi, S. Decurtins, and T. Wandlowski *J. Am. Chem. Soc.*, vol. 134, pp. 19425–19431, 2012.

[66] A. Villares, G. Pera, S. Martin, R. J. Nichols, D. P. Lydon, L. Applegarth, A. Beeby, P. J. Low, and P. Cea *Chem. Mater.*, vol. 22, pp. 2041–2049, 2010.

[67] P. Samori, V. Francke, V. Enkelmann, K. Müllen, and J. P. Rabe *Chem. Mater.*, vol. 15, pp. 1032–1039, 2003.

[68] C.-A. Palma, P. Samori, and M. Cecchini *J. Am. Chem. Soc.*, vol. 132, pp. 17880–17885, 2010.

[69] J. Björk, F. Hanke, C.-A. Palma, P. Samori, M. Cecchini, and M. Persson *J. Phys. Chem. Lett.*, vol. 1, p. 3407, 2010.

[70] O. V. Ershova, T. C. Lillestolen, and E. Bichoutskaia *Phys. Chem. Chem. Phys.*, vol. 12, pp. 6483–6491, 2010.

[71] G. R. Desiraju *Acc. Chem. Res.*, vol. 24, pp. 290–296, 1991.

[72] G. R. Desiraju *Acc. Chem. Res.*, vol. 29, pp. 441–449, 1996.

[73] T. Gu, Y.; Kar and S. Scheiner *J. Am. Chem. Soc.*, vol. 121, pp. 9411–9422, 1999.

[74] J.-F. Zhao, Y.-B. Li, Z.-Q. Lin, L.-H. Xie, N.-E. Shi, X.-K. Wu, C. Wang, and W. Huang *J. Phys. Chem. C*, vol. 114, pp. 9931–9937, 2010.

Chapter 4

Electronic Structure of the Organic Molecules in the Gas Phase and on Graphene

After studying the structural properties of the self-assembled monolayers of phenyleneethynylene (PE) molecules we want to investigate their electronic properties. In this chapter, we have investigated how the electronic properties, especially the gap between the highest occupied molecular orbital (HOMO) and lowest unoccupied molecular orbital (LUMO), of PE molecules depend on their structure and the chemical motifs present in them. We find that the HOMO-LUMO gap of PE molecules can be predicted by using a simple descriptor. This work has been done in collaboration with the experimental group of Prof. K. George Thomas and his student Pratap Zalake (IISER Thiruvananthapuram, India). The experimental results mentioned in this chapter have already been discussed in the thesis of Dr. Pratap Zalake.[1]

4.1 Introduction

Molecular motifs of the organic molecules play an important role in determining their various physical and chemical properties. In the previous chapter we have

studied how the architecture of the molecular self-assembly could be governed by the nature of the building blocks of the molecules participating in the assembly. The optoelectronic properties of molecules depend on the chemical components by which a molecule is comprised of. Nowadays, the modern day technology is aligned towards the organic electronics. This field is important due to fundamental interest as well as for industrial applications. The main advantages to use the organic materials in nanotechnology are the following. (1) Device fabrication with organic molecules requires a low cost and low-temperature processing, (2) the technology based on these materials is compatible with large area processes, and (3) more importantly, the molecules and polymers can be tailored according to the required electronic or optical properties. Therefore, it has now become an open challenge to the scientists and engineers to synthesize molecules in order to design devices or machines which can perform more efficiently compared to the already existing materials.

Conjugated polymers have gained much attention in chemistry, materials science, and biology. These molecules have longer π-conjugation length, higher conductivity, higher quantum efficiencies, longer lifetime, simple processing tools, and can form energetically stable self-assembled patterns. All these characteristics make them suitable in device-based applications.

The π-conjugated molecules, e.g., oligophenylenes (OP), oligophenyleneethynylenes (OPE), oligophenylenevinylenes (OPV), oligothiophenes (OT) are very promising elements in the optoelectronic devices. These molecules have been proposed as materials in organic electronics due to their high conductivity and rigid-rod like structure.[2] The conjugated molecules are polyunsaturated compounds, in which the carbon atoms in the backbone are sp or sp^2 hybridized. The π-conjugated molecules can be viewed as the one-dimensional molecular wires in the molecular devices, such as single electron transistors, molecular switches, etc.[3, 4] Optoelectronic devices such as LEDs,[5, 6] lasers,[7] field-effect transistors,[8] optical waveguides,[9] and photovoltaics[10] built from conjugated polymers are very useful in commercial

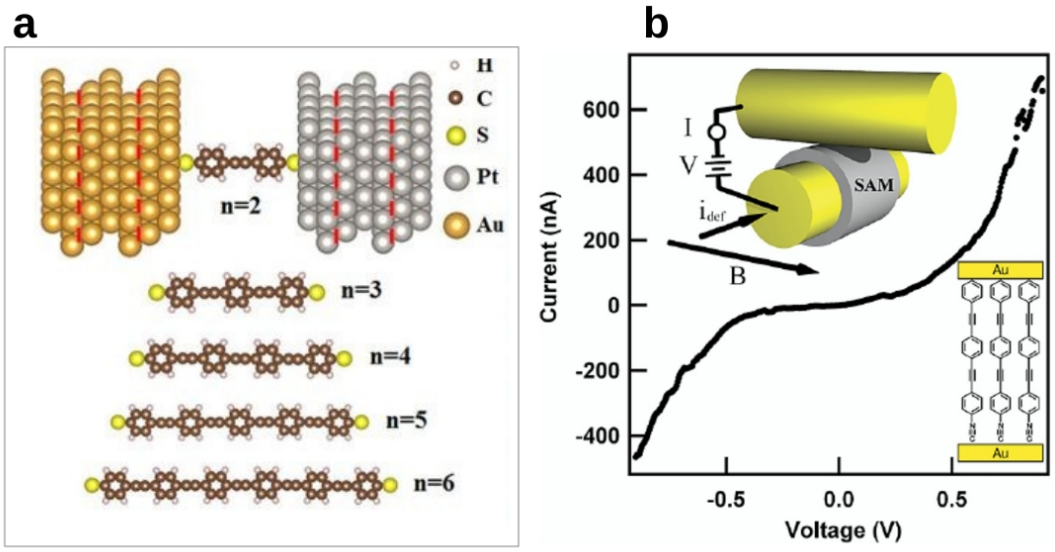

Figure 4.1: Applications of π-conjugated molecules in organic electronics. (a) Oligophenyleneethynylene (OPE) molecules with different length. The phenyl rings (along the backbone) are varied from 2-6. The OPE molecules are placed between the Au (left) and Pt (right) electrodes.[11] This figure is taken with permission from Ref. 11 ©(2014) Springer Nature. (b) I–V characteristics of a metalmoleculemetal junction formed by crossed wires with OPE molecules sandwiched between two Au electrodes. This figure is taken with permission from Ref. 12 ©(2004) American Chemical Society.

applications due to their low cost, low weight, less power consumption, and high flexibility. Fig. 4.1 shows applications of OPE molecules as molecular wires.

During the last few decades, tremendous progress has been achieved in the synthesis of molecular building blocks of phenyleneethynylene molecules having different shapes, geometries, and different functional groups.[13, 14] Previous authors have studied the electrical conductivity and rectifying properties of these conjugated molecules when they are sandwiched between two metal electrodes.[11, 15, 16] Metal-molecule-metal heterojunctions containing π-conjugated molecules show good charge transport properties at low temperature.[12]

The electronic properties of these molecules depend on the conjugation which causes electron delocalization in the molecules. The conjugation in organic molecules is affected by their chemical motifs (e.g., length of the molecule and the alkoxy chains attached to it), and it can modify the optical and electronic properties of the

π-conjugated molecules.[11, 16, 17] Therefore, these building blocks influence the physical or chemical properties of the molecules which can be tuned by varying the molecular lego. For example, previous work has shown that the optical properties of oligo- and poly p-aryleneethylenes (OAEs and PAEs) depend on their chemical structures.[18–21] Changes in chemical structures in a programmed manner can cause modification to the electronic properties of the molecules by introducing electron withdrawing and/or electron donating groups. As we know, for all practical applications, these molecular systems need to be organized on a surface. Thus, the electronic properties of the molecules can be further modified when the assemble on the surfaces.[22, 23]

In this chapter, we study the electronic properties of phenyleneethynylene (PE) molecules in the gas phase and on graphene. We calculate the HOMO-LUMO gap of different PE molecules by varying the conjugation length, number and positions of the alkoxy chains attached to them. First, we investigate how the HOMO-LUMO gap of the isolated molecules can be modified by changing the molecular length and the positions of the alkoxy chains. Combining DFT calculations with experiments, we measure the HOMO-LUMO gap of the isolated PE molecules. Our results on the HOMO-LUMO gap of the PE molecules with different conjugation lengths but the same number and positions of the alkoxy groups are supported by the well-known particle in a box model. For the molecules of the same length but different number and positions of the alkoxy groups, we have identified a descriptor which can predict their HOMO-LUMO gap. This descriptor is verified by considering additional test molecules. Finally, we study how the HOMO-LUMO gap of the PE molecules is modified upon formation of self-assembled monolayers in the gas phase and on graphene.

4.2 Computational Methods

We perform density functional theory (DFT) calculations using the SIESTA package.[24, 25] A double-ζ polarized basis set is used with a confinement energy of 0.01 Ry. The mesh cutoff size of the real-space grid is taken to be 250 Ry. We use Troullier-Martins norm-conserving pseudopotentials for the interactions between the ionic cores and valence electrons.[26] Exchange and correlation interactions between the electrons are treated within the Perdew, Burke, and Ernzerhof (PBE) form of the generalized gradient approximation (GGA).[27] The long-range dispersion interactions are included in the calculations by applying the semiempirical DFT-D2 treatment.[28] A vacuum region of length > 16 Å is introduced along non-repeating directions. For the isolated molecules and the periodic molecular monolayers (in large unit cells), the Brillouin zone is sampled at the zone center Γ only. The geometry optimization is performed using the conjugate gradient (CG) algorithm. All atomic coordinates are relaxed until the forces on all atoms become smaller than 0.03 eV/Å. When calculating the energetics of self-assembled monolayers, basis set superposition errors are eliminated by applying the counterpoise correction procedure.[29, 30] The STM images are simulated using the Tersoff-Hamann approach.[31]

For some calculations, we also use the Gaussian 09 package, together with the B3LYP functional,[32, 33] and 6.31G(d,p) basis sets to calculate the HOMO-LUMO gaps of PE molecules more accurately. Time-dependent density functional theory (TDDFT) calculations are performed using B3LYP to obtain the optical properties of isolated PE molecules in the gas phase.[34]

4.3 Systems

In phenyleneethynylene (PE) molecules the phenyl groups are connected together via acetylenic bridging units as rigid aromatic backbone. The phenyleneethynylene molecules studied in this chapter differ in the length of their central backbone and/or the number of alkoxy side chains and/or their attachment sites. In the literature,

PE molecules of different lengths are often named based on the number of phenyl rings present in the central backbone, with names such as trimer, tetramer, pentamer and hexamer. Thus, the number of phenyl rings for trimer, tetramer, pentamer and hexamer are three, four, five and six, respectively. In the naming convention used here, all these molecules have alkoxy chains attached at the terminal positions of their terminal phenyl rings. The conjugation length of these PE molecules is defined as the distance between the oxygen atoms (d_{O-O}) of the two alkoxy chains, this distance varies from 19.45 Å in the dimer to 40.39 Å in the hexamer. (We note that the conjugation length can, alternatively, be defined as the sum of the C-C bond lengths in the conjugation path connecting the two O atoms, further below we will also consider this alternative definition.) The PE molecules of different conjugation length considered in this study are shown in Fig. 4.2. Studying these molecules allows us to study the effect of varying conjugation length, while keeping all other factors the same.

Next, we wish to study the effect of varying the number of alkoxy side chains and their attachment sites, while keeping the length of the central backbone fixed. To do this, we have chosen to study six PE molecules, which we will refer to as PE1, PE2, PE3, PE4, PE5 and PE6, their structures are shown in Fig. 4.3. All six of these molecules have three phenyl rings in the central backbone, however they have varying number and attachment sites of the alkoxy chains. These six PE molecules are studied using both DFT and experiments. The molecule PE1 has no alkoxy chain. PE2 has two alkoxy chains which are attached to the central phenyl ring. The two alkoxy chains of PE3 are situated at the terminal phenyl rings (PE3 is identical to the molecule that was referred to as the trimer in the previous paragraph). PE4 has one alkoxy chain attached at its central phenyl ring. PE5 has three alkoxy chains; two are at the terminal phenyl rings and one at the central phenyl ring. PE6 contains total four alkoxy chains, two alkoxy chains are attached to the central phenyl ring and the other two are at the terminal phenyl rings.

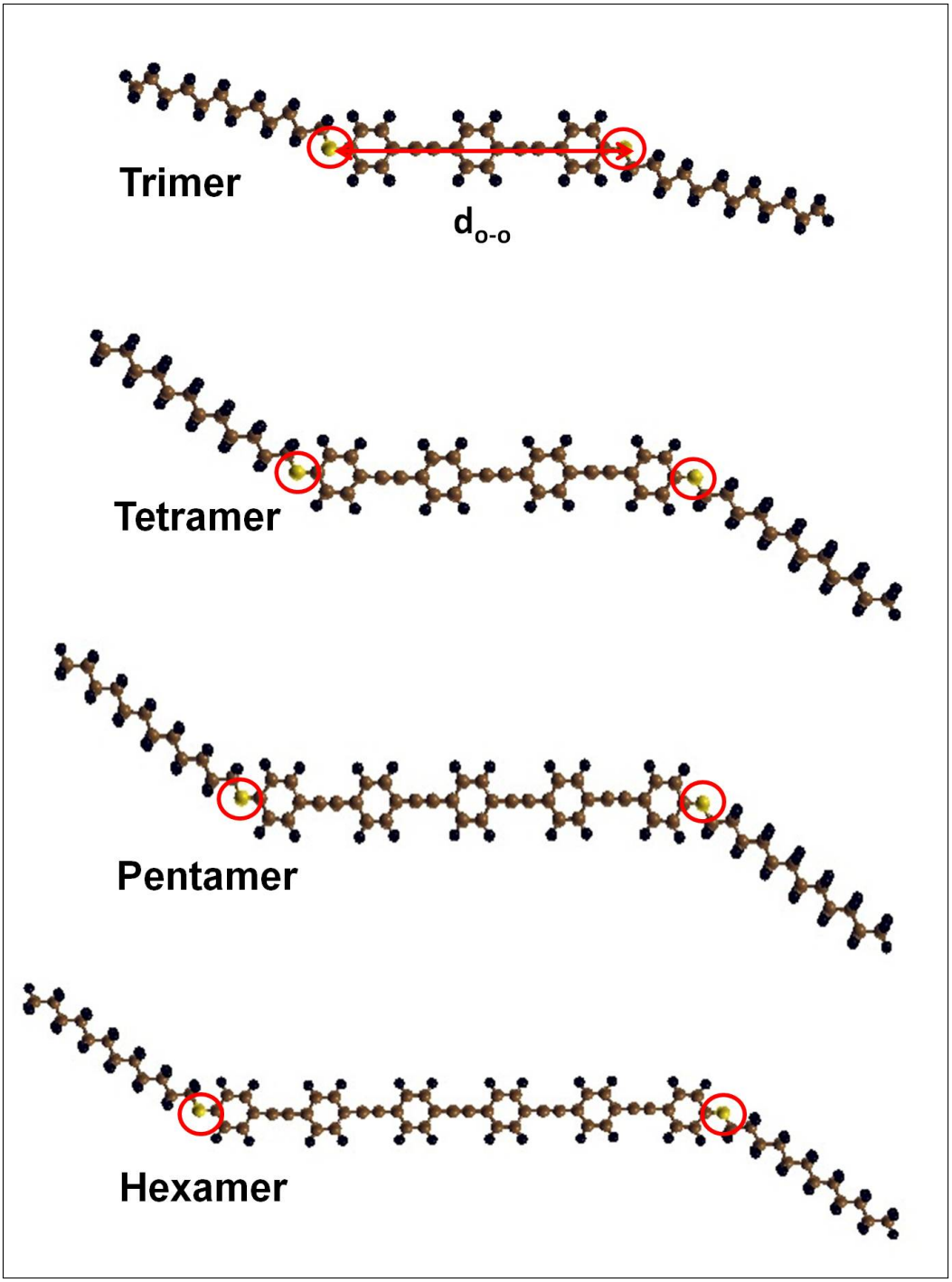

Figure 4.2: Phenyleneethynylene molecules of different lengths but same number and attachment sites of the alkoxy chains. The number of phenyl rings varies from three to six for trimer to hexamer. Color scheme: C, brown; H, black and O, yellow. The O atoms in the alkoxy chains are shown with the red circles.

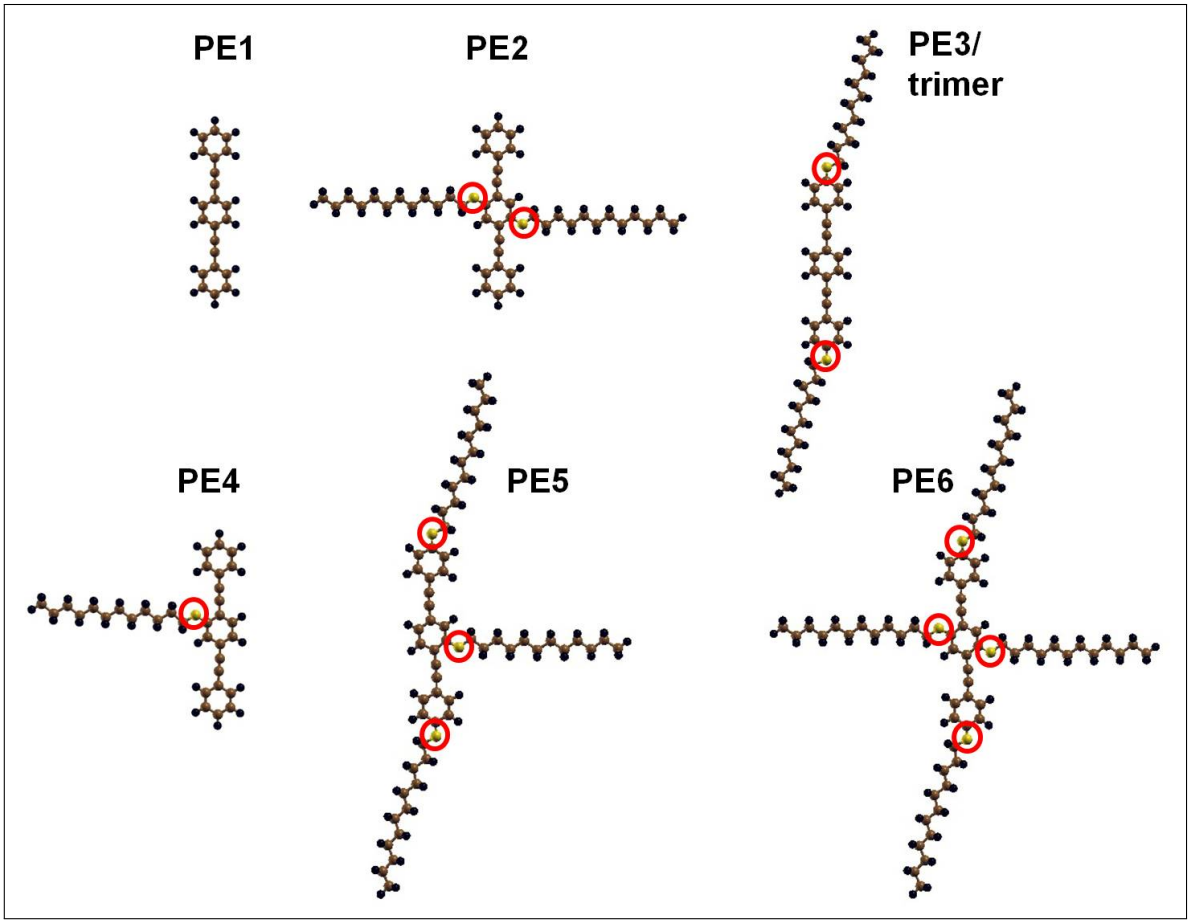

Figure 4.3: Phenyleneethynylene molecules with different number and attachment sites of the alkoxy chains but same backbone-length. Color scheme: C, brown; H, black and O, yellow. The O atoms in the alkoxy chains are shown with the red circles.

4.4 Results

4.4.1 HOMO-LUMO gap of Isolated PE Molecules

Molecules of Different Conjugation Lengths

We calculate the HOMO-LUMO gap of the isolated trimer, tetramer, pentamer, and hexamer in the gas phase. The HOMO-LUMO gap calculated using standard DFT, $E_{\mathrm{g}}^{\mathrm{DFT}}$, is plotted as a function of the distance $d_{\mathrm{O-O}}$ in Fig. 4.4. We see that $E_{\mathrm{g}}^{\mathrm{DFT}}$ decreases quadratically with $d_{\mathrm{O-O}}$. This behavior of $E_{\mathrm{g}}^{\mathrm{DFT}}$ can be explained by using the quantum mechanical model of a particle in a one-dimensional box.

The energy eigenvalues of an electron in a one-dimensional (1D) box with infinite

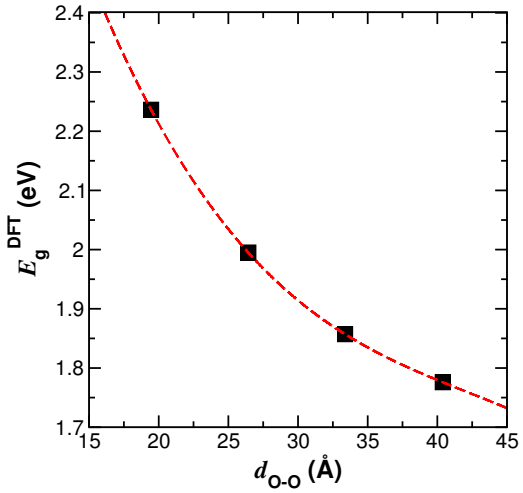

Figure 4.4: Variation of $E_{\mathrm{g}}^{\mathrm{DFT}}$ as a function $d_{\mathrm{O-O}}$ for trimer, tetramer, pentamer and hexamer. $E_{\mathrm{g}}^{\mathrm{DFT}}$ reduces with $d_{\mathrm{O-O}}$.

walls, obtained by solving the Schrödinger equation, are given by:

$$E_n = \frac{n^2 h^2}{8mL^2}, \tag{4.1}$$

where n denotes the quantum number (it can be any integer ≥ 1), m_e is the electron mass, h is Planck's constant and L is the length of the box. From the standard particle in a box model, one can see $E_{\mathrm{n}} \propto 1/L^2$. The wavefunction corresponding to the nth eigenstate in the 1D box is:

$$\Psi_n(x) = \sqrt{\frac{2}{L}} \sin\left(\frac{n\pi x}{L}\right). \tag{4.2}$$

If the total number of electrons present in the box is N, then by the Pauli exclusion principle, the number of occupied states is $N/2$. Thus, the HOMO and LUMO correspond to $n = N/2$ and $n = (N/2) + 1$, respectively. The energy required for the transition from the state $N/2$ to $N/2$+1, which is equal to the HOMO-LUMO gap E_g, is:

$$\Delta E = E_g^{\mathrm{1Dbox}} = \frac{h^2}{8mL^2}\left[\left(\frac{N}{2}+1\right)^2 - \frac{N}{2}^2\right] = \frac{h^2}{8mL^2}(N+1) \tag{4.3}$$

Thus, to calculate E_g using the 1D particle in a box model, one needs to know the

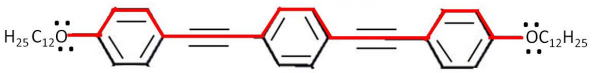

Figure 4.5: Conjugation path in the trimer shown by the red lines.

total number of the electrons N that constitute the 'free electron gas' that is trapped in the potential well, and the length L of the molecular backbone.

In our case, to calculate N, we calculate the number of π electrons along the conjugation path. For example, in the case of the trimer, N is equal to 20 (12 electrons from the phenyl rings, 4 electrons from between the successive phenyl rings and 4 electrons from the two oxygen atoms). The red line in Fig. 4.5 shows the path along which the electrons are counted for the trimer.

As already mentioned above, L can be computed in two ways:[35] (1) measuring the distance between the oxygen atoms in the alkoxy chains attached to the terminal phenyl rings, i.e., setting $L = d_{\mathrm{O-O}}$, or (2) calculating the sum of the bond lengths along the conjugation path (the red line in Fig. 4.5), $L = d_{\mathrm{sum}}$. In the literature, the second method is the most common way to calculate the conjugation length for such molecules. We have calculated $E_{\mathrm{g}}^{\mathrm{1Dbox}}$ using Eq. (4.3) (for the molecules shown in Fig. 4.2) and compared these results with $E_{\mathrm{g}}^{\mathrm{DFT}}$, the HOMO-LUMO gap obtained using DFT (see Fig. 4.6). We see that $E_{\mathrm{g}}^{\mathrm{1Dbox}}$ correlates approximately linearly with $E_{\mathrm{g}}^{\mathrm{DFT}}$, when $E_{\mathrm{g}}^{\mathrm{1Dbox}}$ is calculated using both $L = d_{\mathrm{O-O}}$ and $L = d_{\mathrm{sum}}$. Discrepancies between the two are to be expected given the simplicity of the model used, but we see that to a large extent, the basic physics and chemistry involved in the change in HOMO-LUMO gap with the length of the central backbone are captured by the simple particle-in-a-box model.

To summarize the results in this section, $E_{\mathrm{g}}^{\mathrm{DFT}}$ decreases with the conjugation length as one goes from the trimer to the hexamer for PE molecules, and these results can be explained by a simple particle in a box model. Previous authors found

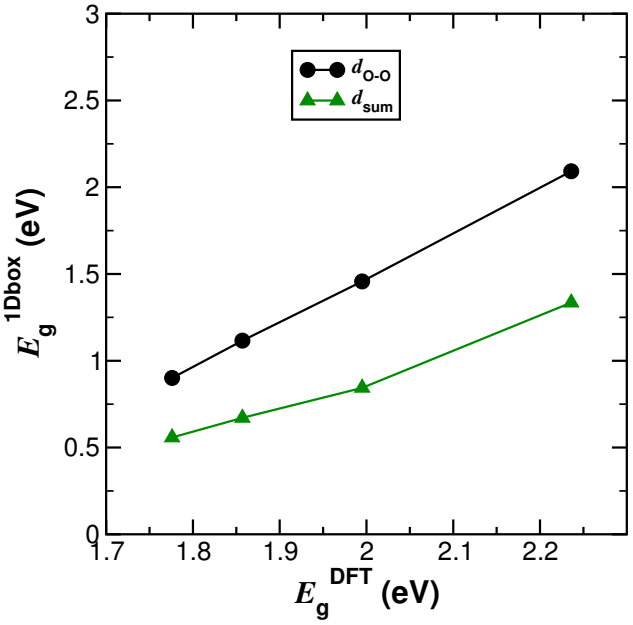

Figure 4.6: Correlation between E_g^{1Dbox} and E_g^{DFT} for different values of d. The values of E_g^{1Dbox} are calculated using particle in a 1D box model and E_g^{DFT} are the HOMO-LUMO gap calculated from DFT. The black squares show the results when E_g^{1Dbox} is calcualted using d_{O-O}, i.e., the distance between the oxygen atoms. The data corresponding to the green triangles are calclulated by taking the sum over all the bond lengths along the molecular backbone.

similar results for the HOMO-LUMO gap vs. conjugation length for various linear organic molecules (including phenyleneethynylene) and organic dyes.[36–38] Thus, the congugation length can work as a descriptor to predict the HOMO-LUMO gap of the molecules.

Molecules with Different Number and Attachment sites of Alkoxy Chains

After studying how HOMO-LUMO gap of the PE molecules changes upon varying the molecular length, we next want to investigate whether and how this gap depends on the number of alkoxy chains and/or their attachment sites. For this purpose, we have considered six PE molecules, varying the number and attachment sites of the alkoxy chains (recall Fig. 4.3). The six PE molecules shown in Fig. 4.3 are studied using both experiments and DFT calculations.

We calculate the HOMO-LUMO gap of PE molecules using both PBE and B3LYP (hybrid) functionals. Since standard DFT with PBE always underestimates the

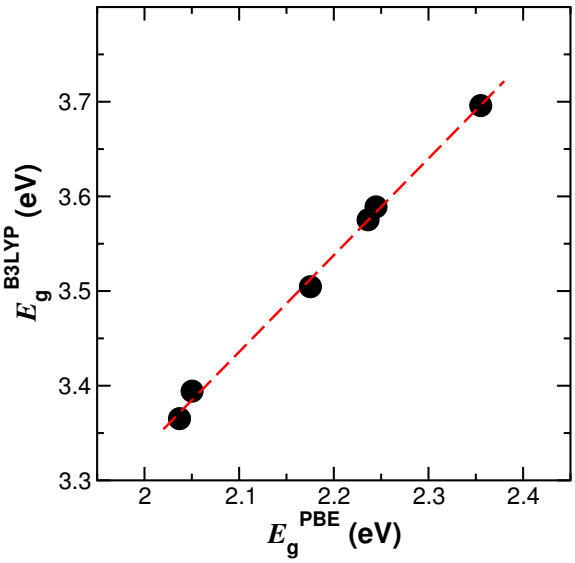

Figure 4.7: E_g^{B3LYP} vs. E_g^{PBE} plot for PE1, PE2, PE3, PE4, PE5 and PE6. HOMO-LUMO gap of the PE molecules calculated using B3LYP functional correlate well with the gap calculated using PBE functional. This implies both these functionals give the same trend of E_g qualitatively.

HOMO-LUMO gap compared to the experiments, in order to obtain better values of the gap we have also used the B3LYP functional, despite its greater computational cost.

In Fig. 4.7 we plot E_g^{B3LYP}, the HOMO-LUMO gap obtained using the B3LYP functional and standard DFT, vs. E_g^{PBE}, the gap obtained using the PBE functional and standard DFT. We see that E_g^{B3LYP} and E_g^{PBE} correlate linearly with each other. This implies that the qualitative trend in E_g remains the same but the numerical values of E_g are different for these two functionals (the HOMO-LUMO gap for each PE molecule obtained using the B3LYP functional is significantly larger than the gap obtained using PBE). This is an encouraging result, since it suggests that if we are primarily interested in looking for trends, it should suffice to perform the less-expensive PBE calculations (as we will do, later, when these molecules are deposited on graphene).

Next, we do one step better: we calculate the HOMO-LUMO gap of the six molecules using time-dependent density functional theory (TDDFT) and the B3LYP functional. From Fig. 4.8 we see that, once again, $E_g^{B3LYP\ TDDFT}$, the gap obtained

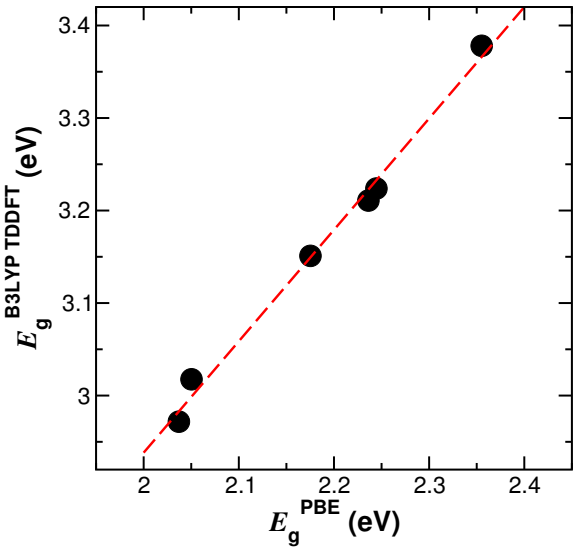

Figure 4.8: $E_g^{B3LYPTDDFT}$ vs. E_g^{PBE} plot for PE1, PE2, PE3, PE4, PE5 and PE6. E_g calculated using TDDFT with B3LYP functional varies linearly with E_g calculated using PBE functional in standard DFT technique.

using the TDDFT calculations together with the B3LYP functional, correlates linearly with E_g^{PBE}. So, we can say that the trend in HOMO-LUMO gaps for the different PE molecules remains the same but the E_g values obtained using these two different techniques (standard DFT and TDDFT) are different. Once again, this is a very encouraging result, showing that in order to obtain trends, it should suffice to perform standard DFT calculations making use of the PBE functional.

In experiments, the HOMO-LUMO gap of the different PE molecules is obtained from optical absorption spectroscopy, where the PE molecules are dissolved in the chloroform solvent. Fig. 4.9 shows the absorption spectra of different PE molecules obtained from both theory (red curve) and experiment (black curve). We see two distinct peaks in the absorption spectra for the PE2 and PE6 molecules, Figs. 4.9(b) and (f). In contrast, the absorption spectra of PE1 and PE3 contain one sharp peak, see Figs. 4.9(a) and (c). The absorption spectra of both PE4 shows one peak with higher intensity and another peak with lower intensity [Figs. 4.9(d)]. In the case of PE5, we see one peak with higher intensity and one shoulder at smaller wavelength from the experimental absorption spectrum, while the spectrum obtained from DFT shows only one peak, see Fig. 4.9(f). The absorption spectrum for each molecule can

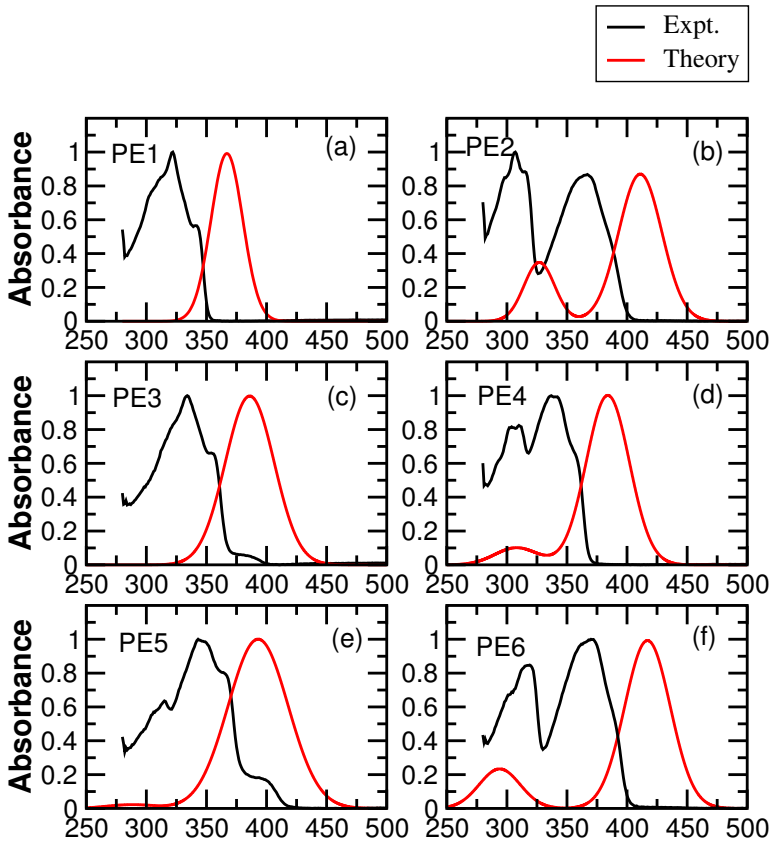

Figure 4.9: Experimental (black curves) and theoretical (red curves) absorption spectra of PE1, PE2, PE3, PE4, PE5, and PE6 molecules. One sharp peak is observed for PE1 and PE3. The absorption spectra of PE2 and PE6 show two strong peaks. In the case of PE4 one stronger and one weaker peak is observed. Experimental spectrum of PE5 shows one stronger peak and one shoulder (at smaller wavelength regime), while the spectrum obtained from theory shows only one peak.

be explained from the results obtained using TDDFT, as reported in Table 4.1.

When any atom or molecule interacts with an external electromagnetic field, it undergoes a transition from an initial state to a final state, with the energy difference between the states equal to the energy of the incident radiation. The transition dipole moment and oscillator strength are important to understand the optical spectra. The transition dipole moment is the electric dipole moment associated with the transition between the two states of a system. When the value of the transition dipole moment is finite, then the transition is possible, and when it becomes zero then the transition is not possible. The oscillator strength is a dimensionless quantity which measures the probability of transition. The higher is the value of the oscillator strength for

Table 4.1: Transition state(s), transition dipole moment, oscillator strength and the maximum wavelength corresponding to the transition, λ_{max} of PE1, PE2, PE3, PE4, PE5 and PE6 calculated using TDDFT.

Molecule	Transition state	Transition Dipole moment a.u.	Oscillator strength	λ_{max} (nm)
PE1	HOMO $\rightarrow$ LUMO	5.10	2.11	367
	HOMO$-1 \rightarrow$ LUMO	0.00	0.00	295
PE2	HOMO $\rightarrow$ LUMO	4.42	1.45	411
	HOMO$-1 \rightarrow$ LUMO	1.57	0.57	327
PE3	HOMO $\rightarrow$ LUMO	5.56	2.41	386
	HOMO$-1 \rightarrow$ LUMO	0.00	0.00	319
PE4	HOMO $\rightarrow$ LUMO	4.88	1.88	384
	HOMO$-1 \rightarrow$ LUMO	1.38	0.19	308
PE5	HOMO $\rightarrow$ LUMO	4.41	1.79	393
	HOMO$-1 \rightarrow$ LUMO	0.61	0.04	288
PE6	HOMO $\rightarrow$ LUMO	4.16	1.53	417
	HOMO$-1 \rightarrow$ LUMO	1.57	0.36	294

a transition, the larger would be intensity of the peak observed in the absorption spectrum.

The states participating in the transition are shown in column two of Table 4.1. The transition dipole moment, oscillator strength, and the maximum wavelength (λ_{max}) corresponding to the transition for each PE molecule are reported in columns three, four and five, respectively in Table 4.1.

In the case of PE1 and PE3, from the values of transition dipole moment and oscillator strength we can see the transition occurs from the HOMO to LUMO state. Therefore, the sharp peak in the absorption spectra of PE1 appears due to the transition from HOMO to LUMO state, recall Fig. 4.9(a). For PE2 and PE6, comparing the values of transition dipole moment and oscillator strength for the transition from HOMO to LUMO and HOMO-1 to LUMO we find both these transitions are almost equally favorable, though the probability of HOMO to LUMO transition is slightly higher than HOMO-1 to LUMO. Therefore, the two strong peaks appearing in the absorption spectra of PE2 and PE6 are attributed to the transition from HOMO to LUMO and HOMO-1 to LUMO.

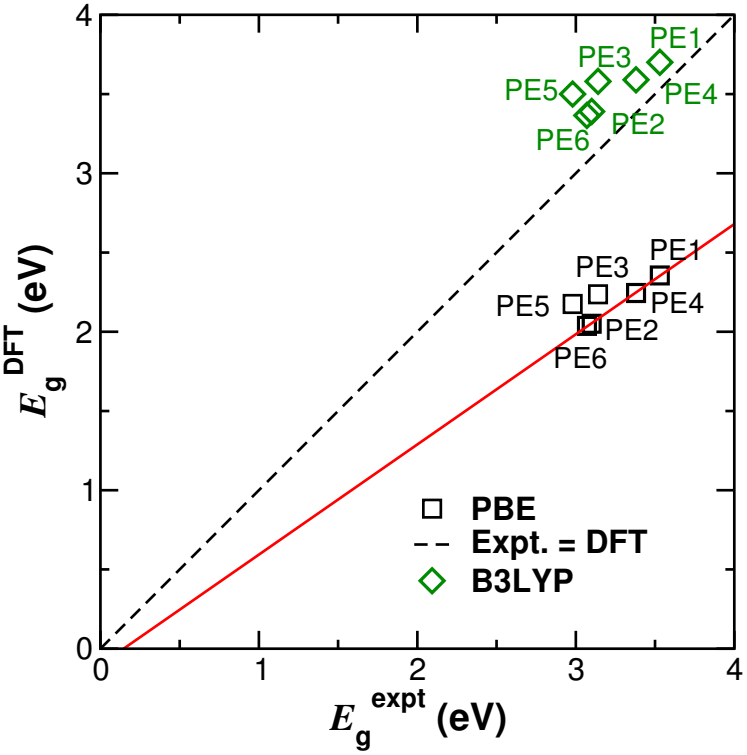

Figure 4.10: Plot of E_g^{DFT} as a function of E_g^{expt}. The black squares and green diamonds show the E_g^{DFT} values calculated using PBE and B3LYP fuctionals, respectively. The black dashed line indicates the ideal situation when the experimental gap becomes equal to the HOMO-LUMO gap obtained from DFT.

From Table 4.1, we find that in the case of PE4 and PE5 the transition from HOMO to LUMO has higher probability than the transition from HOMO−1 to LUMO, since the values of transition dipole moment and oscillator strength are much higher for HOMO to LUMO transition. For this reason in Figs. 4.9(d) and (e) we see one strong peak and one weak peak. Though the wavelengths corresponding to the absorption spectra obtained using TDDFT results differ (by $\approx$ 25 nm) from the experimental wavelengths as seen from Fig 4.9 the nature of both the spectra are found to be quite similar. This mismatch in wavelengths between the theoretical and experimental absorption spectra are typical, and have been reported by previous authors also.[39, 40]

We find that the absorption spectra of the PE molecules depend on the attachment site and the number of the alkoxy chains. Both PE2 and PE6 have two alkoxy chains attached to the central phenyl ring and they have two sharp peaks in the absorption

spectra caused by the transitions from HOMO−1 to LUMO and HOMO to LUMO. Therefore, the alkoxy chains attached to the central ring are responsible for the presence of two large transition dipoles, which in turn cause transitions from HOMO to LUMO and HOMO−1 to LUMO. PE4 and PE5 have one and three alkoxy chains, respectively. Both of them have one alkoxy chain attached to the central phenyl ring. Therefore, the dipole moment generated in PE4 and PE5 due to the interaction between the electron density and the electromagnetic radiation is such that the probability of transition from HOMO to LUMO is much higher than HOMO−1 to LUMO. PE1 and PE3 have no alkoxy chain attached to the central phenyl ring, and both of them have only one sharp peak. The absence of an alkoxy chain attached to the central ring leads to there being a strong transition from the HOMO to LUMO state only. These results imply that the attachment sites of the alkoxy chains plays an important role in determining the nature of the absorption spectra of the PE molecules.

We compare the HOMO-LUMO gap of the PE molecules obtained from the experimental absorption spectra with the gap calculated using standard DFT and different functionals. In Fig. 4.10 we check whether there is a correlation between $E_{\mathrm{g}}^{\mathrm{DFT}}$ and $E_{\mathrm{g}}^{\mathrm{expt}}$. The black squares and green diamonds show the DFT results obtained using PBE and B3LYP functionals, respectively. From Fig. 4.10, we that see the values of $E_{\mathrm{g}}^{\mathrm{DFT}}$ indicated by the black squares lie much below the green diamonds, however they both show the same qualitative trend when compared to $E_{\mathrm{g}}^{\mathrm{expt}}$. The black dashed line indicates the condition when the DFT values would become exactly same as the experimental values. We can clearly see the green diamonds lie much closer to the dashed black line, therefore, as expected, the HOMO-LUMO gaps of the PE molecules obtained using the B3LYP functional lie much closer to the experimental values than those obtained using the PBE functional.

In Fig. 4.11, we look for a correlation between $E_{\mathrm{g}}^{\mathrm{DFT}}$ calculated using standard DFT (PBE functional) and TDDFT (B3LYP functional), shown by the black squares and

purple triangles, respectively. The purple triangles lie close to the dashed black line which indicates the situation of correlation between the experimental and theoretical HOMO-LUMO gap. If we compare between the green diamonds and purple triangles in Figs. 4.10 and 4.11, respectively then we see that (as expected) the HOMO-LUMO gap obtained from TDDFT agrees better with experiment than the $E_{\rm g}^{\rm DFT}$ calculated using standard DFT and the B3LYP functional.

Note that in all cases, the variation in HOMO-LUMO gap between the six molecules considered in this section is rather small, considerably less than the variations observed on going from the trimer to the hexamer in the previous section.

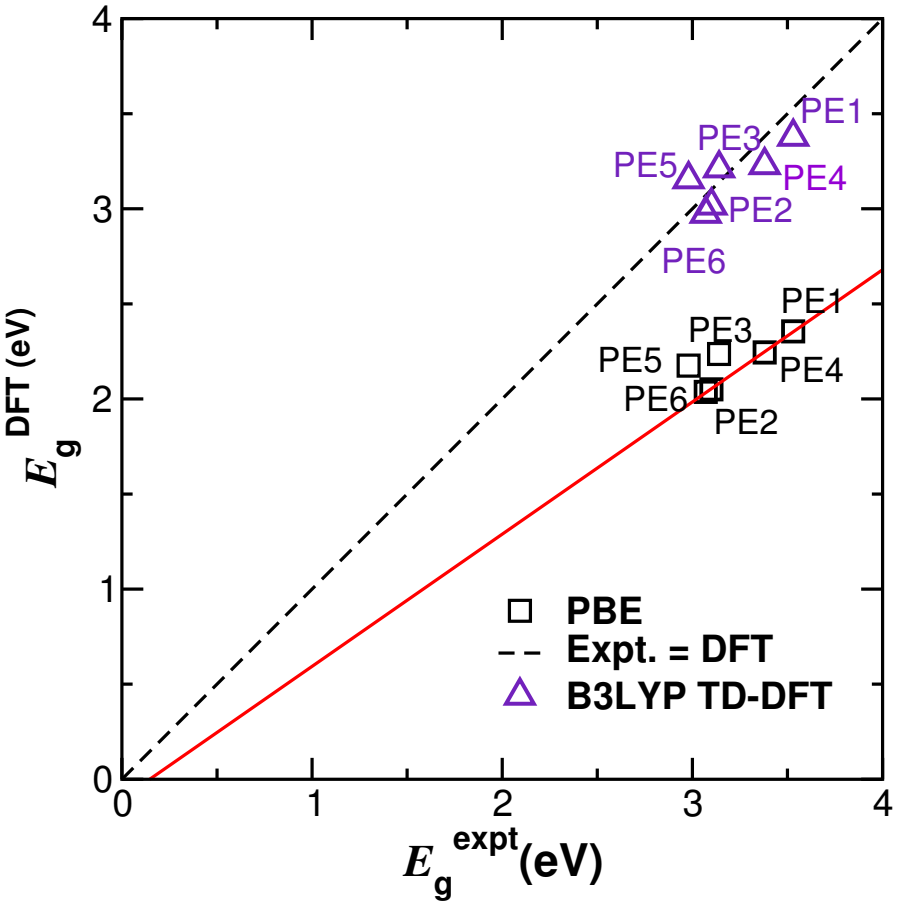

Figure 4.11: Plot of $E_{\rm g}^{\rm DFT}$ vs. $E_{\rm g}^{\rm expt}$. The black squares and purple triangles show the results for $E_{\rm g}^{\rm DFT}$ calculated using standard DFT with PBE functional and TDDFT with B3LYP fuctionals, respectively. The balck dashed line indicates the ideal situation when the experimental and DFT gaps become equal.

Descriptor

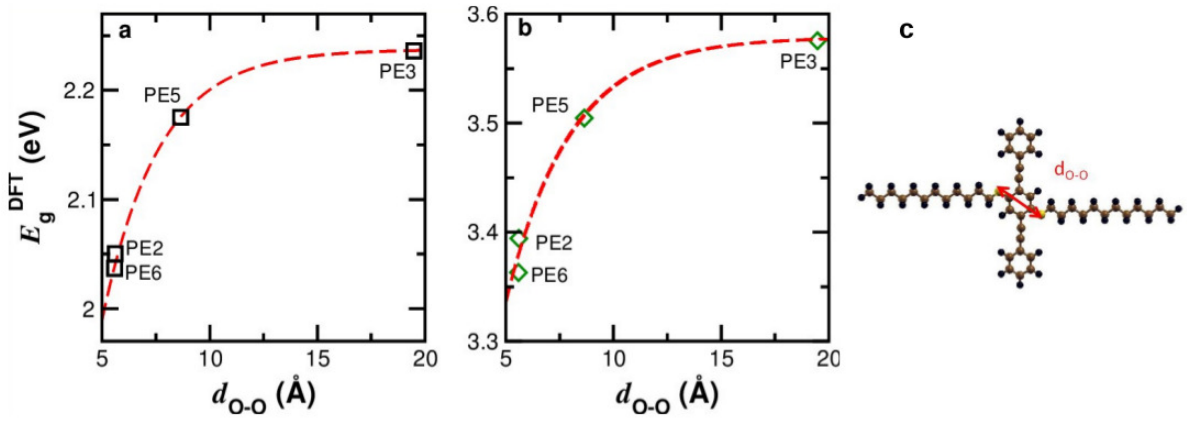

Figure 4.12: Plot of E_g^{DFT} as a function of the descriptor d_{O-O}. E_g^{DFT} is calculated using (a) PBE and (b) B3LYP. (c) Atomistic structure of PE2. The red arrow shows the shortest distance between the oxygen atoms, d_{O-O} for PE2. Color scheme: C, brown, H: balck and O, yellow. The functional form of the red dahsed line in (a) and (b) is: $y = A[1 - e^{-k(x-x_0)}]$.

As we have already mentioned, the length of the molecular backbone is the same for all the six molecules, but they have a different number of alkoxy side chains, with various attachment sites. Therefore, it is likely that the alkoxy chains play a key role in tuning the HOMO-LUMO gap of the PE molecules, since the number and attachment site of the alkoxy chains are the variables in this case. The oxygen atom in an alkoxy chain has two lone pairs of electrons. These electron lone pairs participate in the conjugation with the phenyl rings and the backbone of the molecule. Conjugation causes delocalization of electrons. The jigher is the delocalization. lower would be the HOMO-LUMO gap of the molecule. Note that, from both the DFT and experimental results we see that PE1 has the highest HOMO-LUMO gap of the six PE molecules considered in this section. PE1 has no alkoxy chain, which leads to less electron delocalization and therefore the highest HOMO-LUMO gap.

We find the HOMO-LUMO gap of the PE molecules depends on the shortest distance between the oxygen atoms, d_{O-O}. As d_{O-O} reduces, the value of E_g decreases. In Figs. 4.12 (a) and (b) we plot E_g^{DFT} as a function of d_{O-O} using PBE and B3LYP functionals, respectively. The values of E_g^{DFT} obtained using both these funcitonals show exactly similar trend with d_{O-O}. Fig. 4.12(c) shows one example of how d_{O-O}

is measured. Therefore, the HOMO-LUMO gap of PE molecules can be predicted using $d_{\mathrm{O-O}}$. The higher the value of $d_{\mathrm{O-O}}$, the larger would be the HOMO-LUMO gap. The functional form of the red dashed lines, i.e., the fit to the $E_{\mathrm{g}}^{\mathrm{DFT}}$ vs. $d_{\mathrm{O-O}}$ plot in Figs. 4.12(a) and (b) is given by: $y = A[1 - e^{-k(x-x_0)}]$, where A, k and x_0 are constants. This is a striking and somewhat unexpected result. Based on organic chemistry or simple quantum mechanical models, it is not clear why only the shortest O-O distance should matter. We have attempted to build quantum mechanical models (modifications of the particle in the box model) to explain this result, but have not succeeded thus far. So at present, our finding should be considered in the nature of having empirically found a simple descriptor, $d_{\mathrm{O-O}}$, with which the value of the HOMO-LUMO gap correlates. To know the contribution of each atomic orbital to each molecular state we plot the projected density of states (PDOS) of the PE molecules in Fig. 4.13. From the PDOS plots we see that the oxygen atoms (green curve) provide a major contribution to the occupied states (including HOMO and HOMO-1 states) of the molecules. The HOMO-1, HOMO, and LUMO states of the PE molecules are plotted in Figs. 4.14– 4.19.

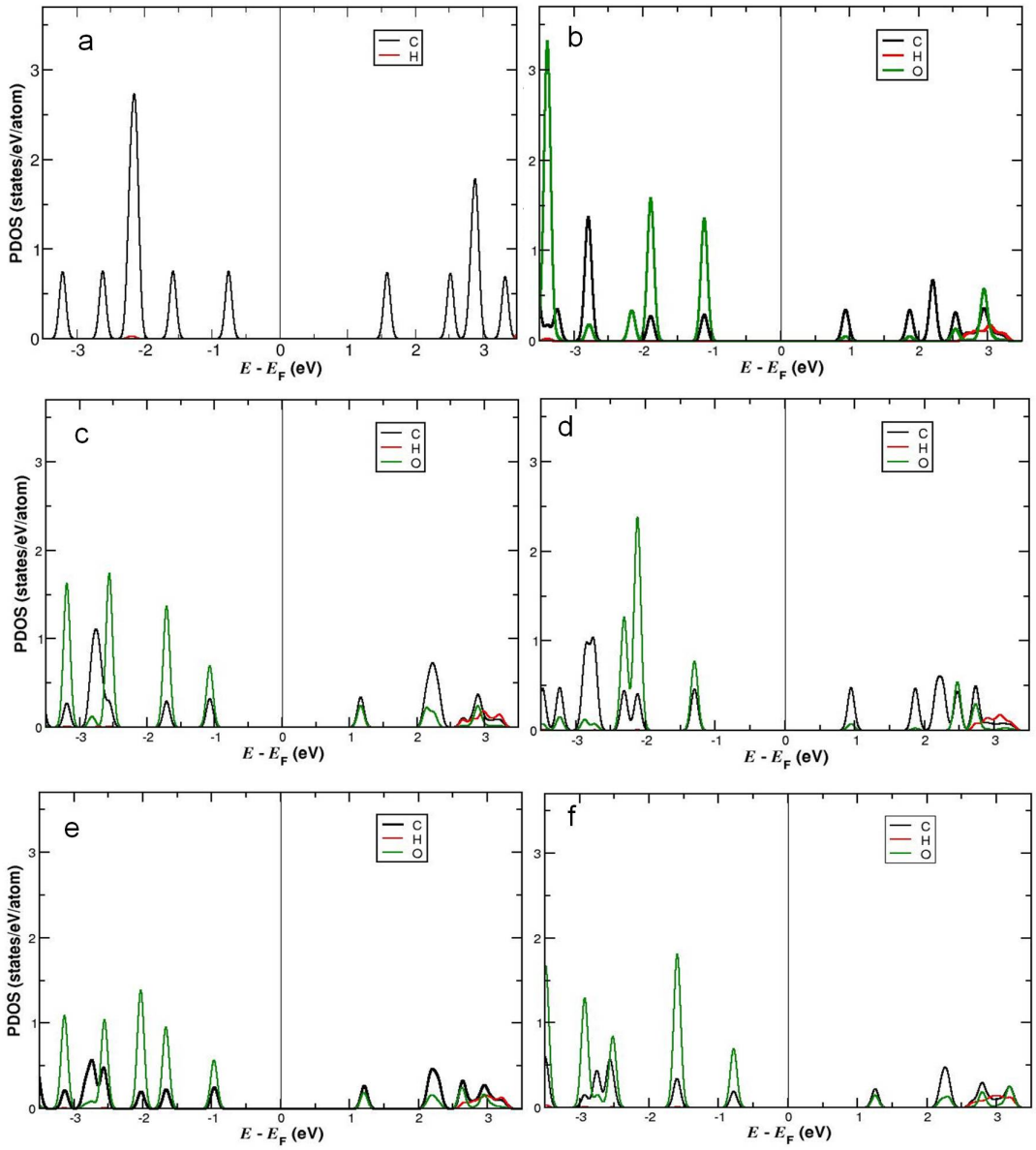

Figure 4.13: The projected density of states (PDOS) plots for isolated PE molecules in the gas phase. The black, red and green curves show the contribution of the C, H and O atoms, respectively to the PDOS of the molecule. PDOS of (a) PE1, (b) PE2, (c) PE3, (d) PE4, (e) PE5 and (f) PE6. The sharp δ-function peaks of the molecular density of states have been broadened using gaussians, for ease of visualization.

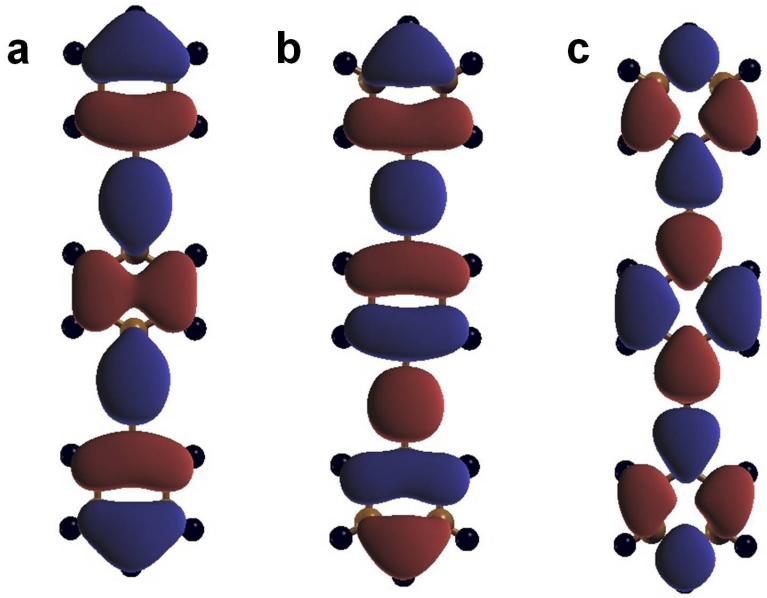

Figure 4.14: Plots of (a) HOMO−1, (b) HOMO and (c) LUMO for the isolated PE1 molecule in the gas phase. The red and blue lobes indicate opposite phases of the wavefunction drawn at the isosurface value 0.03 e/bohr^3.

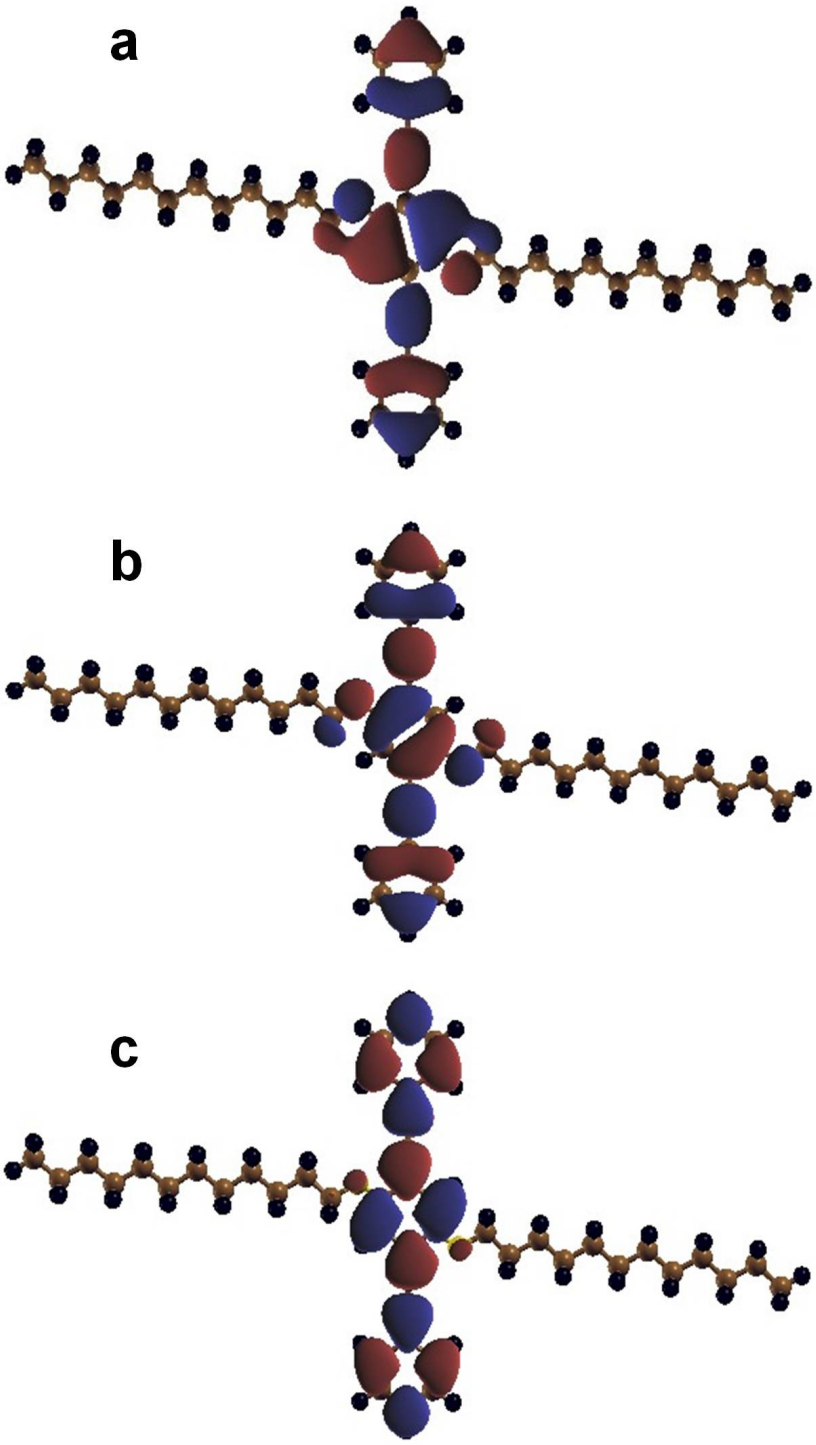

Figure 4.15: Plots of (a) HOMO−1, (b) HOMO and (c) LUMO for the isolated PE2 molecule in the gas phase. The red and blue lobes indicate opposite phases of the wavefunction drawn at the isosurface value 0.03 e/bohr^3.

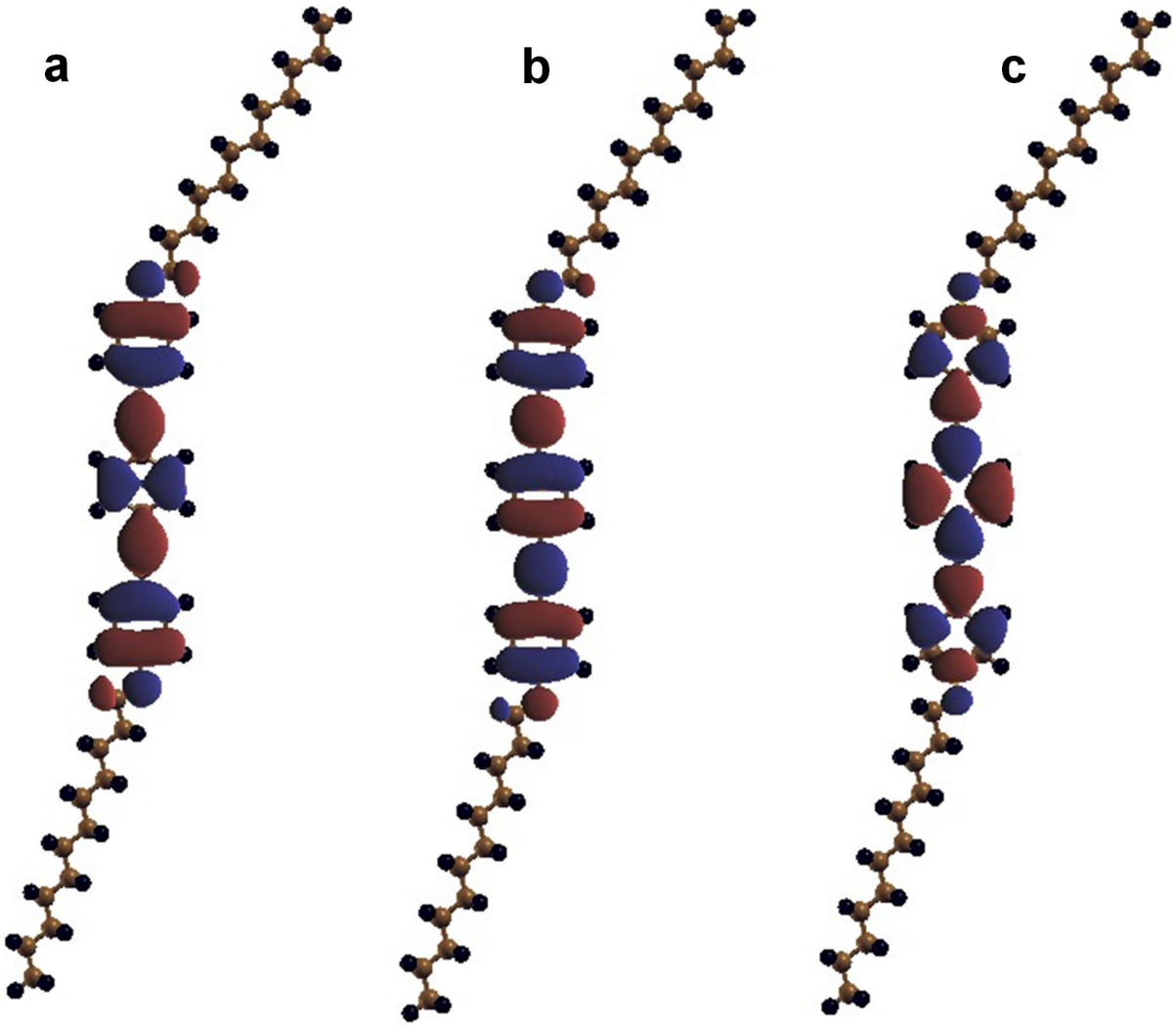

Figure 4.16: Plots of (a) HOMO−1, (b) HOMO and (c) LUMO for the isolated PE3 molecule in the gas phase. The red and blue lobes indicate opposite phases of the wavefunction drawn at the isosurface value of 0.03 e/bohr^3.

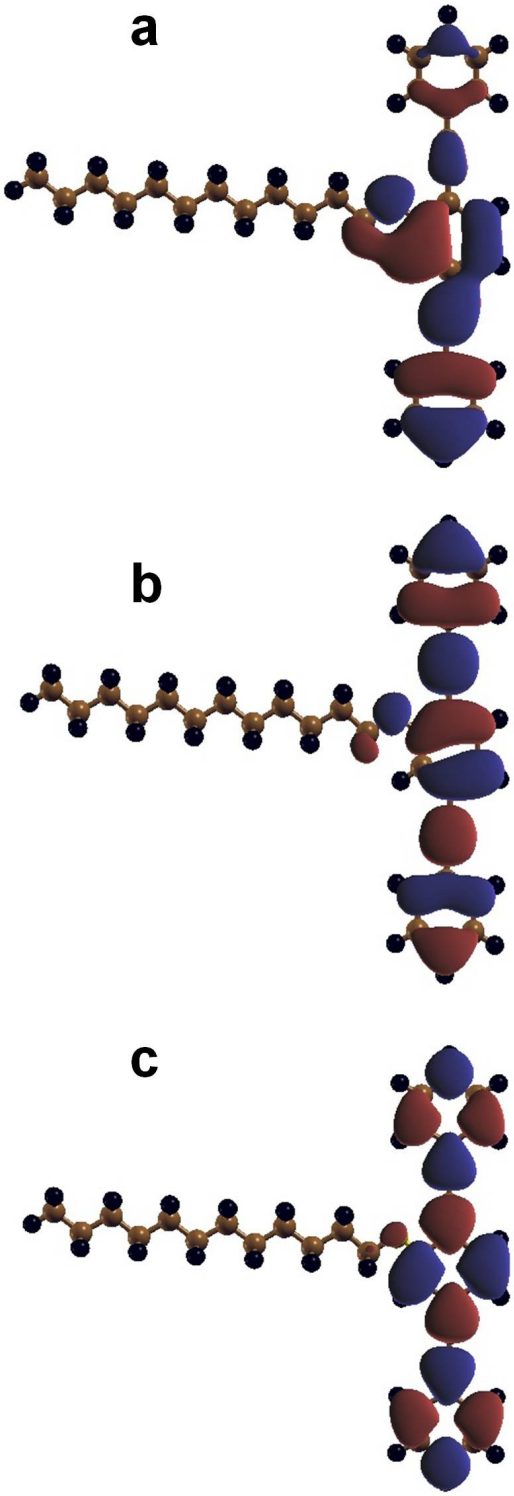

Figure 4.17: Plots of (a) HOMO−1, (b) HOMO and (c) LUMO for the isolated PE4 molecule in the gas phase. The red and blue lobes indicate opposite phases of the wavefunction drawn at the isosurface value of 0.03 e/bohr^3.

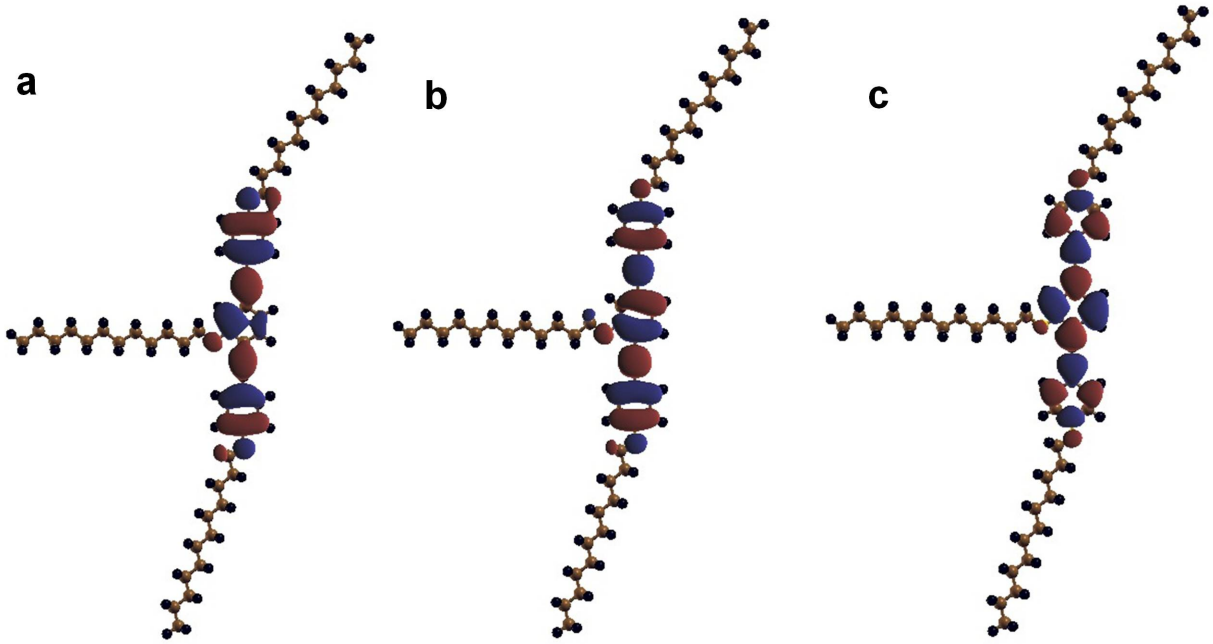

Figure 4.18: Plots of (a) HOMO−1, (b) HOMO and (c) LUMO for the isolated PE5 molecule in the gas phase. The red and blue lobes indicate opposite phases of the wavefunction drawn at the isosurface value 0.03 e/bohr^3.

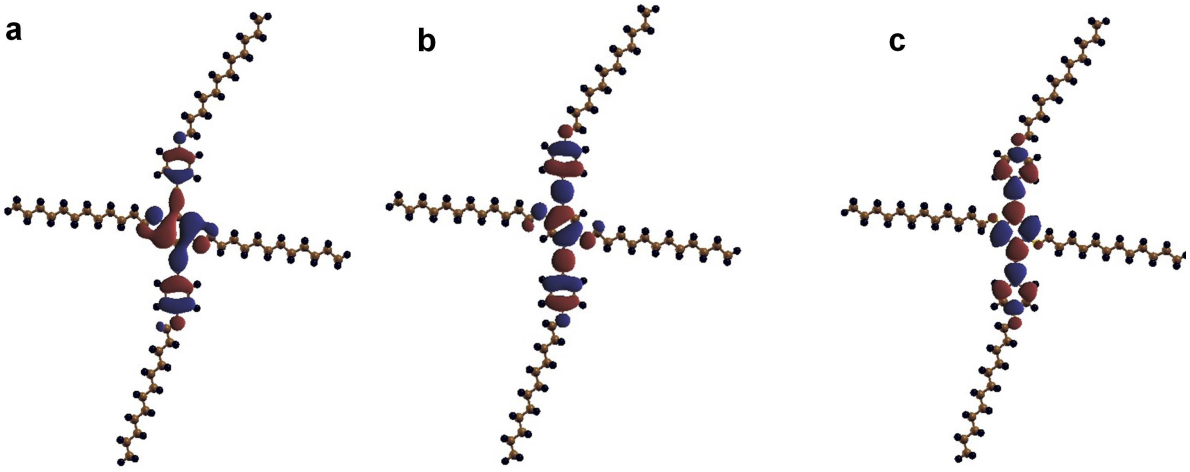

Figure 4.19: Plots of (a) HOMO−1, (b) HOMO and (c) LUMO for the isolated PE6 molecule in the gas phase. The red and blue lobes indicate opposite phases of the wavefunction drawn at the isosurface value 0.03 e/bohr^3.

Test Cases

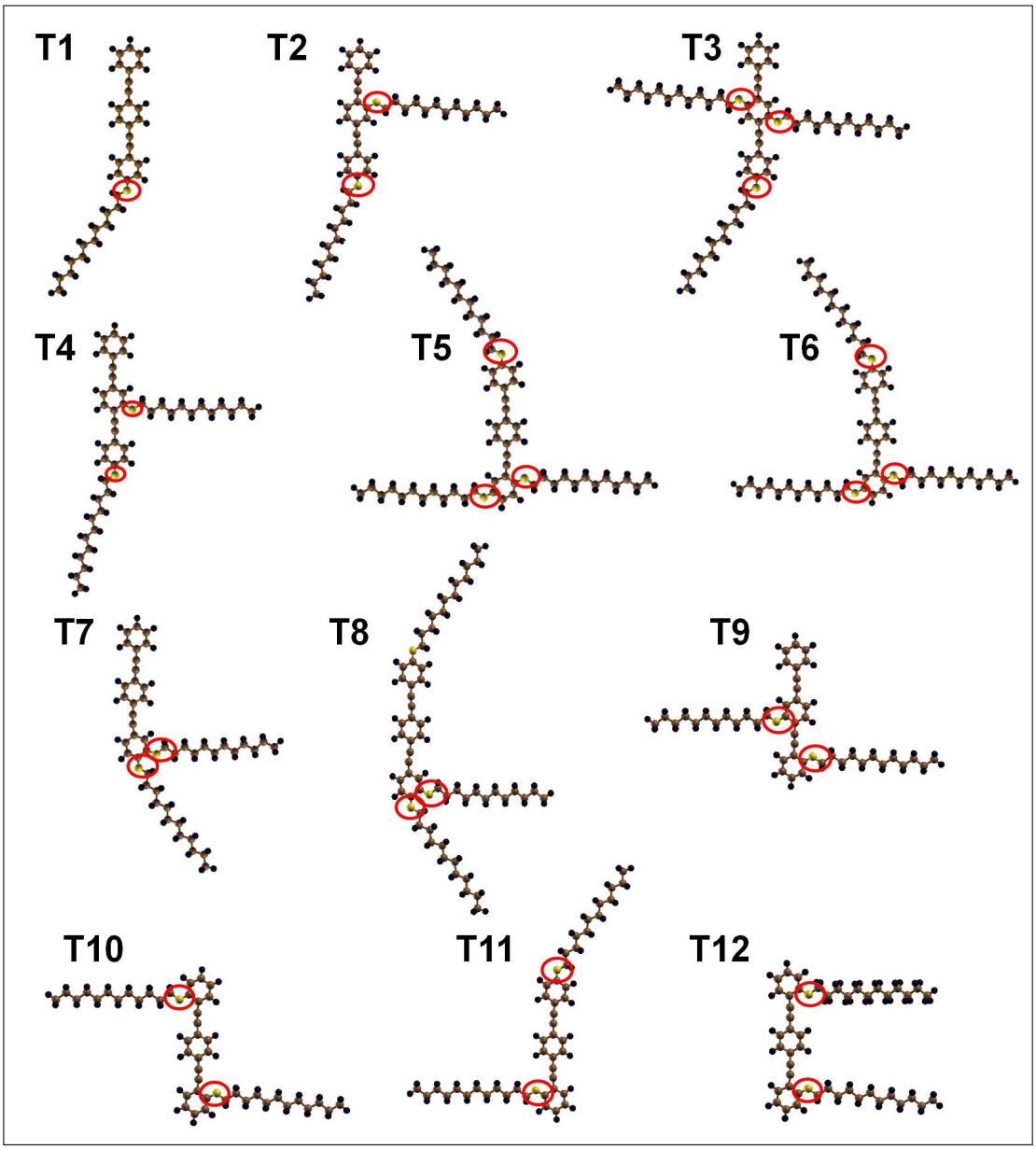

Figure 4.20: Atomistic structure of the isolated PE molecules with different number and positions of the alkoxy chains. All these molecules are considered as the "Test molecules" to proof the validation of the descriptor d_{O-O} in predicting the HOMO-LUMO gap of the PE molecules of same backbone length. Color scheme: C, brown, H: balck and O, yellow. The O atoms are circled in red.

We have found tht the shortest distance between two oxygen atoms in the alkoxy side chains present in a PE molecule acts as a descriptor to predict the HOMO-LUMO gap. This descriptor was obtained by considering a database of six PE molecules.

In order to evaluate the utility of this descriptor, we next want to verify whether this descriptor can successfully predict the HOMO-LUMO gap of other PE molecules. For this purpose, we have chosen twelve test molecules with different numbers and attachment sites of the alkoxy chains. The change in the attachment sites of the alkoxy chains in a PE molecule causes variation in the oxygen-oxygen distance. Therefore, we consider a range of d_{O-O} by changing the mutual separation of the alkoxy chains in the PE molecules.

In Fig. 4.21 we plot the HOMO-LUMO gap of all the PE molecules considered in this study, i.e., the molecules studied as the "database" and the"test molecules". The HOMO-LUMO gap of the PE molecules obtained from the standard DFT technique (using PBE functional), E_g^{DFT} as a function of the shortest oxygen-oxygen distance, d_{O-O} is plotted in Fig. 4.21. We see as d_{O-O} reduces the HOMO-LUMO gap decreases.

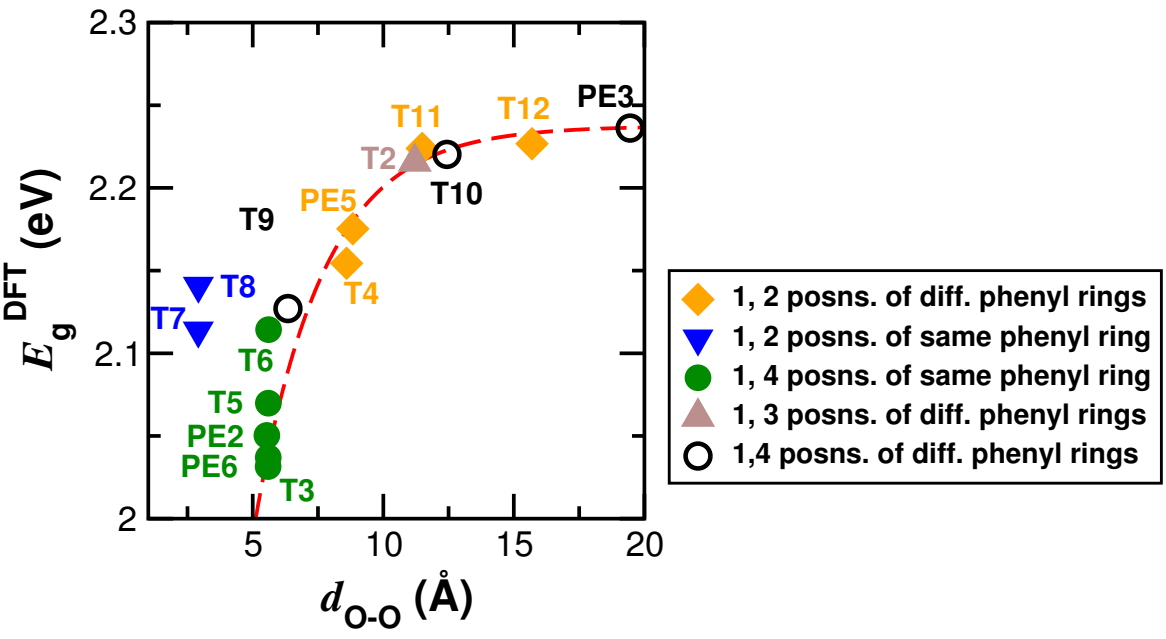

Figure 4.21: E_g^{DFT} vs. d_{O-O} plot for all the PE molecules, including the "training set" (molecules studied using both experiments and theory) and the "test molecules" (studied using DFT only). The green and black circles show the values of E_g^{DFT} when the alkoxy chains are attached to the 1, 4 positions of the same and different phenyl rings, respectively. The blue triangles and orange diamonds show the results for 1, 2 positions of alkoxy chains at the same and different phenyl rings, respectively. The brown triangle is for the PE molecule when the alkoxy chains are attached to the 1, 3 positions of different phenyl rings.

Therefore, d_{O-O} can act as a descriptor to predict the HOMO-LUMO gap of the PE molecules with same length but different value of the shortest oxygen-oxygen distance. Note that in Fig. 4.12 we have shown the results for those PE molecules which are in conjugation, i.e., the alkoxy chains are attached at either the 1, 4 or 1, 2 positions of the same or different phenyl rings. In Fig. 4.21, we see that for the green (1, 4 positions of same phenyl ring) and black circles (1, 4 positions of different phenyl rings) and the orange diamonds (1, 2 positions of different phenyl rings) E_g^{DFT} depends on d_{O-O}, with the same functional form as for the original database of six PE molecules. However, when the alkoxy chains are attached to 1, 2 positions of the same phenyl ring (see the blue triangles in Fig. 4.21) the values of E_g^{DFT} do not lie on the red dashed line.: the HOMO-LUMO gaps of "T7" and "T8" have higher values than predicted by the descriptor. This implies the conjugation is not as effective as predicted by the descriptor, in those molecules with alkoxy chains at 1, 2 positions of the same phenyl ring. This happens because the steric repulsion between the alkoxy chains at 1, 2 positions makes the lone pairs of the oxygen atoms out of plane, which spoils the conjugation. Thus, in these cases, lower conjugation increases the HOMO-LUMO gap.

Though the molecules with alkoxy chains at 1, 3 positions of the same phenyl ring should not, in principle, show conjugation, we find that when the alkoxy chains are attached to the different phenyl rings at 1, 3 positions the computed value of the HOMO-LUMO gap falls on the dashed line (see the brown triangle in Fig. 4.21 which implies that the molecule is in conjugation.

We have also done calculations for PE molecules with alkoxy chains at 1, 3 positions of the same phenyl ring but for those molecules E_g^{DFT} does not show any trend with d_{O-O}. Those results are not shown in Fig. 4.21.

It is still not clear to us why E_g shows such behavior as a function of d_{O-O}. We want to develop a quantum mechanical model to explain the form of the descriptor d_{O-O}.

4.4.2 HOMO-LUMO Gap of PE Monolayers

After calculating the HOMO-LUMO gap of the isolated PE molecules in the gas phase we want to investigate how the HOMO-LUMO gap changes when the molecules form a monolayer. To study the self-assembly of PE2, PE4, PE5 and PE6 in the gas phase and on graphene (not PE1 and PE3). To perform DFT calculations we consider the geometry of the self-assembled patterns observed in the STM experiments as the srating guess. The optimization of unit cell size and atomic coordinates are done to determine the lowest energy configuration for each molecular assembly.

We exclude PE1 and PE3 molecules while studying the self-assembled patterns. PE1 could not form any pattern on highly oriented pyrolitic graphite (HOPG) due to faster adsorption-desorption of the molecules from HOPG. Here lies the importance of the alkoxy group which is important for the molecule-molecule and molecule-substrate interactions to stabilize the molecular self-assembly on graphene. The absence of alkoxy group prevents PE1 to form any pattern. In the case of PE3, it does not form any long-range pattern. Due to these reasons we do not consider PE1 and PE3 while investigating the HOMO-LUMO gap of molecular self-assemblies.

provide the gui PE1 does not form any self-assembled pattern

PE Monolayers in the Gas Phase

First, we study monolayers of PE2, PE4, PE5 and PE6 molecules in the gas phase. This case is studied using DFT calculations only, since this is an artificial situation – in experiments to study any property of the molecular monolayer it has to be deposited on a substrate.

The four PE molecules are found to self-assemble in different kinds of patterns. PE2 and PE4 form closely-packed monomers and dimers, respectively, which further self-assemble into a periodic pattern. Self-assembly of PE5 is comprised of dimer units, while the pattern formed by PE6 is comprised of monomer units. The self-assembled patterns formed by the PE molecules are governed by the number and positions of the alkoxy chains. PE2 and PE6 have two alkoxy chains attached to the central phenyl

ring. This alkoxy position of the alkoxy chains prevents the molecules from forming a densely packed pattern, because to avoid steric repulsion between the alkoxy chains the neighboring molecules need to maintain a distance from each other. PE4 has one alkoxy attached to the central phenyl ring, while PE5 has three alkoxy chains: two are attached to the terminal phenyl rings and one to the central phenyl ring.

The self-assembled patterns of PE2, PE4, PE5 and PE6 are shown in Figs. 4.22(a), (b), (c) and (d), respectively.

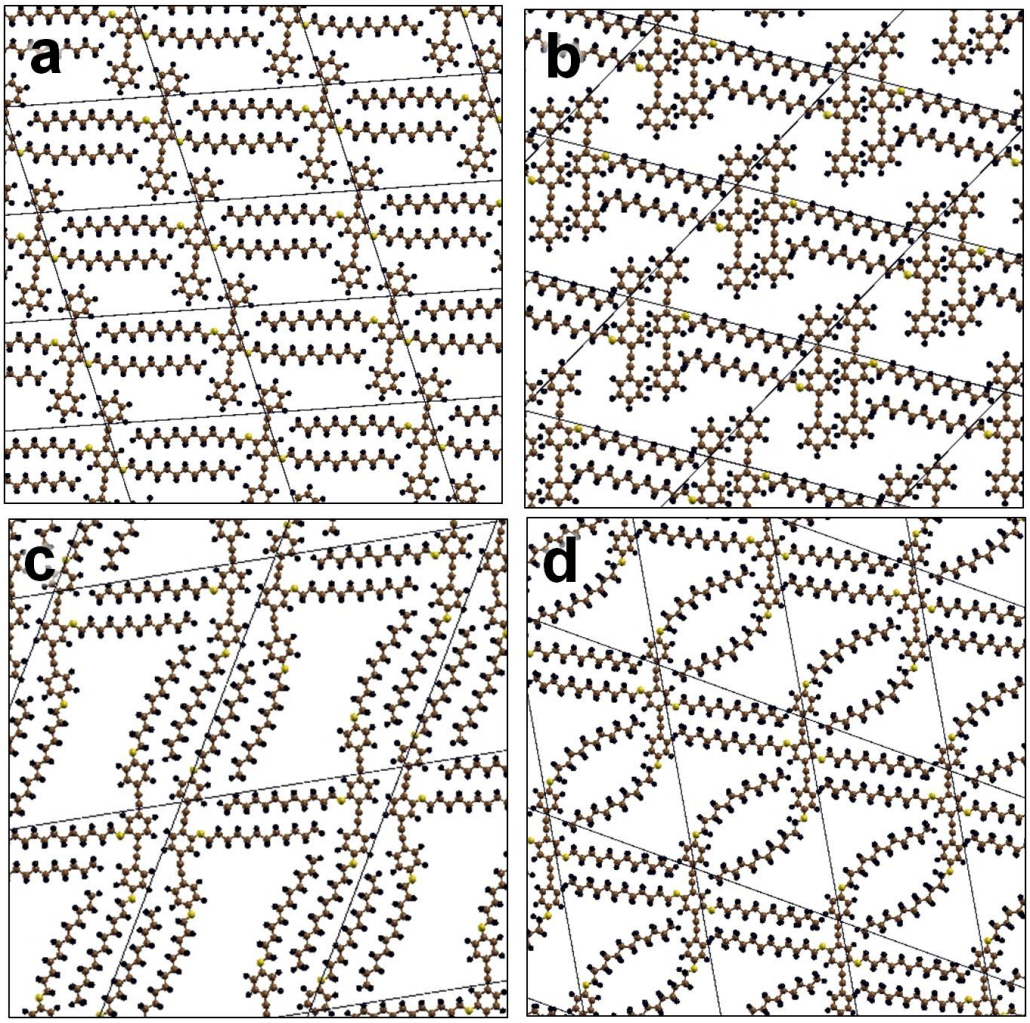

Figure 4.22: Atomistic structure of the self-assembly of PE molecules in the gas phase. Self-assembly of (a) PE2, (b) PE4, (c) PE5 and (d) PE6. Color scheme: C, brown; H, black and O: yellow. The thin black lines show the unit cell boundaries.

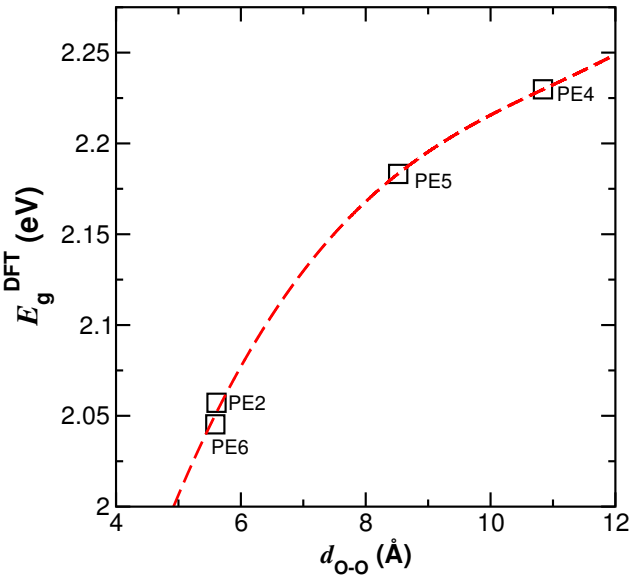

Figure 4.23: Plot of $E_{\rm g}^{\rm DFT}$ as a function of $d_{\rm O-O}$. $E_{\rm g}^{\rm DFT}$ decreases with $d_{\rm O-O}$. The functional form of the red dahsed line is: $y = A[1 - e^{-k(x-x_0)}]$, same as for Fig. 4.12.

We calculate the stabilization energy $E_{\rm stab}$ for each self-assembled pattern:

$$E_{\rm stab} = E_{\rm gas}^{\rm ML} - nE_{\rm gas}^{\rm iso}, \tag{4.4}$$

where $E_{\rm gas}^{\rm ML}$ and $E_{\rm gas}^{\rm iso}$ are the total energies of the molecular monolayer and the isolated molecule in the gas phase, respectively. n is the number of molecules present per unit cell of the assembly. The values of $E_{\rm stab}$ are calculated to be -0.94 meV/Å^2 for PE2, -2.74 meV/Å^2 for PE4, -1.476 meV/Å^2 for PE5 and -1.22 meV/Å^2 for PE6. The self-assembled patterns of the PE molecules get stabilized by several weak interactions, e.g., the aromatic CH–π, alkyl CH-acetylene π and alkyl CH-aromatic π interactions. The strength of these interactions is found to vary from -70 to -180 meV, where the negative sign indicates an attractive interaction.

Next, we calculate the electronic structures and band gaps of the self-assembled monolayers of the PE molecules in the gas phase. In Fig. 4.23 $E_{\rm g}^{\rm DFT}$ is plotted as a function of $d_{\rm O-O}$. The values of the HOMO-LUMO gaps of the monolayers of PE molecules in the gas phase are found to remain almost the same as for the isolated molecules in the gas phase. In the case of the monolayers also, $E_{\rm g}^{\rm DFT}$ is found to

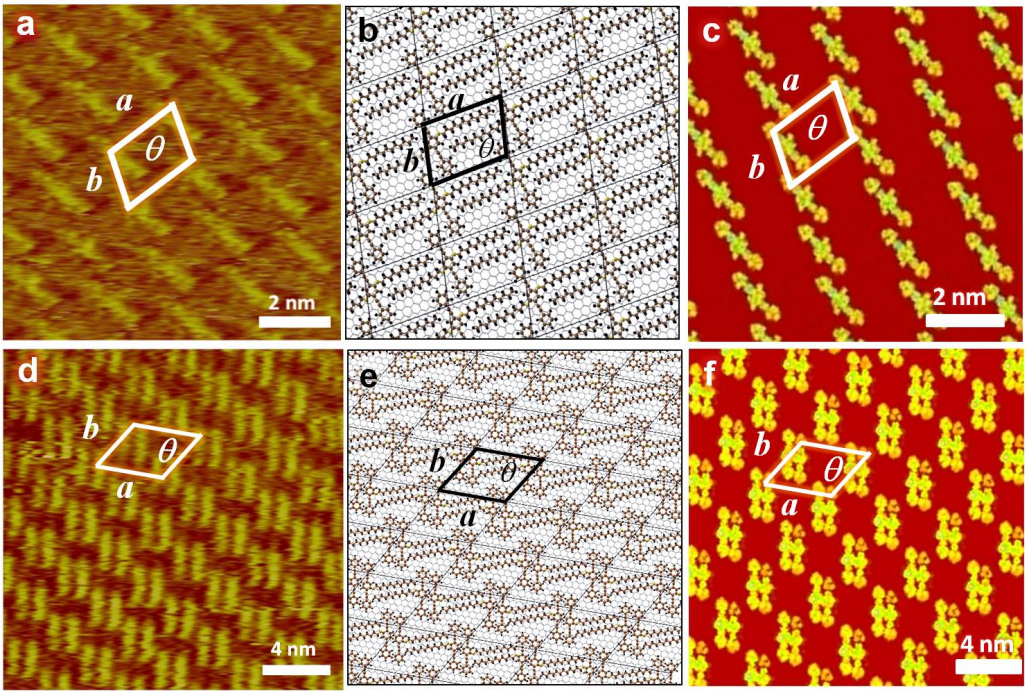

Figure 4.24: Experimental STM images, atomistic structures and simulated STM images of the self-assembly of PE molecules on HOPG/graphene. Experimental STM images of the monolayer of (a) PE2 (V_{bias} =−890 mV, I_t = 250 pA) and (d) PE4 (V_{bias} =−1500 mV, I_t = 102 pA), respectively on HOPG. Atomistic structures of Self-assembly of (b) PE2 and (e) PE4 on graphene. Color scheme: C, brown; H, black and O: yellow. Simulated STM iamges of (c) PE2 and (f) PE4 on graphene at V_{bias} =−2V in constant-height mode with tip-sample distance = 5 Å. The thin black and white lines show the unit cell boundaries. a, b and θ are the unit cell parameters.

depend on $d_{\text{O-O}}$. Note that for PE4 (which has only one alkoxy side chain per molecule) $d_{\text{O-O}}$ is the distance between the oxygen atoms in the PE4 dimer, with the two oxygen atoms belonging to different molecules.

PE Monolayers on Graphene

Finally, we study the self-assembly of PE molecules deposited on graphene using both DFT and experiments.

The adsorption energy E_{ads} of the PE molecules on graphene is given by:

$$E_{\text{ads}} = E_{\text{G}}^{\text{ML}} - nE_{\text{gas}}^{\text{iso}} - E_{\text{G}} \tag{4.5}$$

where E_{G}^{ML} and E_{G} are the total energies of the self-assembled monolayer of PE

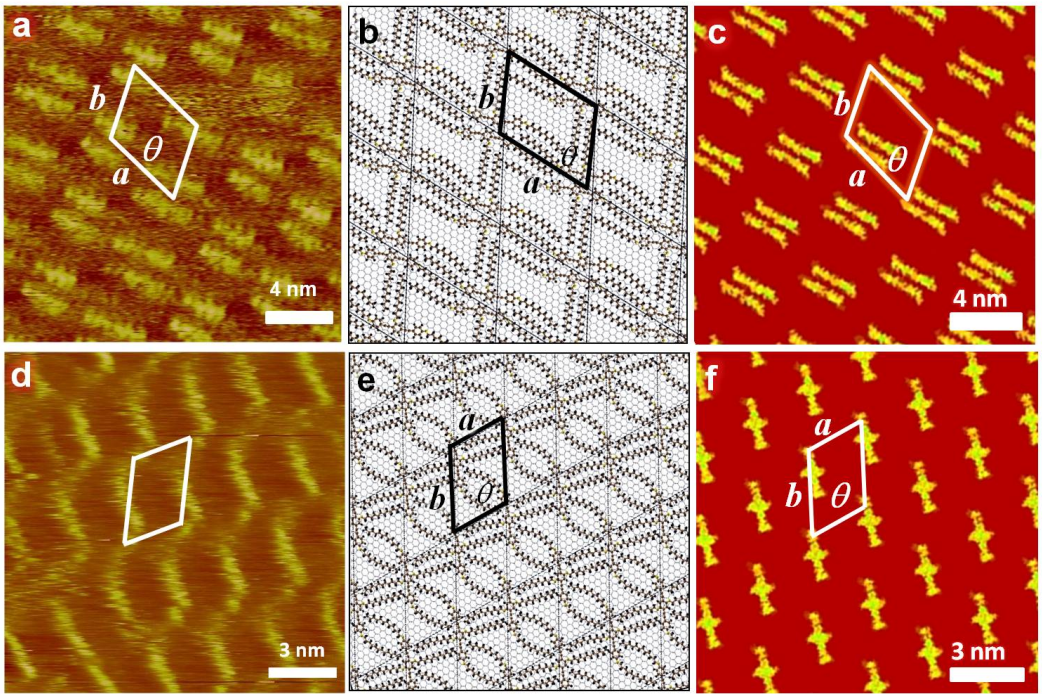

Figure 4.25: Experimental STM images, atomistic structures and simulated STM images of the self-assembly of PE molecules on HOPG/graphene. Experimental STM images of the monolayer of (a) PE5 (V_{bias} =−1500 mV, I_t = 102 pA) and (d) PE6 (V_{bias} =−650 mV and I_t = 120 pA), respectively on HOPG. Atomistic structures of Self-assembly of (b) PE5 and (e) PE6 on graphene. Color scheme: C, brown; H, black and O: yellow. Simulated STM iamges of (c) PE5 and (f) PE6 on graphene at V_{bias} =−2V in constant-height mode with tip-sample distance = 5 Å. The thin black and white lines show the unit cell boundaries. a, b and θ are the unit cell parameters.

molecules on graphene, and the graphene monolayer, respectively. The values of E_{ads} for PE2, PE4, PE5 and PE6 are found to be −10.47 meV/Å^2, −10.39 meV/Å^2,−9.43 meV/Å^2 and −9.40 meV/Å^2, respectively.

The experimental STM images, atomistic structures and the simulated STM images of PE2 and PE4 are shown in Fig. 4.24. Fig. 4.25 shows the self-assembly of PE5 and PE6 on graphene. The simulated STM images agree well with the experimental STM images in all cases.

We calculate the HOMO-LUMO gaps of the monolayers of PE molecules adsorbed on graphene using standard DFT. We see that the HOMO-LUMO gap reduces when the molecular monolayers are adsorbed on graphene. In Fig. 4.26 we plot $E_{\text{g}}^{\text{DFT}}$ as a function of $d_{\text{O-O}}$ and we find that $E_{\text{g}}^{\text{DFT}}$ correlates well with $d_{\text{O-O}}$ when the

Table 4.2: HOMO-LUMO gap the monolayers of PE molecules adsorbed on graphene ($E_g^{ML/G}$) and in the gas phase ($E_g^{ML(gas)}$). The gap of isolated molecules in the gas phase. E_g^{iso}, HOMO-LUMO gap of the isolated PE molecules in the gas phase. $E_g^{ML/G}$ and E_g^{iso} are obtained using both DFT and experiment, while $E_g^{ML(gas)}$ is calculated using DFT only.

m	$E_g^{ML/G}$ (eV)		$E_g^{ML(gas)}$ (eV)	E_g^{iso} (eV)	
	DFT (PBE)	Expt.	DFT (PBE)	DFT (PBE)	Expt.
PE2	1.91	2.95	2.06	2.05	3.10
PE4	1.98	3.14	2.23	2.24	3.38
PE5	1.96	2.79	2.18	2.18	2.98
PE6	1.90	2.98	2.05	2.04	3.07

monolayers are deposited on graphene, see the maroon circles in Fig. 4.26. The values of E_g for the isolated molecules in the gas phase, monolayer in the gas phase and on graphene are shown in Table 4.26.

The reason behind the decrease in the HOMO-LUMO gap of PE molecules is the molecule-substrate interaction. For the self-assembly of these four PE molecules, molecule-molecule interactions are small compared to the molecule-graphene interactions. The projected densities of states plots of the self-assembled monolayers of PE2/graphene and PE4/graphene are shown in Fig. 4.27. In Figs. 4.27(b) and (d) the PDOS plots of the molecular monolayers are normalized by the number of atoms. Comparing Figs. 4.27(b) and (d) with Figs. 4.13 (b) and (d), respectively, we see that the densities of states of PE2 and PE4 change significantly upon adsorption on graphene.

4.5 Conclusions

The HOMO-LUMO gap, E_g, of the PE molecules depends on their chemical motifs, e.g., the length of the central backbone, the conjugation length, and the number and attachment sites of the alkoxy chains. When the number and attachment sites of the alkoxy chains remain constant, the HOMO-LUMO gap of the PE molecules reduces

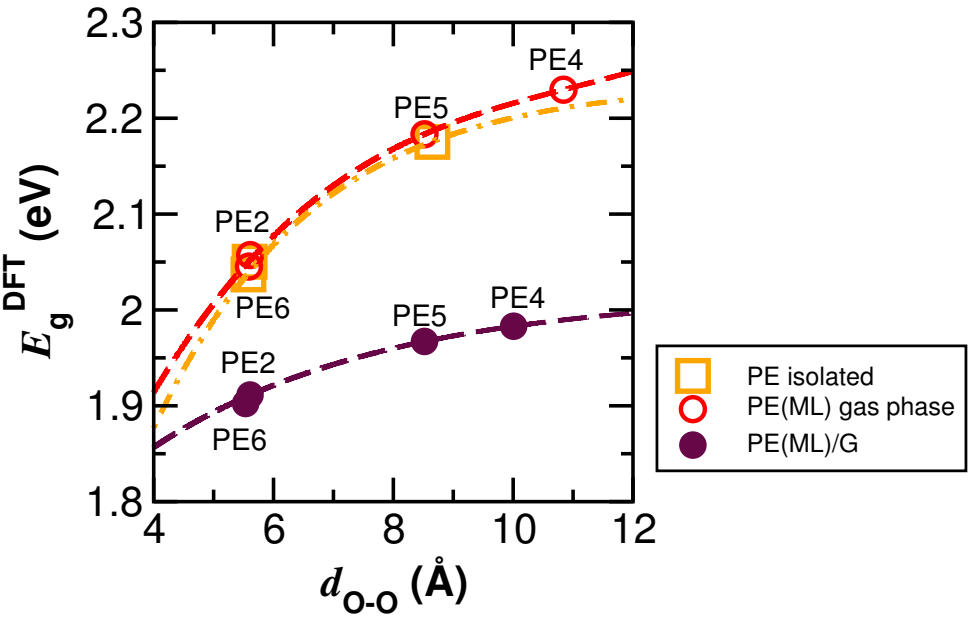

Figure 4.26: E_g^{DFT} as a function of d_{O-O}. The orange squares, red circles and solid maroon circles show the results for isolated PE molecules in the gas phase, monolayer of PE molecules in the gas phase and monolayer of PE molecules on graphene, respectively.

with increase in conjugation length. This feature is in agreement with the particle in a box model, where the energy gaps reduce with an increase in box length.

We have studied another set of PE molecules for which the chain length remains constant but the number and attachment site of the alkoxy chains are varied. The HOMO-LUMO gap for these molecules is obtained using DFT, TDDFT and experimental absorption spectra. We find almost the same qualitative trends in the E_g values obtained from theory and experiment. We find that the HOMO-LUMO gap of these isolated PE molecules depends on the shortest distance between the oxygen atoms (d_{O-O}) in the molecule. The lower is the value of d_{O-O}, the smaller is E_g. Therefore, d_{O-O} works as a descriptor to predict the E_g of the PE molecules of the same length but different positions of alkoxy chains. We have not yet been successful in finding a simple model that can explain such behavior of E_g with d_{O-O}. The HOMO-LUMO gap depends on the conjugation in the PE molecules. Higher conjugation causes more delocalization of electrons which in turn reduces the HOMO-LUMO gap of the molecules. The conjugation in the PE molecules can be modified

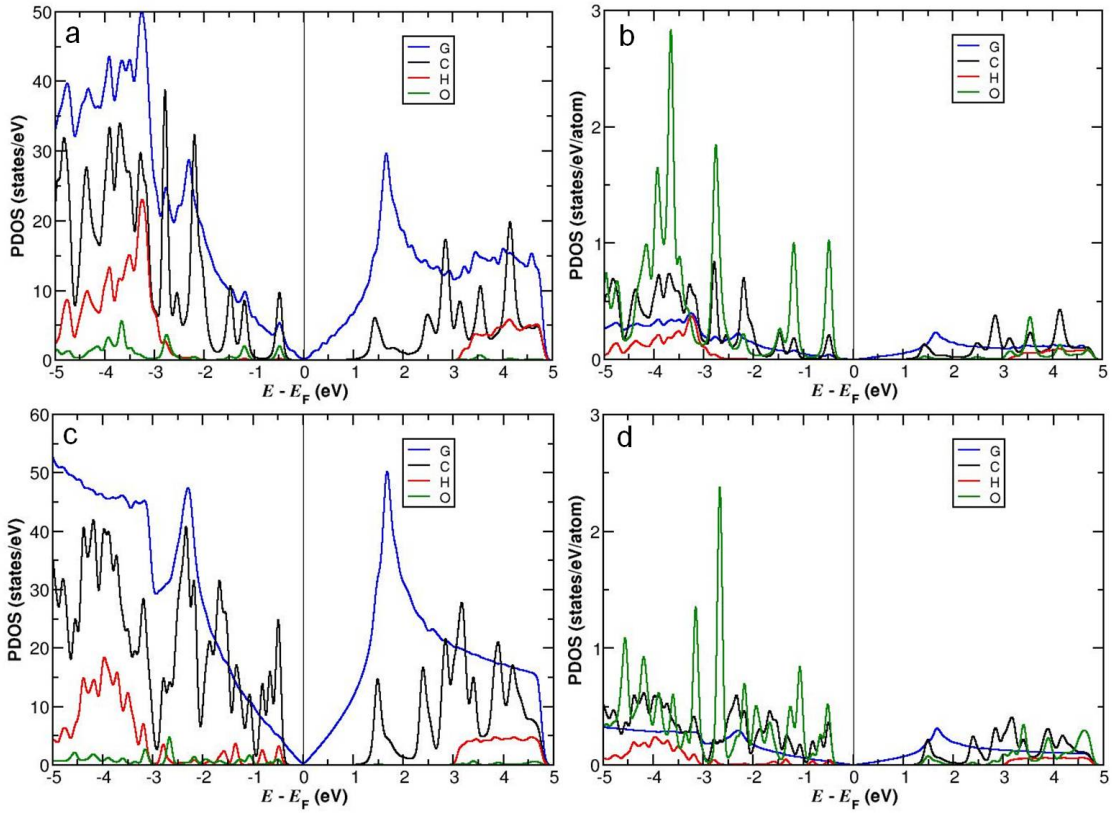

Figure 4.27: Projented density of states plot for the monolayer of (a) –(b) PE2 and (c)–(d) PE4 adsorbed on graphene. The blue curve shows the PDOS of graphene. The contributions of C, H and O atoms of to the molecular PDOS are shown by the black, red and green curves, respectively. The molecular PDOS of PE2 (b) and PE4 (c) are normalized by the number of atoms.

by changing the positions of the alkoxy chains which can modify E_{g}.

Apart from the isolated molecules we study the monolayer of PE molecules in the gas phase and on graphene. We calculated E_{g} for the self-assembled monolayers of PE molecules also. We find similar behavior of E_{g} with $d_{\mathrm{O-O}}$ for the monolayer of PE molecules as we have already seen for the isolated molecules. Both experimental and DFT results show that E_{g} changes significantly when the monolayers are adsorbed on graphene.

Bibliography

[1] Z. P. Mohan, *Supramolecular Organization of Phenyleneethynylenes on Surface: Role of Hydrogen Bonding and Host-Guest Interactions.* PhD thesis, Indian

Institute of Science Education and Research Thiruvananthapuram, India, 2015.

[2] A. Aviram and M. A. Ratner *Chemical Physics Letters*, vol. 29, pp. 277 – 283, 1974.

[3] M. A. Reed and W. P. Kirk, *Nannstructure Physics and Fabrication*. New York: Academic Press, 1989.

[4] M. J. S. *Adv. Mater.*, vol. 2, pp. 495–497, 1990.

[5] J. H. Burroughes, D. D. C. Bradley, A. R. Brown, R. N. Marks, K. Mackay, R. H. Friend, P. L. Burns, and A. B. Holmes *Nature*, vol. 347, p. 539, 1990.

[6] K. Arno, G. A. C., and H. A. B. *Angew. Chem. Int. Ed.*, vol. 37, pp. 402–428, 1998.

[7] M. D. McGehee and A. J. Heeger *Advanced Materials*, vol. 12, no. 22, pp. 1655–1668, 2000.

[8] S. H. Lee, T. Yasuda, and T. Tsutsui *J. Appl. Phys.*, vol. 95, no. 7, pp. 3825–3827, 2004.

[9] X. Hu, Y. Liu, J. Tian, B. Cheng, and D. Zhang *Appl. Phys. Lett.*, vol. 86, p. 121102, 2005.

[10] J. J. M. Halls, C. A. Walsh, N. C. Greenham, E. A. Marseglia, R. H. Friend, S. C. Moratti, and A. B. Holmes *Nature*, vol. 376, pp. 498–500, 1995.

[11] X.-X. Fu, R.-Q. Zhang, G.-P. Zhang, and Z.-L. Li *Sci. Rep.*, vol. 4, p. 6357, 2014.

[12] J. G. Kushmerick, J. Lazorcik, C. H. Patterson, R. Shashidhar, D. S. Seferos, and G. C. Bazan *Nano Lett.*, vol. 4, pp. 639–642, 2004.

[13] F. Maya, A. K. Flatt, M. P. Stewart, D. E. Shen, and J. M. Tour *Chemistry of Materials*, vol. 16, pp. 2987–2997, 2004.

[14] J. StefanS., S. Natalia, L. StephanM., and H. Sigurd *Angew. Chem. Int. Ed.*, vol. 49, pp. 6101–6105, 2010.

[15] M. Mayor, H. B. Weber, J. Reichert, M. Elbing, C. Von Hnisch, D. Beckmann, and M. Fischer *Angew. Chem. Int. ed.*, vol. 42, p. 58345838, 2003.

[16] H. Valkenier, C. M. Guedon, T. Markussen, K. S. Thygesen, S. J. van der Molen, and J. C. Hummelen *Phys. Chem. Chem. Phys.*, vol. 16, pp. 653–662, 2014.

[17] S. Hirata, M. Head-Gordon, J. Szczepanski, and M. Vala *J. Phys. Chem. A*, vol. 107, pp. 4940–4951, 2003.

[18] Y. Yamaguchi, T. Tanaka, S. Kobayashi, T. Wakamiya, Y. Matsubara, and Z.-i. Yoshida *J. Am. Chem. Soc.*, vol. 127, pp. 9332–9333, 2005.

[19] J. N. Wilson, P. M. Windscheif, U. Evans, M. L. Myrick, and U. H. F. Bunz *Macromolecules*, vol. 35, no. 23, pp. 8681–8683, 2002.

[20] J. M. Tour *Acc. Chem. Res.*, vol. 33, no. 11, pp. 791–804, 2000.

[21] H. Thomas, D. René, K. Andreas, K. A. Henning, K. ErikAndreas, and K. Wolfgang *Macromol. Chem. and Phys.*, vol. 201, pp. 627–631, 2000.

[22] L. A. Bumm, J. J. Arnold, M. T. Cygan, T. D. Dunbar, T. P. Burgin, L. Jones, D. L. Allara, J. M. Tour, and P. S. Weiss vol. 271, pp. 1705–1707, 1996.

[23] H. Maeda, R. Sakamoto, and H. Nishihara *J. Phys. Chem. Lett.*, vol. 6, pp. 3821–3826, 2015.

[24] J. M. Soler, E. Artacho, J. D. Gale, A. Garc¨ia, J. Junquera, P. Ordejón, and D. Sánchez-Portal *J. Phys.: Condens. Matter*, vol. 14, p. 2745, 2002.

[25] D. Sànchez-Portal, P. Ordejón, E. Artacho, and J. M. Soler *Int. J. Quantum Chem.*, vol. 65, pp. 453–461, 1997.

[26] N. Troullier and J. L. Martins *Phys. Rev. B: Condens. Matter Mater. Phys.*, vol. 43, pp. 1993–2006, 1991.

[27] J. P. Perdew and M. Burke, K.; Ernzerhof *Phys. Rev. Lett.*, vol. 77, pp. 3865–3868, 1996.

[28] S. Grimme *J. Comput. Chem.*, vol. 27, pp. 1787–1799, 2006.

[29] S. F. Boys and F. Bernardi *Mol. Phys.*, vol. 19, pp. 553–566, 1970.

[30] B. Brauer, M. K. Kesharwani, and J. M. L. Martin *J. Chem. Theory Comput.*, vol. 10, pp. 3791–3799, 2014.

[31] J. Tersoff and D. R. Hamann *Phys. Rev. Lett.*, vol. 50, pp. 1998–2001, 1983.

[32] K. Kim and K. D. Jordan *J. Phys. Chem.*, vol. 98, pp. 10089–10094, 1994.

[33] P. J. Stephens, F. J. Devlin, C. F. Chabalowski, and M. J. Frisch *J. Phys. Chem.*, vol. 98, pp. 11623–11627, 1994.

[34] E. Runge and E. K. U. Gross *Phys. Rev. Lett.*, vol. 52, pp. 997–1000, 1984.

[35] H. Kuhn *J. Chem. Phys.*, vol. 17, pp. 1198–1212, 1949.

[36] S. Fratiloiu, L. P. Candeias, F. Grozema, J. Wildeman, and L. Siebbeles *J. Phys. Chem. B*, vol. 108, p. 19967, 2004.

[37] J. Autschbach *J. Chem. Ed.*, vol. 84, p. 1840, 2007.

[38] S. S. Zade and M. Bendikov *Org. Lett.*, vol. 8, no. 23, pp. 5243–5246, 2006.

[39] P. V. James, P. K. Sudeep, C. H. Suresh, and K. G. Thomas *J. Phys. Chem. A*, vol. 110, pp. 4329–4337, 2006.

[40] G. W. P. van Pruissen, J. Brebels, K. H. Hendriks, M. M. Wienk, and R. A. J. Janssen *Macromolecules*, vol. 48, pp. 2435–2443, 2015.

Chapter 5

Tuning Interfacial Charge Transfer Between Organic Molecules and Graphene using Electric Fields and Nitrogen Doping

In this chapter, we will investigate how an applied electric field can tune the charge transfer between graphene and tetracyanoquinodimethane (TCNQ) molecules adsorbed on it. We find that the combined TCNQ/graphene system acts as an electrostatic dipole with opposite charges in the molecule and the graphene substrate. The change in the charge state causes a shift in the energy positions of the molecular orbitals and the graphene Dirac cone. The movement of molecular levels and the graphene Dirac cone takes place in opposite directions as a function of the electric field. Even the direction of charge transfer can be reversed by appropriately tuning the strength and direction of the electric field. Combining this effect with nitrogen-doping of graphene with the monolayer of TCNQ deposited on it permits one to perform selective reduction of a single TCNQ molecule in the monolayer. Our results suggest that, local gating can be used to tune the charge transfer at the molecule-graphene

interface. Thus, functionalization of graphene with TCNQ in the presence of an external electric field modifies the electron density on graphene, suggesting a novel approach to design optoelectronic devices and volatile memories. It is important to note that this effect is different from the usual control of charge carriers by gating. This study is performed by combining *ab initio* density functional theory (DFT) calculations with scanning tunneling microscopy (STM) and scanning tunneling spectroscopy (STS) experiments. The experiments were performed by Jérôme Lagoute and Van Dong Pham, Université Paris Diderot Paris 7, Sorbonne Paris Cité and CNRS, France.

5.1 Introduction

The discovery of graphene has opened up new routes in the field of modern technology. In the last decade, graphene has drawn a great deal of attention, in part due to its semi-metallic nature, as well as its unique electrical properties like the quantum Hall effect,[1, 2] transport via 'relativistic' Dirac fermions,[3, 4] ambipolar electric field effect, etc.[5] The electronic properties of graphene can be modified by substitutional doping [6–10] and functionalization of graphene by depositing donor or acceptor type organic molecules.[11] The discovery of graphene was accompanied by a demonstration of the field effect in graphene, which can be used in the operation of transistors.[12] Such properties of graphene can lead to novel opportunities for next-generation device-based applications. [13–15]. Field effect transistors are based on electric field control of the channel conductivity, which depends on electronic doping.

Alongside, noncovalent functionalization of graphene by organic molecules has also been considered to be a fruitful technique to modify the charge density on graphene without compromising its sp^2 band structure.[16, 17] The use of functionalized graphene in electronics and nanotechnology requires a tuning of the interfacial charge transfer, which is achieved by the donor or acceptor character of the molecules with

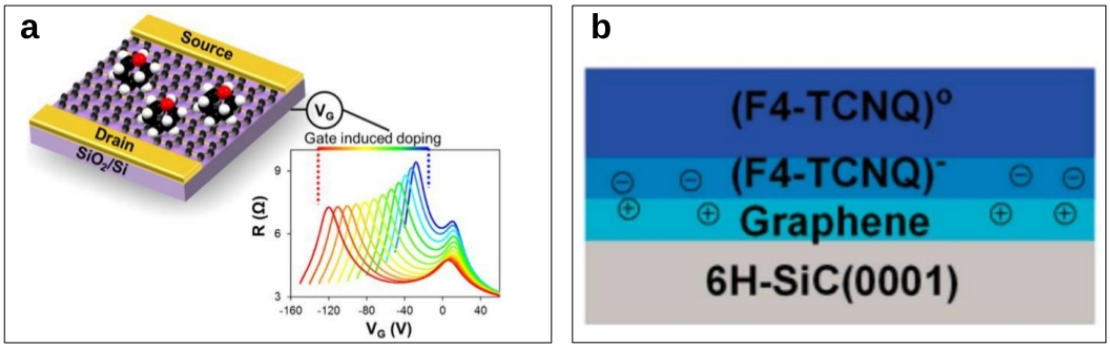

Figure 5.1: (a) Gate-tunable doping of graphene upon adsorption of piperidine molecule. p-n junctions with intermediate coverages can be achieved by varying the doping level in graphene from p- to n-type by gradually increasing the amount of adsorbed piperidine. The doping effect can be further tuned by applying large negative back-gate voltages.[25] This figure is reprinted with permission from Ref. 25 ©(2016) American Chemical Society. (b) Functionalization of epitaxial graphene (thermally grown on 6H-SiC(0001) substrate) by acceptor-type molecule tetracyanoquinodimethane (F4-TCNQ). F4-TCNQ causes p-type doping of graphene. This technique is a novel approach in the field of nanoelectronics.[26] This figure is taken with permission from the Ref. 26 ©(2007) American Chemical Society.

respect to graphene.[18–23] There is a recent speculation in this context about whether an electric field could possibly be used to further tune the amount of molecule-graphene charge transfer, suggesting novel technique for device design.[24]

The interfacial charge redistribution in the molecule-graphene system depends strongly on the orientation, conformation, and nature of the adsorbed molecules on the substrate. Therefore, probing at the single molecule scale is necessary to unravel the electronic interactions between the organic molecules and graphene under electric field. Scanning tunneling microscopy (STM) and scanning tunneling spectroscopy (STS) experiments, supported by *ab initio* density functional theory (DFT) calculations, are ideally suited for such an investigation. The effect of gate voltage on molecular levels deposited on graphene has been studied in recent STM experiments. These studies were focused on the possibility of modifying the alignment of molecular levels and tuning their charge state under the application of global gating. [25, 27, 28]. However, the effect of local gating on molecule-substrate charge transfer has not been explored yet. The effect of an electric field on tuning charge transfer at the molecule-substrate

junction has been studied for very few cases so far.[29, 30] Therefore, the local gating effect on molecule/graphene system remains to be investigated and analyzed. Also, the interplay between chemical doping and electric field in the interfacial charge transfer is an important feature which needs to be investigated in detail.

In this chapter, we have chosen tetracyanoquinodimethane (TCNQ) molecules on graphene as a model system to demonstrate the electric field dependence on the charge transfer between molecule and substrate. TCNQ is a well-known electron acceptor, which has been investigated by previous authors to study its structural and electronic properties, e.g., on graphene supported over Ir(111),[31, 32] on Au(111),[33] and on graphene supported over Ru(0001).[34]

In the experiments, the electric field is generated due to the STM tip. The STM tip is metallic in nature and when a certain bias is applied to the tip it induces an electric field on the sample situated at a certain distance from the tip. In the DFT calculations, an external electric field is applied in the direction perpendicular to the molecule-graphene plane to mimic this experimental condition.

5.2 Computational Details

The DFT calculations are performed using the Quantum ESPRESSO package,[35] using a plane wave basis and ultrasoft pseudopotentials.[36] The exchange-correlation interactions between electrons are treated within the Perdew-Burke-Ernzerhof (PBE) form of the generalized gradient approximation.[37] The Kohn-Sham equations are expanded using a plane wave basis set with kinetic energy and charge density cutoffs of 40 Ry and 400 Ry, respectively. The Brillouin zone is sampled using a 3×3×1 k point mesh for the smallest possible unit cell of the TCNQ/graphene superstructure.[38] The long-range dispersion interactions are included in the calculations using the DFT-D2 treatment.[39] Convergence has been improved by using the Marzari-Vanderbilt smearing technique with a width of 0.001 Ry.[40] Interactions between periodic images are minimized by introducing a vacuum with a spacing of 14 Å along non-repeating

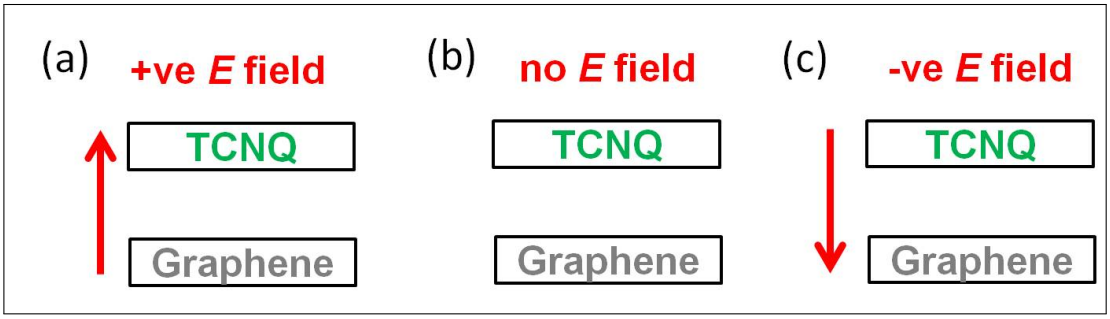

Figure 5.2: Schematic representation of TCNQ on graphene in presence of transverse electric field. (b) Shows the situation without any electric field. In (a) and (c) the external electric field is directed along positive and negative directions, respectively.

directions. All atomic coordinates are allowed to relax until the Hellmann-Feynman forces on all atoms are less than 0.001 Ry/Bohr.[41] The external electric field is applied via a sawtooth potential which is directed perpendicular to the plane of the hybrid TCNQ/graphene system.[42, 43] The electronic charge associated with each atom is obtained by using the Bader prescription.[44, 45] To eliminate spurious electrostatic interactions between the periodic images along the direction perpendicular to the molecule-graphene interface, the 'dipole correction' is applied.[46, 47] Simulated STM images are obtained following the Tersoff-Hamann approach.[48]

5.3 Results

5.3.1 TCNQ Monolayer on Pristine Graphene

First, we deposit TCNQ on pristine graphene in the absence of an electric field, to study the energetics of the molecule-graphene system. Then the charge transfer and shift in molecular states are investigated in the presence of an applied electric field.

Fig.5.2 shows schematic diagrams of the TCNQ/graphene system in the absence and presence of transverse electric fields. Note that the sign convention is such that a positive electric field is directed from the graphene toward the molecular monolayer.

Geometry and Energetics

A single TCNQ molecule prefers to adsorb on pristine graphene in a geometry such that the center of the molecule is at a bridge site (see Fig. 5.3). The adsorption

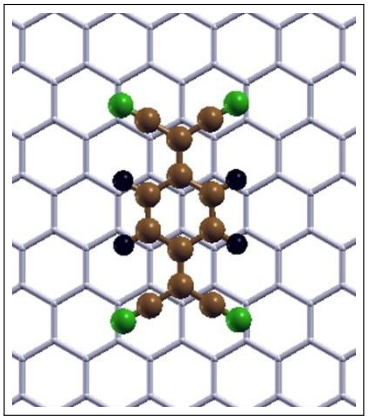

Figure 5.3: Adsorption of single TCNQ molecule on pristine graphene at bridge site. Color scheme:H – black, C – brown, N – green and C (graphene)– gray.

energy of a single TCNQ molecule ($E_{\text{ads}}^{\text{single}}$) on pristine graphene is given by:

$$E_{\text{ads}}^{\text{single}} = E_{\text{TCNQ/G}}^{\text{single}} - E_{\text{G}} - E_{\text{TCNQ}}^{\text{iso}}, \tag{5.1}$$

where $E_{\text{TCNQ/G}}^{\text{single}}$, E_{G} and $E_{\text{TCNQ}}^{\text{iso}}$ are the total energies of a single TCNQ on pristine graphene, a monolayer of graphene, and an isolated TCNQ molecule respectively. $E_{\text{ads}}^{\text{single}}$ for a single TCNQ molecule on pristine graphene is obtained to be -1.27 eV/molecule. This value is in good agreement with the results found by previous authors.[29, 49, 50]

TCNQ molecules can lower their energy by forming two-dimension molecular islands consisting of a self-assembled ordered pattern on pristine graphene, as has been found by STM experiments, and is confirmed by our calculations. The unit cell of this patterned monolayer (ML) is a nearly square lattice with unit cell vectors: $a = 0.93 \pm 0.01$ nm, $b = 0.89 \pm 0.02$ nm and angle $\theta = 85 \pm 2°$, as measured from STM experiments. The corresponding unit cell parameters obtained from our DFT calculations are: $a = 0.90$ nm, $b = 0.86$ nm and angle $\theta = 85°$. The slight discrepancy between the experimental and calculated values of the lattice parameters occurs primarily because of the requirement in the calculations that the TCNQ pattern needs to be commensurate with the graphene unit cell, with a supercell that is not prohibitively large for computational purposes. In our case, the unit cell for the

TCNQ monolayer is $2\sqrt{3} \times \sqrt{13}$ in terms of the primitive unit cell of the graphene substrate. The atomistic structure, simulated and experimental STM images of TCNQ(ML) on pristine graphene are shown in Figs. 5.4(a)–(c), respectively. We find that, in general, the experimental STM image is well reproduced by the simulated STM image, see Figs. 5.4(b) and (c).

The adsorption energy ($E_{\text{ads}}^{\text{ML}}$) of the TCNQ monolayer on pristine graphene is given by:

$$E_{\text{ads}}^{\text{ML}} = E_{\text{TCNQ/G}}^{\text{ML}} - E_{\text{G}} - nE_{\text{TCNQ}}^{\text{iso}}, \tag{5.2}$$

where $E_{\text{TCNQ/G}}^{\text{ML}}$, E_{G} and $E_{\text{TCNQ}}^{\text{iso}}$ are the total energies from DFT of the TCNQ(ML) on pristine graphene, the monolayer of graphene and an isolated TCNQ molecule, respectively. Here, n is the number of TCNQ molecules present per unit cell, and since for TCNQ(ML) on pristine graphene the value of n is always equal to 1 we will subsequently set $n = 1$ in this section. We obtain $E_{\text{ads}}^{\text{ML}}$ for TCNQ(ML) on pristine graphene as -1.98 eV/molecule. This value is in good agreement with previous literature.[29] Note that $|E_{\text{ads}}^{\text{ML}}| > |E_{\text{ads}}^{\text{single}}|$, therefore adsorption of the TCNQ monoloayer on pristine graphene is energetically more stable than the adsorption of a single TCNQ molecule. For this reason, experiments find the two-dimensional molecular island of TCNQ on pristine graphene. The formation of self-assembled monolayer pattern of TCNQ on pristine graphene is in agreement with previous experimental and theoretical studies.[29, 51, 52]

We have also examined the electron transfer from pristine graphene to the TCNQ molecules. The electron transfer from pristine graphene to single TCNQ molecule is 0.45 e/molecule, while for TCNQ(ML) on pristine graphene charge gained by TCNQ(ML) is 0.20 e/molecule. These values are in excellent agreement with previous DFT results.[29]

Two factors can be responsible for the formation of the ordered structure on pristine graphene: molecule-molecule interactions, and molecule-graphene interactions.

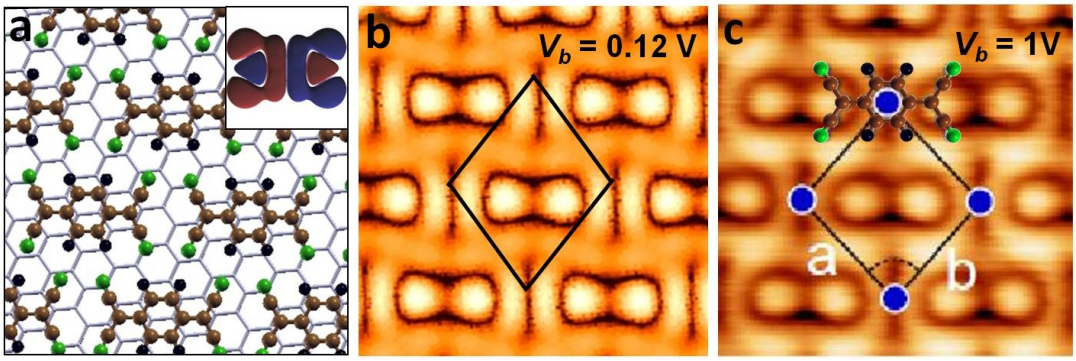

Figure 5.4: TCNQ monolayer adsorbed on pristine graphene. (a) The atomistic structure obtained from DFT calculations. Color scheme: H – black, C – brown, N – green and C (graphene)– gray. The inset shows LUMO of isolated TCNQ molecule. The red and blue lobes show the different signs of the wave function, drawn at isosurface value = 0.002 e/bohr^3. (b) Simulated STM image at V_b = 0.12 V. The corresponding unit cell is shown in black lines. (c) Experimental STM image at V_b= +1 V and I_t= 30pA, with superimposed unit cell and atomic structure of the TCNQ molecule.

In order to see how molecule-molecule interactions are changed in the presence of graphene, we consider a periodic monolayer of TCNQ in the gas phase, i.e., in the absence of the graphene substrate (this is an artificial situation which cannot be achieved experimentally). The stabilization energy ($E^{\rm gas}_{\rm stab}$) of a monolayer of TCNQ in the gas phase is defined as:

$$E^{\rm gas}_{\rm stab} = E^{ML}_{\rm TCNQ} - E^{iso}_{\rm TCNQ}, \tag{5.3}$$

where $E^{\rm ML}_{\rm TCNQ}$ and $E^{iso}_{\rm TCNQ}$ are, respectively, the total energies of the TCNQ monolayer and an isolated TCNQ molecule in the gas phase, The value of $E^{gas}_{\rm stab}$ for TCNQ(ML) is found to be -0.92 eV/molecule, which is in good agreement with previous values in the literature.[29] The creation of this monolayer is stabilized by the formation of hydrogen bonds between N and H atoms of neighboring TCNQ molecules.

Next, we go on to calculate the stabilization energy of a TCNQ(ML) on pristine graphene, this is given by:

$$E^{\rm G}_{\rm stab} = E^{ML}_{\rm TCNQ/G} - E^{single}_{\rm TCNQ/G} + E_{\rm G}, \tag{5.4}$$

note that the last term on the right-hand-side of the equation has to be included to balance out the fact that there is only one term involving the graphene substrate on the left-hand-side, whereas both the first and second terms on the right-hand-side involve the graphene substrate. In the way it is defined, $E^{\mathrm{G}}_{\mathrm{stab}}$ is supposed to contain information only about the effective molecule-molecule interactions in the presence of the graphene substrate. $E^{\mathrm{G}}_{\mathrm{stab}}$ is obtained to be -0.57 eV/molecule. Comparing this with the value of $E^{\mathrm{gas}}_{\mathrm{stab}} = -0.92$ eV, we find that the stabilization energy of TCNQ(ML) reduces when it is adsorbed on pristine graphene. This can be explained as follows: because TCNQ is an acceptor type molecule, electron transfer takes place from graphene to TCNQ, when the molecules are deposited on graphene. This makes all the molecules in the monolayer electron-rich when they are deposited on graphene. The Coulomb repulsion among the negatively charged TCNQ molecules (in the monolayer configuration) deposited on graphene makes the magnitude of the stabilization energy of the monolayer on graphene lower than in the gas phase.

Effect of Tip-Induced Electric Field: STS and STM Experiments

In experiments, the energy position of the TCNQ states adsorbed on pristine graphene are obtained from scanning tunneling spectroscopy (STS). In Fig. 5.5 we show scanning tunneling spectra obtained from a monoloyar of TCNQ on pristine graphene. The differential conductance (dI/dV) spectroscopy of TCNQ shows a broad resonance at positive bias (+0.75 V$\pm$0.05 V), and a sharp, intense peak at negative bias (~ -2.8 V), see Fig. 5.5(a). The biases at which these two peaks are obtained will be referred to as V_b^{LUMO} and V_b^{ch}, for reasons that will be made obvious below. The broad peak at positive bias, centered at V_b^{LUMO}, is attributed to the lowest unoccupied molecular orbital (LUMO) of TCNQ. The scanning tunneling microscopy (STM) image of TCNQ(ML) recorded at a bias voltage of 1 V corresponds to the LUMO state of TCNQ, see Fig. 5.4(c), as can be confirmed by the fact that the shape of the molecules imaged at 1 V looks similar to the shape of the LUMO of an isolated TCNQ molecule [see inset in Fig. 5.4(a)]. A similar result has been

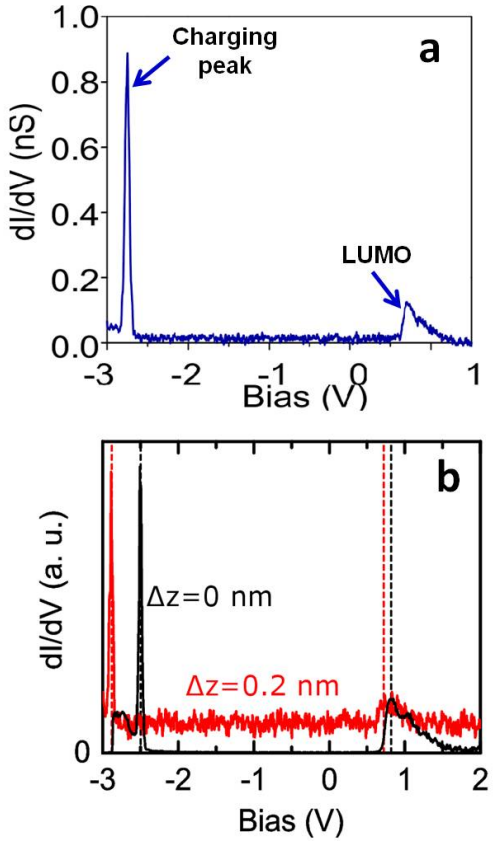

Figure 5.5: STS spectra of TCNQ on pristine graphene. (a) dI/dV spectrum recorded above a TCNQ molecule. The sharp peak at -2.8V appears due to ionization of TCNQ molecule and named as "charging peak". The broad peak at 0.75 V$\pm$0.05 V is the LUMO of TCNQ. (b) dI/dV spectra of a TCNQ molecule when the STM tip is at the setpoint position, i.e., $\Delta z = 0$ nm (black curve), and when it is retracted from it by 0.2 nm, i.e., $\Delta z = 0.2$ nm (red curve).

reported by previous authors for the LUMO state of TCNQ molecules self-assembled on graphene deposited on Ir(111).[31, 32]

The sharp peak at negative bias, at V_b^{ch}, arises due to a different physical phenomenon. This peak occurs due to a charging of the molecule in the presence of the electric field induced by the STM tip. During this process, the molecule gets ionized by the tip-induced electric field which causes electron transfer from the molecule to the STM tip. Similar features regarding the sharp peak at negative bias have previously been observed for other adsorbates on different surfaces.[53–58] Charging of the adsorbate induced by the electric field of the tip shifts the adsorbate state with respect to the Fermi level through a band bending effect.[59]

To investigate the effect of the tip-induced electric field on the molecular states the tip-sample distance, Δz is varied, which in turn changes the tip-induced electric field. In Fig. 5.5(b) two STS spectra are shown for the same substrate and adsorbate but with two different tip-sample distances. The dI/dV spectrum shown in black is obtained when the tip is at the setpoint position. In the case of the red spectrum, the STM tip is retracted from the setpoint position by an amount $\Delta z = 0.2$ nm. It is seen that both V_b^{LUMO} and V_b^{ch} shift upon changing the tip-sample distance. We see in Fig. 5.5(b) that the ionization peak, V_b^{ch} at negative bias shifts significantly upon changing Δz. Remarkably, the LUMO peak, V_b^{LUMO} (at positive bias) also exhibits a shift with Δz, though the shift in this peak is smaller compared to that in the charging peak. Therefore the energy positions of the molecular states (V_b^{LUMO} and V_b^{ch}) obtained from STS are not well-defined since their energy positions are influenced by the tip-induced electric field. Note that in experiments, it is hard to accurately determine the absolute value of the tip-sample distance at the setpoint position of the STM tip.

The shift in V_b^{LUMO} and V_b^{ch} with change in the tip-sample vertical retraction is further verified for different values of tip-sample distance (Δz), see Figs. 5.6(a) and (b). The experimental results for the energy positions of V_b^{LUMO} and V_b^{ch} as a function of Δz are plotted in the black squares in Figs. 5.6(a) and (b). Thus, Fig. 5.6 shows that both the V_b^{LUMO} and V_b^{ch} move with Δz, and the shift in V_b^{ch} is larger than V_b^{LUMO} as a function of Δz.

Effect of Transverse Electric Field: DFT Results

We have noted above that the STM tip induces an electric field on the sample when a certain bias voltage is applied between the tip and the sample. To reproduce the effects of this in DFT calculations, an external electric field $\mathcal{E}$ is applied in the direction perpendicular to the molecule-graphene interface.

The HOMO-LUMO gap of TCNQ adsorbed on pristine graphene is found to be 1.37 eV (this does not change much as a function of $\mathcal{E}$) from our DFT calculations, which

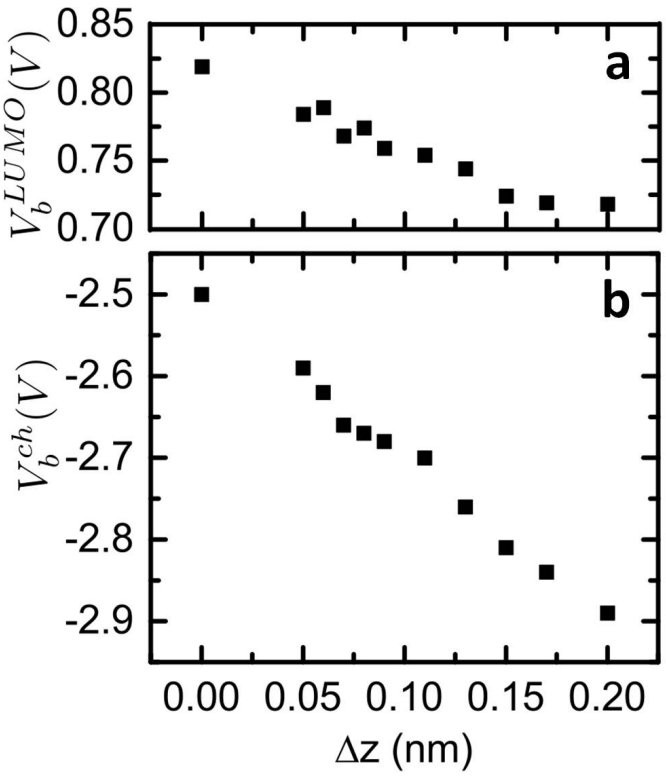

Figure 5.6: Positions of (a) the LUMO peak V_b^{LUMO} and (b) the charging peak V_b^{ch} of TCNQ adsorbed on pristine graphene as a function of the tip-sample vertical retraction Δz.

is lower than the experimental HOMO-LUMO gap. It is well-known that standard DFT always underestimates the band gap in comparison with the experimental value.

To investigate whether and how the energy positions of the LUMO and highest occupied molecular orbital (HOMO) of TCNQ are influenced by the electric field $\mathcal{E}$, we examine the projected density of states (PDOS) of the TCNQ/graphene (henceforth abbreviated as TCNQ/G) system as a function of the electric field. In Fig. 5.7, we see how the molecular states and the graphene Dirac point shift for different values and polarity of the applied electric field. Fig. 5.7 shows the PDOS of the TCNQ/G system for $\mathcal{E} = +1$V/Å , 0V/Å and -1V/Å. Fig. 5.4(b) shows a simulated STM image obtained at a bias voltage $V_b = +0.12$ V in the absence of any electric field. The LUMO state of TCNQ (adsorbed on pristine graphene) is captured in the simulated STM image since, in the DFT calculations, it lies at 0.12 V for $\mathcal{E} = 0$ V/Å (see Fig. 5.7), and the shape of the molecular state is similar to the shape of the

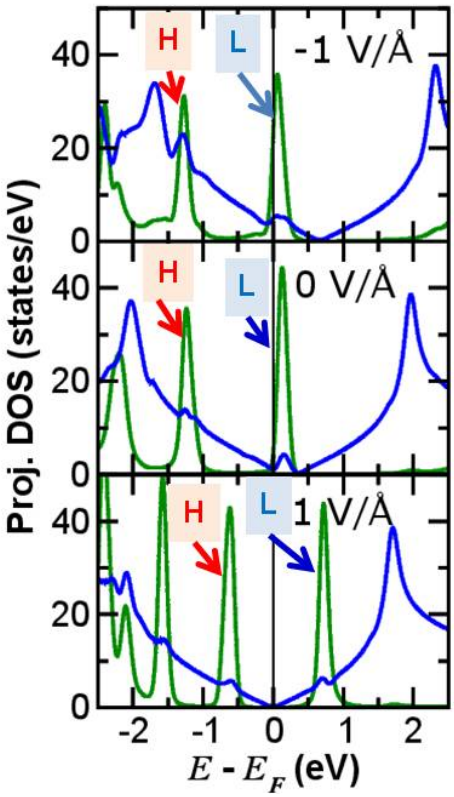

Figure 5.7: Projected density of states (PDOS) of TCNQ(ML) on pristine graphene obtained from DFT when the applied electric field values are −1 V/Å, 0 V/Å, and +1 V/ÅṖDOS on graphene and TCNQ are shown by blue and curves, respectively. Dirac cone of graphene moves from right to left as the electric field changes from −1 V/Å to +1 V/ÅṪhe TCNQ states move in the direction opposite to the graphene Dirac cone as a function of electric field.

TCNQ LUMO in the gas phase [see inset of Fig. 5.4(a)]. It is important to note that because of the well-known 'band-gap' problem of DFT, the energy of the LUMO is considerably underestimated in the DFT calculations with respect to experiment (as already mentioned previously).

Our DFT results in Fig. 5.7 show that the energies ot the HOMO and LUMO states of TCNQ (E_{HOMO} and E_{LUMO}, respectively) are downshifted when the electric field has negative polarity, i.e., is directed from TCNQ to graphene, while the movement in molecular states gets reversed as the polarity of the electric field becomes opposite. We see in Fig. 5.7 that on changing V_b from 0 to +1 V/Å, the two (green) peaks corresponding to the HOMO and LUMO shift to significantly higher values of V_b. At the same time, by looking at the blue curves in Fig. 5.7 which show the PDOS

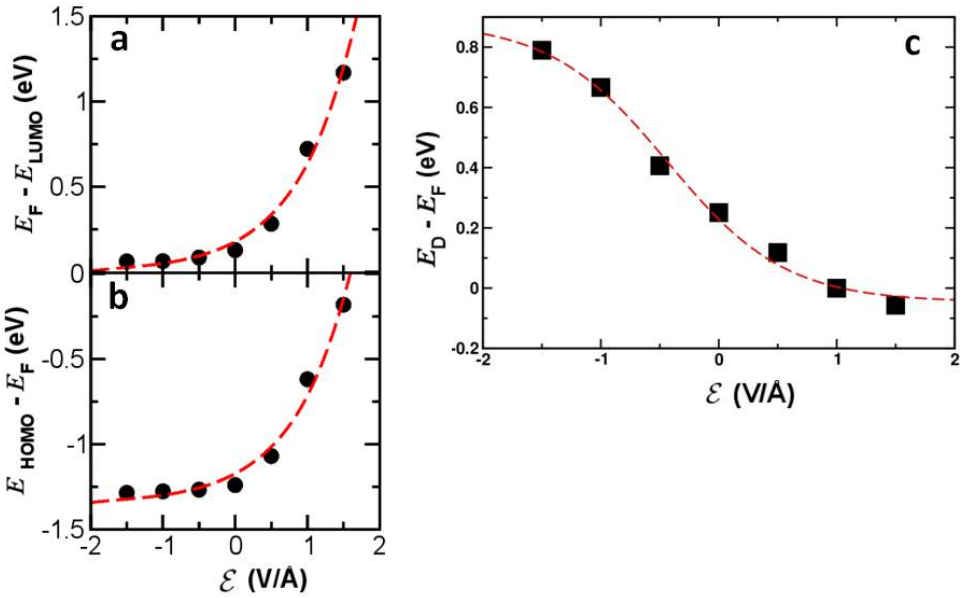

Figure 5.8: Change in the energy positions of the (a) LUMO (E_{LUMO}) and (b) HOMO (E_{HOMO}) states of TCNQ with respect to the Fermi energy (E_{F}) as a function of the applied electric field ($\mathcal{E}$). (c) Movement of the graphene Dirac cone (E_{D}) with respect to E_{F} as a function of $\mathcal{E}$ (with the TCNQ(ML) adsorbed on it). Note: movement of the molecular states and graphene Dirac point are opposite with $\mathcal{E}$.

of graphene, we see that the Dirac point of graphene always moves in the direction *opposite* to that of the TCNQ HOMO and LUMO peaks, i.e., the TCNQ/G system does *not* behave as a single rigid system. The Dirac point of graphene shifts towards higher/lower energies as the electric field becomes more negative/positive. To see the shift in E_{HOMO} and E_{LUMO} of TCNQ more clearly as a function of electric field, the energy positions of these states with respect to the Fermi energy (E_{F}) are plotted as a function of $\mathcal{E}$, this is plotted in Figs. 5.8(a) and (b). Note that the movement of both the HOMO and LUMO of TCNQ is investigated in the DFT calculations. However, the HOMO of TCNQ cannot be observed in the experiments since it falls beyond the range which STS or STM can capture.

The movement of the graphene Dirac point with respect to the Fermi level, $E_{\mathrm{D}} - E_{\mathrm{F}}$, as a function of $\mathcal{E}$, is plotted in Fig. 5.8(c). From this figure we see that as $\mathcal{E}$ becomes more negative, E_{D} moves away from the E_{F} and shifts towards higher

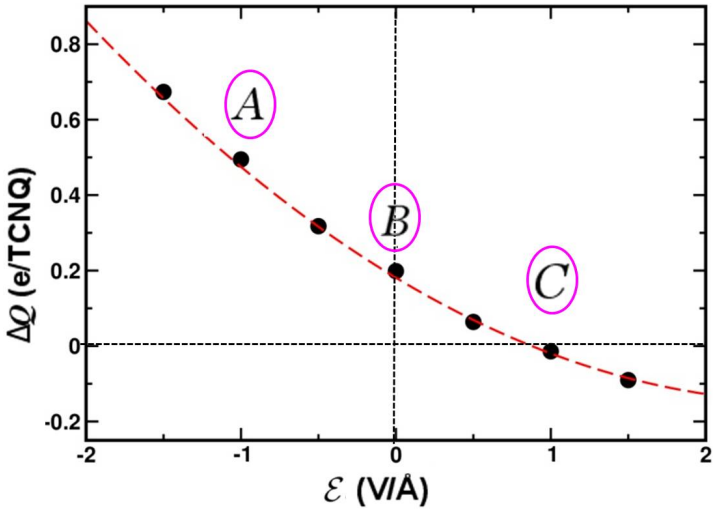

Figure 5.9: Charge gained by TCNQ molecule (ΔQ) adsorbed on pristine graphene as a function of $\mathcal{E}$. ΔQ_{TCNQ} becomes more positive as $\mathcal{E}$ becomes more negative. This implies electron transfer takes place from graphene to TCNQ for negative $\mathcal{E}$. Opposite phenomena happens as the direction of $\mathcal{E}$ gets reversed. A, B and C represent the situations when $\mathcal{E} = -1$ V/Å , 0 V/Å and $+1$ V/Å , respectively.

energies.

The simultaneous movement of TCNQ states and the graphene Dirac point in opposite directions (in energy) with change in $\mathcal{E}$ implies that the molecular levels are not pinned to the graphene states in the presence of the external electric field. We find that the shifts in molecular states and the graphene Dirac point arise due to electric field dependent charge transfer between the TCNQ molecules and graphene. To investigate this feature, we examine our DFT results to see how the charge transfer between the monolayer of TCNQ and graphene is affected by the electric field. These results are shown in Fig. 5.9, where we see that ΔQ, the number of electrons gained by TCNQ from graphene, varies monotonically with $\mathcal{E}$. Note that the sign convention used is such that a positive value of ΔQ implies that electrons are gained by TCNQ from graphene.

Since TCNQ is an acceptor-type molecule, in the absence of an electric field, electron transfer takes place from graphene to TCNQ. As the electric field becomes more negative, we find that electron accumulation in TCNQ and electron depletion in graphene increases. However, this tendency is reversed on flipping the polarity

of the electric field (making $\mathcal{E}$ more positive). Interestingly, at a sufficiently large positive electric field (>1 V/Å) the direction of electron transfer takes place from TCNQ to graphene, see Fig. 5.9, i.e., TCNQ behaves like a donor-type molecule in the regime of $\mathcal{E} > 1$. Therefore, electron transfer between TCNQ and graphene can be tuned by the application of electric field. Note that the variation of ΔQ is not uniform with change in $\mathcal{E}$. ΔQ changes more rapidly as a function of $\mathcal{E}$ when the electric field is directed from TCNQ to graphene, i.e., has negative polarity, than when it has positive polarity, due to TCNQ being an acceptor-type molecule.

The values of ΔQ plotted in Fig. 5.9 are obtained from Bader analysis. We remark that the qualitative trend of ΔQ vs. $\mathcal{E}$ remains the same when the values of ΔQ are calculated using Löwdin charges, however the magnitudes of ΔQ become smaller, at least in part due to the usual spilling of electronic charges in Lowdin population analysis when the wave functions are projected on atomic orbitals.[60] We also note that previous authors have found that for a single molecule adsorbed on graphene, the charge transfer can be modified by application of an electric field, this has been shown for CO_2, NH_3, CO and benzene-graphene.[30]

The evolution of the spatial redistribution of the electron density for TCNQ/graphene system as a function of $\mathcal{E}$ is shown in Fig. 5.10. In this figure, we have plotted the isosurfaces of $\Delta\rho = \rho_{\mathrm{TCNQ/G}} - \rho_{\mathrm{TCNQ}} - \rho_{\mathrm{G}}$, where ρ_X is the electronic density of the system X. The red and blue lobes correspond to electron accumulation and depletion respectively. In the absence of an electric field (image B) electrons are transferred from graphene to TCNQ, see red lobes on TCNQ and blue lobes on graphene. This charge redistribution gets enhanced when $\mathcal{E}$ becomes -1V/Å (image A), which in turn increases the red lobes on TCNQ molecules and blues lobes on graphene. There is almost no electron transfer between TCNQ and graphene when $\mathcal{E} = +1$V/Å (image C).

Since electron transfer takes place from graphene to TCNQ for negative polarity of the electric field, electron occupancy in the TCNQ states increases, which in turn

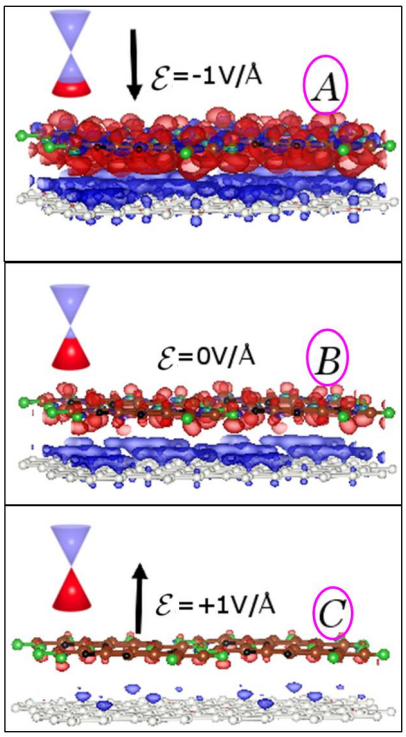

Figure 5.10: Charge density difference, $\Delta\rho$ plots for TCNQ(ML) on pristine graphene for three values of the electric field obtained at isosurfaces value of 0.0007 e/bohr^3. Red and blue lobes correspond to electron accumulation and depletion, respectively. A, B and C represent the conditions when $\mathcal{E} = -1$ V/Å, 0 V/Å and $+1$ V/Å, respectively. Color code for atoms: C (of graphene) – gray, C (of TCNQ) – brown, H – black , N – green. Color code for Dirac cone schemes: blue – empty states, red – filled states.

shifts the energy position of the TCNQ levels towards the left (or to lower energies), this fact is supported by the results seen in Fig. 5.7 and Figs. 5.8(a)–(b). At the same time, the graphene Dirac point shifts to higher energies due to electron loss for a negative electric field, see Fig. 5.8(c). The opposite features occur when the direction of electric field gets reversed. Thus, electron transfer between the TCNQ(ML) and graphene can explain the shift in molecular levels and the graphene Dirac point.

The charge transfer between the TCNQ(ML) and the graphene induces dipole moment at the combined TCNQ(ML)–graphene interface, which varies with the applied electric field. The dipole moment of the combined system is computed as

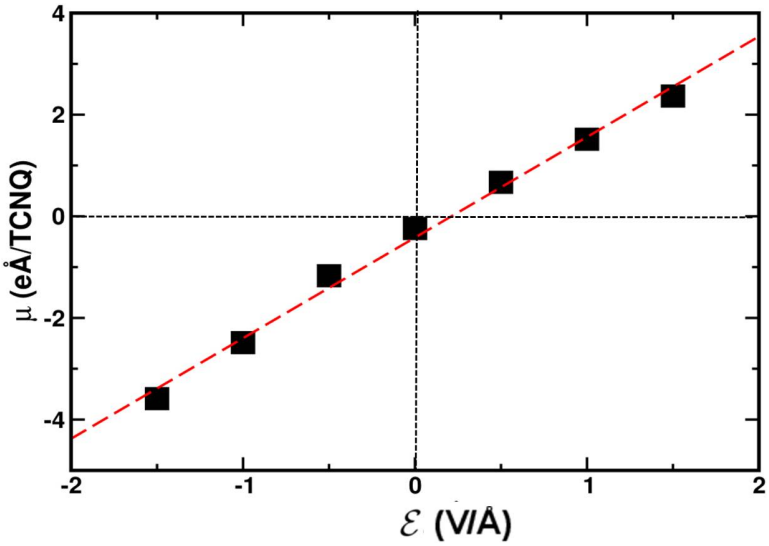

Figure 5.11: Dipole moment μ of the TCNQ/graphene system as a function of $\mathcal{E}$. The slope of μ vs. $\mathcal{E}$ plot gives the polarizability (α) of the combined TCNQ(ML)/graphene system.

follows:

$$\mu = \sum_i z_i Z_i - \int z\rho(z)dz, \tag{5.5}$$

where z_i and Z_i are the nuclear position and charge, respectively for the ith atom. The first term in Eq. (7.4) represents nuclear dipole moment. The second term is the dipole moment of the system due to the electrons present in it. $\rho(z)$ is the planar average of electron density along z direction, i.e., perpendicular to the plane of the oxide/metal interface.

$$\rho(z) = \frac{1}{A}\int dx \int dy\rho(x, y, z), \tag{5.6}$$

where A is the unit cell area.

Note that the dipole moment is actually a vector pointing along the z direction, a positive value of μ means that the dipole moment is pointing from the graphene toward the TCNQ. Fig. 5.11 shows how the dipole moment (μ) of the TCNQ(ML)/G system changes as a function of $\mathcal{E}$. Since, in the absence of any electric field, electron

transfer takes place from graphene to TCNQ, μ is slightly negative (i.e., points from TCNQ to graphene) for $\mathcal{E} = 0$. As $\mathcal{E}$ becomes more negative, μ becomes more negative. In contrast, when $\mathcal{E}$ becomes more positive, μ becomes more positive. The (almost) linear variation of μ with $\mathcal{E}$ indicates that the TCNQ(ML)/G system behaves like an induced electrostatic dipole. The slope of the graph in Fig. 5.11 gives the polarizability α of TCNQ(ML)/G, which is obtained to be 29 Å^3/molecule along the direction perpendicular to the molecule/graphene plane. This value is larger than the polarizability of an isolated TCNQ molecule in the gas phase in the direction perpendicular to the molecular plane, which we compute to be 12.9 Å^3/molecule; this is in good agreement with the previous values reported in literature.[61, 62]

Determining Absolute Values of the TCNQ LUMO Energy and Tip-Sample Distance in Experiments: An Analytical Model

From the experimental results (recall Fig. 5.5), we have already seen that STS cannot determine the 'actual' position of the LUMO. We have also remarked that the absolute value of the tip-sample distance at the setpoint position is difficult to measure in STM measurements, though relative displacements (the amount by which the tip is retracted or advanced) can be measured. To quantify these two quantities, as well as to validate our understanding of the variation of V_b^{LUMO} and V_b^{ch} with Δz, we now develop an analytical model.

In this model, we consider that the LUMO state of TCNQ, U_0, varies linearly with the electric field $\mathcal{E}$. This feature is expected when the molecule/graphene system behaves like an induced dipole and the density of states of the molecule becomes constant around the Fermi level (which implies that the HOMO and LUMO states are situated far from the Fermi level). In this case, the charge of the molecule has to be proportional to the electric field, and the spectrum of the molecule should shift proportionally to the electric field. Our results on the TCNQ/graphene system satisfy all these expectations. From the DFT results, we have found that the TCNQ/graphene system behaves like an induced dipole (see Fig. 5.11 above). We have seen that both

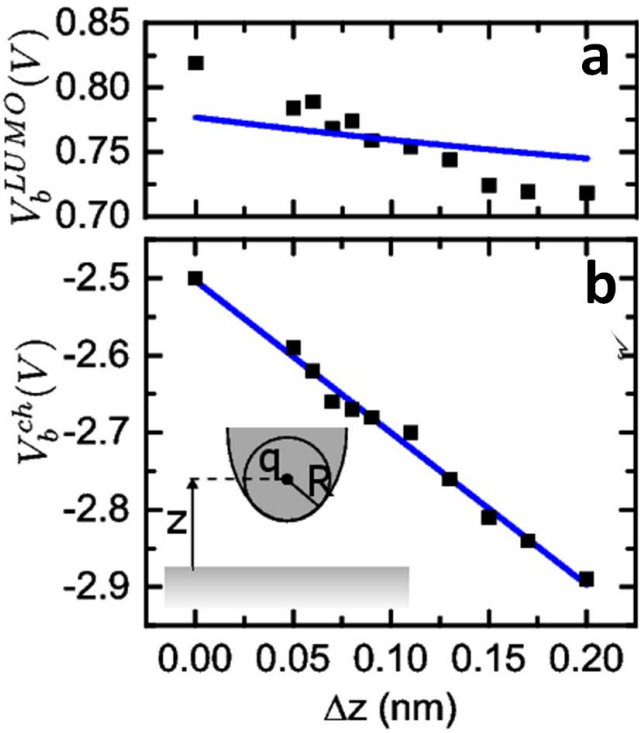

Figure 5.12: Positions of (c) the charging peak and (d) the LUMO peak of TCNQ adsorbed on pristine graphene as a function of the tip-sample vertical retraction. The blue lines are fits to the model described in the text. The inset in (d) shows the schematic of the STM tip and tip-sample distance. q, R and z are the charge on the tip, radius of the tip and tip-sample distance, respectively.

the HOMO and LUMO states of TCNQ shift monotonically with $\mathcal{E}$ from Figs. 5.8(a) and (b). Note that when the LUMO state is well separated from the Fermi energy, i.e., for higher values of $\mathcal{E}$, E_{LUMO} changes almost linearly with $\mathcal{E}$.

Applying this model to the TCNQ/graphene system, we assume U_0 to be the actual position of the TCNQ LUMO without any electric field. The energy position of the LUMO state shifts to $U_0 + \kappa\mathcal{E}$ when a negative bias is applied, where κ is the proportionality factor which relates the energy shift in the LUMO to the electric field.

The TCNQ molecule becomes ionized when the LUMO state is situated at the Fermi energy, which is named as the "charging process". During this process, $U_0 + \kappa\mathcal{E} = 0$ (since the LUMO is then at the Fermi energy). The electric field induced on the sample by the STM tip can be written as $\mathcal{E} = V_b/(z_0 + \Delta z)$ assuming a planar junction geometry, where V_b is the bias voltage, z_0 is the tip-sample distance at the

setpoint position, and Δz is the retraction of the tip-sample separation from the setpoint position z_0. The sharp charging peak occurs when $V_b^{ch} = -U_0 z_0/\kappa - U_0 \Delta z/\kappa$. Therefore, the energy position of this peak should depend linearly on the tip-sample separation, which is indeed observed in the experimental data [recall Fig. 5.6(b)]. A linear fit to the experimental data of V_b^{ch} vs. Δz (see Fig.5.12) gives $U_0/\kappa = 1.97$ V/nm and $z_0 = 1.3$ nm. The value of z_0 for the setpoint distance is a very reasonable and plausible value.

In order to obtain the value of U_0, we will make use of the variation of V_b^{LUMO} with Δz. The LUMO peak appears when $V_b^{LUMO} = (z_0 + \Delta z)U_0/(z_0 + \Delta z - \kappa)$. The best agreement with the experimental data is obtained for $U_0 = 0.6$ V [blue line in Fig. 5.12(a)] which gives the value of κ to be 0.3 nm. This result suggests that in the experiments, the position of the LUMO state is overestimated by around 150 mV due to the influence of the tip-induced electric field.

Our model can successfully explain why the energy positions of V_b^{LUMO} and V_b^{ch} change with tip-sample distance Δz. The strength of tip-induced electric field depends on the tip-sample distance which in turn affects the molecular spectra. It also successfully predicts that V_b^{LUMO} changes less with Δz than does V_b^{ch}, though the variation of the former in the experiments is larger than it is in our simple model.

Therefore, with the help of an analytical model, the actual position of the TCNQ LUMO (without any electric field) and the tip-sample distance at the setpoint position are determined.

5.3.2 TCNQ Monolayer on Nitrogen-Doped Graphene

So far we have considered the functionalization of graphene by depositing an acceptor type molecule, TCNQ, on it. Now, we want to combine this technique with substitutional doping of graphene by nitrogen, which is a donor type impurity. In this section, we again investigate the electric field-induced charge transfer (already considered in the earlier part of this chapter), but now combined with nitrogen doping of graphene, in order to achieve a selective reduction of a single TCNQ molecule in

the molecular monolayer. The insertion of nitrogen atoms in graphene causes the presence of electron donating point defects which allows one to shift the energy levels of the TCNQ molecules adsorbed directly above these N-sites, and to selectively charge these molecules when the appropriate bias voltage is applied.

Geometry and Energetics

To determine the lowest energy configuration of TCNQ(ML) on N-doped graphene, both the adsorption site of the molecule and the position of the dopant with respect to the molecule are varied. As on pristine graphene, we find that the TCNQ molecule prefers to adsorb with its center positioned over a bridge site on N-doped graphene.

The adsorption energy ($E_{\text{ads}}^{\text{ML}}$) of TCNQ(ML) on N-doped graphene is given by:

$$E_{\text{ads}}^{\text{ML}} = E_{\text{TCNQ/N-G}}^{\text{ML}} - E_{\text{N-G}} - E_{\text{TCNQ}}^{\text{iso}}, \tag{5.7}$$

where $E_{\text{N-G}}$ is the total energy of N-doped graphene, and all other terms have been previously defined.

The geometries shown in Fig. 5.13 are for a N-doping concentration of 3.57%, with one dopant N atom present per TCNQ molecule. The different configurations vary in the lateral position of the N dopant relative to that of the TCNQ molecule. The configuration labeled "b4" shows the most stable adsorption geometry of TCNQ(ML) on N-doped graphene with $E_{\text{ads}}^{\text{ML}} = -2.34$ eV/molecule. (In this configuration, the N dopant atom is positioned directly below one of the four N atoms at the corners of the TCNQ molecule, and is therefore barely visible.) In general, it is found that the adsorption energy of TCNQ(ML) on N-doped graphene increases as the nitrogen atom in N-doped graphene comes closer to a cyano (CN) group of the TCNQ. This happens because the cyano group is the main acceptor center for the TCNQ molecule. As the nitrogen atom in the doped graphene substrate comes closer to the cyano group in TCNQ, the TCNQ molecule gains more electrons from the substrate, which in turn increases the adsorption energy.

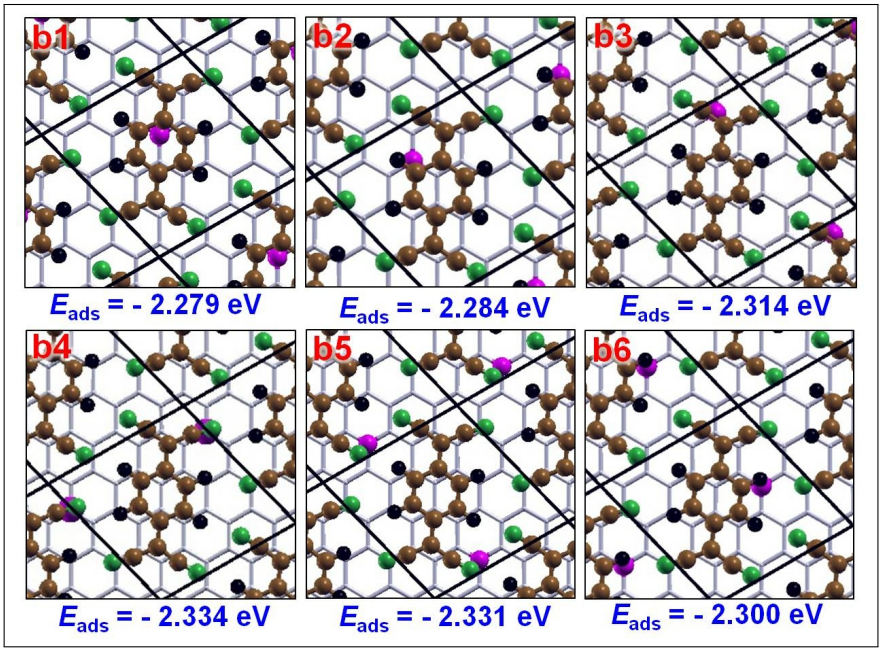

Figure 5.13: Adsorption energy of TCNQ(ML) on N-doped graphene for different positions of the nitrogen atoms. The adsorption site of TCNQ molecule is kept fixed at the bridge position. The numbers (in blue) are the adsorption energies of TCNQ(ML) on N-doped graphene for different positions of the N atom in graphene. "b4" is found to be the lowest energy configuration for TCNQ(ML) on N-doped graphene with E_{ads} = −2.334 eV. Color scheme: C(TCNQ) – brown, H(TCNQ) – black, N(TCNQ) – green, C(graphene) – gray and N(graphene) – magenta.

Next, we vary the doping concentration, larger unit cells are used to achieve lower doping concentrations. Therefore, the number of TCNQ molecules present per N atom is no longer equal to 1. In these cases, some of the TCNQ molecules are situated above the N-site and others above C-sites of graphene. The charges on the TCNQ molecules, ΔQ at the N-site and at C-sites, are calculated using Bader analysis. The ΔQ values shown by the black circles in Fig. 5.14(a) are averaged over all the TCNQ molecules present in the unit cell. The red circles in Fig. 5.14(a) correspond to the charge gained by the TCNQ molecule situated above the N-site. Comparing the black and red circles. we see that ΔQ for the TCNQ molecule situated at a N-site is higher than that averaged over all the TCNQ molecules present in the unit cell. This implies that the TCNQ molecule at the N-site gains more electrons than those at C-sites. Also, we see from the figure that for both the red and black circles, ΔQ increases as a function of the N-doping concentration. Nitrogen is a donor

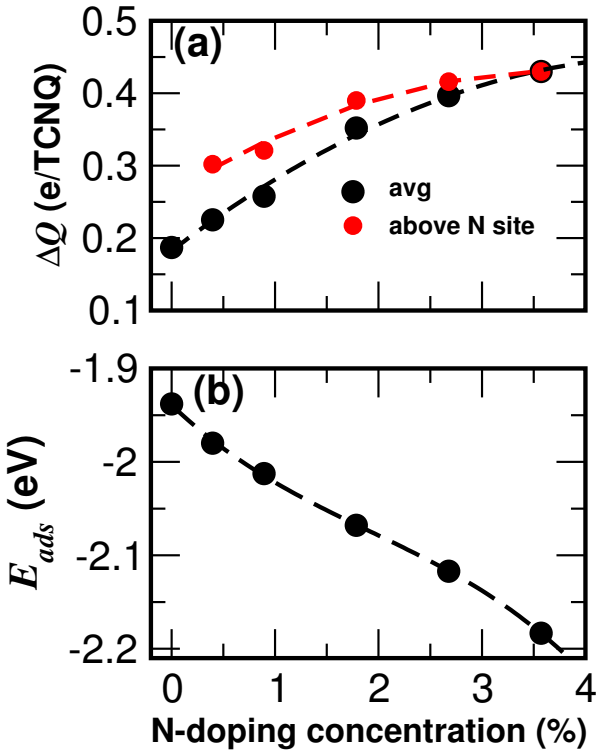

Figure 5.14: (a) Charge gained by TCNQ, ΔQ as a function of N-doping concentration in graphene. The black circles show ΔQ values average over all the TCNQ molecules present in the monolayer, while the ΔQ values of TCNQ molecules adsorbed at N-site are shown by the red circles. ΔQ increases with doping concentration. (b) E_{ads} of TCNQ(ML) on N-doped graphene increases with the doping concentration.

type impurity for graphene and N-doping in graphene makes it electron-rich, this in turn increases the electron transfer from N-doped graphene to the acceptor molecule TCNQ. Therefore, from Fig. 5.14(a) we see that, apart from the applied electric field another possible technique to tune the electron transfer between TCNQ and graphene is by changing the concentration of N atoms in graphene. As the concentration of N atom in graphene increases, more electrons are transferred from N-doped graphene to TCNQ [see Fig. 5.14(a)]. The increase in N-doping concentration and ΔQ also enhances the molecule-substrate interaction, and hence the adsorption energy of TCNQ(ML) on N-doped graphene increases as a function of the doping concentration, see Fig. 5.14(b).

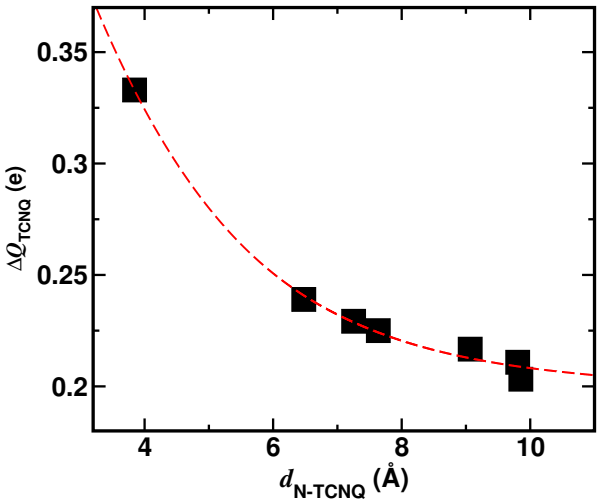

Figure 5.15: Variation in charge gained by TCNQ molecule (ΔQ_{TCNQ}) with $d_{\mathrm{N-TCNQ}}$ for TCNQ(ML) adsorbed on N-doped graphene at 0.22% doping concentration. $d_{\mathrm{N-TCNQ}}$ is the distance between the N atom in graphene at a TCNQ molecule present in the two-dimensional molecular lattice. ΔQ_{TCNQ} reduces as $d_{\mathrm{N-TCNQ}}$ increases. Local charging of TCNQ occurs upon N-doping in graphene.

Local Charging due to Doping

We have seen above that nitrogen-doping in graphene enhances the electron transfer between the acceptor-type molecule TCNQ and the graphene substrate. From Fig. 5.14(a) we see that a TCNQ molecule in the monolayer that is adsorbed directly above a N-site gains more electrons from graphene than those TCNQ molecules that are situated above C-sites. To theoretically study this local charging of TCNQ in more detail, we consider a large enough unit cell with sixteen TCNQ molecules present per unit cell, and containing, within this unit cell, a single N dopant in the graphene substrate. In this way the doping concentration of nitrogen is achieved to be 0.22%. To investigate how local the charging effect is, we plot ΔQ, the charge gained by a TCNQ molecule, as a function of $d_{\mathrm{N-TCNQ}}$, the distance between the N atom in graphene and the TCNQ molecule, see Fig. 5.15. We find that as $d_{\mathrm{N-TCNQ}}$ increases, ΔQ decreases rapidly. This implies that the charging of TCNQ upon N-doping in graphene is a strongly local effect: the closer the TCNQ molecule is to the N dopant in graphene, the higher is the electron transfer from the N-doped graphene to TCNQ.

Effect of Electric Field: STM, STS and DFT Results

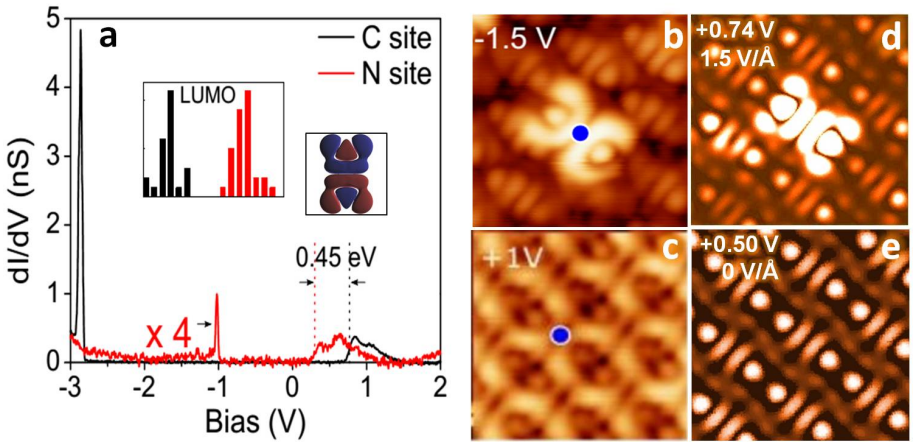

Figure 5.16: STS and STM images of TCNQ(ML) on N-doped graphene. (a) dI/dV spectra recorded above TCNQ molecules adsorbed at the C-site (black curve) and the N-site (red curve) of graphene. The charging peak of TCNQ molecules above the C-site and the N-site appear at -2.8 V and -1.5 V, respectively. The histogram shows the distribution in the position of LUMO peaks for the C-site and N-site. The LUMO peaks for TCNQ at the C-site and the N-site are separated by 0.45 V. The inset shows the LUMO state of isolated TCNQ molecule in the gas phase (drawn at isosurface value = 0.002 e/bohr^3). The red and blue lobes show different signs of the wave function. Experimental STM images of TCNQ(ML) on N-doped graphene at (b) V_b= -1.5 V and (c) V_b= +1 V. Clear contrast between the molecules at the C-site and the N-site is observed in (b), while molecules at the C-site and the N-site look similar in (c). Simulated STM images of TCNQ(ML) on N-doped graphene when (d) $\mathcal{E}$ = +1.5 V/Å and V_b= +0.74 V and (e) $\mathcal{E}$ = 0 V/Å and V_b= +0.50 V. The blue circles indicate the position of the molecule situated directly above the N atom in graphene.

Previous authors have found that when a molecule is deposited above a N-site of nitrogen-doped graphene, the energy positions of the molecular states are downshifted due to a local charge transfer [63]. From DFT calculations we have already verified that a TCNQ molecule above a N-site gains more electrons than TCNQ molecules above a C-site [see Fig. 5.14(a) and Fig. 5.15]. Consequently, a TCNQ molecule at a N-site has more electronic states occupied than at a C-site, therefore a lower energy is required to ionize the molecule above a N-site than at a C-site. This fact is supported by comparing the STS spectra of TCNQ molecules taken above the C-site and N-site on N-doped graphene, see Fig. 5.16(a). The charging peak of TCNQ at N-site lies at much lower energy (less negative value) than at a C-site. The ionization or charging

peak V_b^{ch} of TCNQ at N-site lies at -1.5 V while V_b^{ch} of TCNQ at C-site is situated at -2.8 V. This feature implies that extraction of electron from the TCNQ above N-site is easier than above C-site.

The experimental STM image of TCNQ(ML) on N-doped graphene recorded at $V_b = -1.5$ V shows sharp contrast between TCNQ at the N-site and the C-site, see Fig. 5.16(b). This happens because as the bias voltage of the STM image lies in the close vicinity of the energy position of the charging peak of TCNQ at the N-site then the STS captures that state of the TCNQ from which electrons are transferred to the STM tip. Since the shape of the brighter molecule in Fig. 5.16(b) corresponds to the shape of the LUMO of isolated TCNQ in the gas phase [see inset in Fig. 5.16(a)], it is revealed that during the charging process electron transfer takes place from the LUMO of TCNQ to the STM tip. The LUMO of TCNQ was already occupied upon adsorption on N-doped graphene. Therefore the STM image obatined at $V_b = -1.5$ V captures the LUMO of TCNQ above N-site while it can not capture any state of TCNQ above C-site, since they lie in the gap at this voltage.

From the STS of TCNQ(ML) on pristine graphene we already know the broader reasonance observed in the positive bias corresponds to the LUMO state of TCNQ. The LUMO peaks for TCNQ molecules at the N-site and C-site are situated at 0.35 ± 0.06 V (red curve) and 0.85 ± 0.06 V (black curve), respectively; see Fig. 5.16(a). Therefore, the shift in the LUMO for TCNQ above N-sites and C-sites is less than the shift in the charging peaks of TCNQ above N-sites and C-sites. For this reason, the experimental STM image recorded at $V_b = +1$ V, see Fig. 5.16(c), does not show any contrast between TCNQ molecules at the N-site and at C-sites. The LUMO of TCNQ above a N-site is situated close to the Fermi energy, this confirms an increase in electron transfer from graphene to TCNQ molecules at N-sites. A similar feature has been previously reported for porphyrin on N-doped graphene.[63]

Our DFT calculations show that, in the absence of any electric field, the number of electrons gained by the TCNQ molecules at N-sites and C-sites is 0.33 e and 0.20 e,

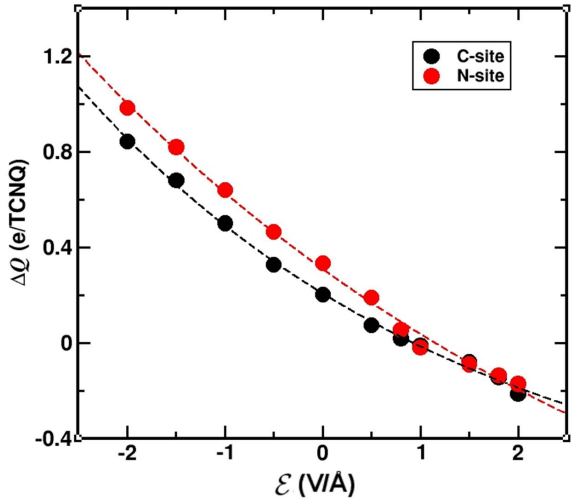

Figure 5.17: Charge gained by TCNQ, ΔQ as a function of $\mathcal{E}$. The black and red circles show TCNQ at C-site and N-site, respectively.

respectively. (The molecule at C-site is chosen to be that molecule which is situated at the farthest distance, within the unit cell, from the N atom in graphene – or any of its periodic images.) As a consequence of this, the charging peak at the N-site is situated closer to the Fermi level [see the red peak in Fig. 5.16(a)], and hence a lower electric field is required to bring the LUMO state to the Fermi level.

In Fig. 5.17 we have shown how the charge gained by TCNQ at the N-site and the C-site changes as a function of the applied electric field $\mathcal{E}$. The black and red circles show ΔQ for TCNQ above C-site and N-site, respectively. As $\mathcal{E}$ becomes more negative, the TCNQ molecule above the N-site gains more electrons than the TCNQ molecule above the C-site. For both the cases (the N-site and the C-site), ΔQ increases with $\mathcal{E}$. As $\mathcal{E}$ becomes more positive, and the substrate now acts as an acceptor, ΔQ becomes almost the same at the C-site and N-sites. In the case of the TCNQ(ML) on N-doped graphene also we see a non-uniform slope for the graph of ΔQ vs. $\mathcal{E}$, as was also seen in Fig. 5.9 for TCNQ(ML) on pristine graphene. This happens for the same reason which was already discussed in the previous section.

We have already mentioned that since a TCNQ molecule at a N-site gains more electrons than at a C-site, the molecular states of TCNQ at N-site are more occupied than at a C-site. This implies that the TCNQ states above N-site and C-site should

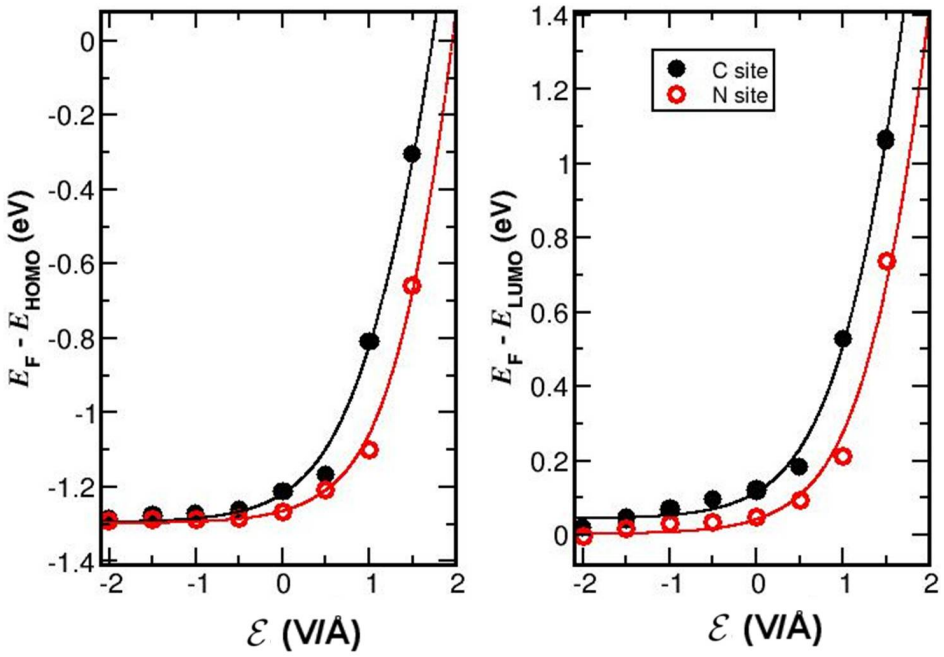

Figure 5.18: Change in HOMO (E_{HOMO}) and LUMO (E_{LUMO}) of TCNQ with $\mathcal{E}$. The molecular states of TCNQ at the C-site and the N-site are shown by solid black and hollow red circles, respectively.

be positioned differently in energy. To determine the energy positions of the molecular levels at these two different sites, DFT calculations are performed. Similar to the case of adsorption on pristine graphene, in the case of N-doped graphene also we want to study the movement of TCNQ states as a function the applied electric field. The positions of E_{HOMO} and E_{LUMO} of TCNQ with respect to the Fermi energy E_{F} are plotted as a function of $\mathcal{E}$ for TCNQ at a N-site and a C-site in Fig. 5.18. The energy levels of TCNQ at the N-site are downshifted with respect to those at the C-site, for all values of $\mathcal{E}$, because TCNQ at the N-site becomes more electron-rich than at the C-site due to electron transfer from the graphene substrate.

As $\mathcal{E}$ becomes more positive, both the HOMO and LUMO states of TCNQ at the N-site become well separated from the HOMO and LUMO of TCNQ at the C-site. The LUMO of TCNQ adsorbed above N lies closer to the Fermi level than above C.

The simulated STM image shown in Fig. 5.16(d) is obtained for $\mathcal{E} = +1.5$ V/Å and $V_b = +0.74$ V (at 0.22% doping concentration). Under this condition, the LUMOs of TCNQ on N- and C-sites are situated at 0.74 eV and 1.06 eV, respectively. Therefore,

at $V_b = +0.74$ V one is mimicking the situation where the bias voltage includes the LUMO for TCNQ above N, while remaining in the gap of the surrounding molecules. The simulated STM image [see Fig. 5.16(d)] reproduces well the experimental image, which confirms our interpretation, though the physical origins of these two STM images are different: the experimental STM is imaged at the bias voltage corresponding to the charging peak of TCNQ above N-site, whereas the simulated STM is taken at the bias volatge corresponding to the LUMO peak of TCNQ above N-site.

The simulated STM image shown in Fig. 5.16(e) is obtained at $V_b = +0.5$ V without any electric field. Fig. 5.16(e) does not show any contrast between the TCNQ above the C-site and above the N-site. This happens becuase the LUMOs of TCNQ at the N-site and C-site are situated quite close to each other for $\mathcal{E} = 0$ V/Å (see Fig. 5.18). Therefore, at $V_b = +0.5$ V the LUMO of TCNQ molecules above both the N-site and C-site are captured.

5.4 Conclusions

In this chapter, we have shown that the charge transfer between organic molecules and graphene can be tuned in the presence of an external electric field. The results presented in this chapter are primarily focused on TCNQ(ML) on pristine and N-doped graphene. Electron transfer between TCNQ and graphene induces a dipole moment in the TCNQ/graphene system. The TCNQ molecule-on-graphene hybrid structure behaves as an electrostatic dipole. The dipole moment of the combined system is proportional to the applied electric field.

The charge density on graphene can be further modified by doping it with a donor type impurity. The insertion of nitrogen atoms as the donor-type dopant in graphene causes a shift in the energy levels of the molecules adsorbed directly above these N-sites. N-doping in graphene enhances electron transfer from graphene to TCNQ. Charging of TCNQ upon N-doping is a local effect. In experiments, we see that when an appropriate bias voltage is applied through the STM tip, selective charging of

these molecules takes place by transferring electrons from the molecule to the tip.

Combining the effect of the external electric field with N-doping of graphene permits one to perform selective reduction of a single TCNQ in the monolayer of the molecule. This implies that the molecular states above N-sites and C-sites lie at different energy poistions and they shift by different amounts (with respect to the Fermi level) as a function of the applied electric field. In the case of the TCNQ(ML) on N-doped graphene system also, the interfacial charge transfer can be tuned by varying the electric field.

Though the results presented in this chapter are primarily focussed on cases where a monolayer of TCNQ molecules are adsorbed on either pristine or N-doped graphene, we have also studied cases where a single TCNQ molecule is adsorbed on pristine and N-doped graphene as a function of electric field. The results obtained for single TCNQ on pristine and N-doped graphene substrates are similar to as obtained for the monolayer of TCNQ.

The results discussed in this chapter show how the molecule-graphene charge transfer can be selectively tuned by an applied electric field and nitrogen doping. This study suggests a novel way to modify the charge density in graphene, which should be useful for device-based applications.

Bibliography

[1] V. P. Gusynin and S. G. Sharapov *Phys. Rev. Lett.*, vol. 95, pp. 146801–146804, 2005.

[2] D. C. Pregibon, M. Toner, and P. S. Doyle *Science*, vol. 315, pp. 1393–1396, 2007.

[3] K. S. Novoselov, A. K. Geim, S. V. Morozov, D. Jiang, M. I. Katsnelson, I. V. Grigorieva, S. V. Dubonos, and A. A. Firsov *Science*, vol. 315, pp. 1393–1396, 2007.

[4] S. Y. Zhou, G.-H. Gweon, J. Graf, A. V. Fedorov, C. D. Spataru, R. D. Diehl, Y. Kopelevich, D.-H. Lee, S. G. Louie, and A. Lanzara *Nat. Phys.*, vol. 2, pp. 595–599, 2006.

[5] K. S. Novoselov, A. K. Geim, S. V. Morozov, D. Jiang, Y. Zhang, S. V. Dubonos, I. V. Grigorieva, and A. A. Firsov *Science*, vol. 306, pp. 666–669, 2004.

[6] F. Joucken, Y. Tison, J. Lagoute, J. Dumont, D. Cabosart, B. Zheng, V. Repain, C. Chacon, Y. Girard, A. R. Botello-Méndez, S. Rousset, R. Sporken, J.-C. Charlier, and L. Henrard *Phys. Rev. B*, vol. 85, p. 161408, 2012.

[7] R. Lv and M. Terrones *Mater. Lett.*, vol. 78, pp. 209–218, 2012.

[8] H. Wang, T. Maiyalagan, and X. Wang *ACS Catal.*, vol. 2, pp. 781–794, 2012.

[9] X. Wang, G. Sun, P. Routh, D.-H. Kim, W. Huang, and P. Chen *Chem. Soc. Rev.*, vol. 43, pp. 7067–7098, 2014.

[10] L. K. Putri, W.-J. Ong, W. S. Chang, and S.-P. Chai *Appl. Surf. Sci.*, vol. 358, pp. 2–14, 2015.

[11] V. Georgakilas, M. Otyepka, A. B. Bourlinos, V. Chandra, N. Kim, K. C. Kemp, P. Hobza, R. Zboril, and K. S. Kim *Chem. Rev.*, vol. 112, pp. 6156–6214, 2012.

[12] K. S. Novoselov, A. K. Geim, S. V. Morozov, D. Jiang, Y. Zhang, S. V. Dubonos, I. V. Grigorieva, and A. A. Firsov *Science*, vol. 306, pp. 666–669, 2004.

[13] P. Avouris *Nano lett.*, vol. 10, pp. 4285–4294, 2010.

[14] F. Schwierz *Nat. nanotechnol.*, vol. 5, pp. 487–496, 2010.

[15] K. S. Novoselov, V. Fal, L. Colombo, P. Gellert, M. Schwab, and K. Kim *Nature*, vol. 490, pp. 192–200, 2012.

[16] T. Kuila, S. Bose, A. K. Mishra, P. Khanra, N. H. Kim, and J. H. Lee *Prog. Mater. Sci.*, vol. 57, pp. 1061–1105, 2012.

[17] K. P. Loh, Q. Bao, P. K. Ang, and J. Yang *J. Mater. Chem.*, vol. 20, pp. 2277–2289, 2010.

[18] Q. H. Wang and M. C. Hersam *Nat. Chem.*, vol. 1, pp. 206–211, 2009.

[19] X. Dong, D. Fu, W. Fang, Y. Shi, P. Chen, and L.-J. Li *Small*, vol. 5, pp. 1422–1426, 2009.

[20] X. Wang, J.-B. Xu, W. Xie, and J. Du *J. Phys. Chem. C*, vol. 115, pp. 7596–7602, 2011.

[21] M. Cui, Y. Guo, Y. Zhu, H. Liu, W. Wen, J. Wu, L. Cheng, Q. Zeng, and L. Xie *J. Phys. Chem. C*, vol. 122, pp. 7551–7556, 2018.

[22] C. Coletti, C. Riedl, D. S. Lee, B. Krauss, L. Patthey, K. von Klitzing, J. H. Smet, and U. Starke *Phys. Rev. B*, vol. 81, pp. 235401–235408, 2010.

[23] W. Chen, S. Chen, D. C. Qi, X. Y. Gao, and A. T. S. Wee *J. Am. Chem. Soc.*, vol. 129, pp. 10418–10422, 2007.

[24] P. Solis-Fernández, S. Okada, T. Sato, M. Tsuji, and H. Ago *ACS Nano*, vol. 10, pp. 2930–2939, 2016.

[25] P. Sol´is-Fernández, S. Okada, T. Sato, M. Tsuji, and H. Ago *ACS Nano*, vol. 10, pp. 2930–2939, 2016.

[26] W. Chen, S. Chen, D. C. Qi, X. Y. Gao, and A. T. S. Wee *J. Am. Chem. Soc.*, vol. 129, pp. 10418–10422, 2007.

[27] A. Riss, S. Wickenburg, L. Z. Tan, H.-Z. Tsai, Y. Kim, J. Lu, A. J. Bradley, M. M. Ugeda, K. L. Meaker, K. Watanabe, T. Taniguchi, A. Zettl, F. R. Fischer, S. G. Louie, and M. F. Crommie *ACS Nano*, vol. 8, pp. 5395–5401, 2014.

[28] S. Wickenburg *et al. Nat. Commun.*, vol. 7, p. 13553, 2016.

[29] I. S. S. de Oliveira and R. H. Miwa *J. Chem. Phys.*, vol. 142, p. 044301, 2015.

[30] M. Muruganathan, J. Sun, T. Imamura, and H. Mizuta *Nano Letters*, vol. 15, pp. 8176–8180, 2015.

[31] S. Barja, M. Garnica, J. J. Hinarejos, A. L. Vazquez de Parga, N. Martin, and R. Miranda *Chem. Commun.*, vol. 46, pp. 8198–8200, 2010.

[32] D. Maccariello, M. Garnica, M. A. Nio, C. Navo, P. Perna, S. Barja, A. L. Vzquez de Parga, and R. Miranda *Chem. Mater.*, vol. 26, pp. 2883–2890, 2014.

[33] I. F. Torrente, K. J. Franke, and J. I. Pascual *Int. J. Mass Spectrom.*, vol. 277, pp. 269 – 273, 2008.

[34] M. Garnica, D. Stradi, S. Barja, F. Calleja, C. Diaz, M. Alcami, N. Martin, A. L. Vazquez de Parga, F. Martin, and R. Miranda *Nat. Phys.*, vol. 9, pp. 368–374, 2013.

[35] P. Giannozzi *et al. J. Phys. Condens. Matter*, vol. 21, p. 395502, 2009.

[36] D. Vanderbilt *Phys. Rev. B.*, vol. 41, pp. 7892–7895, 1990.

[37] J. P. Perdew, K. Burke, and M. Ernzerhof *Phys. Rev. Lett.*, vol. 77, p. 3865, 1996.

[38] H. J. Monkhorst and J. D. Pack *Phys. Rev. B*, vol. 13, p. 5188, 1976.

[39] S. Grimme *J. Comput. Chem.*, vol. 27, pp. 1787–1799, 2006.

[40] N. Marzari, D. Vanderbilt, A. D. Vita, and M. C. Payne *Phys. Rev. Lett.*, vol. 82, pp. 3296–3299, 1999.

[41] R. P. Feynman *Phys. Rev.*, vol. 56, pp. 340–343, 1939.

[42] K. Kunc and R. Resta *Phys. Rev. Lett.*, vol. 51, p. 686, 1983.

[43] B. Kozinsky and N. Marzari *Phys. Rev. Lett.*, vol. 96, p. 166801, 2006.

[44] R. F. W. Bader, *Atoms in Molecules: A quantum theory.* Oxford University Press, New York, 1990.

[45] W. Tang, E. Sanville, and G. Henkelman *J. Phys.: Condens. Matter*, vol. 21, p. 084204, 2009.

[46] T. C. Leung, C. L. Kao, and W. S. Su *Phys. Rev. B*, vol. 68, p. 195408, 2003.

[47] S. Ling, M. B. Watkins, and A. L. Shluger *Phys. Chem. Chem. Phys.*, vol. 15, pp. 19615–19624, 2013.

[48] J. Tersoff and D. Hamann *Phys. Rev. Lett.*, vol. 50, p. 1998, 1983.

[49] J. T. Sun, Y. H. Lu, W. Chen, Y. P. Feng, and A. T. S. Wee *Phys. Rev. B*, vol. 81, pp. 155403–155409, 2010.

[50] S. Yang, Y. Jiang, S. Li, and W. Liu *Carbon*, vol. 111, pp. 513 – 518, 2017.

[51] M. Garnica, D. Stradi, S. Barja, F. Calleja, C. Diaz, M. Alcam´i, A. L. Mart´in, Nazario Vázquez de Parga, and Marti

[52] S. Barja, M. Garnica, J. J. Hinarejos, A. L. Vazquez de Parga, N. Martin, and R. Miranda *Chem. Commun.*, vol. 46, pp. 8198–8200, 2010.

[53] I. Fernández-Torrente, D. Kreikemeyer-Lorenzo, A. Stróżecka, K. J. Franke, and J. I. Pascual *Phys. Rev. Lett.*, vol. 108, p. 036801, 2012.

[54] N. Kocic, P. Weiderer, S. Keller, S. Decurtins, S.-X. Liu, and J. Repp *Nano Lett.*, vol. 15, pp. 4406–4411, 2015.

[55] N. A. Pradhan, N. Liu, C. Silien, and W. Ho *Phys. Rev. Lett.*, vol. 94, p. 076801, 2005.

[56] V. W. Brar, R. Decker, H.-M. Solowan, Y. Wang, L. Maserati, K. T. Chan, H. Lee, C. O. Girit, A. Zettl, S. G. Louie, M. L. Cohen, and M. F. Crommie *Nat. Phys.*, vol. 7, pp. 43–47, 2011.

[57] Y. Wang, V. W. Brar, A. V. Shytov, Q. Wu, W. Regan, H.-Z. Tsai, A. Zettl, L. S. Levitov, and M. F. Crommie *Nat Phys*, vol. 8, pp. 653–657, 2012.

[58] K. Teichmann, M. Wenderoth, S. Loth, R. G. Ulbrich, J. K. Garleff, A. P. Wijnheijmer, and P. M. Koenraad *Phys. Rev. Lett.*, vol. 101, p. 076103, 2008.

[59] W. Schottky *Zeitschrift für Physik*, vol. 113, pp. 367–414, 1939.

[60] Z. Maksić and G. Alagona, *Theoretical Models of Chemical Bonding*. Springer-Verlag, Berlin Heidelberg, 1991.

[61] R. M. Metzger *Ann. NY Acad. Sci.*, vol. 313, pp. 145–165, 1978.

[62] R. M. Metzger *J. Chem. Phys.*, vol. 74, pp. 3458–3471, 1981.

[63] V. D. Pham, J. Lagoute, O. Mouhoub, F. Joucken, V. Repain, C. Chacon, A. Bellec, Y. Girard, and S. Rousset *ACS Nano*, vol. 8, pp. 9403–9409, 2014.

Chapter 6

A Descriptor for the Degree of Ionicity of Chemical Bonds in Binary Compounds

In this chapter, our aim is to formulate a descriptor that can describe the degree of ionicity in chemical bonds, from first principles. For this purpose, we have performed density functional theory calculations on several binary compounds. We believe that the ionicity of these compounds correlates well with a simple descriptor. This descriptor depends on the electronegativities and the atomic sizes of the cations and anions forming those binary compounds.

6.1 Introduction

Conventional bonds in chemical compounds fall into two main categories: ionic and covalent (there are, of course, also other types of bonds, e.g., metallic bonds in metals, and various kinds of weak bonds such as hydrogen bonds and van der Waals bonds, which we will not concern ourselves with in this chapter).

A bond can be perfectly ionic when two oppositely charged chemical species are bound together via electrostatic interactions. In the case of perfect ionic bonding

one atom or molecule completely donates electrons from its outermost orbital(s) to another atom or molecule. Therefore, the ionic model is based on the assumption that the molecules and crystals are composed of spherical ions with integral charges held together via the Coulombic attraction between these ions. The ionic compounds form crystal structures in their solid phase. The two main parameters that determine the structure of the ionic compounds are the difference in the charges between the ions and their relative sizes. The formation energy or lattice energy of the ionic compounds can be obtained by using the Born-Haber cycle. For example, in the case of sodium chloride the lattice energy is calculated to be 787 kJ/mol.[1] The electrostatic potential in an ionic compound can be determined by using the Madelung constant which approximates the ions as point charges.[2]

In contrast, in the case of covalent bonding, sharing of electron pairs takes place between the atoms participating in the bond. According to Lewis, an electron pair is shared between two atoms if it is used to complete the valence shell of both the atoms participating in the bond. This "sharing" of electrons between two atoms is not so clear in terms of the electron density. It simply implies that in a covalent bond the electron density is accumulated between the two atoms. The electrostatic attraction between this electron density and the two nuclei holds the two atoms together and stabilizes the molecule or compound. The purely covalent bonds are those where the sharing of electron pair(s) takes place between identical atoms, such as the C-C bond in ethane. Thus there is a large number of bonds having a character intermediate between an ionic and covalent bond. These bonds are usually known as 'polar covalent' bonds.

There is often some ambiguity about whether a bond is "ionic" or "covalent" in character. Actually, almost all the compounds which are known to form ionic bonds have some degree of covalency, or tendency to share electrons. When a bond is considered to have more "ionic character" then it is usually assumed that this bond has a small covalent character. Finally all these bonds, no matter how they

are described, are the result of the attractive electrostatic interaction between the electron density and the nuclei and the repulsion between the nuclei. Therefore, these terminologies to describe a bond in a particular compound are unfortunately not rigorously defined.

In this chapter, we will consider the question of whether it is possible to quantify the degree of ionicity of bonds, focusing on the particular case of binary compounds. The utility of the concepts and tools developed in this chapter should become more obvious in the next chapter, where these ideas will be applied in the context of aliovalent doping of oxides. Before going into details regarding how to analyze whether a bond is ionic or covalent, and the degree of ionicity in particular bonds, let us first discuss some properties which a perfect ionic compound should have. Ionic compounds are good conductors of electricity, especially in the solid phase. They usually have a high melting point that depends on the nature of the composite ions. The higher are the charges on the composite ions, the stronger are the cohesive forces, and the higher is the melting point of the compound. Ionic compounds tend to be soluble in water; their solubility depends on the cohesive forces.

6.1.1 Previously Known Ionicity Scales

Insight into and characterization of the bonds in any molecule or crystal finally depend on the analysis and understanding of the electron density distribution among the atoms participating in the bonding. In the literature, there exist some previously defined ionicity scales.

The first ionicity scheme proposed by Pauling (1932) was based on a thermochemical approach.[1] According to Pauling's definition, electronegativity is considered as the strength of an atom in a molecule to attract electrons towards itself. This definition highlights the historical origins of the concept of charge flow in electrochemistry. However, even if the complete charge distribution in the molecule or crystal is known precisely, one would still need a prescription which can decompose the total distribution into a superposition of charge distributions centered on the

atoms composing the solid. To solve this difficulty, Pauling turned from charge distributions to bond energies, which are known as the heats of formation. Let E_{XY} be the formation energy of a diatomic molecule XY. Then, for a molecule AB, consider the quantity $\epsilon_{AB} = E_{AB} - (E_{AA} + E_{BB})/2$, this is a measure of $(\chi_A - \chi_B)$, the difference in electronegativity between atom A and B. When the atoms A and B form a bond, then electron transfer takes place from the less to the more electronegative atom. Pauling introduced the concept of fractional ionic character by defining a quantity f_{AB}, where $f_{AB} = f_{BA}$ and $0 \leq f_{AB} \leq 1$, and $f_{AB} = 1$ for the ionic extreme. According to Pauling's model, $(\chi_A - \chi_B)^2 = \gamma \epsilon_{AB}$. The term γ ensures that χ_A and χ_B change by 0.5 with each unit change in valency in the first row of the periodic table: $f_{AB} = 1 - e^{[-\frac{\chi_A - \chi_B}{4}]} = 1 - e^{-\frac{\gamma \epsilon_{AB}}{4}}$. For crystals, the above mentioned form of f_{AB} is modified as: $f_{AB} = 1 - \frac{N}{M} e^{-\frac{\gamma \epsilon_{AB}}{4}}$. The N/M factor reflects the increased ionic character of resonant bonds, which appear when the classical valency N is smaller than the coordination number M.[3] f_{AB} is the quantity which is used to understand the chemical behavior of the bonds in any compound. The term f_{AB} depends only on the difference in electronegativities, and is independent of other quantities (e.g., bond lengths, bond angles, etc.) Clearly, f_{AB} measures the fraction of ionic character in any compound, and lies between 0 and 1.

Coulson, Redei, and Stockers (1962) developed a theory to define the ionicity based on the molecular-orbital approach.[4] Their method was proposed for the study of the tetrahedrally coordinated octet binary compounds $A^N B^{8-N}$. The bonding orbital can be written in the form $\psi = \phi_A + \lambda \phi_B$, where ϕ_A and ϕ_B are the sp^3 hybridized atomic orbitals centered on atoms A and B, respectively. The term λ can be determined variationally. Upon normalization, the bond ionicity can be defined as: $i_C = \frac{\lambda^2 - 1}{\lambda^2 + 1}$, by considering the relative weights of the atomic orbitals in ψ. Using this approximation the net atomic charges can be calculated as: $Q_A = \frac{N\lambda^2 - (8-N)}{(1+\lambda^2)}$ $= -Q_B$. Thus, the method proposed by Coulson *et al.* to measure the ionicity of chemical bonds is applicable for tetrahedrally coordinated octet compounds, taking

into account the relative weights of the atomic orbitals.

The ionicity scale introduced by Phillips (1970) is based on a dielectric model of the chemical bonds in $A^N B^{8-N}$ crystals, which depends on two band gap parameters C and E_h.[5] E_h is the homopolar gap which is defined as the symmetric part of the total potential $\frac{1}{2}(V_A + V_B)$, while the ionic or charge-transfer gap C originates from the effect of the antisymmetric part $\frac{1}{2}(V_A - V_B)$. The average gap between valence and conduction bands is given by $E_g^2 = E_h^2 + C^2$. Phillips's model defines the ionicity as $f_i = \frac{C^2}{E_g^2}$. For example, the homopolar gap (E_h) for a compound of lattice constant a can be calculated by scaling the optical gaps of group-IV elements, e.g., diamond and silicon: $E_h = E_h(Si)(\frac{a(Si)}{a}^{2.5})$. One of the most important features of Phillips's ionicity model is that a critical value of f_i separates the tetrahedral compounds from the octahedral compounds.

The ionicity scale proposed by Garcia and Cohen (1993) is based on the asymmetry of the electronic charge distribution.[6] They calculated the valence charge densities of the $A^N B^{8-N}$ binary compounds using *ab initio* calculations. In this model the electronic charge density is decomposed into symmetric ρ_S and asymmetric ρ_A components: $\rho_S(\mathbf{r}) = 1/2\ [\rho(\mathbf{r}) + \rho(\text{-}\mathbf{r})]$ and $\rho_A(\mathbf{r}) = 1/2\ [\rho(\mathbf{r}) - \rho(\text{-}\mathbf{r})]$. The quantities S_S and S_A measure the strength of the symmetric and anti- symmetric components of the electronic charge density ρ over the entire unit cell, which are actually probability densities. The charge asymmetery coefficient g is defined as: $g = \sqrt{\frac{S_A}{S_S}}$. Due to the physical constraint $\rho(\mathbf{r}) \geq 0$ on the valence electron density, $|\rho_A(\mathbf{r})| \leq |\rho_S(\mathbf{r})|$, therefore, $0 \leq g \leq 1$. The value $g = 0$ corresponds to homopolar compounds and purely covalent bonds. In the case of "purely" ionic materials g becomes close to unity.

6.2 Computational Details

All calculations are performed using *ab initio* density functional theory (DFT) as implemented in the Quantum ESPRESSO package.[7] A plane wave basis set is

used to solve the Kohn-Sham equations,[8] with cut-offs of 45 Ry and 400 Ry for the wavefunctions and charge densities, respectively. Ultrasoft pseudopotentials are used to describe the electron-ion interactions,[9] and the exchange-correlation interactions are treated within the Perdew-Burke-Ernzerhof (PBE) form of the generalized gradient approximation (GGA).[10] The 'topological' charges on each atom are calculated using the charge partitioning method proposed by Bader.[11, 12]

6.2.1 Bader Analysis

Richard Bader proposed a method to 'divide' molecules into atoms. The definition of an atom according to Bader's model is purely based on topological properties of the electronic charge density. Bader's prescription uses zero flux surfaces to separate the atoms present in a molecule or solid. A zero flux surface consists of a two-dimensional area on which the electronic charge density becomes a minimum perpendicular to the surface. In the case of any molecular system the charge density becomes a minimum between the atoms, therefore this is the most obvious place to separate the atoms from each other.

Bader analysis is a charge partitioning method which helps us to quantify the charge associated with each atom in a molecule or solid. Apart from charge analysis, Bader's prescription has applications in measuring the multipole moments of the interacting atoms or molecules in a compound, and also in defining the chemical hardness of the atoms.[11]. We have followed the terminology used by previous authors[13] in terming the charge calculated using the Bader method the topological charge $\mathcal{Q}_T$, to avoid confusion we wish to emphasize that this terminology arises from the fact that the charge has been determined by making use of the topological properties of the charge density, and does not have any connection with the novel topological phases that have recently attracted much attention in condensed matter physics.

Note that in an "ionic" compound, we rarely have perfect ionicity and therefore rarely is the topological charge $\mathcal{Q}_T$ identically equal to the nominal oxidation state

Table 6.1: List of the different elements whose binary compounds are considered in this chapter, together with the values of their electronegativity (χ) and covalent radii. Values of χ and R are taken from Refs. 14 and 15 respectively.

Element X	Electronegativity χ	Covalent radius R (Å)
Na	0.93	1.54
Ca	1.00	1.74
Mg	1.31	1.30
Al	1.61	1.18
Cu	1.90	1.38
Pt	2.28	1.28
F	3.98	0.71
O	3.44	0.73
Cl	3.16	0.99
N	3.04	0.75
S	2.58	1.02

OS. Usually, the bond has some amount of covalent character, as a result of which $|\mathcal{Q}_T| < |OS|$ for both the cations and anions.

6.3 Systems

To quantify the degree of ionicity in various binary compounds we choose several elements from the periodic table with different electronegativities and covalent radii, listed in Table 6.1. The binary compounds made out of those elements are listed in Table 6.2. The stoichiometry and crystal structures of the compounds were taken from the crystallographic database (Ref. 16), the structures were further refined by performing geometric relaxation and optimizing lattice constants using density functional theory calculations.

6.4 Results

To quantify the degree of ionicity in binary compounds we are looking for a "descriptor" which would help to determine whether a given compound is ionic or not. Before looking for a descriptor one needs to decide the "target property". In this study we have chosen the quantity $\mathcal{Q}_T/OS$ as the target property; this is the

Table 6.2: List of the binary compounds formed by different cations and anions. The crystal structures of the compounds were taken from the crystallographic database in Ref. 16.

Cation \ Anion	F	O	Cl	N	S
Na	NaF	Na_2O	$NaCl$	Na_3N	Na_2S
Ca	CaF_2	CaO	$CaCl_2$	Ca_2N	CaS
Mg	MgF_2	MgO	$MgCl_2$	No compound found	MgS
Al	AlF_3	Al_2O_3	$AlCl_3$	AlN	Al_2S_3
Cu	CuF CuF_2	CuO Cu_2O	$CuCl$ $CuCl_2$	Cu_3N	CuS CuS_2
Pt	PtF_4	PtO PtO_2	$PtCl_2$	PtN	PtS PtS_2

ratio of the topological charge $\mathcal{Q}_T$ to the nominal oxidation state OS of an atom, and serves as a measure of the degree of ionicity. This ratio is an 'obvious' choice to use as a measure of ionicity, and previous authors have also used it.[13] In the case of "perfect" ionic compounds this ratio approaches 1, i.e., the value of topological charge approaches the value of the nominal oxidation state. Thus, the ratio of the topological charge, $\mathcal{Q}_T$, to the nominal oxidation state, OS, provides a measure of the deviation from the ideal ionic model for any chemical bond.

To formulate a descriptor which can predict the ionicity of any binary compound, we have considered various parameters which involve different properties of the atoms of which the system is comprised. In this context, electronegativity is obviously an important parameter to determine the charge distribution between any two atoms participating in a bond. Electron transfer between the atoms of different elements depends on their electronegativity difference. In a binary compound, the difference in electronegativity between the cations and anions participating in a bond is given as: $\Delta\chi = \chi(\text{anion}) - \chi(\text{cation})$, where $\chi(X)$ is the electronegativity of the element X.

It is known that the ionicity or covalency of bonds can also be affected by the sizes or radii of the atoms involved. Therefore, next, we considered various combinations of $\Delta\chi$ and the atomic radii R of the two elements involved in forming the compound,

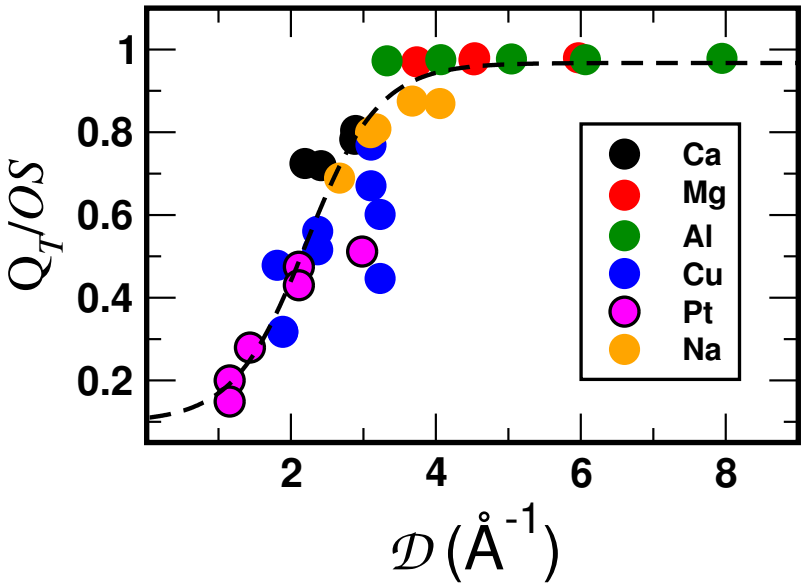

Figure 6.1: $\mathcal{Q}_T/OS$ is plotted as a function of the descriptor $\mathcal{D}$. $\mathcal{Q}_T/OS$ shows approximately hyperbolic tangent (dashed line) behavior with the descriptor. As the value of $\mathcal{Q}_T/OS$ approaches 1 the compounds become "purely" ionic.

as possible descriptors.

After trying with several functional forms built up out of terms $\Delta\chi$ and the radii R of the elements involved, we obtain the best correlation (least deviation) between the target property $\mathcal{Q}_T/OS$ and the descriptor when the latter has the functional form:

$$\mathcal{D} = \frac{\Delta\chi}{\Delta R} = \frac{\chi_{anion} - \chi_{cation}}{R_{cation} - R_{anion}} \tag{6.1}$$

Note that we have tried to build up descriptors using different definitions for the atomic sizes for the elements considered in this study, e.g., covalent radii,[15] ionic radii,[17] and van der Waals radii.[18] Finally, we find the best correlation between the target property and the descriptor when we use the covalent radius for each element. The numerical values of the covalent radii, R are taken from Ref. 15; see the tabulated values in Table 6.1.

The variation of the target property, $\mathcal{Q}_T/OS$ as a function of the descriptor, $\mathcal{D}$ is plotted in Fig. 6.1. $\mathcal{D}$ shows $\sim$ hyperbolic tangent behavior with the target property

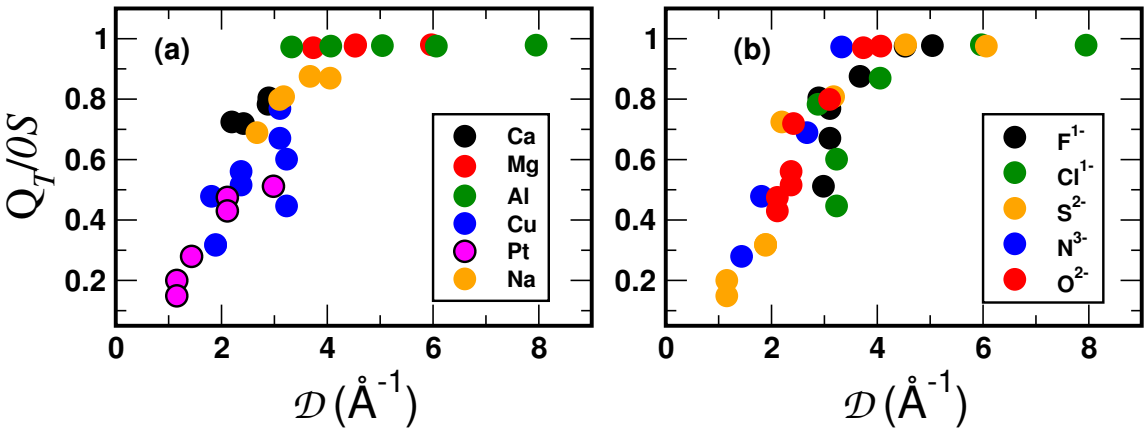

Figure 6.2: $\mathcal{Q}_T/OS$ is plotted as function of the descriptor $\mathcal{D}$. The compounds are labeled and colored with respect to the (a) cations and (b) anions. Data points of a given color seem to cluster together when they are colored with respect to the cations, however data points of the same color are quite scattered when they are colored based on the anions.

(see the dashed line in Fig. 6.1). From Fig. 6.1 we see that $\mathcal{Q}_T/OS$ increases with $\mathcal{D}$ and approaches 1 when $\mathcal{D} \geq 4$. The value of $\mathcal{Q}_T/OS \approx 1$ implies perfect ionic character of a bond. The binary compounds for which the target property approaches 1 are those that are perfectly ionic. As $\mathcal{D}$ becomes < 4, $\mathcal{Q}_T/OS$ reduces, hence the compounds become less ionic. For smaller values of $\mathcal{D}$ the compounds tend to show more covalent character than ionic since the value of $\mathcal{Q}_T/OS$ deviates quite significantly from 1. The compounds composed of Mg and Al are purely ionic, see the red and green circles in the figure, whereas the compounds of Na are somewhat less so; we have verified the reproducibility of this result by using different pseudopotentials, increasing the plane wave cut-off, etc. The blue points corresponding to Cu compounds show some scatter – while some of them fall on the dashed curve, others seem to fall quite off the curve. This may be due to the fact that Cu in different Cu compounds can have different oxidation states, and trying to use a single descriptor to capture the behavior of Cu in all these various situations does not suffice.

In Fig. 6.2 we have once again plotted $\mathcal{Q}_T/OS$ as a function of $\mathcal{D}$, same as Fig. 6.1, but here the compounds are labeled in two ways. All the binary compounds studied in this chapter are labeled with respect to their cations in Fig. 6.2(a), while the

compounds are labeled with respect to their anions in Fig. 6.2(b). In Fig. 6.2(a), when the data points are colored according to the cations, symbols of a given color seem to be clustered together. In contrast, in Fig. 6.2(b) we see no obvious clustering of the data points when the compounds are colored with respect to the anions and the data points are actually quite scattered if we compare the data points with the same color. This suggests that cations play a more dominant role than anions in determining the ionicity of the bonds in a compound.

From Figs. 6.1 and 6.2 we see the data corresponding to the binary compounds where the cation is either Pt or Cu and the anion is either F or Cl, fall slightly off from the hyperbolic tangent fit. It is possible that this feature can be improved by measuring the radii of these elements based on some other approach, suggesting a possible future direction to pursue.

6.5 Conclusions

We have formulated a simple descriptor $\mathcal{D} = \Delta\chi/\Delta R$ to quantify the degree of ionicity of chemical bonds in binary compounds. We have found a reasonably good correlation between $\mathcal{D}$ and the target property $\mathcal{Q}_T/OS$, where $\mathcal{Q}_T$ is the topological (Bader) charge on the cation or anion, and OS is the nominal oxidation state of the cation or anion. As the descriptor $\mathcal{D}$ becomes ≥ 4, $\mathcal{Q}_T/OS$ approaches 1, therefore the compounds become "purely" ionic. The compounds having smaller values of $\mathcal{D}$, and hence the value of $\mathcal{Q}_T/OS$ much less than 1, are less ionic or more covalent. Therefore $\Delta\chi/\Delta R$ can be used as a descriptor for the measure of ionicity. To the best of our knowledge this is the first time that a descriptor for ionicity has been formulated that explicitly involves not just differences in electronegativity but also differences in atomic sizes. The ideas that have emerged in this chapter will be further extended and utilized in the next chapter.

Bibliography

[1] L. Pauling, *The Nature of the Chemical Bond*. Cornell University Press, 1960.

[2] C. Kittel, *Introduction to Solid State Physics*. Wiley - India, 2007.

[3] L. Pauling, *The Nature of the Chemical Bond*. Cornell University Press, 1939.

[4] C. A. Coulson, L. B. Redei, and D. Stocker *Proc. R. Soc. London*, vol. 270, p. 352, 1962.

[5] J. C. Phillips *Rev. Mod. Phys.*, vol. 42, pp. 317–356, 1970.

[6] A. Garc´ia and M. L. Cohen *Phys. Rev. B*, vol. 47, pp. 4215–4220, 1993.

[7] P. Giannozzi, S. Baroni, N. Bonini, M. Calandra, R. Car, C. Cavazzoni, D. Ceresoli, G. Chiarotti, M. Cococcioni, I.Dabo, A. D. Corso, S. de Gironcoli, S. Fabris, G. Fratesi, R. Gebauer, U. Gerstmann, C. Gougoussis, A. Kokalj, M. Lazzeri, L. Martin-Samos, N. Marzari, F. Mauri, R. Mazzarello, S. Paolini, A. Pasquarello, L. Paulatto, C. Sbraccia, S. Scandolo, G. Sclauzero, A. P. Seitsonen, A. Smogunov, P. Umari, and R. M. Wentzcovitch *J. Phys. Condens. Matter*, vol. 21, p. 395502, 2009.

[8] W. Kohn and L. J. Sham *Phys. Rev.*, vol. 140, p. A1133, 1965.

[9] D. Vanderbilt *Phys. Rev. B.*, vol. 41, pp. 7892–7895, 1990.

[10] J. P. Perdew, K. Burke, and M. Ernzerhof *Phys. Rev. Lett.*, vol. 77, p. 3865, 1996.

[11] R. F. W. Bader, *Atoms in Molecules - A quantum theory*. New York: Oxford University Press, 1990.

[12] W. Tang, E. Sanville, and G. Henkelman *J. Phys. Condens. Matter*, vol. 21, p. 084204, 2009.

[13] P. Mori-Sánchez, A. M. Pendás, and V. Luaña *J. Am. Chem. Soc.*, vol. 124, pp. 14721–14723, 2002.

[14] L. Pauling *J. Am. Chem. Soc.*, vol. 54, pp. 3570–3582, 1932.

[15] "Periodic table of the elements." http://www.onlineperiodictable.com, 2017. [Online; accessed Jan-2018].

[16] N. Day, "Open-access collection of crystal structures of organic, inorganic, metal-organics compounds and minerals, excluding biopolymers." http://www.crystallography.net/cod/, 2018. [Online; accessed June 2018].

[17] S. A. Nelson, "Coordination and pauling's rules." https://www.tulane.edu/~sanelson/eens211/paulingsrules.htm, 2014. [Online; accessed Jan-2018].

[18] A. Bondi *J. Phys. Chem.*, vol. 68, pp. 441–451, 1964.

Chapter 7

A Descriptor for the Efficacy of Aliovalent Doping and its Application for the Charging of Supported Au Clusters

In this chapter, we have used the doping of a substrate to tune the charge state of deposited Au nanoclusters. We have carried out calculations of substitutional doping of MgO with various kinds of impurity atoms. An Au monomer or Au dimer are then deposited on the doped MgO(001) substrates. We investigate how the charge state of the deposited Au clusters can be varied by changing the nature and concentration of the dopants. Next, the oxide substrate is further modified by placing it on the Mo support. We identify descriptors which can successfully predict the charge state and adsorption geometry of small Au clusters deposited on different substrates.

7.1 Introduction

It is hard to imagine modern day life without semiconductors. This era is based on semiconductor electronics. In this Information Age all our computers, the internet,

tablet devices, smartphones and all of the other things that make communication so easy these days are all dependent upon semiconductor technology. Doping of semiconductors modifies their electronic properties and conduction mechanisms, which play important roles in making them suitable for device applications.[1, 2]

Similar to the doping of semiconducting elements, such as Si and Ge, the doping of inorganic oxides plays an important role in advanced technologies such as catalysis, microelectronics, magnetism, superconductivity, optoelectronics, sensors, ferroelectrics, etc.[3–6] The doping of oxides is one of the most important activities in materials science since it modifies the physical, chemical, electronic and mechanical properties of the oxides, which can give rise to exciting physical and chemical properties, and open new perspectives for a variety of possible applications. Selective doping of semiconducting oxides like TiO_2, ZnO, Zn_2GeO_4, Zn_2WO_4, SnO_2, etc., has drawn great attention from both industrial and scientific communities, due to its potential applications. For example, F-doping in TiO_2,[7] Zn_2WO_4,[8] and SnO_2[9] results in band gap narrowing, which improves their photocatalytic acitivity; Nb/N [10] and Sb/N [11] co-doped TiO_2 show good activity for water splitting; and N/F co-doped Zn_2GeO_4 performs as a good photocatalyst under visible light irradiation.[12]

More interestingly, suitable doping can radically alter the electronic properties of other oxides also which are insulators and chemically inert, e.g., MgO, CaO, etc. For example, doping of MgO with N is found to result in ferromagnetism,[13] Li-doped and Ni-doped MgO have been used for methane coupling catalysis and in catalytic dissociation of N_2O, respectively,[14–17] Cr-doped MgO can work as a laser source in the near-infrared range,[18] and Al-doped MgO and Mo-doped CaO can alter the morphology of an adsorbed Au_{20} cluster from a three-dimensional tetrahedral structure to a two-dimensional planar structure by transferring an appreciable amount of charge,[19, 20] which in turn improves the catalytic activity of Au_{20}.[21]

To dope a material, one obvious question is how to choose the impurity atom. One possible way is substituional doping, for which the most obvious choice may

be to choose a donor type element that is immediately to the right of the element which we want to substitute in the periodic table, or with an acceptor type element immediately to the left. However, this need not necessarily be the best choice, this is the question we wish to explore here. In this study we dope MgO with both acceptor and donor type impurities to modify its electronic properties, so that MgO can serve as a suitable substrate to tune the charge state of deposited Au nanoclusters.

Bulk gold is inert, which makes it a precious metal with popular use in jewellery and decorations. However, in nano-dimensions gold has enhanced magnetic, optical and chemical properties that can be successfully used for a variety of applications. These properties can be tuned by varying not just the size and morphology of the particles, but also their charge state. For example, it has been shown that the magnetism of thiolate-protected gold nanoclusters can be turned off or on by changing their charge state.[22, 23] Similarly, adding electrons to gold nanorods has been shown to result in a blue shift in their absorption spectrum.[24]

The chemical properties of gold nanoparticles are especially remarkable. Au nanoparticles are well known for showing good catalytic activity for a variety of chemical reactions.[25] The catalytic activity of nano-sized Au was discovered in 1987 by Haruta *et al.*, who found that gold nanoparticles supported on semiconducting transition metal oxides could catalyze CO oxidation efficiently at low temperatures.[26] This finding started a new field towards investigation of new and unrecognized properties of gold in nano dimensions.[25] The oxidation resistant nature of Au clusters makes them effective catalysts for oxidation reactions, e.g., the oxidation of poisonous carbon monoxide to carbon dioxide.[27] Apart from oxidation, Au nanoparticles are found to catalyze several other reactions, e.g., the water-gas shift reaction,[28] the epoxidation of propene to propene oxide,[29] the selective hydrogenation of unsaturated hydrocarbons,[30] and various liquid phase oxidation reactions which have applications in the cosmetics and food industries. Ligand-stabilized Au nanoparticles are also used in nanoelectronics and biomedicine.[31]

The substrate on which Au nanoclusters are deposited plays an important role in modifying their physical and chemical properties. One of the most important roles of the substrate is to tune the charge state of the deposited Au nanoclusters by causing charge transfer between the substrate and the cluster,[32] which affects their catalytic activity. Similar to the magnetic and optical properties, the reactivity too is significantly enhanced by the charge state of the Au nanoparticles.

Previous authors have suggested several ways by which the charge state of Au nanoparticles can be tuned. One way is through charge transfer from an appropriately chosen (pristine) support. [33–44] This approach can be applied by modifying the support in one of three ways: (a) doping the support with an electron donor or acceptor,[19, 21, 45–48] (b) placing an ultrathin layer of the oxide support on a metal substrate, so that electrons from the metal can tunnel through the oxide,[33, 34, 49–53] (c) by deliberately introducing defects into the oxide support, such as oxygen vacancies (F-centers). [33, 54–58] Two further ways that have been suggested of tuning the charge state of Au nanoparticles are doping or alloying the nanoparticles themselves,[56, 59–62] and the application of an external electric field.[63]

Among these different possible ways of tuning the charge state of Au nanoclusters, substrate doping is perhaps the most appealing and easy method to implement in practice. Several authors have shown that substitutionally doping the cations of oxide supports with an aliovalent dopant (i.e., one with a different valency) results in a change in the morphology and charge state of Au atoms and/or clusters placed on the support.[19, 33, 34, 38, 43] The change in morphology and change in charge state are intimately connected, with charged clusters preferring to wet the oxide support. Importantly, the change in morphology of supported Au nanoparticles induced by aliovalent doping of the oxide support has been confirmed experimentally.[20] Doping the support with an electron donor makes the adsorbed Au nanoclusters negatively charged, while doping with an acceptor is expected to create an electron deficiency in the support, which should increase the tendency of the support to withdraw electrons

from the Au cluster, thus making it positively charged. However, due to the high electronegativity of Au, making the Au clusters positively charged can be a challenging task, and is of great interest.

In this study, our aim is to obtain an estimate of the range over which the charges of small Au clusters, deposited on a doped support can be tuned, either positively or negatively. Previous studies have found that an Au monomer (adatom) deposited on pristine MgO becomes negatively charged, with a charge of −0.30 e,[33, 49] and that this charge can be made more negative by substitutional doping by an electron donor, e.g., 2.22% doping with Cr^{2+} cations increases the charge to −0.81 e.[48] While there is no previous study on the charging of Au dimers by depositing them on doped supports, it has been shown that the charge on a twenty-atom Au cluster changes from −0.60 e to −1.24 e when the support is modified from pristine MgO to 2.78% Al-doped MgO.[19] To the best of our knowledge, the highest positive charge reported for an Au monomer in the literature is a value of +0.45 e, when the Au atom is adsorbed at a hollow site on anatase-TiO_2; it is important to note, however, that this geometry does not correspond to the global minimum, being energetically less stable than adsorption at the bridge site, for which the Au atom becomes neutral.[44]

We use the substrate modification technique to tune the charge state of deposited Au nanoclusters. We perform calculations where we dope the substrate with different types of dopants: both anionic and cationic, as well as acceptor-type and donor-type, in a model system like MgO. In this study, we wish to obtain an estimate of the range over which the charges can be tuned, either positively or negatively, by electron transfer either from the Au to the doped support or vice versa. In the literature, all of the studies up to now deal with cation doping of the oxide substrate to tune the charge state of the deposited nanoparticles, we wish to explore the possibility of anion doping also, and compare the two. The electronic properties of the MgO substrate are further modified by placing the doped MgO systems on a metal support, Mo.

Finally, we wish to formulate descriptors which can predict the efficacy of the

dopants towards charging an Au cluster adsorbed on the doped oxide surface. Descriptors are combinations of physical and chemical entities of a system which correlate well with some property of interest. The advantage of descriptors is they can be computed more easily than performing experiments and first principles calculations. Descriptors are often obtained by extracting information contained in large databases. In materials science, descriptors have been increasingly used to predict various properties of materials, e.g., the catalytic activity of nanoparticles, the crystal structure of octet compounds, the self-assembly of organic molecules, etc.[21, 64–67] In this chapter, we use descriptors to predict the charge gained or donated by aliovalent dopants in MgO, and also to determine the geometry and charge state of deposited Au nanoclusters on the doped MgO substrates, with the change in both the nature and concentration of the dopants. In Section 2, we discuss aliovalent doping of bulk MgO and formulate a descriptor to predict the charge acquired by each dopant atom. Section 3 describes the geometry and charge state of the deposited Au nanoclusters on doped MgO(001) substrates, and we show how the descriptor obtained in Section 2 can predict the efficacy of the dopants in tuning the charge state of the deposited Au nanoclusters on the doped MgO surfaces. In Section 4, we introduce a metal support, the Mo(001) surface, below the doped MgO substrate, to investigate the geometry and charge state of the adsorbed Au nanoclusters. We have calculated the work function of the doped MgO and MgO/Mo systems and have shown how the adsorption site, morphology and charge state of the deposited Au nanoclusters can be predicted using the work function of the support, in Section 5. After first considering one fixed position of the dopants while varying their concentrations, in Section 6, we show how the work function of the doped MgO/Mo systems varies with the change in position of the dopant. Finally, we summarize all our results as discussed in this chapter, in Section 7.

7.2 Aliovalent doping of bulk MgO with impurity atoms

In this section, we dope bulk MgO with different types of dopants, viz., with both anionic and cationic impurities, and compare the performance of the dopants using density functional theory calculations and by formulating a simple descriptor. Doping MgO with donor type impurities is expected to make the oxide electron-rich. In contrast, doping the oxide with acceptors is expected to create electron deficiency in the oxide. To choose the elements which can serve as possible donors, we first look immediately to the right of Mg and O in the periodic table and select anionic F and cationic Al to replace O and Mg, respectively in the oxide. Similarly, we first look immediately to the left of O and Mg in the periodic table for the acceptor type dopants of MgO, and select N as the anionic acceptor which can replace O in the oxide, while Na is the cationic acceptor which replaces Mg in the oxide. The concentration of the dopant atoms in bulk MgO is kept fixed at 3.70%.

7.2.1 Computational Details

Our calculations were performed using spin-polarized *ab initio* density functional theory (DFT) as implemented in the Quantum ESPRESSO package.[68] A plane wave basis set was used to solve the Kohn-Sham equations,[69] with cut-offs of 30 Ry and 240 Ry for the wavefunctions and charge densities, respectively. Electron-ion interactions were described using ultrasoft pseudopotentials,[70] and exchange-correlation interactions were treated within the Perdew-Wang 91 (PW91) form of the generalized gradient approximation.[71]

To study bulk doped MgO, with doping concentration of 3.70%, we considered a $3 \times 3 \times 3$ supercell, where one of the Mg atoms or O atoms was replaced by a dopant. Brillouin zone sampling was performed using a $4 \times 4 \times 1$ Monkhorst-Pack k-point mesh.[72] Convergence was improved by using Marzari-Vanderbilt smearing

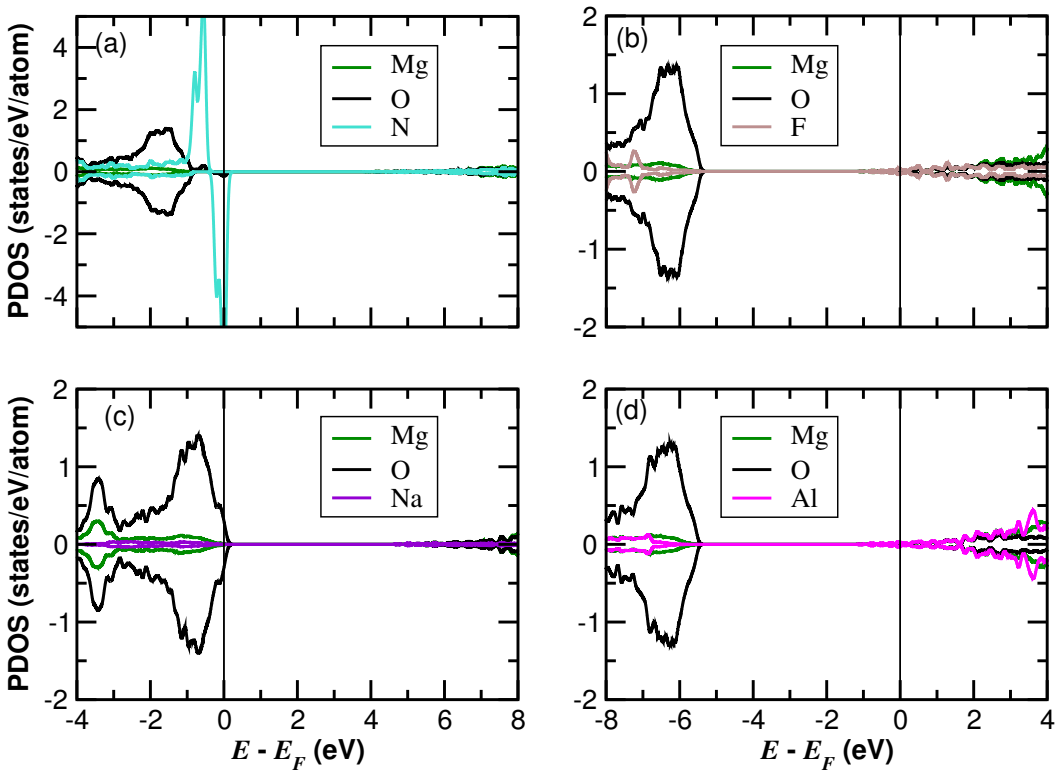

Figure 7.1: Projected density of states (PDOS) plots of bulk MgO doped with (a) nitrogen, (b) fluorine, (c) sodium and (d) aluminium at 3.70% doping concentration. The black, green, turquoise, maroon, indigo and magenta curves show the PDOS of oxygen, magnesium, nitrogen, fluorine, sodium and aluminium atoms, respectively.

with a width of 0.005 Ry.[73] Geometries were relaxed making use of Hellmann-Feynman forces and the BFGS algorithm, [74] with a force convergence threshold of 0.001 Ry/Bohr. Electronic charges on atoms and charge-transfers were calculated by partitioning the charge density making use of its topological properties, following the procedure laid out by Bader.[75, 76] As in the previous chapter, we will refer to the Bader charges as the topological charge,[77] in doing so we are following the convention of Ref. 83, this should not be confused with, e.g., the topological insulators and other 'exotic' systems that have been recently discovered.

7.2.2 Results

Cationic and Anionic Impurity Doped Bulk MgO

We find that in all the cases, when the oxide is doped with donors and acceptors, the system becomes electron-rich and electron-deficient, respectively. However, these

Table 7.1: Parameters used to obtain the efficacy of the dopants in bulk MgO, and formulate a descriptor for it. OS is the nominal oxidation state, χ is the Pauling electronegativity, R is the atomic radius as computed from DFT, and $\mathcal{D}$ is the descriptor as defined by Eq. (1). $\mathcal{Q}_T$ is the topological charge on the atoms of the element X, $\mathcal{I}$ is the efficacy of doping, given by $\mathcal{Q}_T/OS$. The first two rows are for bulk MgO, the remaining rows are for pristine bulk MgO doped with 3.70% of the element X.

Element X	OS	χ	R (Å)	$\mathcal{D}$ (Å^{-1})	$\mathcal{Q}_T$ (e)	$\mathcal{I}$
O	−2	3.44	0.999	4.12	−1.71	0.86
Mg	+2	1.31	1.516	4.12	+1.71	0.86
F	−1	3.98	1.089	6.25	−1.00	1.00
Al	+3	1.61	1.359	5.08	+3.00	1.00
N	−3	3.04	0.936	2.98	−1.87	0.62
Na	+1	0.93	1.713	3.51	+0.81	0.81
P	−3	2.19	1.228	3.05	−1.76	0.59
Li	+1	0.98	1.426	5.76	+1.00	1.00
K	+1	0.82	2.147	2.28	+0.65	0.65

effects are found to vary depending on the dopant element. The electronic densities of states for bulk MgO doped with the anionic impurities N and F, and the cationic impurities Na and Al, are shown in Fig. 7.1. For both donor dopant atoms, Al and F, we see that upon doping, the Fermi level of the doped system shifts to the bottom of the conduction band, as has been reported also by previous authors for similar systems.[19, 46, 78–80] When MgO is doped with the acceptor cation Na, we find that the Fermi level shifts to the top of the valence band, however, when doped with the acceptor anion N, we find that the Fermi level lies at a defect state that appears just above the valence band. Our results are in good agreement with previous results on similar acceptor-doped oxide systems.[46, 78, 79, 81, 82]

Next, we wish to look at the charge on each atom, computed using the Bader prescription,[75, 76] in both the doped and undoped bulk MgO. The nominal oxidation state, OS, of the Mg cations in MgO is +2, while O anions have an OS of −2. However, on computing the topological charges $\mathcal{Q}_T$ on the atoms using the Bader prescription, we find that in undoped MgO, the charges on the Mg and O ions are $\mathcal{Q}_T$(Mg) and $\mathcal{Q}_T$(O) = +1.71 e and −1.71 e, respectively. We believe the reason for this discrepancy

is that the bonds in MgO are not perfectly ionic in nature. This value of Bader charge acquired by Mg/O in bulk MgO is in good agreement with previous reports in the literature. [33, 83] In the sixth column in Table 7.1, we have listed the computed topological (Bader) charges $\mathcal{Q}_T(X)$ on the dopant ions X for $\theta = 3.70\%$ in bulk MgO. From this Table, we can see that the donors Al and F behave exactly as expected from their nominal valencies. Thus, upon being placed in the oxide, Al surrenders all three of its valence electrons, whereas F acquires one electron, thereby achieving an octet in the valence shell. This suggests that Al and F are able to make the oxide electron-rich, to the maximum extent possible. However, the acceptors seem to behave very differently. The cationic acceptor Na and the anionic acceptor N acquire charges of +0.81 e and −1.87 e, respectively, instead of their expected or nominal oxidation states (OS) +1 e and −3 e, respectively. Thus from Table 7.1 we see, that for the donor type dopants (anionic F and cationic Al), $\mathcal{Q}_T$ is equal to OS, while for the acceptor type dopants, anionic N and cationic Na, the values of $\mathcal{Q}_T$ differ from the corresponding nominal oxidation states, OS. Therefore, neither N nor Na acts as an ideal acceptor type dopant for MgO. This suggests we need to look for other elements which can serve as better acceptor type dopants for MgO. Instead of blindly trying all other possibilities, we first try to formulate a descriptor for the efficacy of the doping, that could guide us in making a suitable choice for the 'perfect' acceptor type impurity.

Descriptor for Aliovalent Doping

After having computing topological charges $\mathcal{Q}_T$ on the atoms using the Bader prescription, we wish to determine some descriptor on which the charge acquired by each atom depends. While looking for descriptors, one first selects a target property that one aims to 'predict'. Here, we define this target to be $\mathcal{I} = \mathcal{Q}_T(X)/OS(X)$, where $OS(X)$ is the nominal oxidation state of the element X.[84] This ratio is equal to 1 for perfectly ionic bonds and its deviation from unity is considered to be a measure of the deviation from 'perfect' ionicity of the bonds involving the element X.

In the present context, when the ratio is equal to 1, we have also found a maximally efficient dopant.

To construct a descriptor, we have considered various parameters which are based on various properties of the atoms that the system is comprised of. The distribution of electronic charge density between two atoms should depend on the difference in electronegativity between the two elements. Accordingly, we take one of the quantities out of which we will build up a descriptor to be $\Delta\chi = \chi(\text{anion}) - \chi(\text{cation})$, where $\chi(X)$ is the electronegativity of the element X. Note that for cationic dopants $\Delta\chi = \chi(\text{O}) - \chi(\text{dopant})$, whereas for anionic dopants, $\Delta\chi = \chi(\text{dopant}) - \chi(\text{Mg})$.

It is also known that the ionic or covalent nature of bonds depends on the sizes of the atoms participating in the bonding.[85, 86] The effective size of an atom changes with its coordination number. Therefore, to determine the radii of the elements which we have used in this section, we have constructed simple cubic (SC) lattices for each element X, and performed DFT calculations to obtain the optimal lattice constant $a(X)$. We choose the SC lattice since its coordination number of 6 is same as the coordination number of the rock salt structure of MgO. The atomic radius is then $R(X) = 0.5\ a(X)$. The values of $R(X)$ are listed in the fourth column of Table 7.1. Note that these values follow the expected trends, with the possible exception of N, O and F, where we find $R_{\text{N}} < R_{\text{O}} < R_{\text{F}}$. One would normally expect the radii to decrease in the order N, O, F, which is observed in many tabulated values of ionic and covalent radii,[87] however, note that some previous authors have also obtained values of covalent radii that display other trends.[88, 89]

Further, in formulating a descriptor, we have, as in the previous chapter, tried to combine $\Delta\chi$ with different combinations of the atomic sizes of two elements X and Y forming a bond: $R(X) - R(Y)$, $R(X)/R(Y)$, $R(X) + R(Y)$, etc. After trying with several combinations we find that the best correlation between the target property $\mathcal{I}$

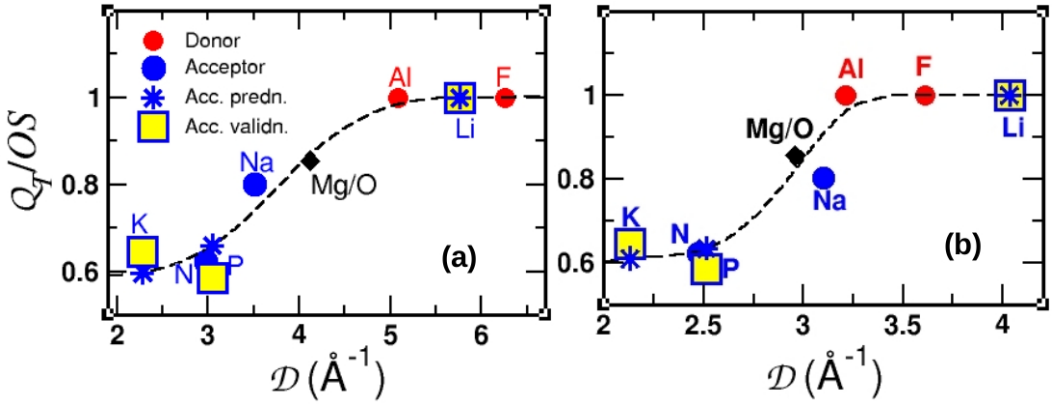

Figure 7.2: The correlation between $\mathcal{Q}_T(X)/OS(X)$ and $\mathcal{D}$ when bulk MgO is doped with the impurity atoms at 3.70% doping concentration. The data corresponding to donor and acceptor type impurities are shown using red and blue circles, respectively. The black diamomd shows the data for undoped MgO. The blue stars for the acceptor dopants P, K and Li predict their values for $\mathcal{Q}_T(X)/OS(X)$ using the corresponding $\mathcal{D}$ values and the black dashed line. The $\mathcal{Q}_T(X)/OS(X)$ values for the acceptor dopants P, Li and K obtained from DFT calculations are shown using the yellow squares. The value of R for each element is obtained from (a) simple cubic structure, (b) using covalent radii as reported in Ref. 90.

and the descriptor $\mathcal{D}$ is obtained for:

$$\mathcal{D} = \frac{\Delta\chi}{\Delta R} = \frac{\chi(\text{anion}) - \chi(\text{cation})}{R(\text{cation}) - R(\text{anion})}. \tag{7.1}$$

In Fig. 7.2 we have plotted the correlation between the descriptor $\mathcal{D}$ and the target property $\mathcal{I}$. The donor and acceptor type imurities are shown by the red and blue dots, respectively. For a perfect dopant, we expect the value of $\mathcal{I}$ should approach 1. The position of the red and blue dots on this graph establishes the fact that the two donor type impurities, F and Al perform well according to the ideal expectation, whereas the acceptors N and Na do not serve as a perfect dopant. The dashed curve on this graph is a fit of a hyperbolic tangent to the data points (red and blue circles). From the $\mathcal{I}$ vs. $\mathcal{D}$ plot, we see that a high value of the descriptor $\mathcal{D}$ results in a high value of the target property or the doping efficacy, $\mathcal{I}$.

Since the two donors we considered, Al and F, already have high values of $\mathcal{D}$ and therefore $\mathcal{I}$, we do not consider any further possibilities for donor dopants due to the satisfactory performance of F and Al. However, we will explore whether we can find

a better acceptor dopant for MgO. For this purpose, we next consider the elements P, Li and K as possible acceptors. P and K lie below N and Na, respectively, while Li lies above Na in the periodic table of elements. The computed values for R and $\mathcal{D}$ for these three elements are also listed in Table 7.1. We see that the values of the descriptor $\mathcal{D}$ for K and P are lower (2.28 and 3.05, respectively) than both N and Na, however $\mathcal{D}$ for Li is high (5.76). Thus, based upon the predictions using the descriptor $\mathcal{D}$ (see the blue stars in Fig. 7.2) one would expect that K should act as an even worse acceptor dopant than N or Na, P should have almost the same performance as N, while Li should be an excellent acceptor dopant.

Next, we perform DFT calculations to verify our prediction made using the descriptor $\mathcal{D}$. We find that $\mathcal{Q}_T$ for P, Li and K is -1.76 e, $+1.00$ e and $+0.65$ e, respectively. We plot the values of $\mathcal{Q}_T/OS$ as a function of $\mathcal{D}$ for P, Li and K, see the blue stars in Fig. 7.2. The yellow squares lie close to the blue stars, see Fig. 7.2(a). Therefore the descriptor, $\mathcal{D}$ has successfully predicted the ratio of $\mathcal{Q}_T(X)/OS(X)$ for P, Li and K.

A graph similar to that in Fig. 7.2 using tabulated values of covalent radii [90] for each element (instead of our computed R) is shown in Fig. 7.2(b). The values of ΔR in the descriptor, $\mathcal{D}$ for Fig. 7.2(b) are obtained by using the tabulated values for the covalent radii of the elements,[90]. The graphs in Fig. 7.2 (a) and (b) are similar in nature since the qualitative behavior of $\mathcal{Q}_T/OS$ with $\mathcal{D}$ is the same in both these graphs.

Thus, we have successfully been able to explain the observed values for $\mathcal{Q}_T$ based on simple quantities like the difference in electronegativities, $\Delta\chi$, and the difference in atomic radii, ΔR, between the dopant and the atom (Mg/O) to which it is bonded. In Fig. 7.2, we see $\mathcal{Q}_T(X)/OS(X)$ increases as a function of the descriptor, $\mathcal{D}$ which is the ratio of $\Delta\chi$ to ΔR.

In summary, in this section, we have used *ab initio* density functional theory calculations to study aliovalent doping of bulk MgO. We have used both anionic and

cationic dopants. We find the dopants do not always acquire the expected charge when placed in the oxide. We have formulated a descriptor which can predict the topological charge ($\mathcal{Q}_T$) on each dopant using the Bader prescription. The descriptor, $\mathcal{D}$, is formulated using two quantities, the difference in electronegativities ($\Delta\chi$) and the difference in radii (ΔR) between the dopant atom and the atom (Mg/O) in the oxide to which it is bonded. This descriptor is a good indicator of the topoligical charge ($\mathcal{Q}_T$) on a given dopant. For high values of $\Delta\chi/\Delta R$, the value of $\mathcal{Q}_T(X)/OS(X)$ becomes close to 1, i.e., $\mathcal{Q}_T$ approaches the expected nominal oxidation state (OS). Based on values of $\Delta\chi$ and Δr, we predict (correctly) that the cationic dopant Li may perform as a better acceptor than Na or N, while the donor type dopants Al (cation) and F (anion) should perform almost equally well.

7.3 Deposition of Au clusters on Doped MgO(001) Surfaces

After studying bulk MgO, we wish to explore the MgO(001) surface doped with various impurity atoms. We want to investigate how doping of MgO(001) can tune the charge state of the deposited Au clusters. In the previous section, we have found a descriptor ($\mathcal{D}$) which can predict the topological (Bader) charge on the dopants. In this section, we want to see whether the same descriptor can predict the efficacy of a dopant in tuning the charge state of Au nanoclusters adsorbed on F-doped, Al-doped, N-doped, Na-doped and Li-doped MgO(001) substrates. To test the efficacy of our descriptor, $\mathcal{D} = \Delta\chi/\Delta R$, we perform Density Functional Theory calculations where Au nanoclusters are adsorbed on the doped MgO surfaces.

7.3.1 Methods

In our calculations, the Au monomer or dimer was placed on a $3 \times 3 \times 1$ supercell of MgO(001). The support was comprised of four layers of MgO. These thicknesses

were found sufficient to obtain satisfactory convergence of the surface and interface energies. Periodic images of the slabs were separated by ∼14 Å of vacuum along the z direction (normal to the surface). The 'dipole correction' was applied to eliminate the spurious dipole-dipole electrostatic interaction between periodic images along the z direction.[91, 92] Brillouin zone sampling was performed using a $4 \times 4 \times 1$ Monkhorst-Pack k-point mesh.[72] Convergence was improved by using Marzari-Vanderbilt smearing with a width of 0.005 Ry.[73] Geometries were relaxed making use of Hellmann-Feynman forces and the BFGS algorithm, [74] with a force convergence threshold of 0.001 Ry/Bohr. Electronic charges on atoms were calculated by partitioning the charge density making use of its topological properties, following the procedure laid out by Bader.[75, 76]

7.3.2 Results

Au monomer and dimer on pristine and doped MgO(001): Geometries and Energetics

We first check the adsorption geometries and energetics for an Au monomer (adatom) and an Au dimer adsorbed on undoped MgO(001). We find that the most favored adsorption site for the Au adatom is atop an O atom, with the Au-O bond distance = 2.28 Å. Adsorption atop O is found to be energetically favored over adsorption atop a Mg atom by 0.41 eV, while no stable adsorption geometry is found for the monomer at the hollow site on the surface. We find that on undoped MgO(001), the Au dimer prefers to adsorb atop oxygen in an upright geometry, with an Au-O distance of 2.12 Å and an Au-Au distance of 2.49 Å. We find that this geometry is preferred over a flat geometry (where both Au atoms are bonded to two nearest-neighbor Mg atoms on the surface) by 1.14 eV.

The adsorption energy of a supported Au_n cluster is defined as

$$E_{\text{ads}}(\text{Au}_n) = -[E(\text{Au}_n/\text{supp}) - E(\text{supp}) - E(\text{Au}_n)], \tag{7.2}$$

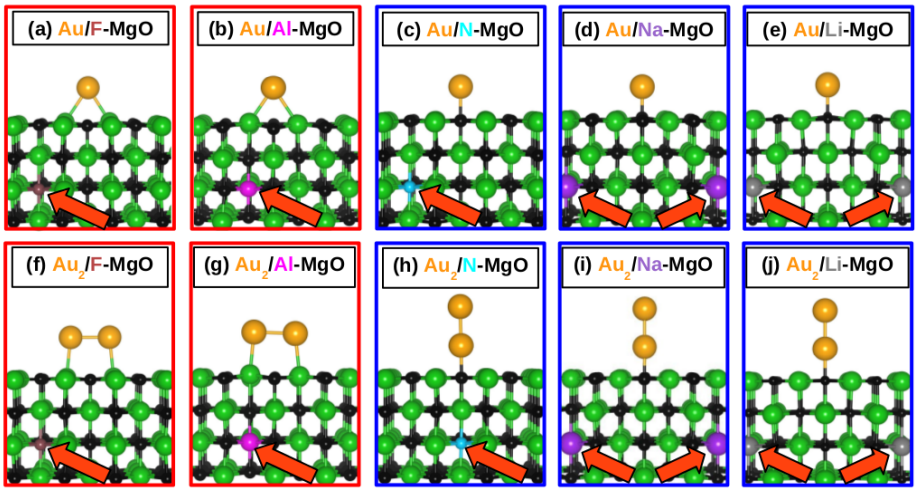

Figure 7.3: Atomistic structures as determined from DFT calculations of an Au adatom and Au dimer on doped-MgO(001) substrates. Au monomer on (a) F-doped, (b) Al-doped, (c) N-doped, (d) Na-doped and (e) Li-doped MgO. Au dimer on (f) F-doped, (g) Al-doped, (h) N-doped, (i) Na-doped and (j) Li-doped MgO. Color scheme for atomic spheres: Mg, green; O, black; N, cyan; F, brown; Na, purple; Al, magenta; Li, dark gray and Au, yellow. The orange arrows show the position of the dopant atoms. The red and blue frames correspond to situations where the doping is done by donor and acceptor type dopants, respectively.

where the three terms on the right-hand-side are the total energies, from DFT, of the supported Au_n cluster, the bare support, and the Au_n cluster in the gas phase, respectively. For an Au monomer and Au dimer on pristine MgO(001), we obtain $E_{\rm ads}({\rm Au}) = 0.75$ eV and $E_{\rm ads}({\rm Au_2}) = 1.53$ eV. All these results are in good agreement with previous values in the literature.[33, 34, 49, 50, 93]

In Fig. 7.3, we show the lowest-energy geometries found by us for an Au monomer [Figs. 7.3(a)–(e)] and an Au dimer [Figs. 7.3(f)–(j)] on the various doped MgO(001) substrates. In all cases, the geometries correspond to a dopant concentration $\theta = 2.78\%$, with the dopant atoms placed in the third MgO layer. Note that all values mentioned in this section for doped substrates correspond to this dopant concentration and position, unless explicitly mentioned otherwise.

When the dopant is an electron donor (either anionic F or cationic Al), the Au monomer acquires a larger negative charge than when placed on the undoped support (this will be discussed in greater detail further below), and it becomes favorable for it

to adsorb at a hollow site on the surface [see Figs. 7.3(a) and (b)]. The adsorption site of the Au monomer on donor-doped MgO remains unchanged with a change in doping concentration. However, when the dopant is an electron acceptor (either anionic N or cationic Na/Li), the Au monomer prefers to adsorb atop an O atom of the MgO substrate [see Figs. 7.3(c), (d) and (e)], as was the case for the undoped MgO support. Like the case of donor-doped MgO systems, the adsorption site of the Au monomer remains unchanged as a function of doping concentration for acceptor-doped MgO systems. The lowest energy geometries, the corresponding adsorption energies (E_{ads}) and the distance between the adsorbed Au atom and the support (d), for the different doped systems are listed in Table. 7.2 for different doping concentrations. When the Au monomer is adsorbed on a hollow site of the MgO support, d is the average distance between the Au atom and the two nearest Mg atoms in the support.

On comparing Figs. 7.3(a)–(e), one also notices variations in the lateral position of the Au monomer relative to that of the dopant atoms, though energy differences between different lateral configurations of the dopant atoms are found to be less than 0.04 eV.

For the Au dimer, similarly, we see that the adsorption geometry on the doped oxide surface depends on whether the dopant is an acceptor or donor. When the dopant is an electron donor (either anionic F or cationic Al), it becomes favorable for the dimer to adsorb in a flat geometry, with the two Au atoms forming bonds to two nearest-neighbor Mg atoms [see Figs. 7.3(f) and (g)]. This wetting transition is reminiscent of the change found previously in the favored structure of an Au_{20} cluster from a three-dimensional tetrahedral geometry to a two-dimensional planar geometry upon doping the MgO support with Al donors,[19] and is in accordance with the higher negative charge acquired by the cluster due to the effect of doping (this will be discussed in greater detail further below). In marked contrast, we see from Figs. 7.3(h)–(j) that for Au_2 the upright geometry atop an O site is retained when the dopant is an electron acceptor, i.e., for anionic N and cationic Na or Li.

The adsorption energies for the stable geometries, and d, the length of the bond(s) made by the Au atom(s) with the oxide support, on the various doped surfaces at different doping concentrations, are listed in Table 7.3. When Au_2 prefers to adsorb in the flat geometry on the MgO support, then d is defined as the average distance between the two Au atoms and the two Mg atoms directly below them.

Au Monomer and Dimer on Pristine and Doped MgO(001): Charge Transfer

On undoped MgO(001), we find that the Au monomer acquires a charge of −0.27 e and the Au dimer acquires a charge of −0.28 e. These values are in excellent agreement with previous results in the literature.[33, 34, 93]

In Fig. 7.4 we show again the structures of the Au monomer and dimer placed on the doped supports, but now indicating the charge redistribution between the support and the Au clusters that occurs upon cluster deposition. In these figures, we have plotted isosurfaces of $\Delta\rho = \rho(\mathrm{Au_n/supp}) - \rho(\mathrm{Au_n}) - \rho(\mathrm{supp})$, where the three terms on the right hand side are the electronic charge densities of the Au cluster (monomer or dimer) on the support, the isolated Au cluster and the bare support, respectively. Note that the latter two terms are evaluated using geometries corresponding to their coordinates in the combined system. In Fig. 7.4, red and blue lobes correspond to electron gain and depletion, respectively.

It is clear from Fig. 7.4 that in all cases, there is considerable charge transfer between the support and the Au clusters; the results obtained from Bader analysis support this conclusion. Most interestingly, we find that depending on the dopant, the Au monomer can be negatively or positively charged. For F, Al, N, Na and Li dopants in the MgO substrate, the charge on the Au monomer is −0.84 e, −0.84 e, −0.24 e, +0.11 e and +0.21 e, respectively, at 2.78% doping concentration (see Table 7.2). This is in accordance with the fact that we see predominantly red lobes surrounding the Au atom in the cases where the dopant is F, Al or N [see Figs. 7.4(a), (b) and (c)], but the shape of the red lobe around the Au monomer is different on

Table 7.2: Results for Au monomer adsorbed on doped MgO(001). Adsorption site of Au monomer, E_{ads}(Au): adsorption energy of Au, d: distance between Au monomer and the support, Q_{T}(Au): topological or Bader charge on Au monomer. The Au monomer adsorbs atop O on undoped MgO with E_{ads}(Au) = 0.75 eV, d = 2.28 Å and Q_{T}(Au)= −0.2740 e. A negative sign for Q_{T}(Au) implies that electrons are transferred to Au from the support.

Dopant (X)	doping conc.	Adsorption site	E_{ads}(Au) (eV)	d (Å)	Q_{T}(Au) (e)
F	2.78%	hollow	2.68	2.81	−0.832
	5.55%		2.92	2.79	−0.855
	8.33%		3.11	2.78	−0.870
Al	2.78%	hollow	2.72	2.81	−0.843
	5.55%		2.97	2.80	−0.868
	8.33%		3.11	2.78	−0.885
N	2.78%	atop O	1.13	2.18	−0.238
	5.55%		1.19	2.15	−0.152
	8.33%		1.30	2.08	−0.130
Na	2.78%	atop O	1.73	1.99	0.113
	5.55%		1.91	1.99	0.125
	8.33%		2.02	1.98	0.135
Li	2.78%	atop O	1.70	1.97	0.209
	5.55%		1.84	1.99	0.232
	8.33%		1.92	1.99	0.247

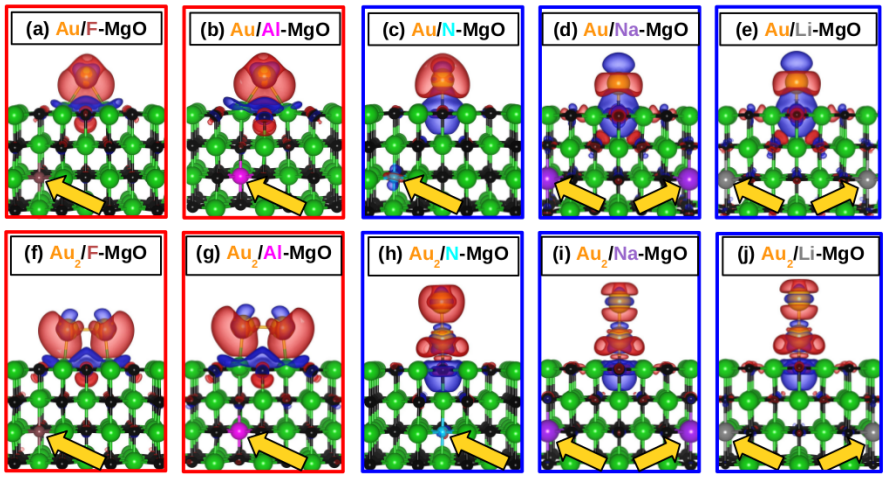

Figure 7.4: The charge redistribution plots for Au monomer (first row) and dimer (second row) on (a), (f) F-doped, (b), (g) Al-doped, (c), (h), N-doped, (d), (i) Na-doped and (e), (j) Li-doped MgO systems. All systems shown here are at a doping concentration of 2.78%, and the dopant atoms are situated in the third layer of the oxide. Red and blue lobes show electron accumulation and depletion respectively, drawn at isosurface value 0.001 e/bohr^3. Color scheme for atomic spheres: Mg, green; O, black; N, cyan; F, brown; Na, purple; Al, magenta; gray, Li and Au, yellow. The yellow arrows show the position of the dopant atoms. The red and blue frames correspond to situations where the doping is done by donor and acceptor type dopants, respectively.

N-doped MgO than on donor-doped MgO systems. We can see predominant blue lobes in the case where the dopants are Na and Li [see Fig. 7.4(d) and (e)]. Note that the electron acceptors N, Na and Li have reduced (made more positive) the charge on Au relative to the value of −0.27 e on undoped MgO(001), whereas the electron donors F and Al have significantly increased (made more negative) the charge on Au. It is also worth noting that we find the charge on the dopant ions themselves does not change appreciably upon deposition of the Au monomer; this is in contrast with what has been observed, e.g., for Mo dopants in CaO.[48, 94] The change in charge state of Au monomer as a function of doping concentration is plotted in Fig. 7.5(a). In the case of acceptor (N, Na and Li) doped MgO systems, the charge on the Au monomer decreases with increase in doping concentration. Q_{T}(Au) becomes more negative with doping concentration for F-doped and Al-doped MgO systems. Q_{T}(Au) varies in a smaller range as the doping concentration varies from 2.78% to 8.33% for

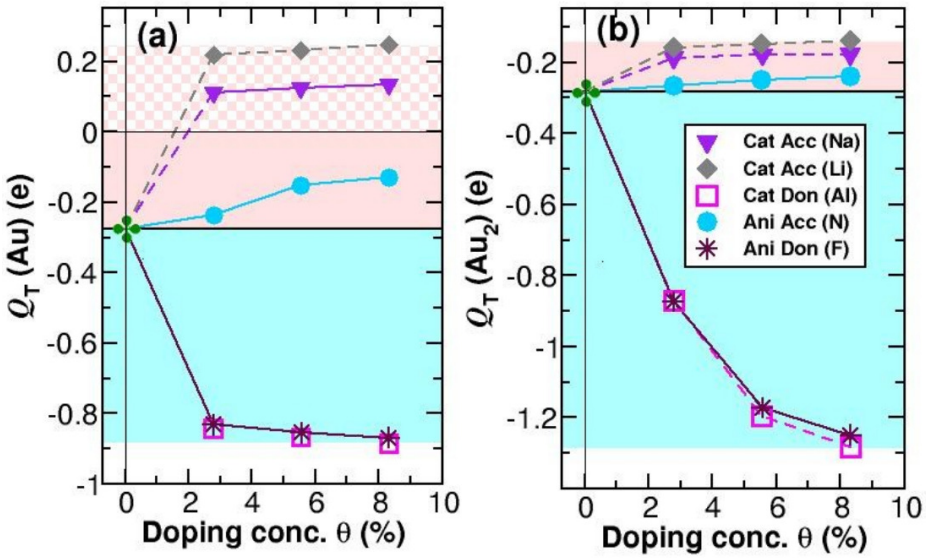

Figure 7.5: Variation of (a) Q_T(Au) and (b) Q_T(Au_2) with doping concentration θ on doped MgO (001) systems. Violet triangles, gray diamonds, magenta squares, turquoise circles and maroon stars show data for Na-doped, Li-doped, Al-doped, N-doped and F-doped systems, respectively. The legend labels indicate whether the dopant is a cation or anion, and acceptor or donor.

F-doped, Al-doped, Na-doped and Li-doped systems, see Table 7.2 for the tabulated values.

As in the case of the Au monomer, one observes appreciable charge transfer within the Au_2/doped-MgO(001) systems, as indicated by the sizeable red and blue lobes corresponding to electron gain and depletion, respectively in Figs. 7.4(f)–(j). These lobes are obviously positioned differently for the upright and flat adsorption geometries. However, the size and shape of these lobes also differ depending on the dopant species, indicating that once again, the charge gained or lost by the Au atoms is not the same for the four cases considered here. This is confirmed upon quantifying the charge gained by the Au dimer, Q_T(Au_2) using Bader analysis. We find that for F, Al, N, Na and Li dopants in the MgO substrate, the charge on the Au dimer is −0.87 e, −0.87 e, −0.27 e, −0.19 e and −0.16 e, respectively, at 2.78% doping concentration; these values are in accordance with the sizes of the red lobes in Figs. 7.4(f)–(j) (see Table 7.3). We recall that Q_T(Au_2) was −0.28 e on undoped MgO(001), i.e., we see that the electron donors F and Al have significantly

Table 7.3: Results for Au dimer (Au_2) adsorbed on doped MgO(001). Adsorption site, $E_{ads}(Au_2)$: adsorption energy of Au dimer, d: distance between Au dimer and the support, $Q_T(Au_2)$: charge on Au dimer. On undoped MgO(001), the Au dimer adsorbs in an upright geometry atop O with $E_{ads}(Au_2)$= 1.53 eV, d = 2.12 Å and $Q_T(Au_2)$= −0.2838 e. A negative sign for $Q_T(Au_2)$ implies that electrons are transferred to Au_2 from the support.

Dopant (X)	Doping conc.	Adsorption site	$E_{ads}(Au_2)$ (eV)	d (Å)	$Q_T(Au_2)$ (e)
F	2.78%		2.21	2.72	−0.874
	5.55%	flat, bonded to Mg	2.59	2.63	−1.172
	8.33%		2.98	2.59	−1.250
Al	2.78%		2.20	2.72	−0.871
	5.55%	flat, bonded to Mg	2.69	2.61	−1.194
	8.33%		3.02		−1.284
N	2.78%		1.69	2.09	−0.266
	5.55%	upright, atop O	1.53	2.09	−0.250
	8.33%		1.52	209	−0.239
Na	2.78%		1.73	2.08	−0.187
	5.55%	upright, atop O	1.76	2.06	−0.179
	8.33%		1.78	2.06	−0.177
Li	2.78%		1.73	2.07	−0.160
	5.55%	upright, atop O	1.76	2.05	−0.148
	8.33%		1.78	2.04	−0.1398

increased (made more negative) $Q_{\mathrm{T}}(\mathrm{Au}_2)$, whereas the electron acceptors N, Na and Li have reduced it. However, in contrast to the case of the Au monomer, we have not succeeded in making $Q_{\mathrm{T}}(\mathrm{Au}_2)$ positive by doping the support. The charge state of the Au dimer on different doped MgO systems as a function of doping concentration is reported in Table 7.3. Fig. 7.5(b) shows the variation in charge state of Au_2 as a function of doping concentration. $Q_{\mathrm{T}}(\mathrm{Au}_2)$ increases with doping concentration for F-doped and Al-doped MgO. In the case of acceptor-doped MgO substrates, $Q_{\mathrm{T}}(\mathrm{Au}_2)$ does not change much as a function of doping concentration.

Correlation between Charge State of Deposited Au Clusters and the Descriptor

Now, we want to compare the performance of the dopants in tuning the charge state of the deposited Au nanoclusters on the doped MgO(001) surfaces. We wish to investigate the efficacy of the dopants by using the descriptor, $\mathcal{D} = \Delta\chi/\Delta R$, as formulated in the previous section. For this purpose, we first calculate a quantity $\Delta Q_{\mathrm{T}}(\mathrm{Au}_n)$, the difference in the charge acquired by the Au clusters on X-doped MgO(001) (at a given doping concentration) and the undoped MgO(001). Therefore, $\Delta Q_{\mathrm{T}}(\mathrm{Au}_n) = Q_{\mathrm{T}}(\mathrm{Au}_n)(X\text{-doped MgO}) - Q_{\mathrm{T}}(\mathrm{Au}_n)(\text{undoped MgO})$. To find the correlation between $\Delta Q_{\mathrm{T}}(\mathrm{Au}_n)$ and the descriptor $\mathcal{D}$, we plot the values of $\Delta Q(\mathrm{Au}_n)$ for F-, Al-, N-, Na- and Li-doped MgO systems as a function of $\mathcal{D}$ at fixed value of doping concentration, see Fig. 7.6. In Figs. 7.6(a), (c) and (e) the blue circles and triangles show the results for the Au monomer and Au dimer, respectively on Li-, Na- and N-doped MgO(001) systems at 2.78%, 5.55% and 8.33% doping concentrations, respectively. The red circles and triangles in Figs. 7.6 (b), (e) and (f) show the results for the Au nanoclusters on F- and Al-doped MgO(001) at 2.78%, 5.55% and 8.33% doping concentrations, respectively. We see the value of $\Delta Q_{\mathrm{T}}(\mathrm{Au}_n)$ for the Au nanoclusters on the doped systems becomes more positive from N- to Li-doped MgO, i.e., following the order: Li-MgO > Na-MgO > N-MgO. Recall that on undoped MgO, the Au monomer acquires a charge of -0.27 e; now on doping MgO with Li atoms,

we find that the Au monomer gains a larger positive charge than on Na-doped and N-doped MgO(001), respectively. This is in perfect agreement with our expectations, since in Section 2 we have found that Li is a better acceptor dopant for MgO than N and Na. We see the same trend in the case of the Au dimer, however the Au dimer does not become positively charged due to the fact that it has a higher ionization potential as compared to an Au monomer, which makes it difficult to remove electrons from the Au dimer.[95] Also, we see that the variation of $\Delta Q_{\mathrm{T}}(\mathrm{Au}_n)$ for the Au dimer from N-doped to Li-doped MgO is less than for the Au monomer at the same value of doping concentration. The $\Delta Q_{\mathrm{T}}(\mathrm{Au}_n)$ values for Au clusters on donor-doped systems are almost the same for Al-doped and F-doped MgO(001) for any value of doping concentration, in agreement with our finding in Section 2 that both Al and F act as 'perfect' donors in MgO. From Figs. 7.6(b), (d) and (f) we see that the values of $\Delta Q_{\mathrm{T}}(\mathrm{Au}_n)$ are almost the same for Al- and F- doped MgO systems for any value of doping concentration and both sizes of Au cluster. In We note that in Fig. 7.6, we have plotted graphs of $\Delta Q_{\mathrm{T}}(\mathrm{Au}_n)$ vs. $\mathcal{D}$ plots, for the Au nanoclusters on the acceptor and donor-doped MgO supports are plotted in the separate graphs. The $\Delta Q_{\mathrm{T}}(\mathrm{Au}_n)$ values for the acceptor and donor-doped systems do not collapse on a single graph, since the electronegativity of Au, and its difference with respect to the elements in the support, also matter.

The relatively large positive charge (+0.25 e at 8.33% doping concentration) of the Au monomer obtained when placed on Li-doped MgO is of great interest. A previous theoretical study has reported the highest positive charge acquired by an Au monomer deposited on anatase-TiO_2 to be +0.45 e, however, it is to be noted that this value corresponds to a geometry when the monomer is adsorbed at a hollow site which is energetically less stable than the bridge site, where the Au monomer becomes neutral. [44]

To summarize, in this section, using *ab initio* density functional theory calculations we have studied aliovalent doping of the MgO(001) substrate and the use of the

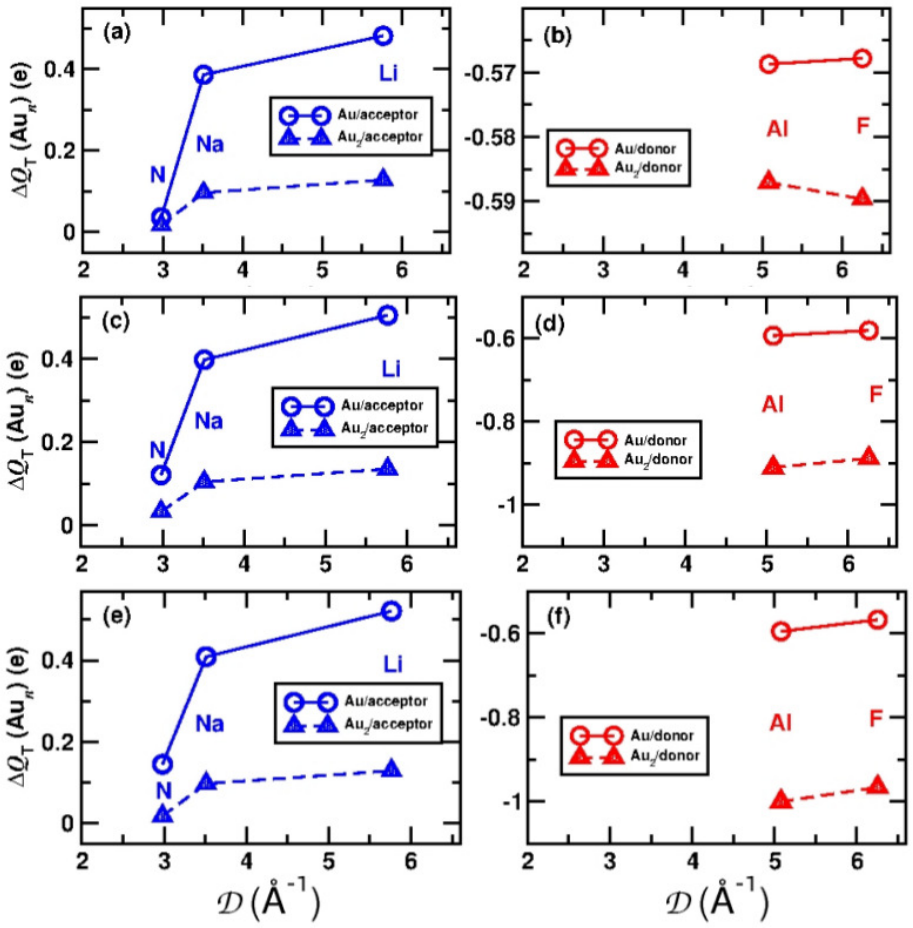

Figure 7.6: Correlation between $\Delta Q_{\mathrm{T}}(\mathrm{Au}_n)$ and the descriptor $\mathcal{D}$ for Au monomer (open circles) and dimer (triangles) on doped MgO(001) systems, at (a)–(b) 2.78%, (c)–(d) 5.55% and (e)–(f) 8.33% doping concentrations, respectively. Au clusters on acceptor-type (N, Na and Li) [(a), (c) and (e)] and donor-type impurity (Al and F) [(b), (d) and (f)] doped MgO(001).

doped MgO substrates to tune the charge state of small Au nanoparticles which are placed on them. We have already found that the charge on the dopant can be predicted using the descriptor, $\mathcal{D} = \Delta\chi/\Delta R$, which is the ratio of the difference in electronegativity and the difference in radii between the dopant atom and the atom in the oxide that it is bonded to. This descriptor is also an indicator of the charge that an Au nanoparticle would acquire when placed on the doped support, since in this section we see that $\Delta Q_{\mathrm{T}}(\mathrm{Au}_n)$ has a correlation with the descriptor $\mathcal{D}$. We have considered the adsorption of an Au monomer and a dimer on the undoped and doped MgO systems. We find that the charge of Au clusters is correlated with its adsorption

geometry on the support. On undoped MgO and MgO doped with acceptors like N, Na and Li, we find that the monomers prefer to adsorb atop O, while on MgO doped with donors like Al and F, due to the increased negative charge on Au, they prefer to adsorb at a hollow site on the surface. Similarly, we see that on undoped MgO and MgO doped with acceptors, the dimer prefers an upright geometry, where one of the Au atoms is bonded to a surface O atom, whereas on MgO doped with donors, due to the increased electron transfer from the support to Au_2, the dimer prefers to lie flat on the surface, bonding to two surface Mg atoms. In agreement with our expectations, the donor dopants, F and Al, make the deposited Au cluster significantly more negatively charged than in the undoped case, and the acceptor dopants, N, Na and Li, make the deposited Au cluster less negatively charged than in the undoped case. On comparing the donor atoms, we see that both Al and F do 'as expected'. Both dopants make the Au cluster negatively charged to the same extent. The charge on Au_n differs only very slightly for the two dopants. In Section 2, from the values of $\mathcal{D}$ we had found that the performance of the acceptor dopants is expected to increase in the order N < Na < Li, while both F and Al are equally good donor type dopants. From Fig. 7.6 we see that for a given doping concentration our DFT calculations support the same trend regarding the efficacy of the dopants as already mentioned in Section 2. The Au monomer on Na- and Li-doped MgO gains positive charge, while on N-doped MgO it gains a lower negative charge as compared to when placed on undoped MgO. We have successfully formulated a suitable descriptor, $\Delta\chi/\Delta R$, that can predict the charge state of Au clusters supported on the doped MgO(001) systems. As already mentioned, this descriptor is very simple, can be calculated easily and depends only on the electronegativity and size of the dopant atom.

7.4 Effects of Oxide Doping and Metal Support on Deposited Au Nanoparticles

Next, we want to study the effect of a metal support placed below a thin layer of the oxide substrate. In this section, we investigate how the presence of metal support below the MgO(001) layer can affect the adsorption geometry and charge state of the deposited Au nanoclusters. We have chosen Mo(001) as the metal support over which an ultrathin film of MgO(001) is placed. An Au monomer (Au) and Au dimer (Au_2) are deposited on top of the undoped and doped MgO/Mo systems.

7.4.1 Computational Details

In our calculations, a four-layer thick MgO(001) film is placed on a four-layer thick Mo(001) substrate; these thicknesses are found sufficient to obtain satisfactory convergence of the surface and interface energies, work function and interlayer distances. The optimized lattice constant of bulk Mo is found to be 3.17 Å, which agrees well with the experimental value of 3.15 Å [96, 97]. For bulk MgO, we obtain the equilibrium lattice constant to be 4.22 Å, which is again in good agreement with the experimental value of 4.21 Å, as well as previous DFT calculations [98]. This implies that on an unstrained MgO (100) surface, the shortest Mg-Mg distance is 3.02 Å; thus, when we deposit MgO pseudomorphically on the Mo(001) substrate, the MgO layers are strained in-plane by 5%. Periodic images of the slabs are separated by ∼14 Å of vacuum. Since our slabs are asymmetric, the dipole correction is applied to eliminate the electrostatic interaction between dipoles in periodic images in the direction perpendicular to the surface.[91, 99] Anions in the MgO substrate are substitutionally doped by either nitrogen or fluorine, and the cations in the MgO substrate are doped by either lithium, sodium or aluminium, the concentrations of each dopant considered are 2.78% 5,55% and 8.33%. As for freestanding MgO(001) substrates, we have used $3 \times 3 \times 1$ supercells for MgO/Mo systems. Brillouin zone sampling is performed using a $12 \times 12 \times 1$ Monkhorst-Pack [72] k-point mesh for the

1×1 surface unit cell; the mesh is varied commensurately for larger cells. During geometry optimization of MgO/Mo systems, the two bottom-most layers of Mo are kept fixed at the bulk interlayer spacing, while all other atomic positions are relaxed until the force in each direction is lower than 0.001 Ry/Bohr.

The work function (Φ) of the metal or oxide/metal system is defined as the difference in energy between the vacuum level and the Fermi level of the slab; this is computed by calculating the average electrostatic potential as a function of z (the coordinate normal to the surface), following the method suggested by previous authors.[100, 101]. As already mentioned in the previous section, electronic charges on atoms and charge-transfers are calculated by partitioning the charge density making use of its topological properties, following the procedure laid out by Bader [75].

7.4.2 Results

Au clusters on Doped MgO/Mo: Adsorption Geometry and Energetics

First, we deposit an Au adatom and an Au dimer on undoped MgO/Mo. We find that on undoped MgO(001)/Mo, an Au adatom prefers to adsorb in the hollow position. The adsorption energy of Au clusters on the (undoped or doped) MgO/Mo systems is given by:

$$E_{\mathrm{ads}}(Au_{\mathrm{n}}) = -[E(Au_{\mathrm{n}}/\mathrm{supp}) - E(\mathrm{supp}) - E(Au_{\mathrm{n}})], \tag{7.3}$$

where $E(Au_{\mathrm{n}}/\mathrm{supp})$ and $E(\mathrm{supp})$ are the total energies of the Au nanoclusters on the (undoped or doped) MgO/Mo support and the bare (undoped or doped) MgO/Mo support, respectively. The adsorption of an Au monomer at the hollow site is found to be energetically more stable than atop O by 0.44 eV, with the optimal Au-Mg distance = 2.80 Å . The Au dimer prefers to adsorb atop oxygen in an upright geometry, with Au-O and Au-Au distances of 2.10 Å and 2.49 Å, respectively. The upright geometry is preferred over the flat geometry by 0.36 eV. For adsorption of the Au monomer and dimer on pristine MgO/Mo, we obtain E_{ads}(Au)= 1.72 eV

Table 7.4: Results for Au monomer adsorbed on doped MgO(001)/Mo. Adsorption site, E_{ads}(Au): adsorption energy of Au monomer, d: distance between Au dimer and the support, Q_{T}(Au): charge on Au monomer. Q_{T}(MgO) and Q_{T}(Mo) are the charges of the MgO film and the Mo support, respectively in the 3×3×1 surface cell. The Au monomer adsorbs at the hollow position with E_{ads}(Au)= 1.72 eV, d = 2.80 Å and Q_{T}(Au)= −0.836 e on undoped MgO(001)/Mo. A negative sign for Q_{T} implies electron gain and positive sign implies electron loss.

Dopant (X)	Doping conc.	Adsorption site	E_{ads}(Au) (eV)	d (Å)	Q_{T}(Au) (e)	Q_{T}(X-MgO) (e)	Q_{T}(Mo) (e)
F	2.78%		2.34	2.82	−0.844	1.069	−0.225
	5.55%	hollow	2.75	2.79	−0.856	1.691	−0.835
	8.33%		2.93	2.77	−0.865	2.358	−1.493
Al	2.78%		2.45	2.79	−0.858	0.994	−0.135
	5.55%	hollow	2.77	2.79	−0.869	1.618	−0.750
	8.33%		2.93	2.77	−0.880	2.218	−1.338
N	2.78%	hollow	1.20	2.82	−0.704	−0.157	0.861
	5.55%	atop O	1.11	2.22	−0.379	−0.706	0.979
	8.33%	atop O	0.88	2.21	−0.318	−0.985	1.304
Na	2.78%	hollow	1.30	2.83	−0.6916	−0.1641	0.8566
	5.55%	atop O	1.16	2.18	−0.352	−0.696	1.049
	8.33%	atop O	1.01	2.17	−0.277	−1.349	1.626
Li	2.78%	hollow	1.29	2.83	−0.709	−0.152	0.862
	5.55%	atop O	1.12	2.21	−0.315	−0.697	1.011
	8.33%	atop O	0.94	2.18	−0.287	−1.322	1.611

and E_{ads}(Au_2)= 1.62 eV, respectively. All these results are in good agreement with previous DFT results reported in the literature.[33, 49]

Next, an Au adatom is adsorbed on F-, Al-, N-, Na- and Li-doped MgO/Mo, where the concentration of the dopants in the MgO film is varied from 2.78% to 8.33%, and the position of the dopant atom is kept fixed in the third MgO layer. We find that the Au adatom prefers to adsorb on different sites for acceptor- and donor-doped systems.

In the case of acceptor-doped MgO/Mo, the Au adatom prefers to adsorb atop oxygen, instead of in the hollow site, when the doping concentration becomes more than 2.78%. In the case of 2.78% doping concentration, the Au monomer prefers to adsorb at the hollow site, bonded to the nearest neighbor (NN) Mg atoms. For 5.55% and 8.33% doping concentrations, adsorption of Au adatom atop O becomes

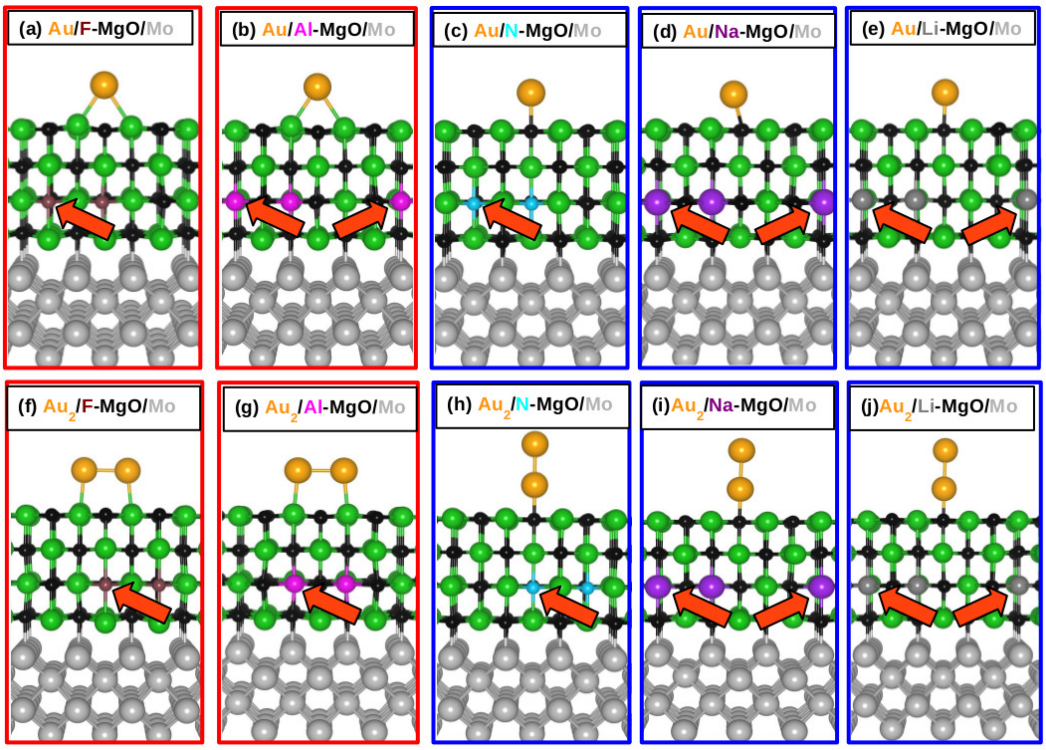

Figure 7.7: Atomistic structures of Au monomer and Au dimer on doped-MgO(001)/Mo. Au monomer on (a) F-doped, (b) Al-doped, (c) N-doped, (d) Na-doped and (e) Li-doped MgO/Mo. Au dimer on (f) F-doped, (g) Al-doped, (h) N-doped, (i) Na-doped and (j) Li-doped MgO. Color scheme for atomic spheres: Mo, light gray; Mg, green; O, black; N, cyan; F, brown; Na, purple; Al, magenta; Li, dark gray and Au, yellow. The orange arrows show the position of the dopant atoms. The red and blue frames correspond situations where the doping is by donor and acceptor type dopants, respectively.

energetically more favorable than the hollow site or atop Mg for acceptor-doped MgO(001)/Mo systems. Figs. 7.7(c)–(e) show adsorption of an Au monomer on N-doped, Na-doped and Li-doped MgO/Mo systems, respectively, at 5.55% doping concentration.

For donor-doped MgO/Mo systems, the most stable adsorption site for an Au adatom is at the hollow site, bonded to the NN Mg atoms, similar to undoped MgO/Mo systems. The adsorption site remains unchanged with increase in doping concentration, see Figs. 7.7(a) and (b) for the adsorption geometries of the Au monomer on F-doped and Al-doped MgO/Mo, respectively, at 5.55% doping concentration.

E_{ads}(Au) and d, for each kind of doped MgO/Mo system, are reported in Table 7.4,

as a function of the doping concentration. The adsorption energy of an Au adatom increases slowly with an increase in the doping concentration in the case of donor-doped MgO/Mo systems, while the opposite happens for acceptor-doped MgO/Mo. d is the distance between the Au monomer and the substrate. Note that when the Au monomer prefers to adsorb at hollow site on doped-MgO/Mo support, d is defined as the average distance between the Au atom and the two nearest neighbor Mg atoms in the support (as for Au/MgO systems). From Table 7.4, we can see d decreases with an increase in doping concentration, for both donor- and acceptor-doped MgO/Mo systems. This trend can be explained by calculating topological charges on the Au monomer and the support; we will do this further below.

We now turn to the cases where an Au dimer is adsorbed on MgO/Mo. In general, the adsorption geometries are similar to those on doped MgO(001). In the case of acceptor-doped systems, the Au dimer prefers an upright geometry atop O. The adsorption site remains unchanged as a function of the doping concentration. The Au dimer prefers to adsorb in a flat geometry with the two Au atoms forming bonds to two nearest-neighbour Mg atoms for donor-doped MgO/Mo substrates. Figs. 7.7(f)–(j) show the adsorption of an Au dimer on doped MgO/Mo systems. The values of $E_{ads}(\mathrm{Au_2})$ and d for Au dimer on doped MgO/Mo systems are listed in Table 7.5. We see that $E_{ads}(\mathrm{Au_2})$ increases with the donor doping concentration and decreases with an increase in the concentration of acceptor type dopant. Note that when $\mathrm{Au_2}$ adsorbs in a flat geometry on MgO/Mo, d is defined as the average of the distance between each Au atom and the Mg atom directly below it.

Au Clusters on Doped MgO(001)/Mo: Charge Transfer

The Au monomer acquires a charge of -0.83 e on undoped MgO/Mo(001). The Au dimer acquires a charge of $Q(\mathrm{Au_2}) = -0.30$ e on undoped MgO/Mo(001), which is almost the same as on undoped MgO(001) (-0.28 e). We note that this is in contrast to the case of the Au monomer, where the magnitude of $Q_{\mathrm{T}}(\mathrm{Au})$ increases significantly in the presence of the Mo support. In Figs. 7.8(a)–(j) we show the

Table 7.5: Results for Au dimer (Au_2) adsorbed on doped MgO(001)/Mo. Adsorption site, $E_{ads}(Au_2)$: adsorption energy of Au dimer, d: distance between Au dimer and the support, $Q_T(Au_2)$: charge state of Au dimer. $Q_T(MgO)$ and $Q_T(Mo)$ are the charges of the MgO film and the Mo support, respectively in the 3×3×1 surface cell. The Au dimer adsorbs in an upright geometry atop O with $E_{ads}(Au_2)$= 1.62 eV, d = 2.10 Å and $Q_T(Au_2)$= −0.296 e on undoped MgO(001)/Mo. A negative sign for Q_T implies electron gain and a positive sign implies electron loss.

Dopant (X)	Doping conc.	Adsorption site	$E_{ads}(Au_2)$ (eV)	d (Å)	$Q_T(Au_2)$ (e)	$Q_T(MgO)$ (e)	$Q_T(Mo)$ (e)
F	2.78%		1.82	2.69	−0.8542	1.0857	−0.2329
	5.55%	flat, bonded to Mg	2.24	2.67	−0.9672	1.6971	−0.7295
	8.33%		2.60	2.61	−1.1719	2.3041	−1.1323
Al	2.78%		1.95	2.71	−0.8566	0.9876	−0.1298
	5.55%	flat, bonded to Mg	2.36	2.61	−0.9884	1.6926	−0.704
	8.33%		2.73	2.58	−1.1926	2.2643	−1.0712
N	2.78%		1.70	2.10	−0.2955	−0.189	0.4864
	5.55%	upright, atop O	1.69	2.09	−0.295	−0.822	1.116
	8.33%		1.65	2.09	−0.291	−1.193	1.484
Na	2.78%		1.64	2.09	−0.289	−0.202	0.492
	5.55%	upright, atop O	1.57	2.09	−0.286	−0.858	1.144
	8.33%		1.52	2.08	−0.279	−1.225	1.504
Li	2.78%		1.68	2.09	−0.293	−0.218	0.520
	5.55%	upright, atop O	1.61	2.09	−0.291	−0.835	1.129
	8.33%		1.57	2.08	−0.285	−1.215	1.500

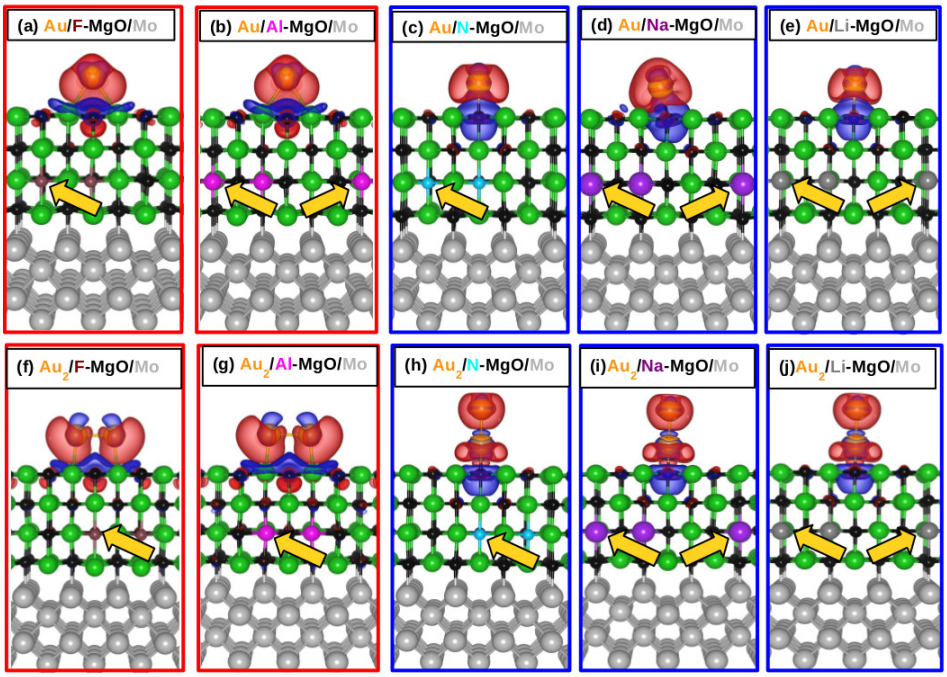

Figure 7.8: The charge redistribution plots for Au monomer (first row) and dimer (second row) on (a), (f) F-doped, (b), (g) Al-doped, (c), (h), N-doped, (d), (i) Na-doped and (e), (j) Li-doped MgO/Mo systems. All systems shown here are at a doping concentration of 5.55% and dopant atoms are situated in the third layer of the oxide. Red and blue lobes show electron accumulation and depletion respectively, drawn at isosurface value 0.001 e/bohr^3. Color scheme for atomic spheres: Mg, green; O, black; Mo, light gray; N, cyan; F, brown; Na, purple; Al, magenta; Li, dark gray; and Au, yellow. The yellow arrows show the position of the dopant atoms. The red and blue frames correspond to situations where the doping is by donor and acceptor type dopants, respectively.

charge redistribution plots of the Au monomer and Au dimer placed on the doped MgO/Mo(001) supports.

Next, we want to investigate the charges on Au clusters deposited on doped MgO/Mo systems. The Au monomer gains a different amount of charge from the support for different dopants. The charge redistribution plots are shown in Figs. 7.8(a)–(f) for an Au monomer on different doped supports at 5.55% doping concentration. We see larger red lobes around the Au monomer when the dopants are F and Al than for N-doped, Na-doped and Li-doped MgO/Mo supports. From Bader analysis, we quantify the charge of the Au monomer on these doped MgO/Mo systems. We find

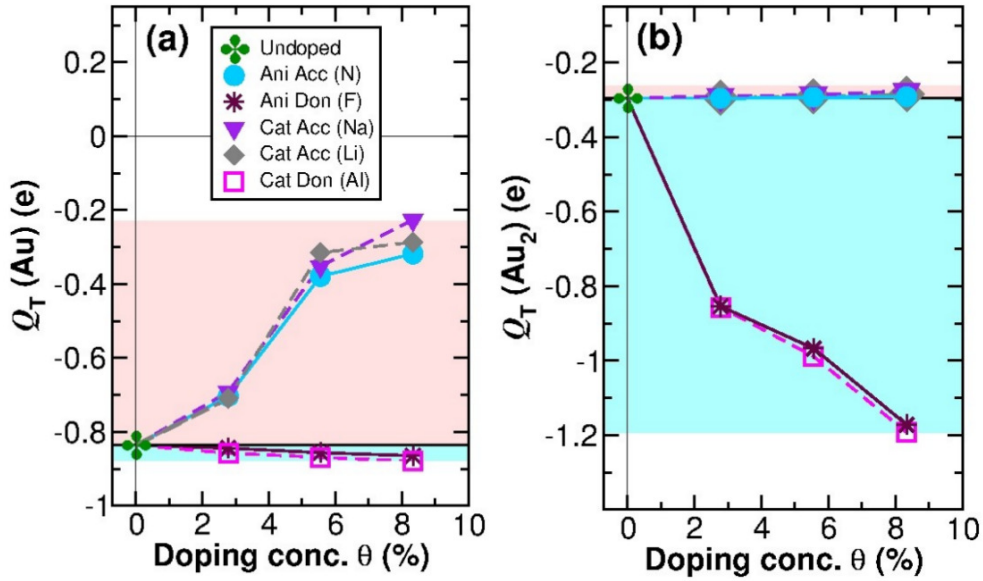

Figure 7.9: Variation of (a) $Q_{\mathrm{T}}(\mathrm{Au})$ and (b) $Q_{\mathrm{T}}(\mathrm{Au_2})$ with doping concentration θ on doped MgO(001)/Mo substrates. The green 'four-leaf clover' symbol, violet triangles, gray diamonds, magenta squares, turquoise circles and maroon stars correspond to data for undoped, Na-doped, Li-doped, Al-doped, N-doped and F-doped systems, respectively. The cyan and salmon pink shaded areas highlight regions where Au_n becomes more or less negatively charged, respectively, when compared to Au_n on the undoped substrate.

the charge on Au is −0.86 e, −0.87 e, −0.38 e, −0.35 e and −0.32 e for F, Al, N, Na and Li dopants, respectively at 5.55% doping concentration.

The change in charge state of the Au monomer with doping concentration θ is plotted in Fig. 7.9(a). We see that as θ increases, the charge gained by the Au monomer, $Q_{\mathrm{T}}(\mathrm{Au})$, increases for donor (F and Al) doped MgO/Mo systems, whereas $Q_{\mathrm{T}}(\mathrm{Au})$ decreases with increase in doping concentration for acceptor (N, Na and Li) doped systems. The rate of change in $Q_{\mathrm{T}}(\mathrm{Au})$ with doping concentration is larger for acceptor-doped systems than donor-doped MgO/Mo systems. Note that the value of $Q_{\mathrm{T}}(\mathrm{Au})$ is higher for donor-doped systems with respect to the undoped MgO/Mo, whereas for acceptor-doped systems $Q_{\mathrm{T}}(\mathrm{Au})$ is always lower than on undoped MgO/Mo for any value of doping concentration. The values of $Q(\mathrm{Au})$ at different doping concentrations are listed in Table 7.4. In the case of donor (F and Al) doped MgO/Mo, $Q_{\mathrm{T}}(\mathrm{Au})$. the charge gained by Au, and $Q_{\mathrm{T}}(\mathrm{Mo})$. the charge

gained by Mo, increases with doping concentration, and simultaneously the number of electrons lost by donor-doped MgO increases. This implies, from donor-doped MgO, electrons are transferred in both ways, to the Au monomer and the metal support. Similarly, in the Au/acceptor-doped MgO/Mo system, electrons are transferred to both the acceptor-doped MgO and the Au monomer from Mo. From Table 7.4, we can see that the charge gained by the Au monomer reduces with doping concentration, but acceptor-doped MgO gains more electrons as the doping concentration increases. Now, we will see how the charge gained by an Au dimer varies for different doped MgO/Mo substrates and as a function of doping concentration. Charge redistribution plots for Au dimers on doped MgO/Mo substrates are shown in Figs. 7.8(f)–(j). The Au dimer gains a significant amount of charge on F-doped and Al-doped MgO/Mo, see Figs. 7.8(f) and (g). The charge gained by the Au dimer is less for acceptor (N, Na and Li) doped substrates. We see that the shapes of the red lobes around Au_2 are different for donor-doped and acceptor-doped MgO/Mo systems. We have quantified the charge gained by the Au dimer, $Q_T(Au_2)$, using the Bader prescription. The values of $Q_T(Au_2)$ on F-doped, Al-doped, N-doped, Na-doped and Li-doped MgO/Mo systems are -0.97 e, -0.99 e, -0.30 e, -0.29 e, -0.29 e, respectively. The variation of $Q_T(Au_2)$ with doping concentration θ is shown in Fig. 7.9(b). Similar to Au/X-MgO/Mo systems, for Au_2/X-MgO/Mo systems also we see that for donor type dopants, Au_2 and Mo gain electrons from MgO. In the case of acceptor-doped MgO/Mo, electrons are transferred from Mo to the acceptor-doped MgO and Au_2. We can clearly see that $Q_T(Au_2)$ increases significantly with increase in doping concentration for F-doped and Al-doped MgO/Mo systems. The value of $Q_T(Au_2)$ does not vary appreciably with θ for acceptor-doped systems.

7.5 Descriptor to Predict the Energetics and Charge State of Au Nanoclusters

In the previous sections, we have already seen that the adsorption geometry and charge on the Au nanoclusters depend on the nature of the substrate. The oxide substrate can be modified by varying both the nature and concentration of the dopant introduced into the MgO layers and also by introducing a metal support below the ultrathin film of the MgO substrate. However, performing DFT calculations on supported Au clusters can be computationally demanding, especially as one needs to explore the phase space of various possible adsorption sites and structural configurations. One would, therefore, like to know whether one can predict the ground state geometry and/or the charge acquired by the Au clusters from properties of the doped supports alone.

Along these lines, one property of the support that one might immediately consider examining is the work function of the support. The work function Φ is defined as the difference in energy between the Fermi level of the support and the vacuum energy, it is a measure of how easy it is to remove electrons from the system. One would, in general, expect that the lower the work function, the easier it would be for the support to donate electrons to adsorbed metal clusters, and thus higher is the negative charge acquired by the Au clusters.

7.5.1 Work function of Doped MgO(001) and Doped MgO(001)/Mo Systems

We compute the work function of doped MgO(001), undoped and doped MgO(001)/Mo. Undoped MgO(001) is an insulator so there is no question of computing the work function for this case. Doping MgO(001) with an acceptor type impurity (either anionic or cationic) shifts the Fermi energy to the top of the valence band, while doping with a donor type impurity (either anionic or cationic) causes the Fermi energy

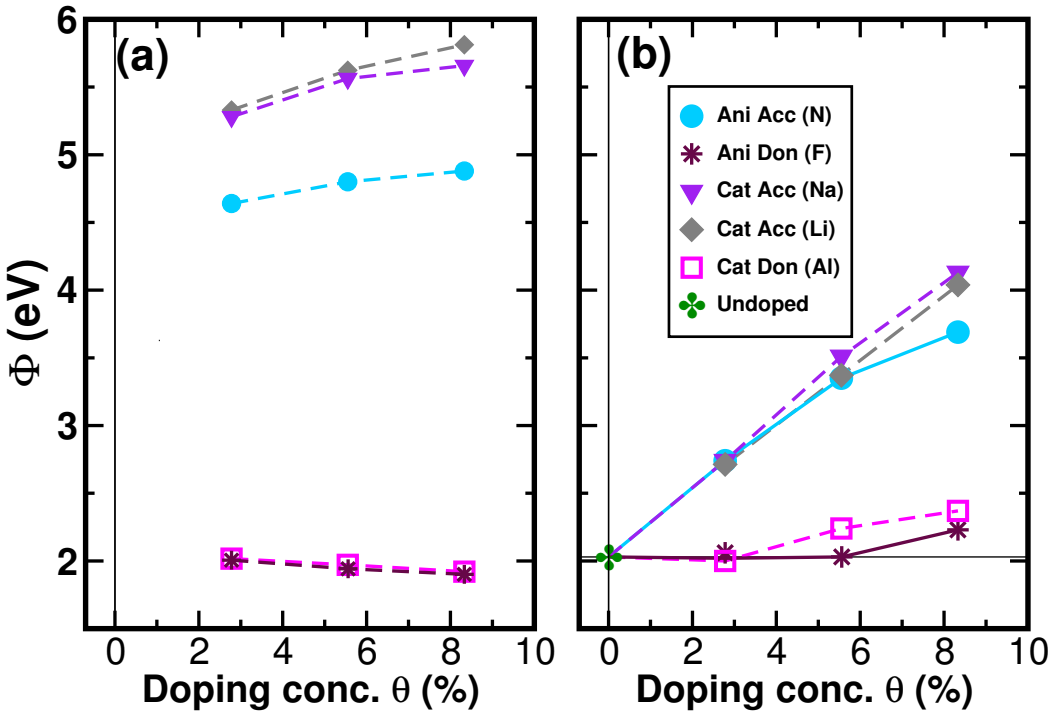

Figure 7.10: Work function Φ as a function of doping concentration θ for (a) doped MgO and (b) doped MgO/Mo systems. The green 'four-leaf clover' symbol, cyan circles, brown stars, purple triangles, dark gray diamonds and magenta squares show the data for undoped, N-doped, F-doped, Na-doped, Li-doped and Al-doped systems, respectively. The horizontal line in (b) shows Φ of undoped MgO/Mo. The labels in the legend indicate whether the dopant is a cation or anion, and acceptor or donor.

to shift to near the bottom of the conduction band. Therefore MgO behaves as a p-type and n-type semiconductor when it is doped with acceptor and donor type impurity atoms, respectively. In Fig. 7.10 we have shown how the work function of the support can be changed as a function of the doping concentration θ, Figs. 7.10(a) and (b) show the change in work function Φ of (a) MgO(001) and (b) MgO/Mo(001), respectively, with doping concentration θ, when the dopant is present in the third layer of the oxide film.

The trends observed in Fig. 7.10(a) are as expected: doping with an electron acceptor (either anionic N or cationic Na/Li) causes electron deficiency in the support. It therefore costs more energy to remove electrons from the surface, and the work function Φ increases. The greater the doping concentration θ, the larger the increase in Φ. For a given value of θ, Φ is larger when the dopant is Na and Li, than when it

is N. This is because the value of $\mathcal{Q}_T/OS$ for Na and Li in MgO is larger than N. The values of Φ for F-doped and Al-doped MgO do not differ appreciably with doping concentration, since $\mathcal{Q}_T/OS$ is almost the same for F and Al. Φ decreases with doping concentration for donor (F or Al) doped MgO systems, since the donor type impurity makes the oxide surface electron-rich. Therefore we see that Li performs best out of the acceptor type dopants considered, while the performance of the donor type dopants F and Al is almost the same.

For the case of the doped MgO/Mo(001) systems, the scenario is more complicated than the doped MgO(001) surfaces because the presence of the metal support plays an important role in tuning the work function of the combined oxide/metal systems. The acceptor dopants act as one might expect, with the work function being increased, relative to its value for the undoped case, upon doping. However, the increase in Φ is noticeably less than it was on MgO(001) [compare Figs. 7.10(a) and (b)]; this is because some of the electron depletion due to the presence of the acceptor dopants is offset by electrons flowing into the MgO layers from the Mo layers. Thus, though the net effect is an increase in work function, the increase is less than it would have been in the absence of the Mo support. Doping MgO with donor type impurities leads to the presence of extra electrons in MgO, which makes the MgO/Mo system electron-rich, so we expect the work function of donor-doped MgO/Mo to decrease with an increase in the doping concentration, as we have already seen for MgO(001). The result that seems quite counter-intuitive is that on MgO/Mo, Φ does not decrease with doping concentration. In the case of F-MgO/Mo, Φ remains almost the same as for the undoped MgO/Mo, at 2.78% and 5.55% doping concentrations, while Φ increases slightly at 8.33% doping concentration. For Al-doped MgO/Mo, Φ increases slightly with doping concentration.

Relationship between Dipole Moment and Work Funciton

Now, we need to understand the quantity on which the work function of a combined oxide/metal system depends. Earlier authors have shown that the change in work

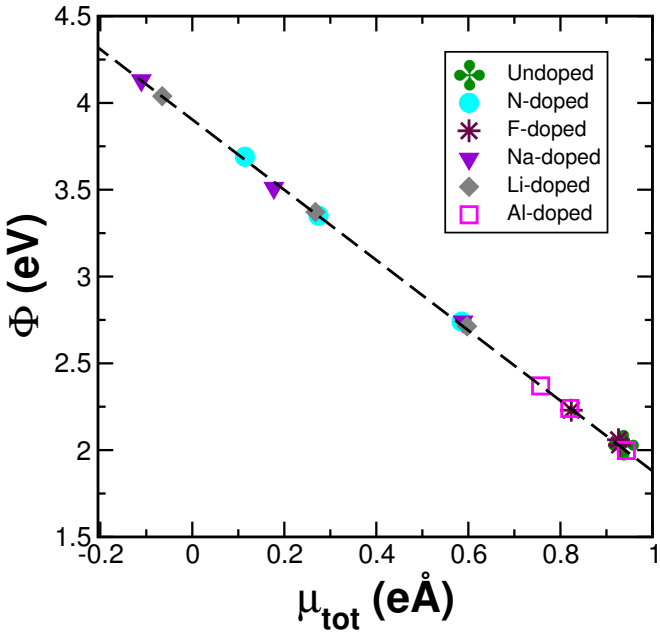

Figure 7.11: Work function Φ vs. total dipole moment $\mu_{\rm tot}$ for doped MgO/Mo(001) systems. The green 'four-leaf clover' symbol, cyan circles, maroon stars, purple triangles, dark gray diamonds, magenta squares show the data for undoped, N-doped, F-doped, Na-doped, Li-doped and Al-doped MgO/Mo systems respectively. Note that all the data collapses onto a single straight line.

function of an oxide/metal system can be viewed as arising from a net dipole. When we plot Φ as a function of the net dipole moment ($\mu_{\rm tot}$) of the MgO/Mo systems in Fig. 7.11, we find a linear relationship between Φ and $\mu_{\rm tot}$ for each kind of MgO/Mo system. The net dipole moment μ of any system arises from the electrons and nuclei, and is given by:

$$\mu = \sum_i z_i Z_i - \int z\rho(z)dz, \tag{7.4}$$

where z_i and Z_i are the nuclear position and charge, respectively for the ith atom. The first term in Eq. (7.4) represents the contribution to the net dipole moment arising from the nuclei. The second term is the dipole moment of the system due to the electrons present in it. $\rho(z)$ is the planar average of electron density n along the z direction, i.e., perpendicular to the plane of the oxide/metal interface:

$$\rho(z) = \frac{1}{A}\int dx \int dy\ n(x,y,z), \tag{7.5}$$

where A is the unit cell area.

There are three main effects which determine the dipole moment of the oxide/metal system. These three effects are:

i) Electrostatic compression: this results from the Coulomb repulsion between metal electrons and oxide anions.[102] The dipole moment induced due to the electrostatic compression effect (μ_{Comp}) depends upon the distance between the oxide and the metal. The smaller the interface distance (d_{int}) the higher is the compression effect. The interface distance, d_{int} is defined as: d_{int}=[1/2(z_{Mg}+z_{O})-z_{Mo}], which is the difference between the z coordinates of the Mo atoms (z_{Mo}) at the topmost layer of Mo(001) surface and the average of the z coordinates of Mg (z_{Mg}) and O (z_{Mo}) atoms at the bottom-most layer of MgO(001) film. A schematic representation of the electrostatic compression effect is shown in Fig. 7.12. The electron density of the bare metal surface spills out into the vacuum. When the oxide film is placed over the metal surface the metal electron density gets compressed due to the electrostatic repulsion it experiences from the oxide anions. The electrostatic compression effect induces a dipole moment, μ_{Comp}, at the oxide-metal interface which makes Φ of the oxide/metal systems lower than Φ of the bare metal surface. As the oxide-metal distance decreases, the metal electron density gets more compressed by the oxide anions and the magnitude of μ_{Comp} reduces, which should decrease the work function of the oxide/metal system. The variation in d_{int} with doping concentration θ is shown in Figs. 7.15(a) and (d) for F-MgO/Mo and N-MgO/Mo systems, respectively, with the dopant present at the third layer of the oxide film.

ii) Charge transfer: Whenever any oxide film is placed on a metal support, electron transfer occurs between them.[102–106] As already discussed, in the case of the MgO/Mo system also, charge transfer takes place between Mo and MgO. For undoped MgO/Mo, there is negligible charge transfer from MgO to Mo. In the case of donor-doped MgO, electron transfer takes place from the doped oxide to Mo, i.e., the oxide loses electrons when the dopants are F or Al. The opposite happens for

acceptor (N, Na or Li) doped MgO on Mo. Since acceptor-doped MgO is electron deficient, Mo serves as a source of electrons for N-doped, Na-doped and Li-doped MgO systems.In the case of doping by donors, μ_{CT}, the dipole moment induced due to charge transfer, is directed from Mo to the donor (F and Al) doped MgO, i.e., along the positive z direction, while for acceptor-doped MgO systems, μ_{CT} is directed from the oxide to the metal. Schematic representations of the charge transfer and μ_{CT} for donor and acceptor-doped MgO/Mo systems are shown in Figs. 7.13 (a) and (b) respectively.

From this simple charge transfer model and the direction of μ_{CT}, we expect the work function of donor-doped MgO/Mo systems should be lower than that of the undoped system and should decrease with doping concentration, while for acceptor-doped MgO/Mo systems, since the charge transfer takes place from metal to the oxide, μ_{CT} should make the work function of the oxide/metal system higher than in the undoped system. The charge transfer between doped MgO and Mo is plotted as a function of doping concentration in Figs. 7.15(b) and (e) for F-MgO/Mo and N-MgO/Mo systems, respectively. Q_T(Mo) is the charge of the Mo support in the 3× 3× 1 cell. A positive sign of Q_T(Mo) implies electrons are lost by Mo, while a negative sign implies the opposite.

iii) Interface rumpling: Interface rumpling results from the surface corrugation of the oxide film deposited on a metal support.[106] The interface rumpling is defined as: $d_{rump} = z_{O,avg}$ - $z_{Mg,avg}$, where $z_{O,avg}$ and $z_{Mg,avg}$ are the averages of the z coordinates of O and Mg atoms respectively present at the interface layer of MgO. Interface rumpling is the result of the interfacial charge transfer.

In the case of donor-doped MgO/Mo systems, electron transfer takes place from MgO to Mo. Therefore, the oxide anions (O atoms) at the interface layer of the oxide experience electrostatic repulsion from the metal surface and move away from the oxide-metal interface, while the cations (Mg atoms) get attracted towards Mo. Hence, d_{rump} becomes positive for the donor-doped systems. The opposite happens

for acceptor-doped MgO/Mo and d_{rump} becomes negative. In the case of donor-doped MgO/Mo systems, the dipole moment induced due to rumpling, μ_{rump}, is directed from the oxide to the metal, i.e., along the negative z direction, while for acceptor-doped systems, μ_{rump} is directed along the positive z direction. The rumpling in donor- and acceptor-doped MgO/Mo systems is shown schematically in Figs. 7.14(a) and (b), respectively. Figs. 7.15(c) and (f) show d_{rump} for F-doped MgO/Mo and N-doped MgO/Mo systems, respectively, as a function of θ. Note that μ_{CT} and μ_{rump} are directed oppositely for both donor- and acceptor-doped systems.

In Fig. 7.15 we show d_{int}, Q_{T}(Mo) and d_{rump} for only F-doped MgO/Mo and N-doped MgO/Mo systems, based on the assumption that the trends observed for F-MgO/Mo systems should be the same as inAl-MgO/Mo systems and the trends found for N-MgO/Mo systems should be similar to those in Na-doped and Li-doped MgO/Mo systems.

Thus, as previous authors have discussed,[91, 99, 108] the net dipole moment (μ_{tot}) is the sum of dipole moments arising due to electrostatic compression (μ_{Comp}), charge transfer (μ_{CT}) and interface rumpling (μ_{R}) effects, i.e., μ_{tot}= μ_{Comp} + μ_{CT} + μ_{R}. We want to separate out the contributions coming from charge transfer, electrostatic compression and interface rumpling to the total dipole moment in our systems. For this purpose, we will attempt to separate out the dipoles arising from charge transfer, and charge transfer + electrostatic compression.

In Fig. 7.16, the black squares, green diamonds and red circles show μ_{tot}, $\mu_{\text{CT+Comp}}$ and μ_{CT}, respectively. μ_{tot} is the net dipole moment present in MgO/Mo systems at their optimum geometries. $\mu_{\text{CT+Comp}}$ denotes the dipole moment of the oxide/metal system in the absence of rumpling. To calculate $\mu_{\text{CT+Comp}}$ we remove rumpling from the oxide layers by making the z coordinates of Mg and O atoms the same. Finally, μ_{CT} is the measure of the dipole moment when only the charge transfer effect is taken into account. This is done by removing rumpling from the oxide layers, while the electrostatic compression effect is removed by making d_{int} for each kind of MgO/Mo

system the same as for undoped MgO/Mo.

We calculate $\mu_{\rm tot}$, $\mu_{\rm CT+Comp}$ and $\mu_{\rm CT}$ as a function of doping concentration for F-MgO/Mo and N-MgO/Mo systems. We find that for both N-doped and F-doped MgO/Mo systems, $\mu_{\rm CT}$, $\mu_{\rm CT+Comp}$ and $\mu_{\rm tot}$ are directed along expected directions. We find that electrostatic compression, which depends on the oxide-metal interface distance, has a negligible contribution to the net dipole moment ($\mu_{\rm tot}$) for both F-doped and N-doped MgO/Mo systems, since in Figs. 7.16(a) and (b) we see that the green diamonds and red circles fall exactly on top of each other. The green diamonds show the computed values of the dipole moment when both charge transfer and electrostatic compression effects are present, (i.e., $\mu_{\rm CT+Comp}$) while the red circles show the dipole moment ($\mu_{\rm CT}$) when only the charge transfer effect is present. We see from Fig. 7.16(a) that the effect of rumpling makes the net dipole moment of F-MgO/Mo systems less positive, since the black squares in Fig. 7.16(a) lie below the red circles and green diamonds at 8.33% doping concentration. The work function plot in Fig. 7.10(b) shows that Φ of F-doped MgO/Mo increases at 8.33% doping concentration with respect to undoped MgO/Mo. At lower doping concentrations (2.78% and 5.55%) Φ of F-MgO/Mo has almost the same value as undoped MgO/MO [see Fig. 7.10(b)]. In Fig. 7.16 (a), for 2.78% and 5.55% doping concentrations the black squares, green diamonds and red circles fall almost on top of each other. Also from Fig. 7.15 (c), we see that the value of $d_{\rm rump}$ is quite small for 2.78% and 5.55% doping concentration values, while for 8.33% there is a significant increase in $d_{\rm rump}$. Therefore the dipole moment induced due to the interface rumpling effect, $\mu_{\rm rump}$, is the reason for the increase in Φ of the F-MgO/Mo system at higher doping concentration (e.g., 8.33% doping concentration). Here recall the fact that $\mu_{\rm CT}$ and $\mu_{\rm rump}$ are always directed oppositely. In the case of F-MgO/Mo, $\mu_{\rm CT}$ is directed along the positive z direction, while $\mu_{\rm rump}$ points along the negative z direction. Now, the more positive the net dipole moment of a system, the easier it is to remove an electron from that system and the lower the work function of the system. Since Φ attains a slightly

higher value at 8.33% doping concentration, this implies that the net dipole moment becomes less positive at this doping concentration. Now, from Figs. 7.15(b) and (c) it is clear that both charge transfer and interface rumpling increase with doping concentration. Interface rumpling plays the dominating role for F-MgO/Mo systems compared to other effects (charge transfer and electrostatic compression) at 8.33% doping concentration, which makes μ_{tot} less positive. This, in turn, increases the work function of F-MgO/Mo systems with doping concentration. In the case of N-doped MgO/Mo systems, the effect of interface rumpling makes the net dipole moment slightly less negative than the dipole moment when the effect of rumpling is absent. For N-MgO/Mo systems also, the effect of electrostatic compression is negligible since the green diamonds and red circles in Fig. 7.16(b) lie on top of each other, therefore there is no difference between μ_{CT} and $\mu_{\text{CT+Comp}}$. μ_{CT} tries to make μ_{tot} less positive with increase in doping concentration, while μ_{rump} tries to make μ_{tot} more positive as a function of doping concentration. The red circles and green diamonds remain below the black squares in Fig. 7.16(b) because the presence of rumpling tries to align the net dipole moment along the positive z direction while the charge transfer effect aligns μ_{tot} along the negative z direction. Since the net dipole moment of N-MgO/Mo systems becomes less positive with the increase in doping concentration, it is clear that μ_{CT} has a greater contribution to the net dipole moment than μ_{rump}, and plays the dominating role in tuning Φ of N-MgO/Mo systems. μ_{tot} of N-MgO/Mo becomes less positive with doping concentration which increases Φ of N-MgO/Mo systems. To summarize, we see that for the oxide/metal systems, the work function depends on the net dipole moment (μ_{tot}) of the system which is governed by the electron redistribution within the oxide-metal system.

7.5.2 Work Function of the Support as a Descriptor for Predicting the Morphology of Deposited Au Clusters

After calculating the work function of the donor and acceptor type impurity doped systems, we want to look at whether the value of the work function (Φ) of the support can be used to predict the adsorption geometry and energetics of the Au dimer and monomer. In Fig. 7.17(a), we have plotted the difference in energy between two competing adsorption geometries, as a function of Φ of the support. In Fig. 7.17(a), for the Au monomer, we consider the two geometries to be adsorption at the hollow site and atop an O atom, and the results are shown for 2.78% doping concentration. Areas of the graph that are shaded yellow and light green correspond to regions where the hollow and atop O sites are favored, respectively. We see that there is a monotonic, and indeed linear, relationship between the difference in energy and Φ. Moreover, the data for MgO(001) and MgO/Mo(001) appear to collapse onto a single line. Note that the Au monomer on acceptor (N, Na and Li) doped MgO(001) prefers to adsorb atop O and the hollow site is not stable at all, so we have considered E_{ads} at the hollow site to be zero for those systems. In the case of donor-doped systems. adsorption at the hollow site is energetically more stable. For both acceptor- and donor-doped MgO/Mo(001) systems, an Au monomer prefers to adsorb at the hollow site at 2.78% doping concentration.

Similarly, for the Au dimer, we have plotted in Fig. 7.17(b) the difference in energies between the upright (atop O) and flat (bonded to two Mg atoms) geometries. Here, yellow and light green shaded regions indicate that the flat and upright geometries are favored, respectively. Once again, we see a monotonic and linear variation of the energy difference with Φ, though in this case the data corresponding to the doped MgO(001) and doped MgO/Mo(001) supports fall on two different lines.

7.5.3 Support Work Function to Predict the Charge State of Deposited Au Clusters

Acceptor-doped MgO(001) surfaces are electron deficient which in turn increases the work function, so ideally, acceptor type impurity doped MgO should pull away electrons from the deposited Au clusters. In the case of Na-doped and Li-doped MgO(001) we see that the deposited Au monomer indeed becomes positively charged, however on N-doped MgO(001) it becomes slightly negatively charged but Q_{T}(Au) is less than for the undoped MgO(001). Doping MgO with a donor type impurity makes the oxide surface electron-rich which reduces the work function of the surface and the deposited Au clusters become more negatively charged.

For acceptor-doped MgO/Mo, electrons are transferred from the metal to the doped oxide and then from the doped oxide to the deposited Au clusters, see the values of Q_{T}(Mo) and Q_{T}(MgO) in Table 7.4 and Table 7.5. Now, as the concentration of acceptor type dopant increases in MgO, it takes away more electrons from Mo to compensate for the electron deficiency in the oxide film, and can therefore transfer less charge to the deposited Au clusters. Thus, the more the concentration of acceptor type dopant, the higher is the work function and less is the charge gained by the Au clusters. In the case of donor-doped MgO/Mo systems, the amount of charge gained by Au clusters does not depend on the work function of the oxide/metal system, since the donor-doped MgO acts as a source of electrons for the deposited Au clusters. Electron transfer takes place from the donor-doped oxide to the deposited Au clusters and the metal support, see the values of Q(Mo), Q(MgO) and Q(Au) in Table 7.4 and Table 7.5. As the concentration of donor type impurity increases, the charge gained by the Au clusters increases. Therefore the charge state of deposited Au clusters does not depend on the electron redistribution at the oxide-metal interface or the work function of the combined oxide/metal system, rather it depends on the concentration of donor type impurity in the oxide film. Therefore, for this case of MgO/Mo(001) doped with donors (unlike all the other cases considered in this chapter), one should

not expect to find a correlation between the work function of the substrate and the charge gained by the deposited Au clusters.

In Fig. 7.18 we examine whether the work function of the doped support can be used to qualitatively and quantitatively predict the charge acquired by Au clusters deposited on these supports. For the reasons already discussed, the data corresponding to MgO/Mo(001) doped with donors are omitted in these graphs. In Fig. 7.18(a), we see that we obtain a perfect linear correlation between the value of Φ for the doped supports, (both in the presence and absence of the Mo support), and the value of $Q_{\mathrm{T}}(\mathrm{Au})$. As in Fig. 7.17(a), areas of the graph shaded yellow and light green indicate regions where the favored adsorption is at the hollow site and atop O, respectively. This graph shows, yet again, that it is possible to tune the charge on the Au monomer over a wide range, and it also indicates that it should be possible to predict what this charge will be, by simply computing the work function of the support. We note that in Fig. 7.18, we have not included data corresponding to MgO/Mo(001) doped with donors; these data do not follow the general trend. This is because of the counter-intuitive trends displayed by Φ for these systems, as has been discussed above.

Figs. 7.18(b)–(e) contain the corresponding data for the Au dimer, with yellow and light green shading indicating regions where the flat and upright adsorption geometries are favored, respectively. It is clear here that the data fall into two groups, corresponding to the two different adsorption geometries. For $\Phi > 2.03$ eV, the upright geometry is preferred, and it is rather difficult to tune $Q(\mathrm{Au_2})$: a rather large change in Φ results in only a small change in the charge on the Au atoms. However, for $\Phi <$ 2.03 eV, the flat geometry becomes favored, and even small changes in Φ result have a huge effect on $Q_{\mathrm{T}}(\mathrm{Au_2})$. Figs. 7.18(c)–(e) contain zoomed-in regions of the data in Fig. 7.18(b). They enable one to compare the effects of cationic and anionic dopants. The variation of $Q_{\mathrm{T}}(\mathrm{Au_2})$ with Φ is more for anionic acceptor-doped MgO systems, than cationic accptor-doped MgO, compare the cyan circles with the purple triangles

or the gray diamonds in Fig. 7.18(c). The change in $Q_T(Au_2)$ as a function of Φ is almost the same when Au_2 is adsorbed on the cationic and anionic acceptor-doped MgO/Mo systems, see Fig. 7.18(d). In the case of donor-doped MgO systems, both $Q_T(Au_2)$ and Φ vary in a smaller range. Also, $Q_T(Au_2)$ changes in a similar manner to Φ for both the cationic and anionic donor-doped systems [Fig. 7.18(e)].

7.6 MgO/Mo systems for Different Positions of the Dopants

So far we have discussed the techniques to modify the substrate by varying the nature of the dopant as well as the doping concentration. To see how the position of the dopant affects the charge transfer between the oxide film and the metal support, the rumpling in the interface layer of the oxide (d_{rump}), the oxide-metal interface distance (d_{int}) and work function (Φ) of the oxide/metal system, we now vary also the position of the dopant from the interface or fourth layer of the oxide film to the second layer for F-doped and N-doped MgO/Mo systems. We assume that all the features mentioned should give similar trends for Li-doped and Na-doped MgO/Mo systems as we find for N-doped MgO/Mo systems while Al-doped MgO/Mo should show the same trend as F-doped MgO/Mo systems.

First, we see, how the work function (Φ) of the N-MgO/Mo and F-MgO/Mo systems changes with variation in the position of the dopant as well as the doping concentration. Figs. 7.19(a) and (b) show Φ of F-MgO/Mo and N-MgO/Mo systems when the dopant atom is placed at the fourth, third and second layer of the oxide at 2.78%, 5.55% and 8.33% concentrations. The blue squares, magenta circles and maroon diamonds show the position of dopant at the fourth, third and second layer of the oxide film, respectively. The red and green dashed lines show the value of Φ of undoped MgO/Mo and the bare Mo(001) surface, respectively. When the dopant is present at the interface or fourth layer of the oxide, Φ of F-MgO/Mo systems is slightly less than Φ of undoped MgO/Mo at 2.78% and 5.55% doping concentrations.

There is a small increase in Φ at 8.33% for the same position of the dopant. The value of Φ for the third layer doped F-MgO/Mo does not change much from the fourth layer doped F-MgO/Mo for the same value of doping concentration, while the value of Φ increases with doping concentration when the dopant is present at the second layer of the oxide film, and for any doping concentration Φ attains appreciably higher values than in the undoped system.

In the case of N-MgO/Mo systems, Φ increases significantly as the dopant moves from the interface or fourth layer of the oxide film to the second layer. Also Φ increases monotonically with doping concentration for a particular position of the dopant. When the dopant is present at the second layer of MgO, Φ of N-MgO/Mo becomes higher than the work function of the Mo surface at 5.55% and 8.33% doping concentrations.

We have already seen Φ depends on the net dipole moment (μ_{tot}) of the MgO/Mo systems. In Fig. 7.20 we plot Φ of F-MgO/Mo and N-MgO/Mo systems for different positions and concentrations of F and N dopants. We see all our data collapse onto a single straight line irrespective of the nature, position and concentration of the dopant.

Now, we want to see how the quantities d_{int}, Q_{T}(Mo) and d_{rump}, (which are responsible for tuning the dipole moment of the MgO/Mo systems) vary with the position of the dopant as well as the concentration.

We find that Q_{T}(Mo) i.e., electron transfer from F-MgO to Mo, increases with doping concentration, see Fig. 7.21(a). The values of Q_{T}(Mo) for a given doping concentration are slightly higher when the dopant is situated at the fourth layer of MgO (i.e., at the interface layer) than the second and third layers, for doped F-MgO/Mo systems. d_{int} increases with doping concentration for F-MgO/Mo systems when the dopant is present at the fourth layer of the oxide film, see Fig. 7.21(b). This happens because in the case of F-MgO/Mo systems Mo gains electrons from the oxide, so oxide anions experience electrostatic repulsion from the Mo surface

and shift away from Mo, i.e., z_{O} increases and z_{Mg} decreases, since Mg atoms get attracted to the Mo surface due to electron accumulation on the upper layers of Mo. Now, since the upward shift in z_{O} plays a more dominant role than the downward shift of z_{Mg}, d_{int}, which is the difference between $1/2(z_{\mathrm{O}} + z_{\mathrm{Mg}})$ and z_{Mo}, increases with doping concentration, since electron transfer from F-MgO to Mo increases with doping concentration. d_{int} does not vary much with doping concentration when the dopant is at the third or second layer, i.e., away from the oxide-metal interface. d_{rump} is higher when the dopant is present at the third layer than for any other position of the F dopant, see Fig. 7.21(c).

In the case of N-MgO/Mo systems, Q_{T}(Mo), i.e., the electron transfer from Mo to N-doped MgO, increases with doping concentration, see Fig. 7.21(d). For a given doping concentration, ΔQ_{Mo} is more when the dopant is present at the fourth layer of MgO. d_{int} decreases with doping concentration when the dopant is present at the fourth layer, see Fig. 7.21(e). For N-MgO/Mo systems, N-MgO gains electrons from Mo, so the oxide anions get attracted to the Mo surface and shift downward, which in turn decreases d_{int}. Now, since Q_{T}(Mo) increases with doping concentration, oxide anions experience more attraction towards the metal surface as the doping concentration increases. d_{rump} attains the highest value when N is present at the third layer of the oxide film, see Fig. 7.21(f), which we see for F-MgO/Mo systems also.

As we have done for the third layer doped MgO/Mo systems, here also we separate out μ_{CT} and $\mu_{\mathrm{CT+Comp}}$ from μ_{tot} for F-Mgo/Mo and N-MgO/Mo systems when the dopant atom is at the fourth and second layer of the oxide. We plot the components of the dipole moment in Fig. 7.22 when the dopant is present at the fourth and second layer of the oxide. The black squares, green diamonds and red circles show μ_{tot}, $\mu_{\mathrm{CT+Comp}}$ and μ_{CT} respectively. Figs. 7.22(a) and (b) show the components of the dipole moment for the fourth and second layer doped F-MgO/Mo respectively. In the case of the fourth layer doped F-MgO/Mo the black squares, green diamonds and

red circles fall almost on top of each other, which implies that the contributions of rumpling and charge transfer to the net dipole moment are almost equal and opposite, i.e., they cancel each other in this case, since rumpling tends to make the dipole moment less positive, while charge transfer tries to make the dipole more positive along the z direction. When F is present at the fourth layer then charge transfer is more than for other positions of the dopant and oxide rumpling is also significant for fourth layer doped F-MgO/Mo, see Figs. 7.21(a) and (c). These two opposite effects cancel each other for the fourth layer doped F-MgO/Mo systems. In the case of the second layer doped F-MgO/Mo systems, the black squares fall below the red circles and green diamonds in Fig. 7.22(b) which implies the effect of rumpling plays a more dominating role than charge transfer.

In the case of N-MgO/Mo systems, the black squares lie higher than the red circles and green diamonds for the fourth layer doped N-MgO/Mo systems, see Fig. 7.22(c). For the second layer doped N-MgO/Mo systems, the dipole moments attain negative values, and they become more negative as the doping concentration increases, see Fig. 7.22(d). This implies that charge transfer plays a dominating role in the case of the second layer doped N-MgO/Mo systems, since μ_{CT} is directed along the negative z direction for N-MgO/Mo systems.

Thus, we see that Φ increases significantly when the dopant is present at the second layer of N-MgO/Mo systems, since the dipole moment becomes more negative for that position of the dopant and charge transfer plays a dominating role among the effects responsible for tuning the net dipole moment of N-MgO/Mo systems. In the case of F-MgO/Mo systems, the work function does not show the trend expected from asimple transfer charge model, and this happens because oxide rumpling plays a more dominant role than the charge transfer effect.

7.7 Conclusions

In summary, we have used *ab initio* density functional theory calculations to investigate the possibility of tuning the charge state of small Au nanoparticles by appropriately doping the oxide support that they are placed on, with aliovalent cations or anions.

We first doped bulk MgO substitutionally with different impurities, keeping the doping concentration fixed at 3.70%. The descriptor, $\mathcal{D} = \Delta\chi/\Delta R$ was found to predict the amount of topological charge ($\mathcal{Q}_T$) on each dopant. From the $\mathcal{Q}_T(X)/OS(X)$ vs $\Delta\chi/\Delta R$ plot we saw that the dopant atoms behave differently from each other. For Al, F and Li dopants the value of the target $\mathcal{I} = \mathcal{Q}_T(X)/OS(X)$ approached 1, i.e., for these dopants, their topological charge approached their nominal oxidation state. We found a nice correlation between $\mathcal{Q}_T(X)/OS(X)$ and $\Delta\chi/\Delta R$. We saw that the value of $\mathcal{Q}_T$ approaches OS as $\Delta\chi/\Delta R$ increases.

Then we proceeded from the bulk doped oxide to the surface. We performed substitutional doping of MgO(001) surface with F, Al, N, Na and Li dopants and adsorbed an Au monomer and an Au dimer on the doped MgO substrates. We found that for the Au monomer, it was possible to make the adsorbed Au atom either positively or negatively charged. For the range of doping concentrations studied here, we were able to vary the charge $Q_{\mathrm{T}}(\mathrm{Au})$ of the monomer from -0.88 e to $+0.25$ e. For the Au dimer, we were able to tune the charge $Q_{\mathrm{T}}(\mathrm{Au_2})$ of the dimer between -1.28 e and -0.14 e on MgO(001) (in no case did the Au dimer become positively charged). These changes in charge state depended on the changes in adsorption geometry: when the Au atoms became more negatively charged, the Au monomer switched its adsorption site from atop an O atom to the hollow site on the surface, while the Au dimer transitioned from an upright to flat geometry. We found that the charge state of Au monomers and Au dimers at a given doping concentration had a direct correlation with the descriptor $\Delta\chi/\Delta R$. Therefore $\Delta\chi/\Delta R$ can successfully predict the performance of the dopants in tuning the charge state of deposited Au

nanoclusters.

We also explored the effects of a metal support placed below an ultra-thin (four atomic layers thick) MgO layer. We studied the MgO/Mo systems by varying both the concentration and position of the dopant atoms and finally we investigated the charge state of Au clusters on doped MgO/Mo systems. We found that the Mo support did not have an appreciable effect in the case of doping with donors in tuning the charge state of deposited Au nanoclusters. The charge on the Au atoms reduced significantly when Mo was placed below acceptor-doped MgO. However, using a combination of a metal support and oxide doping might be feasible as a way of obtaining finer control over the charge state of deposited clusters. In general, the charges and adsorption geometries of the Au clusters changed from deposition over the free-standing MgO(001) substrate to the situation where the MgO substrate was placed over the Mo support, for the same dopant and the same doping concentration. Q(Au) varied in a range of -0.88 e to -0.28 e on MgO/Mo, while $Q(\mathrm{Au_2})$ varied from -1.19 e to -0.28 e.

Since the charge state is correlated with the adsorption geometry of the Au clusters and both of them depend on the type of dopant and doping concentration, we were interested in finding another descriptor which can predict both the adsorption geometry and the charge state of the Au clusters with the change in nature and concentration of the dopant. We found that the work function of the substrate is a quantity with which the adsorption geometry and charge state of the deposited Au clusters correlate well. Our results suggest that both the adsorption geometry and the charge state of the Au monomer and Au dimer can be predicted with reasonable accuracy by simply computing the work function of the bare doped substrate, with the important exception of the case when the oxide is doped with donors as well as supported by a metal. This is because in this case, though the charging of the cluster follows the naive expectations that one might have, based on the fact that one is doping with a donor species, the change in work function occurs in the opposite

direction, due to the effect of the metal substrate. Therefore, we find that the work functions of the doped MgO(001) and MgO/Mo surfaces (except for donor-doped MgO/Mo systems) can serve as a good predictor to determine the adsorption geometry and charge state of the deposited Au clusters as a function of doping concentration on the doped MgO substrates.

We believe that the broad trends found in this work should hold also for clusters of other sizes. Our work suggests a simple way to tune the charge state of Au nanoparticles; this should be of interest in the field of nanocatalysis since it is well known that for different reactions with Au nanocatalysts, different charges on the Au nanoparticles are to be preferred. Despite our success in charging the Au monomer positively by using Na and Li dopants, and finding descriptors to predict the charge state and adsorption geometries of the deposited Au nanoclusters, our results suggest that it will be quite challenging to make larger sized Au clusters positively charged by substrate doping, and this remains an open question to be addressed in future work.

Bibliography

[1] S. M. Sze and K. N. Kwok, *Physics of Semiconductor Devices*. America: A John Wiley and Sons, 2006.

[2] W. Shockley, *Electrons and Holes in Semiconductors: With Applications to Transistor Electronics*. Bell Telephone Laboratories series, Robert E. Krieger, 1950.

[3] A. Fujimori and H. Namatame *Physica C: Superconductivity*, vol. 185-189, pp. 51–56, 1991.

[4] C. Kili and A. Zunger *Appl. Phys. Lett.*, vol. 81, no. 1, pp. 73–75, 2002.

[5] S. B. Ogale *Adv. Mater.*, vol. 22, pp. 3125–3155, 2010.

[6] J. Robertson and S. J. Clark *Phys. Rev. B*, vol. 83, p. 075205, 2011.

[7] S. Tosoni, D. Fernandez Hevia, . Gonzlez Daz, and F. Illas *J. Phys. Chem. Lett.*, vol. 3, pp. 2269–2274, 2012.

[8] H. Sun, W. Fan, Y. Li, X. Cheng, P. Li, and X. Zhao *J. Solid State Chem.*, vol. 183, pp. 3052–3057, 2010.

[9] J. Xu, S. Huang, and Z. Wang *Sol. State Commun.*, vol. 149, pp. 527–531, 2009.

[10] W.-J. Yin, H. Tang, S.-H. Wei, M. M. Al-Jassim, J. Turner, and Y. Yan *Phys. Rev. B*, vol. 82, p. 045106, 2010.

[11] M. Niu, W. Xu, X. Shao, and D. Cheng *Appl. Phys. Lett.*, vol. 99, p. 203111, 2011.

[12] Y. Li, K. Ding, B. Cheng, Y. Zhang, and Y. Lu *Phys. Chem. Chem. Phys.*, vol. 17, pp. 5613–5623, 2015.

[13] P. Mavropoulos, M. Ležaić, and S. Blügel *Phys. Rev. B*, vol. 80, p. 184403, 2009.

[14] T. Ito, J. Wang, C. H. Lin, and J. H. Lunsford *J. Am. Chem. Soc.*, vol. 107, pp. 5062–5068, 1985.

[15] P. Myrach, N. Nilius, S. Levchenko, A. Gonchar, T. Risse, K.-P. Dinse, L. Boatner, W. Frandsen, R. Horn, H.-J. Freund, R. Schlögl, and M. Scheffler *Chem.Cat.Chem.*, vol. 2, pp. 854 – 862, 2010.

[16] Y. Izumi, T. Shimizu, T. Kobayashi, and K.-i. Aika *Chem. Commun.*, pp. 1053–1054, 2000.

[17] F. Kapteijn, J. Rodriguez-Mirasol, and J. A. Moulijn *Appl. Catal. B: Environ.*, vol. 9, no. 1, pp. 25–64, 1996.

[18] S. Kuck, L. Fornasiero, E. Heumann, E. Mix, G. Huber, and A. Kärner, T.and Maaroos *Chem.Cat.Chem.*, vol. 2, 2010.

[19] N. Mammen, S. Narasimhan, and S. de Gironcoli *J. Am. Chem. Soc.*, vol. 133, pp. 2801–2803, 2011.

[20] F. Stavale, X. Shao, N. Nilius, H.-J. Freund, S. Prada, L. Giordano, and G. Pacchioni *J. Am. Chem. Soc.*, vol. 134, pp. 11380–11383, 2012.

[21] N. Mammen, S. de Gironcoli, and S. Narasimhan *J. Chem. Phys.*, vol. 143, p. 144307, 2015.

[22] M. Zhu, C. M. Aikens, M. P. Hendrich, R. Gupta, H. Qian, G. C. Schatz, and R. Jin *J. Am. Chem. Soc.*, vol. 131, p. 2490, 2009.

[23] S. Antonello, N. V. Perara, M. Ruzzi, J. A. Gascón, and F. Maran *J. Am. Chem. Soc.*, vol. 135, p. 15585, 2013.

[24] C. Novo and P. Mulvaney *Nano Letters*, vol. 7, pp. 520–524, 2007.

[25] M. Haruta and M. Daté *Applied Catalysis A: General*, vol. 222, pp. 427–437, 2001.

[26] M. Haruta, T. Kobayashi, H. Sano, and N. Yamada *Chem. Lett.*, vol. 16, no. 2, p. 405, 1987.

[27] H.-G. Boyen, G. Kästle, F. Weigl, B. Koslowski, C. Dietrich, P. Ziemann, J. P. Spatz, S. Riethmüller, C. Hartmann, M. Möller, G. Schmid, M. G. Garnier, and P. Oelhafen *Science*, vol. 297, p. 1533, 2002.

[28] Q. Fu, H. Saltsburg, and M. Flytzani-Stephanopoulos *Science*, vol. 301, p. 935, 2003.

[29] T. Hayashi, K. Tanaka, and M. Haruta *J. Catal.*, vol. 178, p. 566, 1998.

[30] J. Jia, K. Haraki, J. N. Kondo, K. Domen, and K. Tamaru *J. Phys. Chem. B*, vol. 104, p. 11153, 2000.

[31] C. Bianchi, F. Porta, L. Prati, and M. Rossi *Topics in Catal.*, vol. 13, p. 231, 2000.

[32] M. Haruta *Catal. Today*, vol. 36, p. 153, 1997.

[33] P. Frondelius, H. Häkkinen, and K. Honkala *New J. Phys.*, vol. 9, p. 339, 2007.

[34] L. Giordano, M. Baistrocchi, and G. Pacchioni *Phys. Rev. B*, vol. 72, p. 115403, 2005.

[35] S. Dong, Y. Zhang, X. Zhang, J. Mao, and Z. Yang *App. Surf. Science*, vol. 426, pp. 554–561, 2017.

[36] N. Lopez and J. K. Nørskov *J. Am. Chem. Soc.*, vol. 124, pp. 11262–11263, 2002.

[37] X. Lin, B. Yang, H.-M. Benia, P. Myrach, M. Yulikov, A. Aumer, M. A. Brown, M. Sterrer, O. Bondarchuk, E. Kieseritzky, J. Rocker, T. Risse, H.-J. Gao, N. Nilius, and H.-J. Freund *J. Am. Chem. Soc.*, vol. 132, pp. 7745–7749, 2010.

[38] C. Zhang, A. Michaelides, D. A. King, and S. J. Jenkins *J. Am. Chem. Soc.*, vol. 132, pp. 2175–2182, 2010.

[39] Y. G. Wang, D. Mei, V. A. Glezakou, J. Li, and R. Rousseau *Nat. Commun.*, vol. 6, p. 6511, 2015.

[40] J.-C. Liu, Y.-G. Wang, and J. Li *J. Am. Chem. Soc.*, vol. 139, pp. 6190–6199, 2017.

[41] M. M. Schubert, S. Hackenberg, A. C. van Veen, M. Muhier, V. Pizak, and R. J. Behm *J. Catal.*, vol. 197, pp. 113–122, 2001.

[42] A. R. Puigdollers, P. Schlexer, and G. Pacchioni *J. Phys. Chem. C*, vol. 119, pp. 15381–15389, 2015.

[43] M. Gao, A. Lyalin, and T. Taketsugu *Catalysts*, vol. 1, pp. 18–39, 2011.

[44] A. R. Puigdollers, P. Schlexer, and G. Pacchioni *J. Phys. Chem. C*, vol. 119, pp. 15381–15389, 2015.

[45] J. Graciani, A. Nambu, J. Evans, J. A. Rodriguez, and J. F. Sanz *J. Am. Chem. Soc.*, vol. 130, pp. 12056–12063, 2008.

[46] S. Prada, L. Giordano, and G. Pacchioni *J. Phys. Chem. C*, vol. 116, pp. 5781–5786, 2012.

[47] F. Stavale, X. Shao, N. Nilius, H.-J. Freund, S. Prada, L. Giordano, and G. Pacchioni *J. Am. Chem. Soc.*, vol. 134, pp. 11380–11383, 2012.

[48] S. Prada, L. Giordano, and G. Pacchioni *J. Am. Chem. Soc.*, vol. 117, pp. 9943–9951, 2013.

[49] P. Frondelius, H. Häkkinen, and K. Honkala *Phys. Rev. B*, vol. 76, p. 073406, 2007.

[50] K. Honkala and H. Häkkinen *J. Phys. Chem. C*, vol. 96, pp. 1200–1204, 1992.

[51] V. Simic-Milosevic, M. Heyde, N. Nilius, T. Knig, H.-P. Rust, M. Sterrer, T. Risse, H.-J. Freund, L. Giordano, and G. Pacchioni *J. Am. Chem. Soc.*, vol. 130, pp. 7814–7815, 2008.

[52] J. Nevalaita, H. Häkkinen, and K. Honkala *J. Phys. Chem. C.*, vol. 121, pp. 10824–10831, 2017.

[53] T. Risse, S. Shaikhutdinov, N. Nilius, M. Sterrer, and H. J. Freund *Acc. Chem. Res.*, vol. 41, pp. 949–956, 2008.

[54] L. A. Kappers, R. L. Kroes, and E. B. Hensley *Phys. Rev. B*, vol. 1, pp. 4151–4157, 1970.

[55] B. Yoon, H. Häkkinen, U. Landman, A. S. Wörz, J.-M. Antonietti, S. Abbet, K. Judai, and U. Heiz *Science*, vol. 307, pp. 403–407, 2005.

[56] L. Ma, K. Laasonen, and J. Akola *J. Phys. Chem. C.*, vol. 121, pp. 10876–10886, 2008.

[57] A. Del Vitto, G. Pacchioni, F. Delbecq, and P. Sautet *J. Phys. Chem. B*, vol. 109, pp. 8040–8048, 2005.

[58] Z. Yang, R. Wu, Q. Zhang, and D. W. Goodman *Phys. Rev. B*, vol. 65, p. 155407, 2002.

[59] L. Rout, A. Kumar, R. S. Dhaka, G. N. Reddy, S. Giri, and P. Dash *App. Catal. A: General*, vol. 538, pp. 107 – 122, 2017.

[60] C. Gao, Y. Hu, M. Wang, M. Chi, and Y. Yin *J. Am. Chem. Soc.*, vol. 136, pp. 7474–7479, 2014.

[61] L. Zhang, A. Wang, J. T. Miller, X. Liu, X. Yang, W. Wang, L. Li, Y. Huang, C.-Y. Mou, and T. Zhang *ACS Catal.*, vol. 4, pp. 1546–1553, 2014.

[62] T. Joseph, K. V. Kumar, A. Ramaswamy, and S. Halligudi *Catal. Commun.*, vol. 8, pp. 629–634, 2007.

[63] B. Yoon and U. Landman *Phys. Rev. Lett.*, vol. 100, p. 056102, 2008.

[64] L. M. Ghiringhelli, J. Vybiral, S. V. Levchenko, C. Draxl, and M. Scheffler *Phys. Rev. Lett.*, vol. 114, p. 105503, 2015.

[65] F. Göltl, P. Müller, P. Uchupalanun, P. Sautet, and I. Hermans *Chem. Mater.*, vol. 29, no. 15, pp. 6434–6444, 2017.

[66] Y. Zheng, K. Song, J. Jung, C. Li, Y.-U. Heo, M.-S. Park, M. Cho, Y.-M. Kang, and K. Cho *Chem. Mater.*, vol. 27, pp. 3243–3249, 2015.

[67] P. Zalake, S. Ghosh, S. Narasimhan, and K. G. Thomas *Chem. Mater.*, vol. 29, pp. 7170–7182, 2017.

[68] P. Giannozzi, S. Baroni, N. Bonini, M. Calandra, R. Car, C. Cavazzoni, D. Ceresoli, G. Chiarotti, M. Cococcioni, I.Dabo, A. D. Corso, S. de Gironcoli, S. Fabris, G. Fratesi, R. Gebauer, U. Gerstmann, C. Gougoussis, A. Kokalj, M. Lazzeri, L. Martin-Samos, N. Marzari, F. Mauri, R. Mazzarello, S. Paolini, A. Pasquarello, L. Paulatto, C. Sbraccia, S. Scandolo, G. Sclauzero, A. P. Seitsonen, A. Smogunov, P. Umari, and R. M. Wentzcovitch *J. Phys. Condens. Matter*, vol. 21, p. 395502, 2009.

[69] W. Kohn and L. J. Sham *Phys. Rev.*, vol. 140, pp. A1133–A1138, 1965.

[70] D. Vanderbilt *Phys. Rev. B.*, vol. 41, pp. 7892–7895, 1990.

[71] J. P. Perdew and Y. Wang *Phys. Rev. B*, vol. 46, pp. 12947–12954, 1992.

[72] H. J. Monkhorst and J. D. Pack *Phys. Rev. B*, vol. 13, p. 5188, 1976.

[73] N. Marzari, D. Vanderbilt, A. D. Vita, and M. Payne *Phys. Rev. Lett.*, vol. 82, pp. 3296–3299, 1999.

[74] R. P. Feynman *Phys. Rev.*, vol. 56, pp. 340–343, 1939.

[75] R. F. W. Bader, *Atoms in Molecules - A quantum theory*. New York: Oxford University Press, 1990.

[76] W. Tang, E. Sanville, and G. Henkelman *J. Phys. Condens. Matter*, vol. 21, p. 084204, 2009.

[77] P. Mori-Sánchez, A. M. Pendás, and V. Luaa *J. Am. Chem. Soc.*, vol. 124, no. 49, pp. 14721–14723, 2002.

[78] Y. Li, K. Ding, B. Cheng, Y. Zhang, and Y. Lu *Phys. Chem. Chem. Phys.*, vol. 17, pp. 5613–5623, 2015.

[79] R. Saha, S. Revoju, V. I. Hegde, U. V. Waghmare, A. Sundaresan, and C. N. R. Rao *Chem. Phys. Chem.*, vol. 14, pp. 2672–2677, 2013.

[80] J. Xu, S. Huang, and Z. Wang *Solid State Commun.*, vol. 149, pp. 527–531, 2009.

[81] P. Mavropoulous, M. Lezaic, and S. Blugel *Phys. Rev. B*, vol. 80, p. 184403, 2009.

[82] Z. Zhuomao, B. Baoan, and S. Haifeng *J. Semicond.*, vol. 36, p. 102003, 2015.

[83] G. Henkelman, B. P. Uberuaga, D. J. Harris, J. H. Harding, and N. L. Allan *Phys. Rev. B*, vol. 72, p. 115437, 2005.

[84] P. Mori-Sánchez, A. Pendás Martin, and V. Lauña *J. Am. Chem. Soc.*, vol. 124, no. 49, pp. 14721–14723, 2002.

[85] K. Fajans *Naturwissenschaften*, vol. 11, no. 10, pp. 165–172, 1923.

[86] K. Fajans and W. Z. Frankenburger *Zeitschrift für Physikalische Chemie*, vol. 105, no. 1, pp. 255–272, 1923.

[87] B. Cordero, V. Gomez, A. E. Platero-Prats, M. Reves, J. Echeverria, E. Cremades, F. Barragan, and S. Alvarez *Dalton Trans.*, pp. 2832–2838, 2008.

[88] P. Pyykkö and M. Atsumi *Chem. Eur. J.*, vol. 15, no. 1, pp. 186–197, 2008.

[89] P. Pyykkö and M. Atsumi *Chem. Eur. J.*, vol. 15, no. 46, pp. 12770–12779, 2009.

[90] J. Huheey, E. Keiter, R. Keiter, and O. Medhi, *Inorganic Chemistry: Principles of Structure and Reactivity*. Pearson Education India, 2006.

[91] T. C. Leung, C. L. Kao, and W. S. Su *Phys. Rev. B*, vol. 68, p. 195408, 2003.

[92] T. C. Leung, C. L. Kao, W. S. Su, Y. J. Feng, and C. T. Chan *Phys. Rev. B*, vol. 68, p. 195408, 2003.

[93] S. Sicolo, L. Giordano, and G. Pacchioni *J. Phys. Chem. C*, vol. 113, pp. 16694–16701, 2009.

[94] N. Mammen and S. Narasimhan, "Inducing wetting morphologies and increased reactivities of small au clusters on doped oxide supports." Submitted.

[95] C. Jackschath, I. Rabin, and W. Schulze *Phys. Chem.*, vol. 96, pp. 1200–1204, 1992.

[96] S. Prada, L. Giordano, and G. Pacchioni *J. Phys. Chem. C*, vol. 116, pp. 5781–5786, 2012.

[97] C. Zhang, B. Yoon, and U. Landman *J. Am. Chem. Soc.*, vol. 129, pp. 2228–2229, 2007.

[98] J. G. Smith, J. Naruse, H. Hiramatsu, and D. J. Siegel *Chem. Mater.*, vol. 29, pp. 3152–3163, 2017.

[99] S. Ling, M. B. Watkins, and A. L. Shluger *Phys. Chem. Chem. Phys.*, vol. 15, pp. 19615–19624, 2013.

[100] A. J. Logsdail, D. O. Scanlon, C. R. A. Catlow, and A. A. Sokol *Phys. Rev. B*, vol. 90, p. 155106, 2014.

[101] N. E. Singh-Miller and N. Marzari *Phys. Rev. B*, vol. 80, p. 235407, 2009.

[102] S. Ling, M. B. Watkins, and A. L. Shluger *Phys. Chem. Chem. Phys.*, vol. 15, pp. 19615–19624, 2013.

[103] S. Prada, U. Martinez, and G. Pacchioni *Phys. Rev. B*, vol. 78, p. 235423, 2008.

[104] L. Giordano, M. Baistrocchi, and G. Pacchioni *Phys. Rev. B*, vol. 72, p. 115403, 2005.

[105] S. Prada, U. Martinez, and G. Pacchioni *Phys. Rev. B*, vol. 78, p. 235423, 2008.

[106] J. Goniakowski and C. Noguera *Phys. Rev. B*, vol. 79, p. 155433, 2009.

[107] J. Goniakowski and C. Noguera *Phys. Rev. B*, vol. 79, p. 155433, 2009.

[108] L. Sementa, G. Barcaro, F. R. Negreiros, I. O. Thomas, F. P. Netzer, A. M. Ferrari, and A. Fortunelli *J. Chem. Theory and Comput.*, vol. 8, pp. 629–638, 2012.

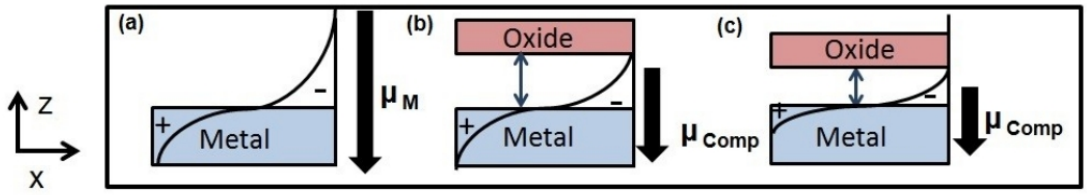

Figure 7.12: Schematic representation of electrostatic compression effect. (a) Electron density spills out into the vacuum from the metal surface, which induces a dipole moment μ_{M} along the negative z direction. (b) Deposition of oxide film on the metal surface. The metal electron density experiences Coulomb repulsion from the oxide anions, which induces a dipole moment μ_{Comp} along the $-z$ direction. (c) As the oxide-metal distance decreases, the metal electron density gets more compressed and the magnitude of μ_{Comp} decreases. This figure has been adapted with permission from Ref. 99 ©Royal Society of Chemistry.

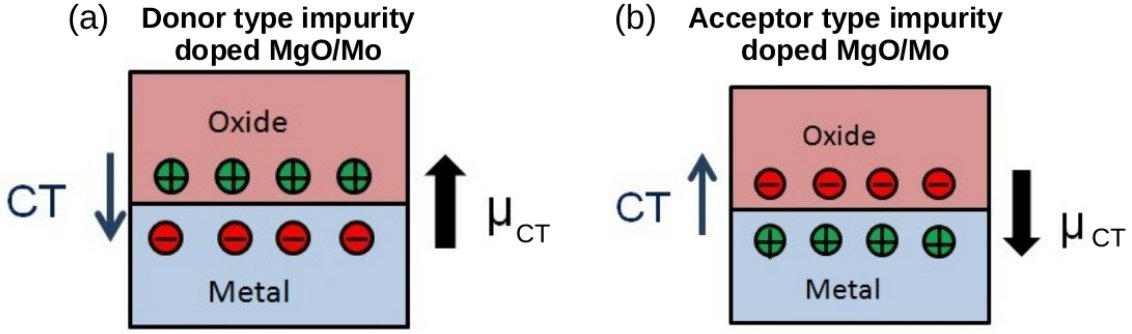

Figure 7.13: Charge transfer between (a) donor-doped MgO and metal, (b) acceptor-doped MgO and metal. μ_{CT} is the dipole moment induced due to charge transfer. The thick black arrow and thin blue arrow show the directions of μ_{CT} and charge transfer respectively. This figure has been adapted from Ref. 103 ©American Physical Society.

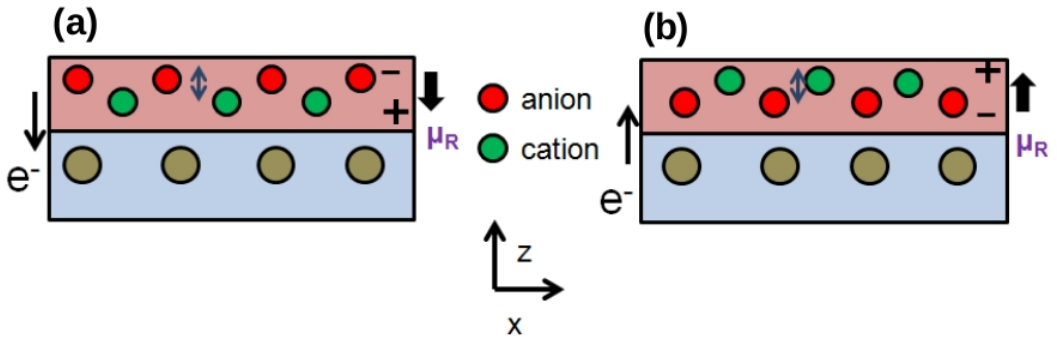

Figure 7.14: Schematic representation of rumpling at interface layer of the oxide film for (a) donor type and (b) acceptor type impurity-doped MgO/Mo systems. The red and green circles show oxide anions and cations respectively. The gray circles show the metal atoms. The thin black arrows show the directions of electron transfer between the oxide and metal for donor type and acceptor type impurity doped MgO/Mo systems. The thick black arrows show the direction of μ_{R}, the dipole moment induced due to rumpling. This figure is adapted from Ref. 107 ©American Physical Society.

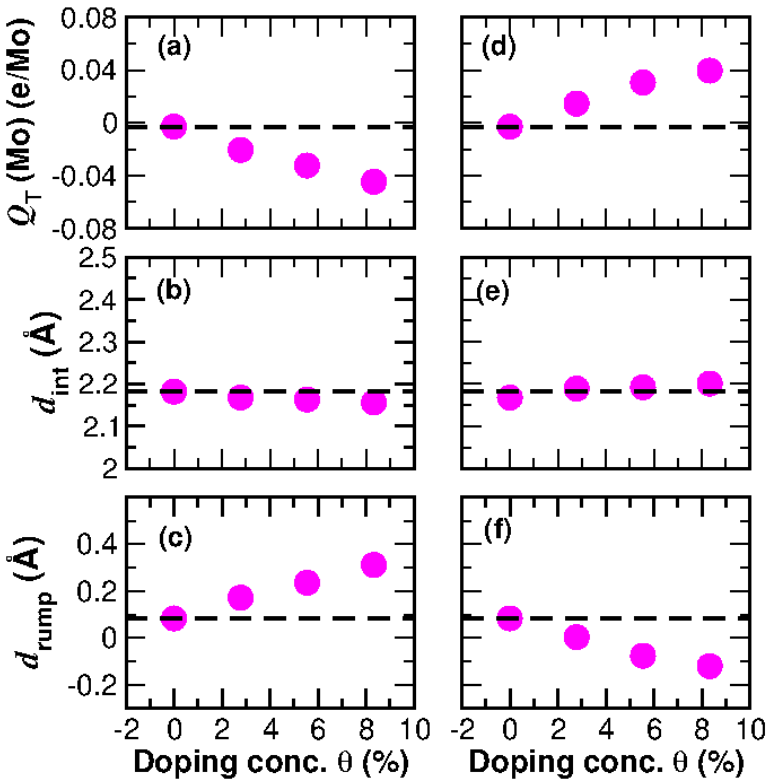

Figure 7.15: Charge transfer, spacing and rumpling in interfaces between doped MgO and Mo. Q_{T}(Mo) of (a) F-MgO/Mo and (d) N-MgO/Mo. d_{int} of (b) F-MgO/Mo and (e) N-MgO/Mo. d_{rump} of (c) F-MgO/Mo and (f) N-MgO/Mo systems as a function of the doping concentration, with the dopant present at the third layer of the oxide film.

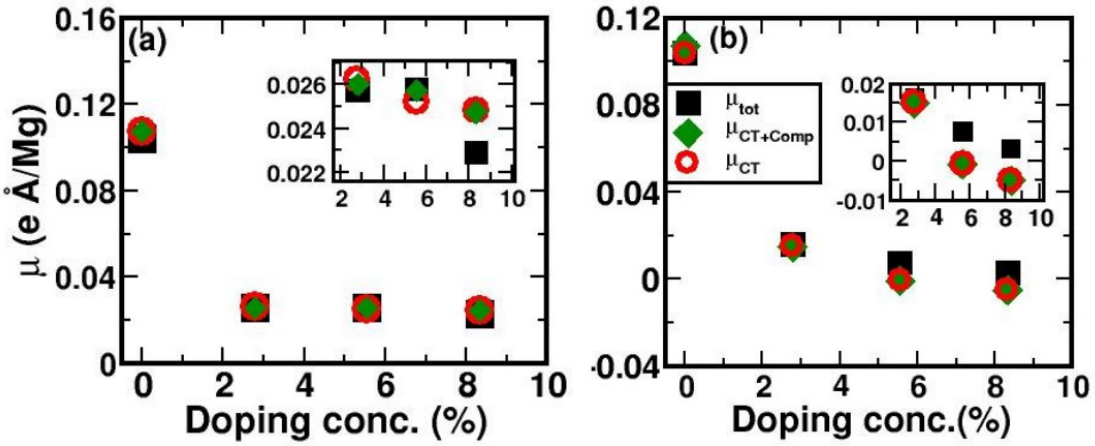

Figure 7.16: Dipole moment (μ) vs. doping concentration plots for (a) F-MgO/Mo and (b) N-MgO/Mo systems as a function of the doping concentration. The black squares, green diamonds and red circles show $\mu_{\rm tot}$, $\mu_{\rm CT+Comp}$ and $\mu_{\rm CT}$, respectively.

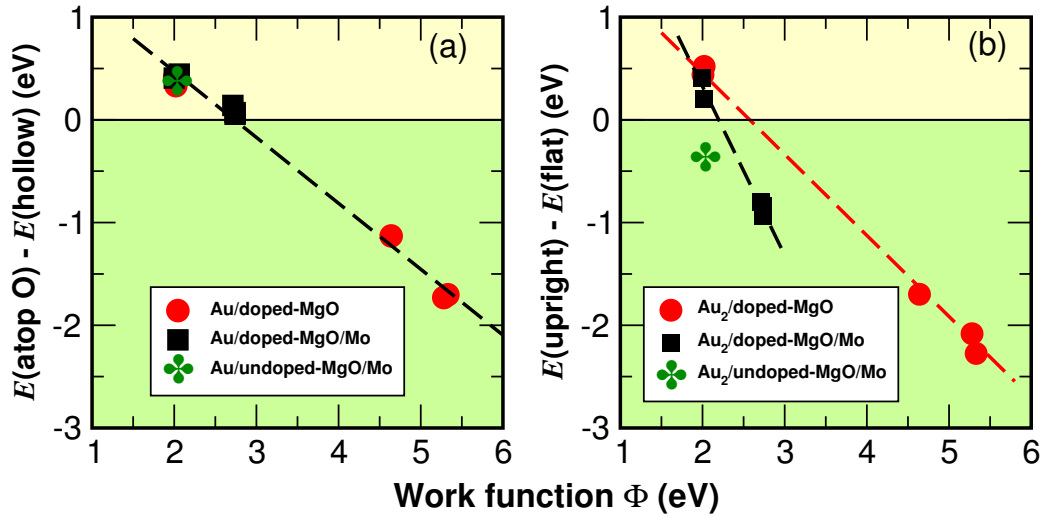

Figure 7.17: The energy difference between atop O and hollow sites for Au monomer with substrate work function, Φ. (b) Difference in energies between the upright (atop O) and flat (bonded to Mg) configurations vs. substrate work function for Au dimer. The results are shown at 2.78% doping concentration. The red circles and black squares show Au_n on doped MgO and doped MgO/Mo systems, respectively. The green 'four-leaf clover' symbol shows undoped MgO/Mo. In (a), the yellow and light green regions show adsorption of Au monomer at the hollow site and atop O, respectively. In (b), yellow and gray regions show the Au dimer in flat and upright configurations, respectively on different substrates.

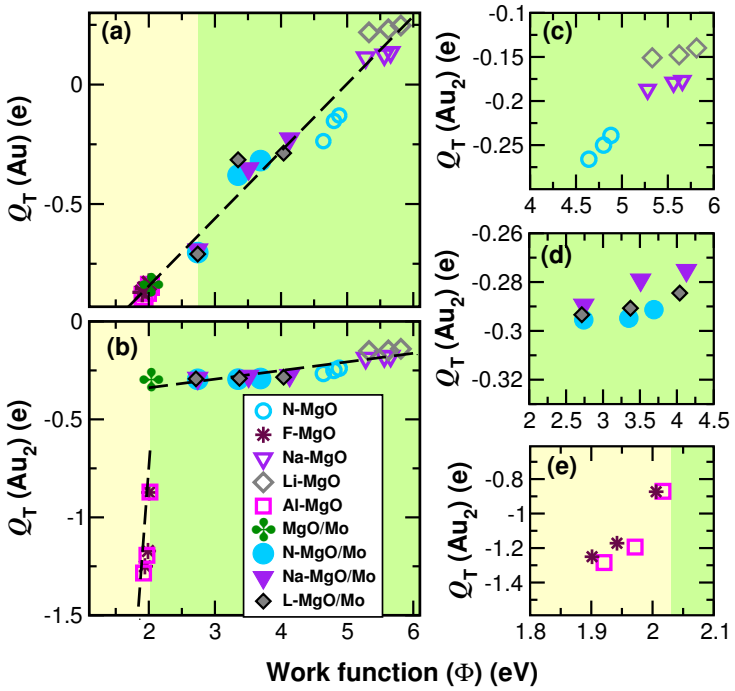

Figure 7.18: Dependence of charge gained by (a) Au monomer and (b)–(e) Au dimer on work function Φ of the substrate. Zoomed in view of Q_T (Au_2) vs. Φ plots for Au_2 on (c) N-doped, Na-doped and Li-doped MgO, (d) N-doped, Na-doped and Li-doped MgO/Mo, and (e) F-doped and Al-doped MgO. The cyan circles, maroon stars, purple triangles, dark gray diamonds, magenta squares show Au clusters on N-doped, F-doped, Na-doped, Li-doped and Al-doped MgO systems, respectively. Solid symbols are used for the doped MgO/Mo systems with the same color conventions as for the doped MgO systems. The green 'four-leaf clover' symbol shows the data for undoped MgO/Mo. In (a), the regions shaded yellow and light green indicate when adsorption of the Au monomer is energetically favored at the hollow site and atop O, respectively. In (b) yellow and gray regions indicate regions corresponding to flat (bonded to Mg) and upright (bonded to O) configurations of Au_2 on the substrate, respectively.

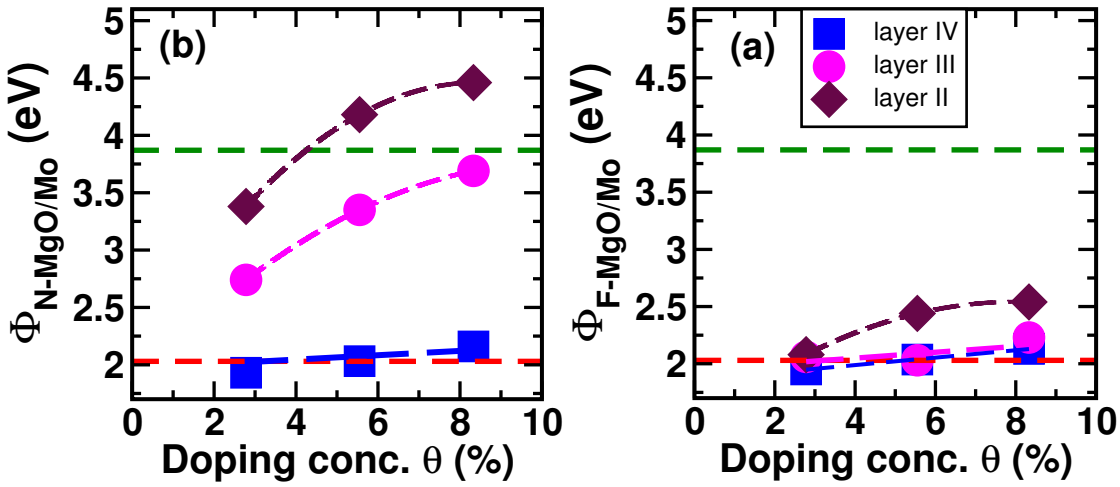

Figure 7.19: Work function Φ of (a) F-MgO/Mo and (b) N-MgO/Mo systems as a function of doping concentration. The blue squares, magenta circles and maroon diamonds show the data for systems where the dopant atoms are present in the fourth, third and second layer of MgO/Mo, respectively. The dashed red and green lines show the Φ of undoped MgO/Mo and the bare Mo surface, respectively.

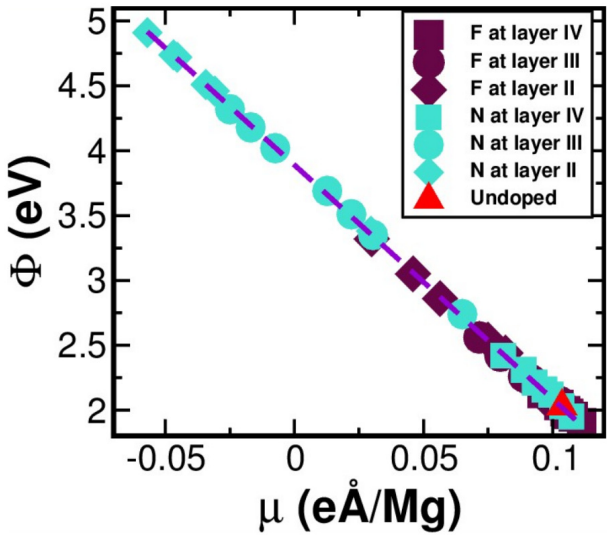

Figure 7.20: Φ vs. μ_{tot} plot for F-MgO/Mo and N-MgO/Mo systems as a function of doping concentration and position of the dopant. The squares, circles and diamonds in brown show the data for F-MgO/Mo systems when the F dopant atoms are present at the fourth (IV), third (III) and second (II) layers, respectively. The squares, circles and diamonds in cyan show the data for N-MgO/Mo systems when the N dopant atoms are at the fourth (IV), third (III) and second (II) layers, respectively. The red triangle shows the data for the undoped MgO/Mo system.

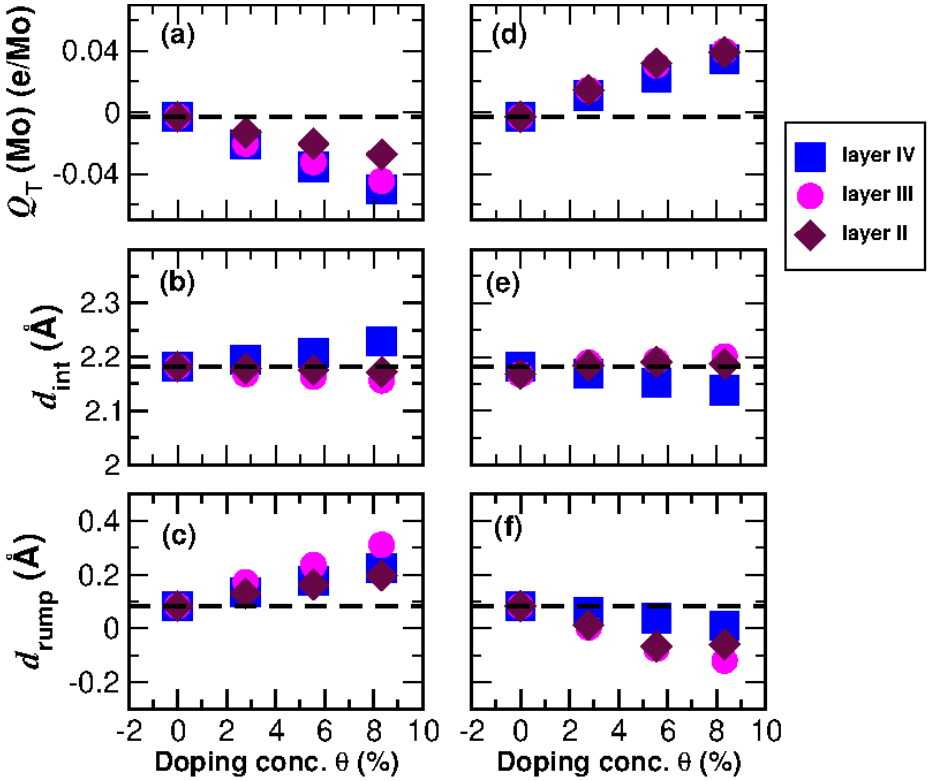

Figure 7.21: Q_T(Mo) of (a) F-MgO/Mo and (d)N-MgO/Mo. d_{int} of (b) F-MgO/Mo and (e) N-MgO/Mo. d_{rump} of (c) F-MgO/Mo and (f) N-MgO/Mo systems as a function of doping concentration. Blue squares, magenta circles and maroon diamonds show, respectively, the data for doped oxide/metal systems where the dopant atoms are present in the fourth, third and second layer.

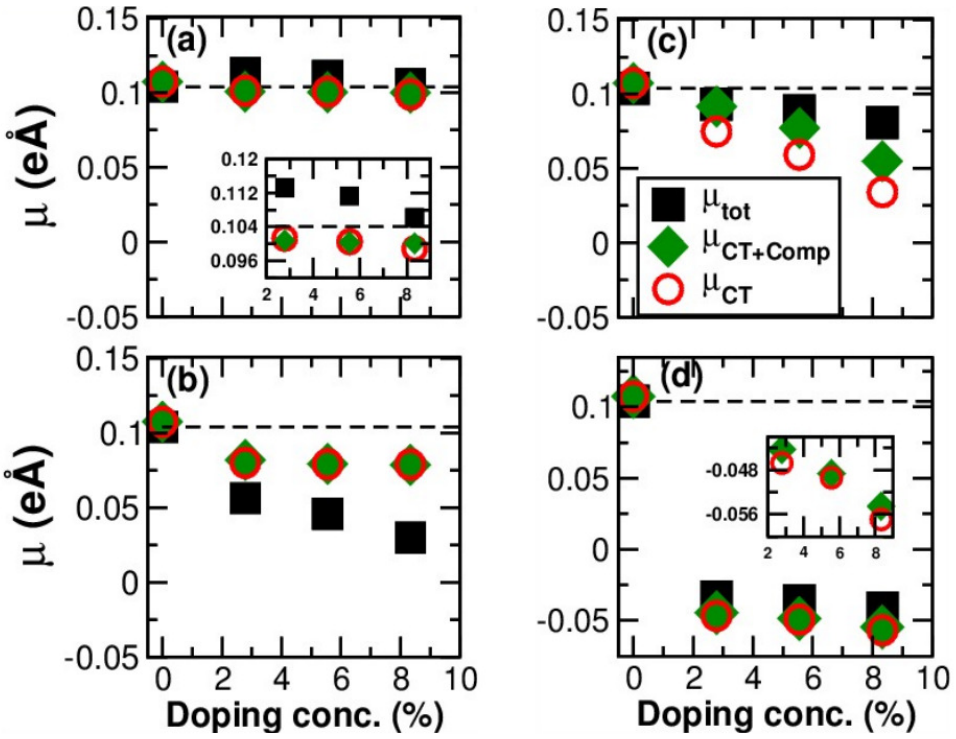

Figure 7.22: Dipole moment (μ) vs. doping concentration plots of F-MgO/Mo systems when dopant atom is present at the (a) fourth (IV) and (b) second (II) layers as a function of doping concentration. N-MgO/Mo systems with dopant at the (c) fourth (IV) and (d) second (II) layers. The black squares, green diamonds and red circles show $\mu_{\rm tot}$, $\mu_{\rm CT+Comp}$ and $\mu_{\rm CT}$, respectively.

Chapter 8

Summary and Outlook

In this chapter, we summarize the main results obtained in this thesis. Also, we give a brief outlook for possible future directions of research.

8.1 Descriptors for the Self-Assembly of Organic Molecules in Two-Dimensions

In chapter 3, we studied the architectures of molecular self-assembly formed by a set of different host and guest molecules. More interestingly, simple descriptors were identified which can successfully predict the pattern of the resulting assemblies.[1]

The self-assembled patterns were stabilized by various noncovalent interactions. We found the geometry of the resulting patterns depends on the molecular building blocks. We considered three host molecules (PE4A, PE4B and PE3A) and five guest molecules (coronene, benzo-ghi-perylene, benzo-c-phenanthrene, phenanthrene, and naphthalene). The host molecules differed from one another by the length of the molecular backbone, number of terminal carboxyl acid groups and number of side alkoxy chains. The host molecule PE4A had a longer backbone with four carboxyl (COOH) groups and four alkoxy side chains. PE4B had two COOH groups and four alkoxy side chains with the backbone length the same as for PE4A. The number of COOH groups and alkoxy chains were four and two, respectively for PE3A. PE3A

had a smaller backbone than PE4A and PE4B. The five guest molecules were of different sizes. Coronene was the largest guest and the other guest molecules can be viewed as angular fragments of coronene.

The host molecules considered in this chapter could, in principle, self-assemble in either a hexagonal or a linear pattern. In the absence of any guest, the three host molecules formed three different sel-assembled patterns. PE4A self-assembled in a hexagonal pattern featuring hexagonal cavities. PE4B formed a densely packed linear pattern containing pentagonal cavities. These cavities could accommodate guest molecules of suitable size. In the case of PE3A, STM experiments did not find any long-range order, while from DFT calculations we found the linear and hexagonal patterns are energetically degenerate. Some of the host assemblies exhibited structural transformations upon introducing specific guests: PE4A always remained in the hexagonal pattern in the presence of any guest, the linear pattern of PE4B transformed into the hexagonal pattern when the size of the guests became larger than phenanthrene; PE3A transformed from the disordered to the ordered hexagonal pattern in the presence of all the guests, except naphthalene.

After studying the energetics of the host assemblies we wanted to identify a descriptor which could predict the geometry of the resulting patterns formed by the host molecules. For this purpose, we chose the difference in Gibbs free energy between the hexagonal and linear patterns as the target property, since the geometry of the resulting host assembly could be determined by this quantity. We identified a descriptor which could predict the structure of the resulting host assemblies. The descriptor for the host molecules, i.e., the "host descriptor" was formulated based on the chemical motifs and geometry of the isolated host molecules. To examine the validity of the host descriptor we considered four additional molecules of the same category, which were labelled as "test molecules". Among these four test molecules, self-assembly of three molecules were already studied experimentally by previous authors. Our host descriptor could successfully predict the resulting

patterns formed by the test molecules. The predictions regarding the energetics of the patterns of the test molecules made by the descriptor was also validated by performing DFT calculations. Therefore, we concluded that the host descriptor had been identified successfully. Next, to answer why some of the host assemblies had structural transformation in the presence of specific guest molecules we identified a simple descriptor for the guest molecules also. The "guest descriptor" was formulated based on the size and geometry of the guest molecules. We found the guest-induced structural transitions in the host assemblies could be explained by the guest descriptor. By combining the host and guest descriptors we found that our results corresponding to the favored pattern and energies of each host and host-guest combination got clustered in the two-dimensional descriptor space. This further prooves that descriptors for the host and guest molecules were identified successfully. Importantly, these descriptors were very simple and obtained at almost zero computational cost, since they depended only on the geometry and form of the isolated host and guest molecules in the gas phase. As per our knowledge, this is the first time that descriptors have been were identified that can predict the architectures of the self-assemblies of organic molecules on surfaces. In this chapter, the descriptors were formulated for a particular class of molecules. Therefore, the form of the descriptor was not universal. These descriptors can be modified so that they can be used to predict the self-assembly of other kinds of molecules also. In this context, the possible extensions for the host descriptor would be to consider the following things, e.g., a different number of alkoxy side chains (including odd numbers), changing the terminal groups (some groups other than COOH) and/or their attachment sites, and altering the chemical nature of the molecular backbone. The guest descriptor could be modified by considering other possible guest molecules of different shapes, sizes and chemical properties.

8.2 Descriptors for the Electronic Structure of Organic Molecules

In chapter 4, we studied the electronic properties of phenyleneethynylene (PE) molecules by varying their chemical motifs, e.g., conjugation length, and the number and position of the alkoxy chains. These parameters were responsible for modifying the HOMO-LUMO gaps of the PE molecules.

We first considered four PE molecules with different conjugation lengths, with however the number and positions of the alkoxy chains remaining the same. We found that the HOMO-LUMO gaps of these molecules decreased with increase in the conjugation length. This result was found to be in agreement with the particle in a box model, with the energy gaps reducing with an increase in box length.[2–4] The increase in conjugation length enhanced electron delocalization in the PE molecules, which reduced the HOMO-LUMO gap.

Next, we studied another set of PE molecules for which the conjugation length was kept fixed but the number and attachment sites of the alkoxy chains are varied. The HOMO-LUMO gaps for these molecules were obtained first using standard density functional theory with both PBE and B3LYP functionals. Since standard DFT with the PBE functional is known to underestimate the HOMO-LUMO gap, the hybrid B3LYP functional was used to get the value of the gap more accurately. Further, the properties related to the electronic transition for each molecule were determined by using time-dependent density functional theory technique. We found that the HOMO-LUMO gaps of the isolated PE molecules having the same conjugation length were related to the shortest distance between the oxygen atoms ($d_{\mathrm{O-O}}$) in the alkoxy chains attached to these molecules. The lower was the value of $d_{\mathrm{O-O}}$, the smaller was the HOMO-LUMO gap. This implies that the HOMO-LUMO gap was affected by the relative position of the alkoxy chains attached to the PE molecules. Therefore, $d_{\mathrm{O-O}}$ can be used as a descriptor to predict the HOMO-LUMO gap of the PE molecules of

the same length but different positions of the alkoxy chains. We used several test molecules to verify this prediction. It was found that whenever the PE molecule was in conjugation the HOMO-LUMO gap could be correlated with the descriptor d_{O-O}. The gap of the PE molecules could therefore be fine-tuned by changing the attachment sites or the distance between the alkoxy groups. We next calculated the HOMO-LUMO gap of monolayers of PE molecules in the gas phase and on graphene. In those cases also we found that the HOMO-LUMO gap depends on the shortest distance between the oxygen atoms in the alkoxy chains, d_{O-O}.

We have not yet been successful in finding a simple model that can explain such dependence of HOMO-LUMO gap on d_{O-O}. One would like to develop a quantum mechanical model to explain why the HOMO-LUMO gap depends on the shortest distance between the oxygen atoms in the alkoxy chains. We hope to succeed in this direction in future work.

8.3 Tuning of Molecule-Graphene Charge Transfer

We showed how the charge transfer between the acceptor-type molecule tetracyanoquinodimethane (TCNQ) and graphene can be modified by the presence of an external electric field in Chapter 5. The molecule/graphene combined system was shown to behave as an electrostatic dipole with a dipole moment proportional to the applied electric field. The electric field was applied in the direction perpendicular to the molecule/graphene plane. The interfacial charge transfer was tuned by changing the direction and magnitude of the electric field. A simultaneous but opposite shift in the molecular states and graphene Dirac point was caused by the application of the external electric field.

The electron transfer from graphene to TCNQ got enhanced by nitrogen doping in graphene. This was shown to be a local effect since the electron transfer from graphene to TCNQ monolayer decreased rapidly as the distance between the TCNQ

and the nitrogen site on graphene got increased. The presence of nitrogen caused a shift in the molecular levels of the TCNQ adsorbed directly above these N-sites. Selective reduction of a TCNQ molecule in a two-dimensional molecular monolayer could be achieved upon N-doping in graphene.

In the future, we can extend this work for other molecule/substrate combinations, e.g., any donor-type molecule on acceptor-doped graphene, or depositing a combination of acceptor and donor-type molecules on graphene or any other substrate under an external electric field. Before we can formulate descriptors that can predict how a certain property (or properties) of different molecule/substrate combinations can be influenced by external electric fields, we need to consider more adsorbate-substrate combinations to create a database. This suggests the future directions for the work described in Chapter 5.

8.4 Measure of Ionicity of Using Descriptors

In Chapter 6, we considered different binary compounds to identify a simple descriptor to predict the ionicity of those compounds. The ratio of the topological charge ($\mathcal{Q}_T$) to the nominal oxidation state (OS) of the cation or anion was chosen as the target property in order to formulate the descriptor. The topological charge on each atom was calculated using Bader analysis.[5, 6] We found a simple descriptor $\Delta\chi/\Delta R$ can predict the ionicity of chemical bonds in the binary compounds, where $\Delta\chi$ and ΔR are the difference in electronegativities and radii, respectively, between the cations and anions in the binary compounds. We obtained a nice correlation between the descriptor $\Delta\chi/\Delta R$ and the target property $\mathcal{Q}_T/OS$. As the value of the descriptor became ≥ 4, $\mathcal{Q}_T/OS$ approached 1, therefore the bonds in the corresponding compounds can be considered to be purely ionic. For the compounds with smaller values of $\Delta\chi/\Delta R$, the target property $\mathcal{Q}_T/OS$ was much less than 1, hence the bonds in the compounds can be considered to be less ionic or more covalent. We found that $\Delta\chi/\Delta R$ can be used as a descriptor or a measure of ionicity. To

the best of our knowledge, this is a novel formulation of a descriptor for ionicity, where it was found that the ionicity of the binary compounds depends not only on the difference in electronegativities between the anions and cations, but also on the difference in the atomic radii between the cations and anions could also play an important role.

In our study, we found that by using the covalent radii of the cations and anions as a measure of atomic size, better correlation to the target property was obtained between the target property and the descriptor compared to the ionic or van der Waals radii. Now, one can think about some other approach to calculate the radii of the cations and anions to see if the performance of the descriptor can be further improved.

8.5 Descriptors for the Efficacy of Aliovalent Doping and its Application in Catalysis

In Chapter 7, we studied aliovalent doping of MgO and the efficacy of the dopants in tuning the charge state of Au nanoparticles adsorbed on doped MgO supports, using *ab initio* density functional theory calculations. We proposed a simple descriptor, $\Delta\chi/\Delta R$ to predict the efficacy of a dopant in modifying the charge state of the supported Au clusters.

First, we performed substitutional doping of bulk MgO with different impurities, keeping the doping concentration fixed at 3.70%. We chose F and Al as the donor-type impurities, while N, P, K, and Li were chosen as the acceptor-type impurities. The descriptor, $\mathcal{D} = \Delta\chi/\Delta R$ was found to predict the amount of charge donated or acceptedby the dopant. Here, $\Delta\chi$ and ΔR are the difference in the electronegativity and the atomic sizes, respectively, between the dopant and the element to which it was bonded. $\mathcal{Q}_T/OS$ vs. The target property, $\mathcal{Q}_T/OS$ became 1 when the dopants were F, Al, and Li, i.e., these dopants acted 'perfectly', since the topological charge became equal to the nominal oxidation state for these dopants. We found a nice

correlation between $\mathcal{Q}_T/OS$ and $\Delta\chi/\Delta R$. As $\Delta\chi/\Delta R$ increases the value of $\mathcal{Q}_T$ approaches OS.

After studying aliovalent doping in bulk MgO we doped the MgO(001) surface with the cationic acceptor Li, cationic donor Al, anionic acceptor N, and anionic donor F. Then we deposited monomers and dimers of Au on the doped MgO(001) surfaces. We found the charge state of the Au clusters adsorbed on the doped MgO(001) supports varies in a wide range depending on the nature and concentration of the dopant. The charge state of the Au clusters affects their adsorption geometry on the doped MgO(001) surfaces. The adsorption site and morphology of the Au nanoclusters on MgO(001) were affected by the type of the dopant. For example, in the case of the donor-doped MgO(001) the Au monomer prefered to adsorb at the hollow site, while on the acceptor-doped MgO, adsorption atop O was energetically more stable. The Au dimer preferred a flat geometry on the donor-doped MgO, while an upright geometry was favored on the acceptor-doped MgO. The descriptor $\Delta\chi/\Delta R$ could successfully predict the performance of the dopant in tuning the charge state of the deposited Au nanoclusters. Investigating the charge state of the Au nanoclusters, we found both Al and F work equally well as donor-type dopants. Li worked as the best acceptor type dopant, since it made the Au monomer positively charged upon adsorption on Li-doped MgO.

The electronic properties of MgO(001) were further tuned by placing it on the Mo(001) support. In the case of Au nanoclusters on the acceptor-doped MgO/Mo systems, electrons were transferred from Mo to the acceptor-doped MgO substrate and then to the deposited Au nanoclusters. For Au nanoclusters on the donor-doped MgO/Mo systems, the MgO substrate works as the source of electrons for the Au nanoclusters and the Mo surface. By comparing the doped-MgO and doped-MgO/Mo systems we found that the probability of electron transfer from the support to the deposited Au nanoclusters got enhanced due to the presence of the Mo surface. The adsorption geometry and the charge state of the Au nanoclusters correlate well with

the work function of the support, except for donor-doped MgO/Mo systems (since for donor-doped MgO/Mo systems charge transfer to Au was not influenced by the electron density at the MgO-Mo interface). A surface with higher work function hinders electron transfer from the support to the Au nanoclusters, while a lower work function of the support enhances electron transfer from the support to the deposited nanoclusters.

The main important result from this study was that we successfully identified a simple descriptor $\Delta\chi/\Delta R$ to predict the efficacy of dopants in MgO. This descriptor was then applied to tune the charge state of Au nanoclusters supported on the doped substrates. Another important result was that we were able to make the charge state of Au monomer +0.25 e. Making the Au monomer positively charged is a challenging task since Au is highly electronegative. One could dope MgO with some other acceptor-type dopant or by changing the support to make the monomer and other clusters of Au more positively charged.

A common theme in much of the work in this thesis is that density functional theory calculations can be used to set up a database which can then be utilized to develop descriptors that correlate with the target property of interest. In the work presented here, these databases have been small, and therefore the descriptors have been formulated using a combination of simple regression techniques and/or physical intuition. As databases get larger, one might instead consider applying machine learning algorithms to large data sets that have been obtained from high throughput searches, so as to extract descriptors. It would be interesting to extend the work done here in this way, and see what emerges.

Bibliography

[1] P. Zalake, S. Ghosh, S. Narasimhan, and K. G. Thomas *Chem. Mater.*, vol. 29, pp. 7170–7182, 2017.

[2] S. Fratiloiu, L. P. Candeias, F. Grozema, J. Wildeman, and L. Siebbeles *J. Phys.*

Chem. B, vol. 108, p. 19967, 2004.

[3] J. Autschbach *J. Chem. Ed.*, vol. 84, p. 1840, 2007.

[4] S. S. Zade and M. Bendikov *Org. Lett.*, vol. 8, no. 23, pp. 5243–5246, 2006.

[5] W. Tang, E. Sanville, and G. Henkelman *J. Phys.: Condens. Matter*, vol. 21, p. 084204, 2009.

[6] R. F. W. Bader, *Atoms in Molecules - A quantum theory.* New York: Oxford University Press, 1990.